SECONDARY RANGE COMPRESSION FOR IMPROVED RANGE/DOPPLER PROCESSING OF SAR DATA WITH HIGH SQUINT

by

ALFRED RUDOLF SCHMIDT

B.Sc. Engineering Physics, Queen's University, 1981

A THESIS SUBMITTED IN PARTIAL FULFILMENT OF

THE REQUIREMENTS FOR THE DEGREE OF

MASTER OF APPLIED SCIENCE

in

THE FACULTY OF GRADUATE STUDIES

Department of Electrical Engineering

We accept this thesis as conforming

to the required standard

THE UNIVERSITY OF BRITISH COLUMBIA

September 1986

Department of Electrical Engineering

The University of British Columbia
2075 Wesbrook Place
Vancouver, Canada
V6T 1W5

Date: September 1986

Abstract

This thesis examines a new algorithm, to be called secondary range compression (SRC), for significantly improving the range resolution of the range/Doppler synthetic aperture radar (SAR) processing algorithm when the radar antenna is significantly squinted away from the zero Doppler direction. The algorithm was recently introduced by Jin and Wu [13] for application to the SEASAT SAR sensor. Significant extensions of their algorithm and models are presented.

First the model of range broadening in the basic range/Doppler algorithm is extended by using a more general form for the range compressed profile. A mathematical theory is developed to examine more closely the approximations involved in both basic range/Doppler processing and SRC and to explore alternate SRC implementations. The theory is used to derive the SRC algorithm as a matched filter directly from the point target response model rather from the simplified range compressed response used by Jin and Wu.

Two new discrete implementations (azimuth SRC and range SRC) are developed for both single-look and multilook processing. In addition two new alternate methods of multilook SRC are presented : fixed SRC and look-dependent SRC. The sensitivity of the SRC algorithms to parameter errors is investigated.

Extensive simulations are developed to quantify the image quality produced by each algorithm for a variety of

processing parameters. The simulation results with nominal RADARSAT parameters show that the SRC algorithms can significantly extend the range of squint angles which can be processed with the range/Doppler type of algorithm.

Table of Contents

List of Symbols and Abbreviations

FM	frequency modulation
FFT	fast Fourier transform
IRW	impulse response width
ISLR	integrated sidelobe ratio
PRF	pulse repetition frequency
RCM	range cell migration
RCMC	range cell migration correction
SAR	synthetic aperture radar
SRC	secondary range compression
TBP	time-bandwidth product
$A_1(f)$	azimuth spectrum broadening function
$A_2(f)$	azimuth reference function broadening function
β_A	azimuth Kaiser-Bessel parameter
β_I	SRC/RCMC Kaiser-Bessel parameter
β_i	incidence angle
β_R	range Kaiser-Bessel parameter
B_r	range -3dB chirp bandwidth
c	propagation velocity of radar pulse
c_1	slope of RCM curve in azimuth time domain
c_2	slope of RCM curve in azimuth frequency domain
D	azimuth antenna length
f	azimuth frequency
f_C	azimuth beam center (Doppler centroid) frequency
f_L	azimuth look center frequency

f_{PBW}	azimuth processed bandwidth
f_r	range frequency
F_{sr}	complex range sampling rate
$g(t)$	SRC range filter
$g_C(t,f)$	combined SRC/RCMC range filter
h_s	satellite altitude
$h(t,\eta)$	point target response before processing
$h_A(t,\eta)$	azimuth point target response
$h_F(t,\eta)$	azimuth reference phase function
$h_{FRB}(t,\eta)$	range bandlimited $h_F(t,\eta)$
$h_R(t,\eta)$	range point target response
$h_{RC}(t,\eta)$	range compressed point target response
$h_{RCP}(t)$	1-D range compressed profile
I	# of SRC/RCMC filter versions
$I_0\{\ \}$	zeroth order modified Bessel function
K_A	azimuth FM rate
K_R	range FM rate
K_{RM}	modified range FM rate for range SRC
K_r	SRC/RCMC FFT array length
K_{SRC}	SRC FM rate
L	length of SRC/RCMC filter versions
λ	wavelength

M	length of range FFT
N	length of azimuth FFT
η	azimuth time
η_{PBW}	azimuth processing interval
$\Delta\eta_{3dB}$	-3dB one-way azimuth antenna timewidth
ρ_{sr}	slant range cell size ($= c/[2F_{sr}]$)
r_C	beam center range
r_e	earth radius at equator
r_o	slant range of closest approach
$r(\eta)$	RCM curve in azimuth time domain
$r_i(f)$	RCM curve in azimuth frequency domain
$s_T(t)$	baseband radar pulse
t	range time
T	range sampling interval
T_A	azimuth sampling interval
τ	range pulsewidth
θ_i	orbit inclination angle
v_b	beam velocity
v_e	earth rotational velocity
v_{eq}	equivalent satellite velocity
v_g	ground velocity
v_s	satellite orbital velocity
v_{ss}	sub-satellite orbital velocity

$w_a(\eta)$	azimuth antenna weighting function
$W_A(f)$	azimuth window function
$W_R(f_r)$	range window function
$*$	2-D convolution
$*_\eta$	azimuth convolution
$*_t$	range convolution

List of Tables

List of Figures

Acknowledgements

I wish to thank my supervisor, Dr. M.R. Ito, for his help and encouragement throughout the course of this research. I also wish to thank Dr. I.G. Cumming of MacDonald, Dettwiler and Associates (MDA) for suggesting the thesis topic and for providing numerous insightful suggestions. Dr. M. Vant of Communications Research Centre (CRC) also provided helpful discussions.

I am grateful for the financial assistance provided by MDA, the University of British Columbia, CRC, and Computing Devices Company (ComDev) of Ottawa.

1. INTRODUCTION

This thesis discusses the application of a new secondary range compression (SRC) algorithm to the range/Doppler synthetic aperture radar (SAR) processing algorithm. Particular consideration is given to the application of SRC to Canada's proposed RADARSAT SAR sensor.

1.1 BACKGROUND

The range/Doppler algorithm [6,18,19,24,26] is a well known method for the efficient compression of SAR data. The compressed point target response of the algorithm becomes severely broadened in the range direction when the -3dB azimuth time-bandwidth product (TBP) becomes small (less than unity). SRC is a new efficient algorithm which significantly reduces the range broadening and associated image quality degradations.

The TBP has a multitude of definitions depending on the desired use. For this thesis the TBP is defined as the product of the actual -3dB widths in the time and frequency domains. The TBP of any signal has a fixed lower bound which is somewhat less than 0.5 using the current definition. A small azimuth TBP may occur in SAR when there is large range cell migration (RCM). RCM is the migration of a point target's energy through more than one range resolution cell over the antenna illumination period. Large RCM may occur in spaceborne SARs, such as Canada's proposed RADARSAT SAR [22] or NASA's SEASAT SAR [11], when the equivalent squint angle

of the antenna relative to the zero Doppler direction is large.

Large RCM causes the azimuth time exposure of a point target in a given range cell to decrease since the target energy migrates rapidly across range cells. Under large azimuth TBP conditions, the time and frequency domain azimuth signals exhibit an approximate one-to-one correspondence. Thus the decrease in azimuth timewidth results in a decreased bandwidth and consequently a decreased azimuth TBP. The time-frequency correspondence is predicted by the principle of stationary phase [17] for large TBP signals. When the azimuth TBP falls below unity, the correspondence is no longer valid and the azimuth spectrum becomes broadened relative to its predicted bandwidth. This spectrum broadening appears after the azimuth FFT, which is used for fast azimuth convolution in the range/Doppler algorithm.

Since the point target energy lies along a sloped curve (the RCM curve) in both range-time/azimuth-time and range-time/azimuth frequency space, the azimuth spectrum broadening causes the point target energy to be similarly broadened in the range time direction. If the range broadening is left uncorrected as in the basic range/Doppler algorithm, the final compressed point target response becomes broadened in range.

SRC was first proposed by Jin and Wu [13] in 1984 as a method for extending the maximum squint angle which can be

processed by the range/Doppler algorithm. Their paper presented a model for the range broadening of the range compressed point target response after the azimuth Fourier transform. Their improved model accounted for the broadening in magnitude and phase of the azimuth spectrum. However the model idealized the range compressed profile as a simple infinite duration sinc function. This approximation does not include the effects of the range and azimuth windows which are usually applied in the respective frequency domains to control sidelobe levels. Also several approximations required to develop the model were not fully stated or validated. A continuous time, infinite duration, azimuth compression filter matched to the approximate range compressed signal model was derived. The filter included a separate SRC filter which was applied as a continuous range time convolution to the azimuth spectrum. The details of the discrete implementation of this filter were not presented. Qualitative simulation results were shown for SEASAT SAR parameters.

1.2 OBJECTIVES

The objectives of this thesis are summarized as follows:

1. The range broadening model of Jin and Wu is to be extended to accurately model the range compressed profile including the effects of range windowing. All approximations and assumptions are to be explicitly

stated and examined for their range of validity.

2. Jin and Wu state that the range compressed point target response may be used as the azimuth matched filter reference function (see equation (20) in [13]). However this is only true when the range compressed profile is approximated by a sinc function and no range bandlimiting or windowing is applied during range compression. The azimuth filter is to be reformulated for the more general case by matching the filter directly to the point target response before range compression.

3. The basic SRC algorithm is to be rederived using the extended azimuth matched filter model. Alternate methods for implementing SRC are to be examined and evaluated in terms of efficiency and accuracy.

4. The SRC algorithm derived by Jin and Wu consisted of a range time convolution with a continuous-time SRC filter of infinite time duration. Methods of implementing this filter as a discrete finite length SRC filter are to be developed. In particular, combinations of the SRC filter with the frequency domain RCMC interpolator are to be explored. This algorithm will be called azimuth SRC.

5. Jin and Wu state that it is possible to perform SRC

during range compression but do not derive the theory or an algorithm. The possibilities of implementing SRC during range compression are to be explored and evaluated. This algorithm will be called range SRC.

6. SAR images are prone to high levels of speckle noise due to the coherent nature of the radar illumination. To reduce the speckle noise the processed aperture is often subdivided into separate "looks" which are then incoherently summed. New methods of implementing SRC with multilook range/Doppler processing are to be developed.

7. The signal parameters used in practical SAR systems may contain estimation errors or errors caused by the use of constant parameters in block processing. The sensitivity of the SRC filter to parameter errors is to be examined.

8. In order to choose the necessary processing algorithms and parameters for a given image quality requirement, quantitative design curves of expected image quality are needed. Computer simulations are to be performed in order to quantify the following items with particular consideration being given to the RADARSAT SAR sensor. The simulated image degradations and improvements are to be measured as a function of squint angle:

a. measure the range and azimuth broadening of the compressed point target response of the basic range/Doppler algorithm to determine the squint limitations of both single-look and multilook algorithms

b. determine the accuracy of the range broadening model in comparison with actual broadening measurements

c. quantify the image quality improvements for the new SRC algorithms for single-look and multilook processing with various processing parameters

d. examine the image degradations caused by SRC parameter errors for all algorithms.

1.3 STRUCTURE OF THE THESIS

The thesis is divided into several sections. Chapter 2 introduces the basic concept of SAR image formation as a 2-D matched filtering operation of a received radar signal which is approximately linear FM in both dimensions. A model of spaceborne SAR geometry is developed to define the variations of target range with azimuth time and other key signal parameters. The image quality measurements of interest are introduced and the measurement procedures are outlined.

Chapter 3 examines the theory and limitations of basic range/Doppler compression without SRC. A model of the signal returned from a point target is developed to use as a reference function for the matched filter. The model is also used in the simulations for creating a simulated range compressed point target response. The results of extensive simulations with nominal RADARSAT parameters are summarized.

Chapter 4 develops a mathematical model of the azimuth spectrum broadening and range broadening which occurs with the basic range/Doppler algorithm at large squint angles. A simple accurate model of azimuth broadening is also presented.

Chapter 5 extends the theory used in chapter 4 to develop an improved matched filter which includes SRC. Two new alternate techniques for the discrete implemention of SRC (azimuth SRC and range SRC) are presented. Extensive simulation results are discussed to evaluate the new algorithms.

Chapter 6 examines the application of SRC to multilook range/Doppler compression. The new concepts of fixed (look-independent) and look-dependent SRC filters are presented. Simulations of multilook compression (with 4-looks) with and without SRC are performed to quantify the improvements.

Chapter 7 examines the effects of SRC parameter estimation errors and block processing invariance regions on image quality. A model is developed to relate these errors

to equivalent phase errors which occur in processing without SRC.

Finally chapter 8 presents final conclusions and suggests areas for further research on SRC.

2. THE SYNTHETIC APERTURE RADAR (SAR) CONCEPT

Synthetic aperture radar processing is a method of obtaining image resolutions much finer than the along-track beamwidth of the radar antenna from a moving platform. It has been successfully applied to both airborne and spaceborne radars to provide all-weather high resolution imaging capabilities. Strip-map mode sensors, such as RADARSAT and SEASAT, orient the boresight of the antenna perpendicular to the direction of travel of the platform, i.e., in the cross-track direction, and off to one side of the ground track.

An azimuth (along-track) antenna aperture much larger than the size of the physical antenna is synthesized by properly combining the received radar pulses over a coherent integration period with appropriate weighting. The azimuth resolution is inversely proportional to the synthesized aperture length. The returns from point targets at different ground positions are resolved in range (cross-track) by differences in the time delay of the transmitted radar pulses and in azimuth by their Doppler shift.

The radar pulse is typically a linearly frequency modulated (FM) pulse with large TBP. In range/Doppler processing the received pulses are compressed in range using standard pulse compression techniques to get a range compressed signal with a small TBP. The azimuth signal has a similar modulation (approximately linear FM) due to the changing distance between the sensor and target. By applying

pulse compression techniques in the azimuth direction a well resolved image can be obtained.

An additional complication of the processing occurs when the change in range to a point target over the azimuth integration period is larger than the range cell size. This effect, called range cell migration (RCM), causes the signal energy from a point target after range compression to migrate across several range cells. Consequently the azimuth compression becomes a 2-D operation. The basic range/Doppler algorithm separates this 2-D azimuth operation into two 1-D operations :

1. Range Cell Migration Correction (RCMC) in which the range compressed point target energy is interpolated and shifted in range so that the energy lies along a single azimuth line.

2. Azimuth correlation with a 1-D reference phase function.

For computational efficiency these operations are performed in the azimuth frequency domain via fast convolution. For large azimuth TBP, linear FM type signals, the magnitude and phase characteristics of the azimuth frequency domain signals can be simply related to the azimuth time domain signals by a linear scale factor using the principle of stationary phase [17]. In such cases, which occur when there is little RCM and a small squint angle, a

zero-phase sinc-type interpolator can be used for RCMC. Block processing efficiency can be achieved since the trajectories of point targets which are adjacent to each other in azimuth time follow a common RCM curve in the azimuth frequency domain. This allows RCMC and azimuth compression to be applied to many targets simultaneously.

However when the azimuth time exposure in a range cell becomes small due to RCM and the azimuth TBP falls below unity, the magnitude and phase characteristics of the frequency domain signal become broadened relative to their corresponding time domain signals. The broadened frequency domain signal can be properly compressed by applying a secondary compression in either the range time or azimuth frequency direction. Since the width in samples of the broadened function is much smaller in range than in azimuth, the filter is more efficiently implemented in range, hence the name secondary range compression (SRC).

The SRC filter can be viewed as convolution with a quadratic phase range filter which recompresses the broadening which occurs in the azimuth Fourier transform. Two efficient implementations of this secondary range filter have been investigated :

1. Azimuth SRC in which the secondary range filter is combined with the RCMC interpolator during azimuth compression.

2. Range SRC where the secondary range filter is combined with the range frequency domain, reference function during range compression.

The next section discusses a model of the spaceborne SAR sensor geometry which is used to derive the range cell migration equation (i.e., the variation of range with azimuth time) and other signal parameters. For the simulations in later sections, a set of nominal RADARSAT parameters has been chosen. These are listed in table 1.

Parameter	Symbol	Value	Units
range -3dB chirp bandwidth	B_r	17.28	MHz
single-look azimuth Kaiser-Bessel parameter	β_A	1.5	
multilook azimuth Kaiser-Bessel parameter	β_A	2.7	
SRC/RCMC Kaiser-Bessel parameter	β_I	2.5	
incidence angle	β_i	20	deg
range Kaiser-Bessel parameter	β_R	2.7	
azimuth antenna length	D	14.0	m
azimuth processed bandwidth (θ_s=0°)	f_{PBW}	942	Hz
complex range sampling rate	F_{sr}	19.872	MHz
satellite altitude	h_s	1007.4	km
# of SRC/RCMC filter versions	I	16	
SRC/RCMC FFT array length	K_r	128	
length of SRC/RCMC filter versions	L	4,8,16,32	
length of range FFT	M	2048	
length of single-look azimuth FFT	N	1024	
wavelength	λ	0.05656	m
azimuth processing interval	η_{PBW}	0.513	s
pulse repetition frequency	PRF	1177.9	Hz
slant range cell size ($c/[2F_{sr}]$)	ρ_{sr}	7.543	m
earth radius at equator	r_e	63716	km
slant range of closest approach	r_o	1072.1	km
range pulsewidth	τ	36.4	μs
orbit inclination angle	θ_i	99.5	deg
beam velocity	v_b	7.4575	km/s
earth rotational velocity	v_e	0.4638	km/s
satellite orbital velocity	v_s	7.35	km/s
equivalent satellite velocity	v_{eq}	7.4575	km/s
azimuth oversampling factor		1.25	
range oversampling factor		1.15	

Table 1. Nominal Radarsat Parameters

2.1 MODEL OF SAR GEOMETRY

The production of high resolution SAR images requires an accurate model of the physical geometry of the space platform with respect to the earth's surface. This study uses a simplified flat earth geometric model which exhibits the essential properties of SAR signals. A more sophisticated spherical earth, circular orbit geometric model is used to derive accurate estimates of the actual signal parameters which are then applied to the simplified model.

The spherical earth, circular orbit geometric model is used to derive an equivalent relative velocity between the sub-satellite point and the surface of the earth. After mapping into the slant range plane (the plane containing the platform velocity vector and the vector joining the platform and a point target on the ground), the equivalent velocity is applied to a locally flat model of the region of the earth under the satellite. Second order effects caused by local curvature of the earth, or variations in the earth's radius or satellite height above the surface are excluded from the simulations since the added complexity adds little insight into the range broadening process. These secondary effects can usually be accounted for by using modified estimates of the signal parameters.

Vant [23] provides a good discussion of a similar spherical earth model. For simplicity, the satellite position is arbitrarily chosen to be above the equator since

the rotation of the earth typically has its greatest effect there. Figure 2.1 shows the geometry of the sub-satellite point in an inertial frame of reference. The sub-satellite point moves with velocity $\bar{v}_{ss}$ and the earth's surface moves at tangential velocity $\bar{v}_e$ beneath it, where

$$\bar{v}_{ss} = \bar{v}_s / C_a \tag{1}$$

and $\bar{v}_s$ is the tangential velocity of the satellite in its orbit. The factor C_a, the ratio between the satellite velocity and the sub-satellite point velocity, is given by

$$C_a = (r_e + h_s) / r_e \tag{2}$$

where r_e is the radius of the earth and h_s is the height of the satellite above the earth's surface. The equivalent relative ground velocity, $\bar{v}_g$, between the sub-satellite point and the earth's surface is given by :

$$\bar{v}_g = \bar{v}_{ss} - \bar{v}_e \tag{3}$$

$$| \bar{v}_g | = [v_{ss}^2 + v_e^2 - 2v_{ss}v_e\cos(\theta_i)]^{1/2} \tag{4}$$

where θ_i is the inclination angle of the satellite orbit. This ground velocity is translated back into an equivalent satellite velocity, $\bar{v}_{eq}$, in the slant range plane as

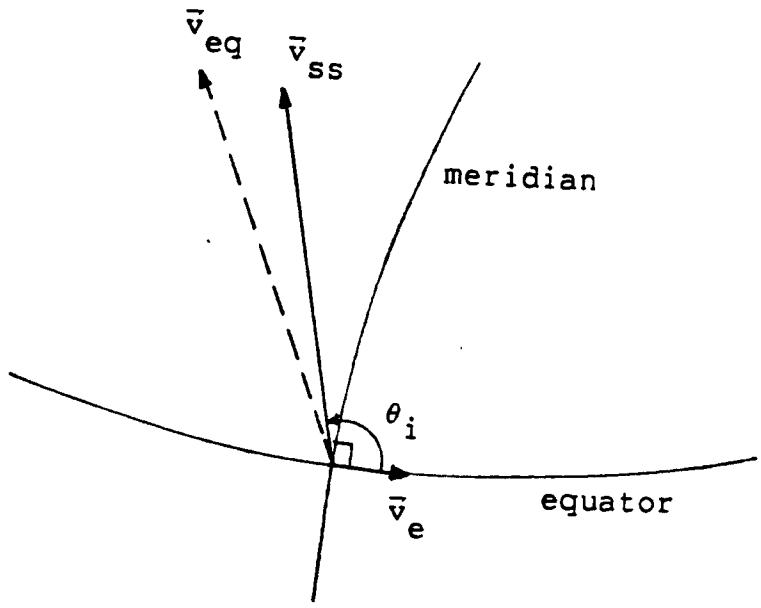

Figure 2.1. Spherical earth model for velocity calculation.

$$\bar{v}_{eq} = \bar{v}_g \, C_a \tag{5}$$

In order to simulate the azimuth antenna weighting function, it is necessary to know the velocity at which a point target travels through the antenna beam in the antenna azimuth direction. For convenience, the beam velocity, $\bar{v}_b$, will be assumed to be constant and equal to $\bar{v}_{eq}$.

The derived equivalent velocities are applied to the flat earth model shown in figure 2.2. The satellite travels with velocity $\bar{v}_{eq}$ at a height h_s above the ground. The slant range of closest approach, r_o, is determined by the incidence angle, β_i, as

$$r_o = h_s \, / \, \cos(\, \beta_i \,) \tag{6}$$

The antenna boresight may be squinted away from the r_o direction by the squint angle θ_s in the slant range plane. The squint angle is defined to be positive when the antenna is pointing behind the zero Doppler direction resulting in a negative Doppler beam center frequency. Azimuth time, η, is measured relative to the ground position of closest approach as shown in figure 2.3. From this figure, the following quantities can be deduced

$$r(\eta) = [r_o^2 + (v_{eq}\eta)^2]^{1/2} \tag{7}$$

$$\eta_C = r_o \tan(\theta_s) \, / \, v_{eq} \tag{8}$$

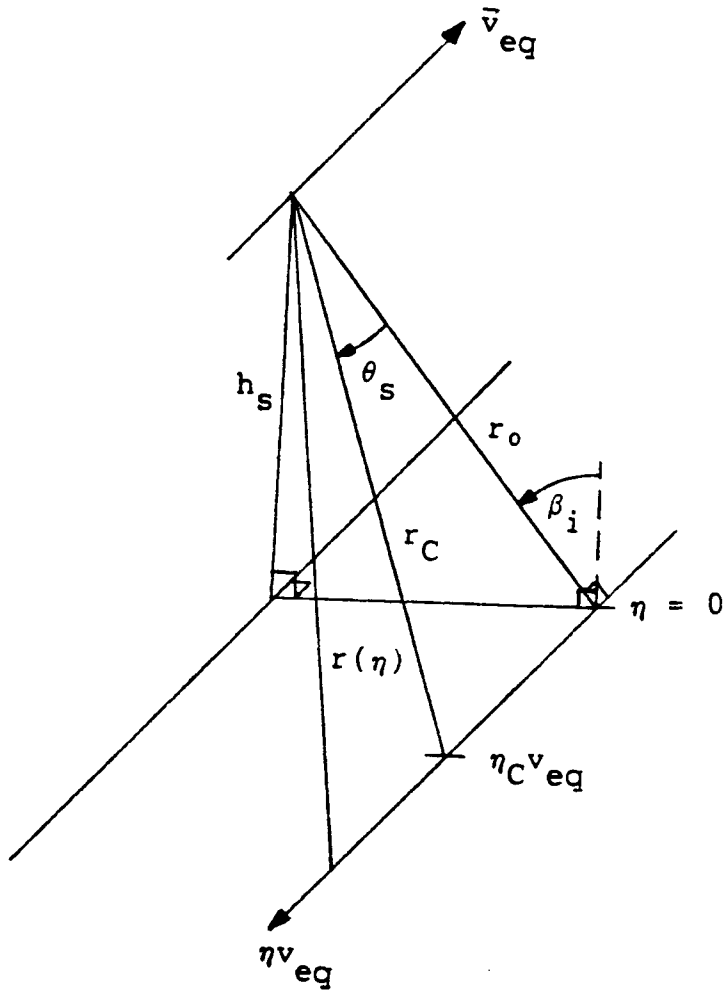

Figure 2.2. Flat earth model for local geometry.

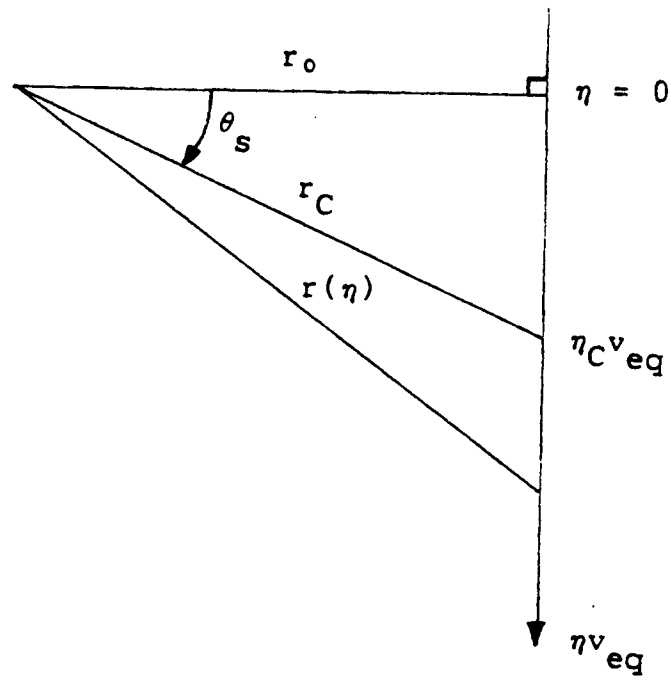

Figure 2.3. Slant range plane.

$$r_C = r(\eta_C) \tag{9}$$

where $r(\eta)$ is the range migration equation which defines the instantaneous range to a point target with range of closest approach, r_o, and η_C and r_C are the beam center azimuth time and range respectively.

It is useful at this point to examine an approximation to the RCM equation in greater detail. The RCM curve can be expanded into a Taylor series form about the azimuth beam center crossing time, η_C, as follows :

$$r(\eta) = r(\eta_C) + r'(\eta_C)(\eta-\eta_C) + r''(\eta_C)(\eta-\eta_C)^2/2 + \ldots \tag{10}$$

The first term represents the range to the beam center point which is constant in the spherical earth/orbit model. The second term is the linear component of RCM and is commonly referred to as range walk. The higher terms will be collectively referred to as range curvature.

In most satellite-borne systems such as RADARSAT range walk is the dominant component of RCM. For nominal RADARSAT parameters, range walk increases almost linearly with squint angle from zero at 0°, to 8.9 range cells at 1°, to 88 range cells at 10°. Range curvature is comparatively small being an approximately constant 0.23 range cells. When range walk and/or curvature exceed the range resolution, some form of RCM correction (RCMC) is required to maintain good azimuth

and range resolutions.

Range walk increases approximately linearly with wavelength whereas range curvature increases approximately as the square of the wavelength. Consequently, for longer wavelength satellite-borne SAR's such as SEASAT, range walk may be several times larger and range curvature may be an order of magnitude larger.

Terms up to the quadratic are usually sufficient for characterizing RCMC whereas higher order terms may be necessary to accurately represent azimuth phase. By dropping terms higher than the quadratic and substituting for $r'(\eta_C)$ and $r''(\eta_C)$ in terms of the instantaneous frequency f_C and frequency rate K_A at the beam center crossing time, the Taylor series can be written as :

$$r(\eta) \simeq r(\eta_C) - (\lambda/2)[\ f_C(\eta-\eta_C) + K_A(\eta-\eta_C)^2/2\ ] \tag{11}$$

$$\simeq r_1 - (\lambda/2)[\ f_1\eta + K_A\eta^2/2\ ] \tag{12}$$

where

$$r_1 = r(\eta_C) + (\lambda/2)[\ f_C\eta_C - K_A\eta_C^2/2\ ] \tag{13}$$

$$f_1 = f_C - K_A\eta_C \tag{14}$$

This approximate form of the RCM equation will be used in subsequent sections to define the azimuth phase response and

its Fourier transform.

2.2 IMAGE QUALITY MEASUREMENTS

This section discusses the relevent image quality measures of the point target response and outlines the methods used in the simulations for their measurement. Several measures computed from the point target response are commonly used to determine the quality of a SAR image. These are as follows :

1. Impulse Response Width (IRW).

   The -3dB impulse response widths in both range and azimuth are standard measures of resolution. They are measured by interpolating in the range and azimuth directions by a factor of 128. The peak magnitude in each direction is determined. Then the distance between the -3dB points is computed using linear interpolation between the already interpolated samples.

2. Integrated Sidelobe Ratio (ISLR).

   The ISLR is the ratio of the integrated energy in the sidelobe region to the integrated energy in the mainlobe region. The sidelobe region is defined as all samples inside of a rectangle whose sides are located at the measured -3dB positions in range and azimuth. The sidelobe region is defined as all samples outside of a rectangle which is 3 times the size of the mainlobe rectangle and which is centered at the same position.

The 2-D ISLR is measured on a 2-D array of size 256x256 which has been interpolated by a factor of 8 in both directions from a 32x32 array. The integrations are performed by summing squared magnitudes. Although this array does not extend out to the ends of the sidelobe regions, it contains most of the sidelobe energy and was chosen because of memory constraints. Summing the sidelobe region over a limited area is a good approximation when little broadening occurs, i.e., for low squint angles. However, the approximation breaks down for large broadening as will be shown in the simulations. Fortunately, the approximation is valid over the broadening levels of interest in the simulated system. The ISLR is also measured on 1-D arrays in range and azimuth. These provide indications of the broadening in each direction. The 1-D ISLR is measured on an array of length 4096 which has been interpolated by a factor of 128 from a length 32 array.

3. Peak Sidelobe Ratio (PSLR).

The PSLR is the ratio of the magnitude of the largest sidelobe in the sidelobe region to the magnitude of the peak of the point target response. In 1-D, range or azimuth, the PSLR is measured on an array which has been interpolated by a factor of 128. In 2-D, the peak sidelobe is measured in the 2-D sidelobe region of an array which has been interpolated by a factor of 8 in

both directions.

4. Peak Magnitude Degradation.

As more energy is spread into the sidelobes, the magnitude of the point target response peak decreases causing a decrease in signal-to-noise ratio (SNR). The decrease in peak magnitude has been measured as a function of squint angle. However the SNR is not directly related to the measured peak magnitude since a normalization based on the noise power distribution must be used. In the simulations the peak magnitudes are normalized to the sum of squares of the RCMC or combined SRC/RCMC filter coefficients. This normalization is appropriate for a white distribution of noise over all range cells. The peak magnitudes are also normalized by the azimuth processed bandwidth which decreases with increasing squint angle. The processed bandwidth is proportional to the noise power if the noise in the azimuth signal is white.

3. BASIC RANGE/DOPPLER COMPRESSION

This section presents a theory to describe the basic range/Doppler compression algorithm. Discrete implementations of the range and azimuth compression operations are presented. Extensive simulations are used to quantify the image degradations which occur for large squint angles.

The range/Doppler algorithm, also known as a frequency domain interpolation algorithm or a frequency domain correlation algorithm, has been described in several good papers [2,6,20,21,24,26]. The theory developed here provides further insight into the approximations involved in deriving the basic range/Doppler algorithm as a filter matched to the point target response. The approximate one-to-one correspondence between the time and frequency domain azimuth signals which is valid for large azimuth TBP signals is used. Later sections provide a refinement of this approximation which accounts for the spectrum broadening process and provides the basis for the SRC algorithm.

A model of the return from a point target which was presented by Jin and Wu [13] is extended to include the range window. The model is used in the simulator to generate a 1-D point target return signal which is subsequently compressed in range. Range compression is performed by range matched filtering and windowing in the range frequency domain to produce a 1-D range compressed profile. From this, a 2-D range compressed signal is simulated by shifting the

range profile peak in range along the RCM curve defined by $r(\eta)$ and multiplying by the azimuth phase coding which is approximately linear FM. Azimuth compression, which is also performed as a fast convolution in the frequency domain, consists of applying an azimuth fast Fourier transform (FFT), performing RCMC, multiplying by a 1-D azimuth reference phase function and window function, and transforming back to the azimuth time domain using an inverse FFT.

The image quality of the simulated compressed point target responses are measured for several squint angles. These measurements provide a baseline for comparison with later simulations using SRC.

3.1 POINT TARGET RESPONSE MODEL

The complex received signal after quadrature demodulation from a point target with range of closest approach r_0 can be modelled in continuous range and azimuth time as [26]

$$h(t,\eta) = h_A(t,\eta) * h_R(t,\eta) \tag{15}$$

$$h_A(t,\eta) = w_a(\eta) \exp[-j4\pi r(\eta)/\lambda] \, \delta[t - 2r(\eta)/c] \tag{16}$$

$$h_R(t,\eta) = \delta(\eta) \, s_T(t) \tag{17}$$

where t is continuous range time measured from the time of transmission of the pulse of interest, $w_a(\eta)$ is the azimuth

antenna function, c is the speed of light, and * denotes 2-D convolution.

The function $h_R(t,\eta)$ represents the response in the range direction after quadrature demodulation and can be closely approximated by the transmitted complex modulation function, $s_T(t)$. This approximation is valid when the Doppler shift is much smaller than the transmitted bandwidth as is usually the case.

The function $h_A(t,\eta)$ represents the hypothetical continuous azimuth response to an impulse-type radar pulse assuming that the radar does not move appreciably during the transit time of the pulse. A good discussion of the validity of this stop-start approximation in which the sensor is assumed to be stationary during pulse transmission and reception is given by Barber [2]. Although azimuth time is actually sampled at the pulse repetition frequency (PRF) of the radar, the continuous azimuth time model is valid if the PRF is chosen sufficiently high to prevent significant aliasing of the azimuth signal.

Optimum SAR processing in a least mean squared error sense consists of filtering the return signal with a 2-D matched filter which is matched to the point target signal. Therefore the ideal matched filter impulse response can be written as :

$$h^*(-t,-\eta) = h_R^*(-t,-\eta) * h_A^*(-t,-\eta) \tag{18}$$

The filter consists of two parts :

1. a range matched filter, $h_R^*(-t,-\eta)$, which compresses the coded range pulse

2. and an azimuth matched filter, $h_A^*(-t,-\eta)$, which compresses the azimuth phase coding and compensates for RCM.

Additional range and azimuth filtering in the form of frequency domain windows is often applied in order to control the tradeoff between sidelobe levels and impulse response widths. In addition the azimuth weighting due to the antenna aperture is dropped from the azimuth matched filter since its effect is similar to the azimuth window.

The following sections describe the approximations required to derive the range and azimuth matched filters of the basic range/Doppler algorithm.

3.2 RANGE COMPRESSION

Range compression may be viewed as a convolution of the received signal with a filter, $h_R^*(-t,-\eta)$, matched to the transmitted pulse and a window function, $w_R(t)$, which is designed to reduce the energy in the sidelobes. The continuous 2-D range compressed signal may be written as

$$h_{RC}(t,\eta) = h(t,\eta) * h_R^*(-t,-\eta) * [\delta(\eta)\ w_R(t)] \qquad (19)$$

$$= h_A(t,\eta) * [\delta(\eta)\ h_{RCP}(t)] \tag{20}$$

where

$$h_{RCP}(t) = s_T(t) *_t s_T^*(-t) *_t w_R(t) \tag{21}$$

is the 1-D range compressed profile which is usually similar in shape to a sinc function, and $*_t$ denotes convolution in range time. In this form the range compressed signal is expressed as a range time convolution of the 1-D range compressed profile with a 2-D phase function, $h_A(t,\eta)$, which is non-zero only along the RCM curve.

It should be noted that the time origin of the range compressed signal has been selected so that the range compressed profile is symmetric about t=0. For RADARSAT and most other satellite SAR's, the transmitted signal is a linear FM pulse which can be represented at baseband as

$$s_T(t) = a(t)\ \exp[-j\phi(t)] \tag{22}$$

$$a(t) = \mathrm{rect}(t/\tau) \tag{23}$$

$$\phi(t) = -\pi K_R t^2 \tag{24}$$

where a(t) is the amplitude function, $\phi(t)$ is the phase modulation function, τ is the pulsewidth, and K_R is the range linear FM rate.

After some manipulation, the range compressed profile can be shown to have the form of a weighted sinc function [23] :

$$h_{RCP}(t) = \{(\tau-|t|)\mathrm{rect}(t/2\tau)\mathrm{sinc}[\pi K_R t(\tau-|t|)]\} *_t w_R(t) \tag{25}$$

The range compression convolution is performed more efficiently in the range frequency domain using fast convolution. Fast convolution is computationally efficient when the length of the convolution kernel in samples is a power of 2 larger than about 32. The fast convolution method consists of :

1. Fourier transforming the range matched filter (which is the complex conjugate of the Fourier transform of the transmitted pulse) and the received pulse (for the simulations the received pulse is assumed to be the same as the transmitted pulse with appropriate delay);

2. multiplying together the received signal, the matched filter, and the sidelobe control window;

3. and inverse Fourier transforming the result.

In continuous time and frequency theory, the fast convolution range compression operation can be expressed as

$$h_{RCP}(t) = F^{-1}\{ W_R(f_R) \ |S_T(f_R)|^2 \} \tag{26}$$

where $W_R(f_R)$ and $S_T(f_R)$ are the Fourier transforms of $w_R(t)$ and $s_T(t)$ respectively.

3.3 SIMULATION OF THE RANGE COMPRESSED PROFILE

This section describes the method used in the simulations to generate a discrete, range compressed profile, $\hat{h}_{RCP}(m)$. Where necessary, the symbol ^ will be used to denote discrete signals. A discrete, linear FM modulation function, $\hat{s}_T(m)$, is formed in the range time domain as

$$\hat{s}_T(m) = a(mT) \exp[-j\phi(mT)] \ , \ -(M/2) < m \leq (M/2) \tag{27}$$

where T is the range sampling period and a(mT) is the rectangular pulse envelope of width τ. This function is transformed with a range FFT of length M where $M > \tau/T$. The frequency samples are squared and a multiplicative sidelobe control window is applied to get

$$\hat{H}_{RCP}(k) = W_R(k) \ |\hat{S}_T(k)|^2 \ , \ -(M/2) < k \leq (M/2) \tag{28}$$

where $\hat{S}_T(k)$ is the FFT of $\hat{s}_T(m)$, $W_R(k)$ is the frequency domain window function, and k is the frequency index.

Many window functions are available for controlling the sidelobes. The principal window used in the simulations is a Kaiser-Bessel window defined as [12]

$$W_R(k) = I_0\{\beta_R[1-(2k/M)^2]^{1/2}\} \;/\; I_0\{\beta_R\} \;, \qquad -(M/2) < k \le (M/2) \tag{29}$$

where β_R is a window parameter which controls the amount of weighting. As β_R is increased, the mainlobe width of the range compressed profile increases whereas the energy in the sidelobes and the magnitude of the peak sidelobe decrease.

The zeroth-order modified Bessel function of the first kind, I_0, is approximated by the power series :

$$I_0(x) = \sum_{p=0}^{P} [\; (x/2)^p \;/\; p! \;]^2 \tag{30}$$

The number of terms used in the simulations (P=15) provides an accuracy of about 14 significant figures for the Bessel function.

Since the simulated range compressed profile defines the weighting along each azimuth line of the simulated 2-D range compressed signal, a close approximation of the continuous profile is desired. Thus the discrete profile is interpolated by a factor I (I=16 in the simulations) by zero padding the frequency array to a length of MI before transforming back into the time domain . This effectively performs interpolation [2] with a time-aliased sinc(x) function. Except for the small differences caused by aliasing errors, the interpolated samples provide a good

simulation of the samples which would be obtained by compressing a set of time delayed return pulses.

In order to interpolate properly, the zero padding must be performed at the ends of the pulse spectrum, i.e., in the middle of the FFT array, as follows

$$\hat{H}'_{RCP}(k) = \begin{cases} \hat{H}_{RCP}(k) & , -(M/2) < k \le (M/2) \\ 0 & , -(MI/2) < k \le -(M/2) \\ & \text{and } (M/2) < k \le (MI/2) \end{cases} \tag{31}$$

where $'$ is used to denote the interpolated signal. After an inverse FFT of length MI is applied, the interpolated, range compressed profile, $\hat{h}'_{RCP}(m')$, $-MI/2 < m' \le MI/2$, is obtained where m' is the interpolated array index and the sampling period is T/I. The peak of the profile occurs at $m' = 0$.

Since the FFT is being used to perform a linear convolution, the FFT length, M, must be large enough to exclude invalid samples which occur because of the FFT's circular convolution. If the pulsewidth is τ and the desired number of valid compressed samples before interpolation is Q, M must satisfy $M > (\tau/T) + Q - 1$. The length M is usually chosen to be the next larger power of 2 to allow the use of efficient FFT algorithms. After interpolation, valid samples occur for $-(QI/2) < m' \le (QI/2)$.

Figure 3.1 shows the simulated range compressed profile after interpolation for the nominal RADARSAT parameters

given in Table 1. The window parameter, $\beta_R = 2.7$, was chosen to produce a 1-D peak sidelobe ratio (PSLR) of -21.7 dB and a 1-D integrated sidelobe ratio (ISLR) of -21.0 dB.

3.4 SINGLE-LOOK AZIMUTH COMPRESSION

This section describes the theory and approximations used in developing the basic range/Doppler azimuth compression algorithm for single-look processing.

As described earlier, the basic range/Doppler algorithm makes use of the approximate similarity between the time and frequency domain signals of large TBP linear FM type signals. Azimuth compression consists of convolving the range compressed signal with an approximation to the azimuth matched filter, $h_A^*(-t,-\eta)$, and an azimuth window to control sidelobes. The antenna function $w_a(\eta)$ is usually dropped from the azimuth filter since its effect is similar to that of the azimuth window. Excluding the azimuth window for the time being, an azimuth reference function (the time-reversed complex conjugate of the azimuth matched filter) can be written as :

$$h_F(t,\eta) = \exp[-j4\pi r(\eta)/\lambda]\ \delta[t-2r(\eta)/c] \tag{32}$$

In order to understand the discrete implementation of this approximate matched filter, the filter must be bandlimited in range to the range sampling frequency, F_{sr}. This excludes frequencies which would be aliased by range

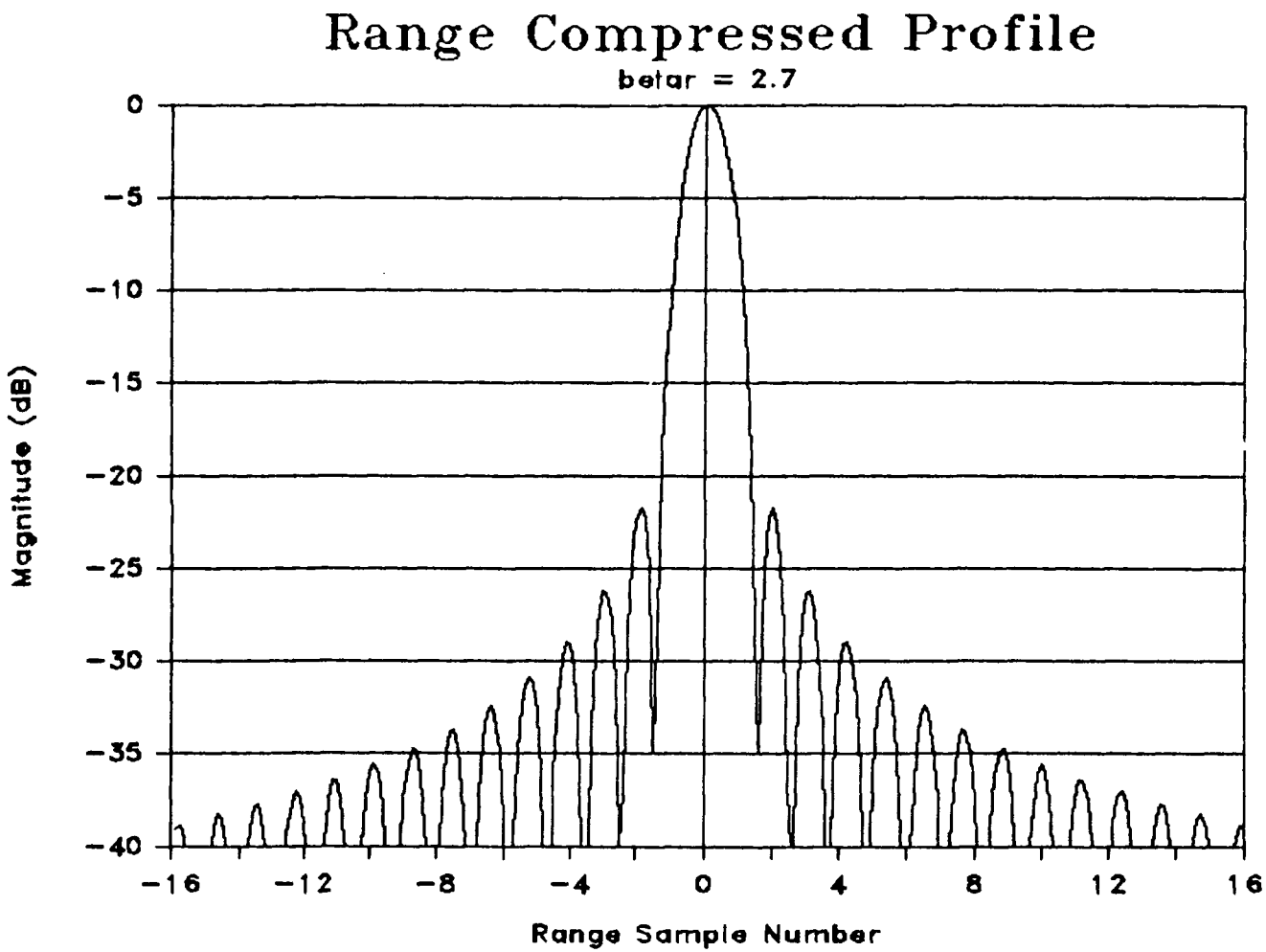

Figure 3.1. Simulated range compressed profile.

sampling and also provides the basis for interpolation in the range direction. Continuous time signals will be used to develop the algorithm. These can be discretized in range and azimuth and time-aliased according to the length of the FFT's in order to provide a discrete model of the algorithm.

The ideal rectangular range bandlimiting filter has the form of a sinc function. Thus the range bandlimited reference function can be formulated as :

$$h_{FRB}(t,\eta) = h_F(t,\eta) *_t \text{sinc}(\pi F_{sr} t) \tag{33}$$

$$= \exp[-j4\pi r(\eta)/\lambda] \text{ sinc}(\pi F_{sr}[t-2r(\eta)/c]) \tag{34}$$

The shape of this 2-D reference function is shown in figure 3.2.

Cross-sections of the function in the azimuth time direction exhibit a linear FM type of phase characteristic which is the same as the phase along the RCM curve in the previous infinite bandwidth reference function, $h_F(t,\eta)$. The envelope of this signal in the azimuth direction is a sinc function centered at the RCM curve with a time-warping effect created by the range curvature terms of the RCM equation, $r(\eta)$. Since the RCM over the azimuth time interval defined by the azimuth antenna beamwidth is predominantly linear, especially for RADARSAT parameters, the time-warping of the sinc envelope is small.

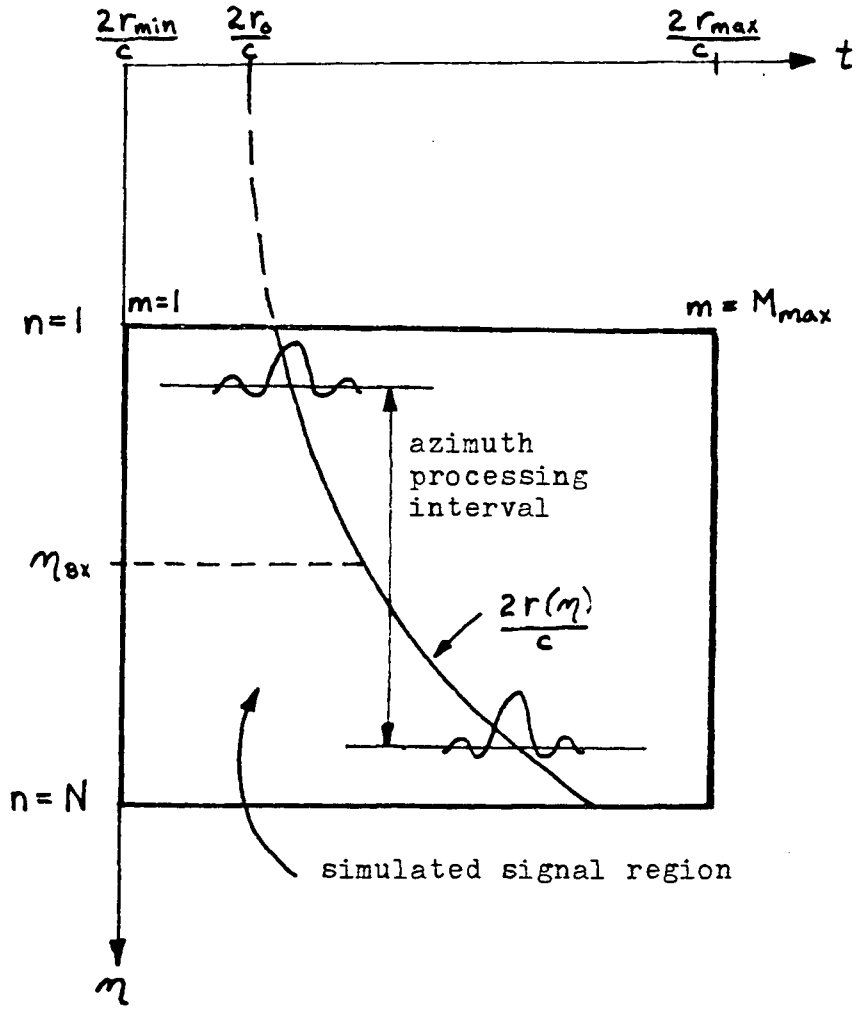

Figure 3.2. Range cell migration curve in azimuth time domain.

The approximate azimuth timewidth of the reference function can be determined by using a linear aproximation to $r(\eta)$ and determining the -3dB azimuth times of the sinc envelope. Using the Taylor series expansion of chapter 2 with only first order terms and evaluating at the beam center range time, $t=2r(\eta_C)/c$, the approximate azimuth envelope is $\mathrm{sinc}(\pi F_{sr}\lambda f_C[\eta-\eta_C]/c)$. The -3dB timewidth of this envelope is given by :

$$\Delta\eta_{3dB} \simeq 0.884\ c\ /\ (\lambda f_C F_{sr}) \tag{35}$$

When the squint angle (and therefore the beam center frequency, f_C) is small, the TBP in the azimuth direction near the beam center range is large. For a large azimuth TBP signal, the Fourier transform of the azimuth signal is similar in phase and magnitude to the azimuth time domain signal except for a scaling constant. Using the principle of stationary phase [17], the scaling between the time and frequency axes can be determined by expressing the instantaneous frequency as a function of azimuth time :

$$f_i(\eta) = -(2/\lambda)\ r'(\eta) \tag{36}$$

Substituting for $r'(\eta)$ with the derivative of equation (7) and rearranging gives the inverse mapping

$$\eta_i(f) = r_o\ /\ \{\ v_{eq}\ [(2v_{eq}/(\lambda f))^2 - 1]^{1/2}\ \} \tag{37}$$

where $\eta_i(f)$ is the azimuth time corresponding to the instantaneous azimuth frequency f. Substituting back into equation (7) gives the approximate frequency domain RCM curve :

$$r_i(f) = r(\eta_i(f)) = r_o(1 + 1/[(2v_{eq}/(\lambda f))^2 - 1])^{1/2} \quad (38)$$

Thus the azimuth Fourier transform of the range bandlimited reference function excluding amplitude constants can be approximated as :

$$H_{FRB}(t,f) \simeq h_{FRB}(t,\eta_i(f)) \quad (39)$$

$$= \exp[-j4\pi r_i(f)/\lambda] \operatorname{sinc}(\pi F_{sr}[t-2r_i(f)/c]) \quad (40)$$

The shape of this azimuth frequency domain reference function is shown in figure 3.3.

This approximate equation forms the basis for the azimuth frequency domain, fast convolution implementation of azimuth compression in the basic range/Doppler algorithm. The approximate azimuth matched filter is the complex conjugate of this frequency domain reference function. An azimuth sidelobe control window is also applied in the azimuth frequency domain. The basic range/Doppler azimuth compression algorithm is expressed as :

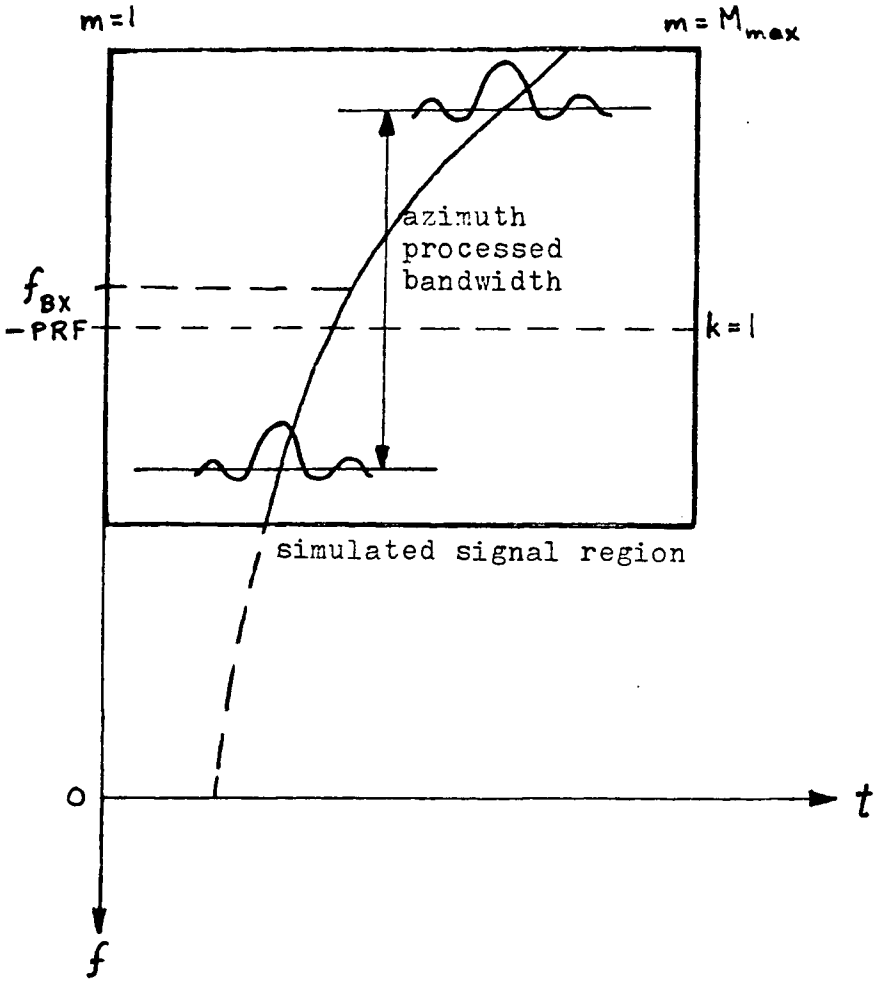

Figure 3.3. Range cell migration curve in azimuth frequency domain.

$$\sigma(t,\eta) = F^{-1}\{[\ H_{RC}(t,f) *_t H^*_{FRB}(-t,f)\ ]\ W_A(f-f_C)\} \quad (41)$$

$$= F^{-1}\{\exp[j4\pi r_i(f)/\lambda]\ W_A(f-f_C)$$
$$\bullet \int_{-\infty}^{\infty} H_{RC}(t',f)\ \mathrm{sinc}(\pi F_{sr}[t'-t-2r_i(f)/c])dt'\} \quad (42)$$

where $\sigma(t,\eta)$ is the final compressed point target image. The procedures may be summarized as follows :

1. Apply an azimuth Fourier transform (approximated by an FFT) to the range compressed point target return to get $H_{RC}(t,f)$.

2. Interpolate in range time with a sinc function matched to the range sampling frequency in order to extract the energy at the range defined by the RCM curve. In practice the RCMC interpolation is performed as a range time convolution with a short windowed sinc function to minimize the number of computations. A Kaiser-Bessel window (β_I=2.5) is used in the simulations.

3. Multiply by the complex conjugate of the azimuth frequency domain reference phase function and the azimuth sidelobe control window. Rather than using the approximate reference function above, a closer approximation is formed by computing the FFT of a discrete time domain reference phase function of unity magnitude. This is the approach used in the simulations.

4. Apply an inverse azimuth Fourier transform (approximated by an inverse FFT) to obtain the final compressed image.

3.5 SIMULATION OF SINGLE-LOOK AZIMUTH COMPRESSION

This section develops a simulation model of single-look azimuth compression for the basic range/Doppler algorithm. The steps involved in generating and compressing a simulated 2-D range compressed azimuth signal are described.

The main steps of the simulation are :

1. generation of the azimuth time domain phase function

2. generation of a frequency domain, single-look, reference phase filter

3. simulation of azimuth weighting due to the azimuth antenna function and RCM

4. azimuth FFT

5. frequency domain RCMC

6. multiplication by the frequency domain azimuth reference phase filter and window

7. azimuth interpolation performed by zero-padding in the frequency domain

8. inverse azimuth FFT to produce a time domain point target image

The azimuth time domain phase function can be expressed in discrete azimuth time as

$$p(n) = \exp[j\psi(n)] \ , \ 1 \le n \le N \tag{43}$$

$$\psi(n) = -(4\pi/\lambda)\ r(\ \eta_C + (2n-N-1)T_A/2\ ) \tag{44}$$

where T_A is the azimuth sampling period, n is the azimuth time index, and N is the length of the azimuth FFT (a power of 2). For convenience, the beam center time, η_C, is placed at the center of the FFT at n = (N+1)/2. The hyperbolic RCM equation given in equation (7) is used throughout the simulations instead of the Taylor series approximation.

A single-look, azimuth reference phase filter in the azimuth frequency domain is formed by computing the FFT of p(n) and taking its complex conjugate to get $P^*(k)$, $1 \le k \le N$.

Each azimuth line of the discrete 2-D range compressed signal, $\hat{h}_{RC}(m,n)$, is created by applying two forms of weighting to p(n). The first form of weighting is the azimuth antenna function, $\hat{w}_a(n)$. In actual SAR's, the azimuth time width of the antenna function varies slowly with squint angle and becomes slightly asymmetrical. Since this complicates the geometric model and introduces small

variations which are not of interest here, the antenna function will be assumed to be constant in time width and shape for the squint angles considered. The two-way azimuth antenna function is approximated by a $\mathrm{sinc}^2(x)$ type function, as produced by a uniform, continuous aperture antenna, and is defined in discrete azimuth time as

$$\hat{w}_a(n) = \mathrm{sinc}^2[\pi D v_b (2n-N-1) T_A/(2\lambda r_o)] \ , \ 1 \le n \le N \qquad (45)$$

where D is the azimuth antenna length and the beam center time occurs at $n = (N+1)/2$. The two-way -6 dB width of the antenna function is

$$\Delta\eta_{6dB} = 0.884 \ \lambda r_o/(D v_b) \qquad (46)$$

The second form of weighting is due to RCM. The weighting is applied by determining the range distance between each azimuth sample and the range migration curve and selecting the nearest amplitude from the interpolated, range compressed profile. The distance between the range migration curve and the desired azimuth line in uninterpolated range samples is computed as

$$d(m,n) = m - 1 - (2/cT)[r(\eta_C + [2n-N-1]T_A/2) - r_{min}] \ , \quad 1 \le n \le N \ , \ 1 \le m \le M_{max} \qquad (47)$$

where m is the range cell index, and M_{max} is the number of

azimuth lines being generated. The positioning of the azimuth lines in range time is arbitrary since it depends only on the phase of the range sampling clock. Therefore the azimuth lines are arbitrarily positioned so that the nearest line (m=1) corresponds to range time $2r_{min}/c$, and the farthest line ($m=M_{max}$) corresponds to range time $2r_{max}/c$. These ranges, r_{min} and r_{max}, are the ranges of the nearest and farthest azimuth lines required for processing. They are determined by the length of the interpolator, the amount of RCM over the processed bandwidth, and the number of desired azimuth lines in the output image.

In order to retrieve the nearest sample from the interpolated range compressed array, $\hat{h}'_{RCP}(m')$, the distance d(m,n) must be converted to an interpolated index as

$$m'_I(m,n) = \text{round}[\ I\ d(m,n)\ ] \tag{48}$$

where the function round[x] rounds x to the nearest integer. Combining the antenna and RCM weightings, the discrete 2-D range compressed signal can be expressed as

$$\hat{h}(m,n) = \hat{w}_a(n)\ p(n)\ \hat{h}'_{RCP}(m'_I(m,n)) \tag{49}$$

Once all the required azimuth lines are generated, each line is transformed to the frequency domain with an azimuth FFT of length N to get the range compressed frequency domain signal, $\hat{H}(m,k)$, $1 \le k \le N$.

As with the range FFT in the previous section, the azimuth FFT must be long enough to produce the desired number of valid compressed samples. However, since the azimuth time domain signal does not fall abruptly to zero due to the sinc^2 form of the antenna function, an arbitrary processing time interval containing most of the signal energy must be chosen. Denoting the processing interval as η_{PBW}, and the desired number of compressed azimuth samples after convolution as R, the FFT length must satisfy

$$N \geq \eta_{PBW}/T_A + R - 1 \tag{50}$$

to prevent wraparound errors due to the circular convolution. For the current simulations, the processing interval is set equal to the two-way -6 dB antenna width.

Before the azimuth reference phase filter can be applied to $\hat{H}(m,k)$, it is necessary to correct for RCM in the azimuth-frequency, range-time domain using a range interpolator. This correction, RCMC, effectively straightens the range migration curve so that the matched filter need only be applied to a single azimuth line to produce a single azimuth line of the final image. The ideal range interpolator for a discrete range signal is a sinc function which is range time aliased according to the length of the range compression FFT.

In order to reduce the length of the interpolator and thereby reduce the number of computations, a finite length

approximation is usually used. Also, rather than generating a different set of interpolator coefficients for each azimuth time, several shifted versions of the interpolator are precomputed for a set of equally spaced fractional range sample shifts and the nearest closest version is used. In the current simulations, the approximate interpolator is formed by applying a discrete Kaiser-Bessel window to a sinc function to get

$$h_I(l,q) = \mathrm{sinc}[\pi(q+lL)T]\ w_I(q+lL)\ ,$$
$$-(L/2) < l \le (L/2)\ ,\ 0 \le q \le Q-1 \qquad (51)$$

$$w_I(i) = I_0\{\beta_I[1-(2i/QL)^2]^{1/2}\}\ /\ I_0\{\beta_I\}\ ,$$
$$-(QL/2) < i \le (QL/2) \qquad (52)$$

where Q is the number of fractionally shifted versions of the interpolator, q denotes the fractional shift, L is the length of each shifted version, l is the index within each shifted version, and β_I is the window weighting factor. These parameters were arbitrarily chosen to be Q = 16, β_I = 2.5, and L = 4, 8, 16, or 32.

To extract the peak energy at each azimuth sample time for a given point target with a range of closest approch, r_0, the interpolator peak is shifted in range so that its peak coincides with the frequency domain RCM curve defined in equation (38). This shift is implemented in two steps. First the interpolator is moved an integer number of samples

so that its peak is less than one sample away from the RCM curve. Secondly, one of the Q interpolator versions is chosen such that the chosen interpolator version has its peak closest to the actual position of the range migration curve. This effectively performs a fractional shift of the interpolator. The range line and the interpolator are then multiplied to complete the approximate interpolator convolution.

RCMC and azimuth reference phase multiplication are performed only over the processed bandwidth, f_{PBW}, which corresponds to the processing interval, η_{PBW}. This bandwidth is centered at the beam center frequency, f_C, given by

$$f_C = f_i(\eta_C) \tag{53}$$

The processed bandwidth is computed from the azimuth processing interval, η_{PBW}, with the assumption that phase terms higher than the quadratic are small over the processing interval, as

$$f_{PBW} = | K_A(\eta_C) | \eta_{PBW} \tag{54}$$

$$K_A(\eta) = -(2/\lambda) r''(\eta) \tag{55}$$

$$= -(2v_{eq}^2/[\lambda r(\eta)]) [1 - (v_{eq}\eta/r(\eta))^2] \tag{56}$$

where K_A is the azimuth linear FM rate which is approximately constant over the processing interval. Since a

discrete azimuth signal is used, the processed band is aliased by the PRF. Figure 3.4 shows the form of the range compressed signal after the azimuth FFT including the spectrum aliasing which is caused by azimuth sampling.

RCMC straightens the point target range migration curve into a single azimuth frequency line. This line is compressed by multiplication with the frequency domain, azimuth reference phase filter and a sidelobe reduction window. As stated previously, the filter is $P^*(k)$.

The azimuth window is computed over the processed bandwidth and set to zero outside. A Kaiser-Bessel azimuth window containing $N_{PBW} = f_{PBW}N/(PRF)$ nonzero samples is computed over frequency indices k = 1 to N as :

$$\hat{W}_A(k) = \begin{cases} I_0\{\beta_A[1-(2[k-1]/N)^2]\} \,/\, I_0\{\beta_A\} , & 1 \le k \le N_{PBW}/2+1 \\ I_0\{\beta_A[1-(2[k-1-N]/N)^2]\} \,/\, I_0\{\beta_A\} , & N-N_{PBW}/2+2 \le k \le N \\ 0 \text{ , otherwise} & \end{cases} \tag{57}$$

Before multiplication, the window is circularly shifted modulo N so that the peak of the window function is at frequency sample k_C, which is the nearest sample equal to or less than the aliased beam center frequency.

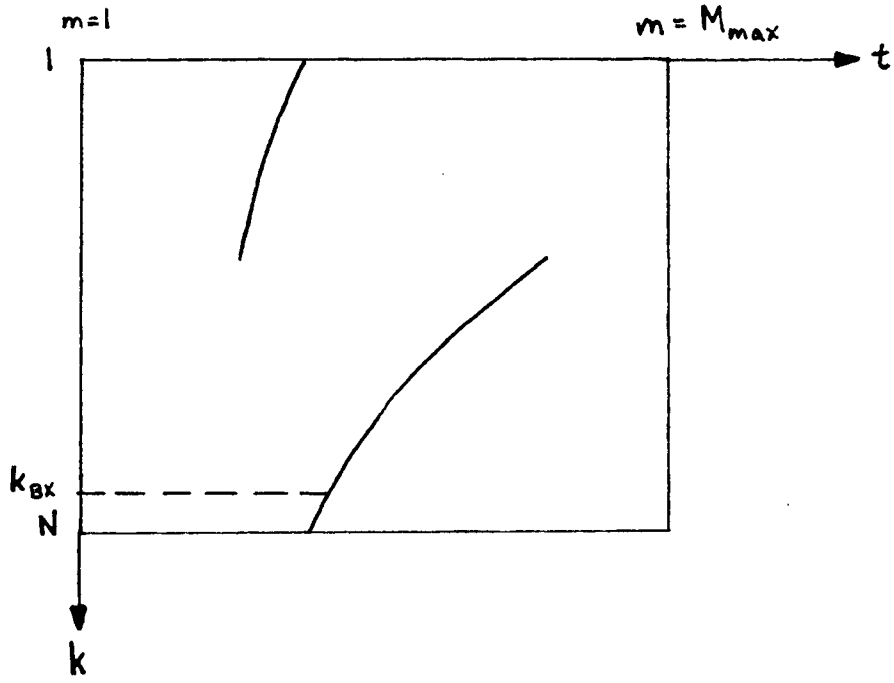

Figure 3.4. Range cell migration curve in discrete azimuth frequency domain.

A single line of the final compressed image is produced by applying an inverse FFT of length N to the spectrum. This line contains the compressed returns from targets with the same range of closest approach, r_0, but different azimuth positions.

The process of RCMC, azimuth reference phase multiplication and windowing is repeated for each of the desired output range cells. In theory, a different RCM curve with different value of r_0 should be used for each range. However, if the range extent is small, as in this case where we are only interested in the immediate region of a point target response, the same range migration curve can be used for all lines by shifting in range by an appropriate number of range cells. When larger regions are processed, a careful analysis is required to determine the range invariance region which is the distance in range over which the compression filters do not vary appreciably. In practice, the entire invariance region is processed as a block to increase efficiency. The issue of range invariance of the azimuth reference phase function has been examined in other reports. Chapter 7 examines range invariance for the new SRC filter function.

Finally, it is desirable to interpolate the compressed azimuth signal for the purposes of image quality measurement and to decrease the loss of information in the subsequent detection of the complex signal. The method used is zero padding in the azimuth frequency domain before the inverse

FFT. First the spectrum is circularly shifted so that the beam center frequency lies nearest to the first FFT array sample. The array is then padded with zeros in the middle to form a length NJ array where J is the interpolation factor. By applying an inverse FFT of length NJ, the desired interpolated signal is obtained.

3.6 SIMULATION RESULTS OF BASIC RANGE/DOPPLER COMPRESSION

This section presents and discusses the results of quality measurements of simulated point target responses which were produced for a range of squint angles. The simulation programs were implemented on an Amdahl 470 V/8 computer in RATFOR (rational FORTRAN) under the MTS (Michigan Terminal System) operating system. RATFOR is a structured precompiler which produces FORTRAN code.

The first step in the simulation was the production of a range compressed profile as in figure 3.1. The second step in the simulation was the production of a simulated range compressed azimuth signal. Figure 3.5 shows the azimuth time domain magnitudes of the simulated antenna weighting, and the antenna plus RCM weightings for a squint angle of 5.0°. The magnitudes are shown for the range cell closest to the beam center range.

The azimuth spectrum produced by the azimuth FFT is shown in figure 3.6. Before RCMC the azimuth bandwidth is quite small. The finite length interpolator used for RCMC is shown in figure 3.7. The figure shows the length 16

interpolator and includes all 16 fractionally shifted versions. Figure 3.8 shows the corrected spectrum after RCMC in which the processed bandwidth is clearly seen.

The azimuth reference phase filter spectrum for a 5.0° squint angle is shown in figure 3.9. The filter is generated in the azimuth time domain without weighting and then transformed with an azimuth FFT. The azimuth Kaiser-Bessel window with β_A = 1.5 is shown in figure 3.10. The point target azimuth spectrum after RCMC, azimuth reference phase filtering, and windowing is shown in figure 3.11. The spectrum ripples are characteristic of the azimuth reference phase filter spectrum.

Upon application of an inverse FFT, the final compressed point target response is produced. Sample 1-D cross-sections of the compressed response are shown in figures 3.12 and 3.13 for squint angles of 0° and 5°. The azimuth window factor was chosen to produce comparable sidelobe levels in the range and azimuth directions for small squint angles as would be done in a practical system.

Figure 3.12 shows that severe range broadening occurs for a squint angle of 5.0°. The range and azimuth broadening are summarized in figures 3.14 to 3.16 for a range of squint angles. Range broadening increases rapidly for squint angles above 4° with 5% and 10% broadening occuring at about 3.65° and 4.23° respectively (for L = 16). However, azimuth broadening is relatively insignificant remaining below 2% for squint angles up to 6°.

The 1-D and 2-D ISLR measurements are summarized in figures 3.17 to 3.19. It shows that both ratios increase significantly as the squint angle increases indicating that the point target response not only becomes broader in range, but also becomes flatter spreading more energy into the sidelobes. The ISLR measurement is seen to be limited to less than 5° since a large amount of the sidelobe energy lies outside of the finite integration region for larger squint angles. This causes the ISLR to drop sharply above 5°.

Another ratio of interest, the PSLR, is summarized in figures 3.20 to 3.22. This shows that the peak range sidelobe is usually the peak 2-D sidelobe as well. The discrepancy at small angles between the three figures is due to the higher interpolation factor used in measuring the 1-D PSLR. At some of the higher angles, the range PSLR dips well below the 2-D curve. This occurs since the closer range sidelobes merge with the mainlobe causing sidelobes further out to be measured as the peak sidelobe. This behaviour can be seen in figure 3.12.

The final measurement of interest is the degradation of the peak magnitude which is plotted in figure 3.23. This measurement was normalized to the sum of squares of the interpolator coefficients and the azimuth processed bandwidth as would be appropriate for a white noise model with noise equally distributed over the range and azimuth cells. Since the actual noise distribution may be somewhat

different, care should be taken in relating the peak magnitude degradation to changes in signal-to-noise ratio. The figure shows a reduction in peak magnitude with increasing squint angle caused by poor compression. At the 5% and 10% range broadening squint angles, the degradations are approximately 0.47dB and 0.83dB respectively. The degradation rises rapidly above this.

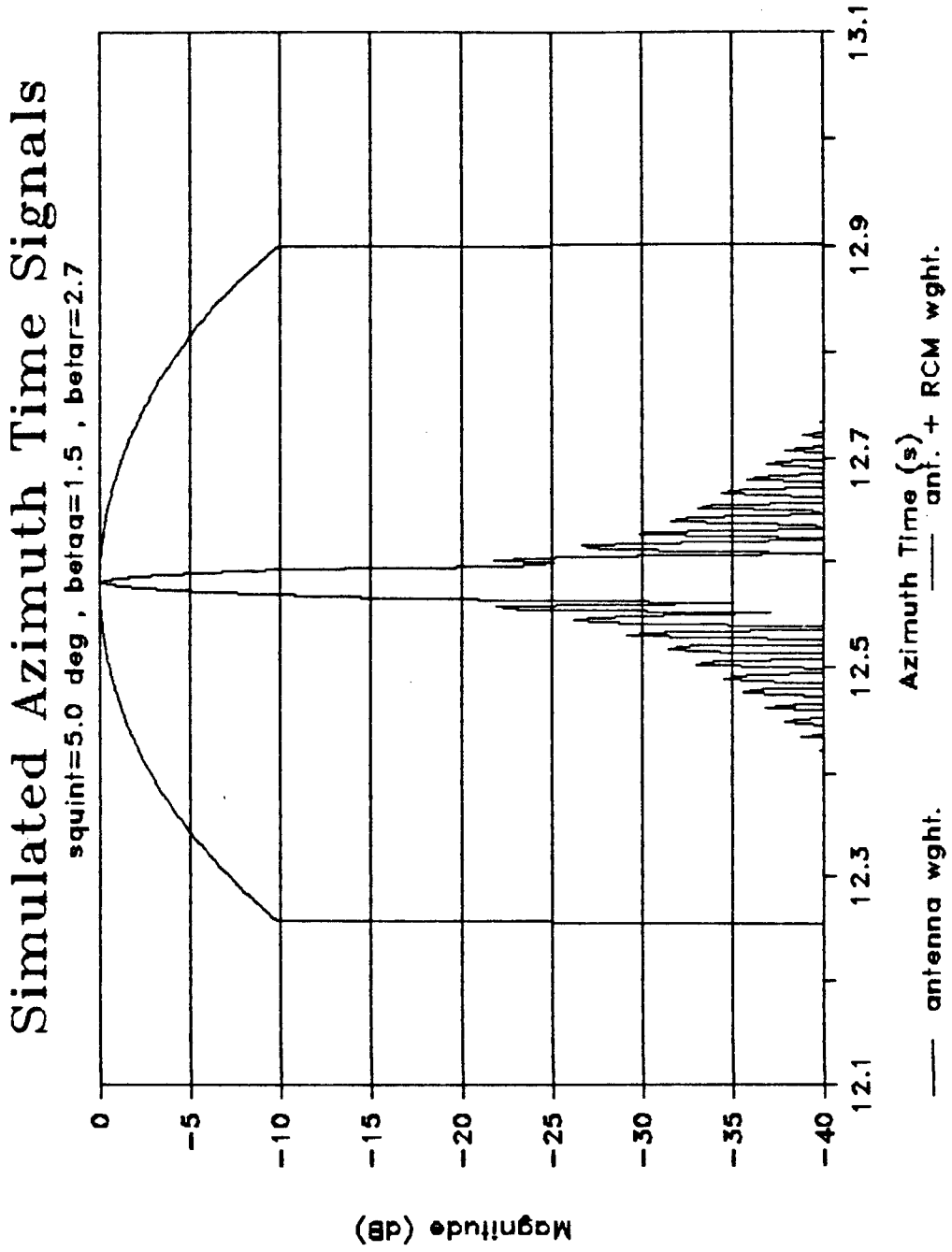

Figure 3.5. Simulated azimuth antenna weighting, and antenna plus RCM weightings in range cell nearest to beam center range for 5° squint.

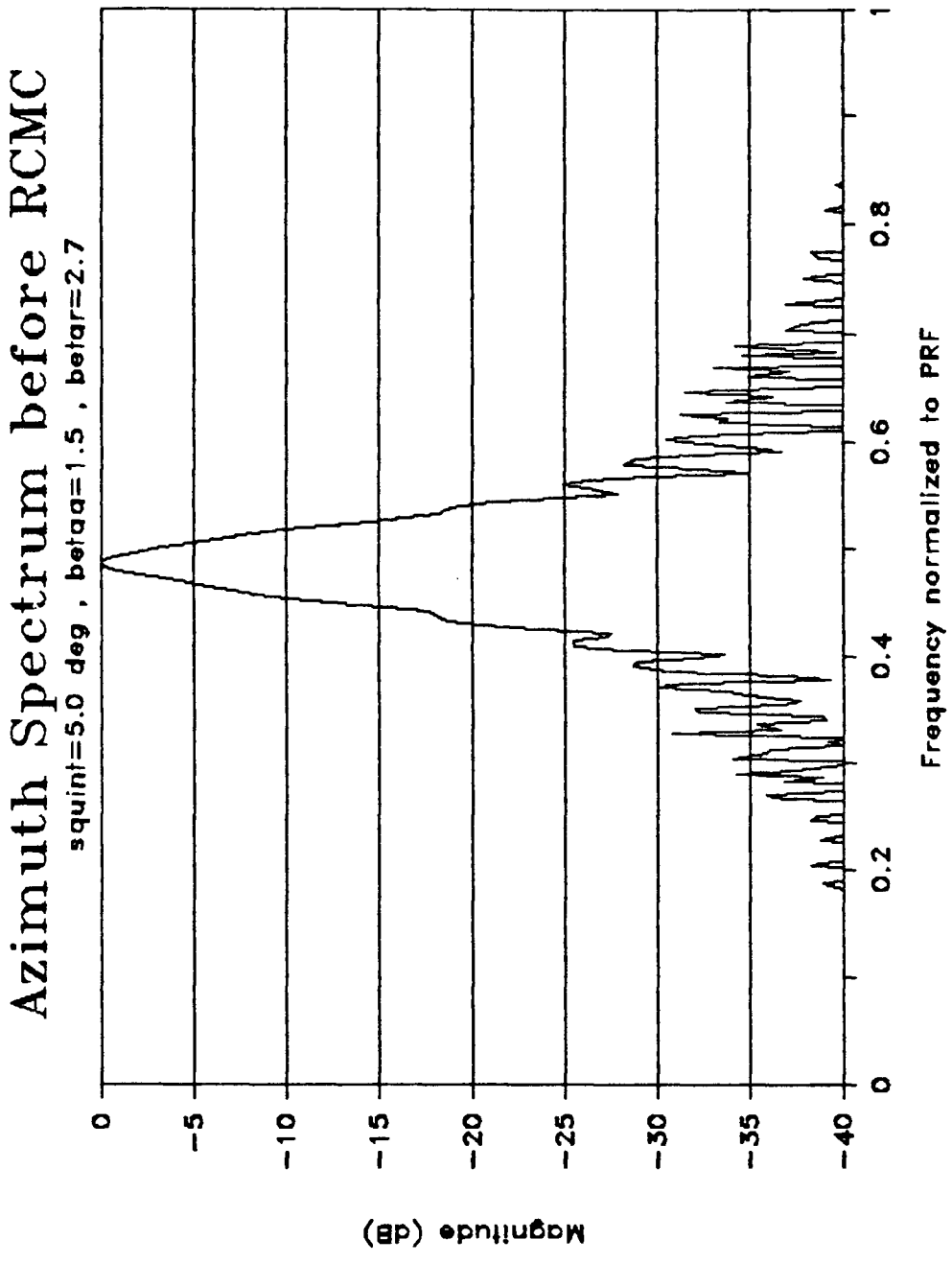

Figure 3.6. Azimuth spectrum before RCMC in range cell nearest to beam center range for 5° squint.

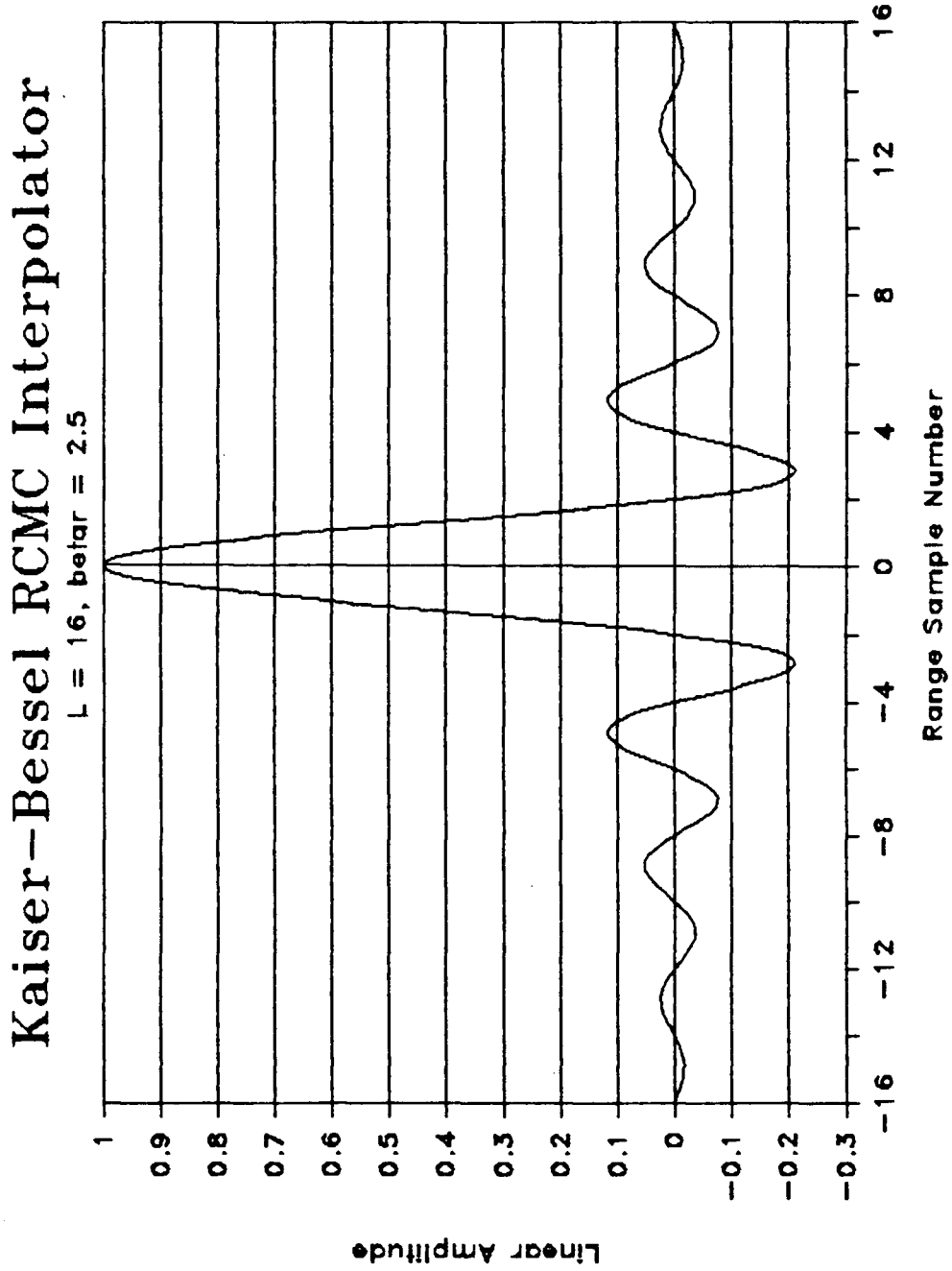

Figure 3.7. Windowed range interpolator of length 16 including 16 fractionally shifted versions.

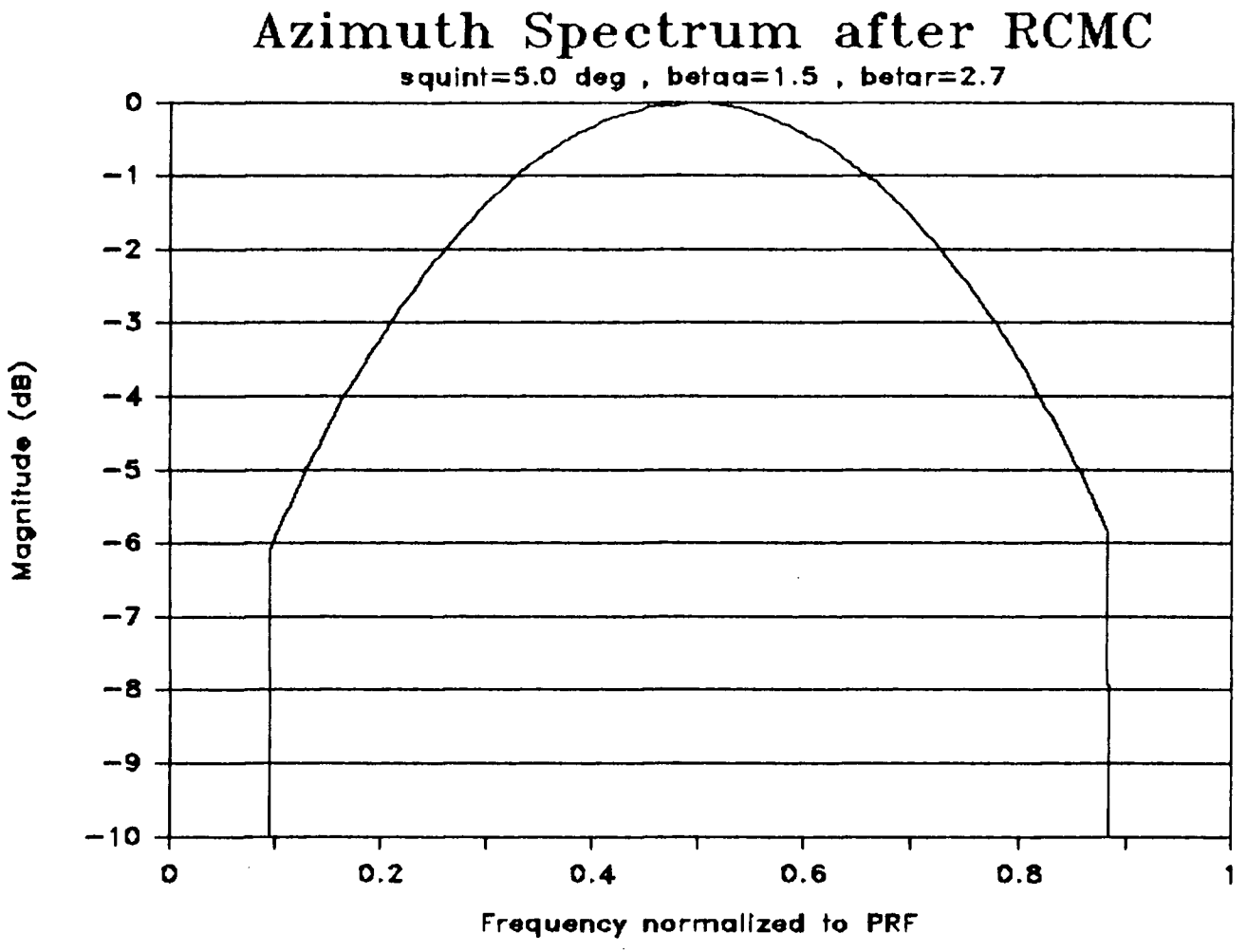

Figure 3.8. Azimuth spectrum after RCMC for 5° squint.

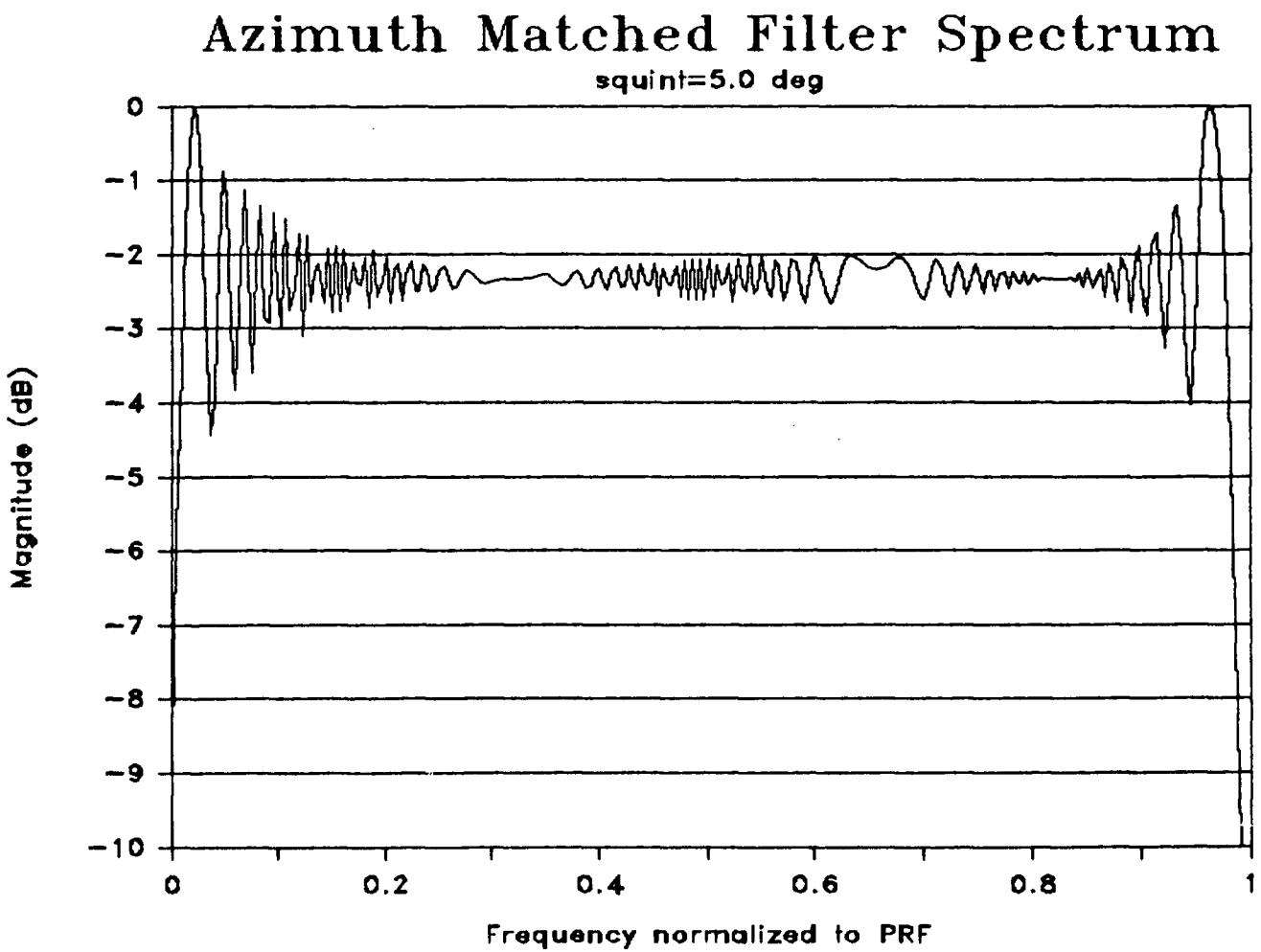

Figure 3.9. Azimuth reference phase filter spectrum for 5° squint.

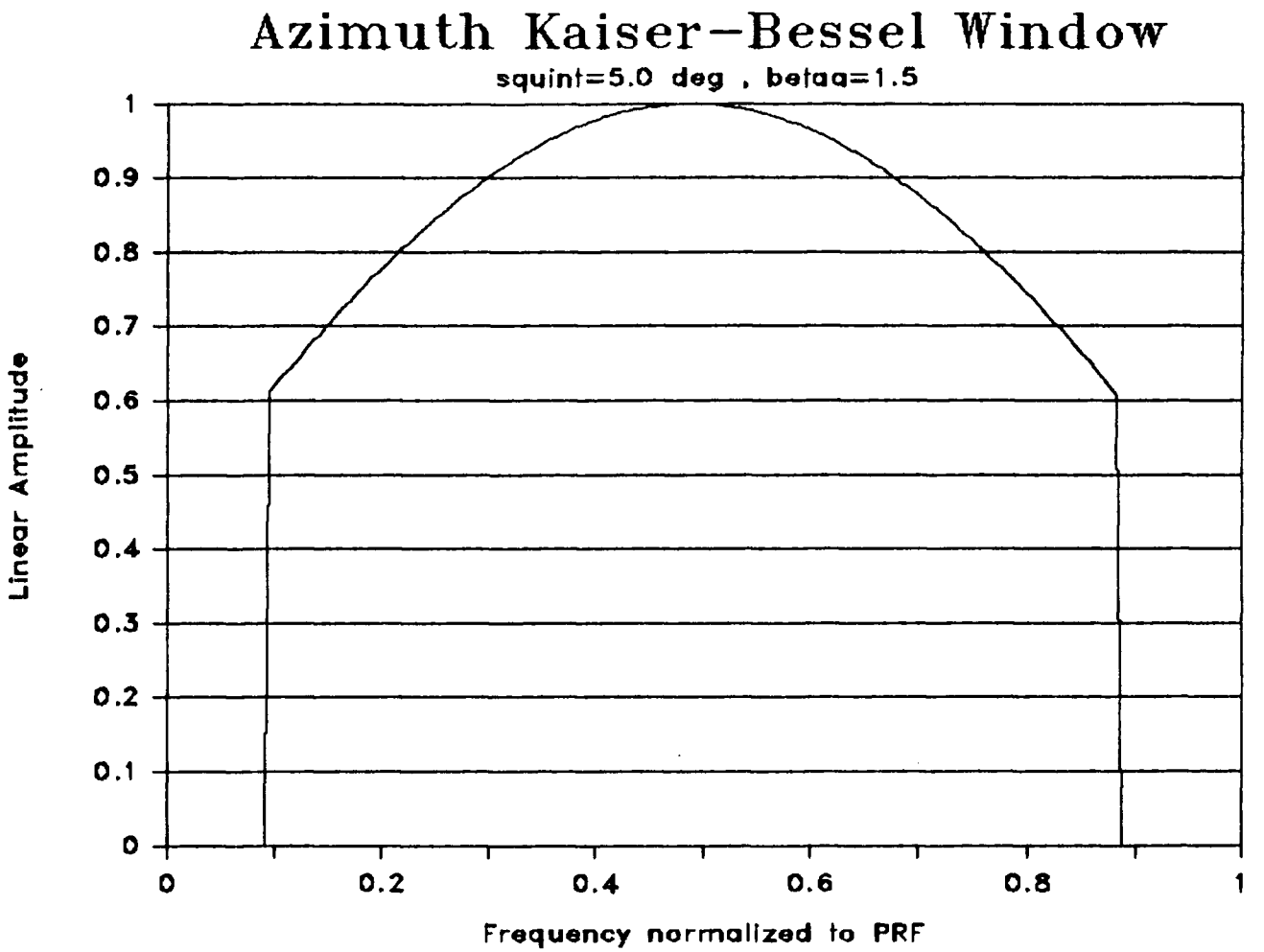

Figure 3.10. Azimuth Kaiser-Bessel window for 5° squint.

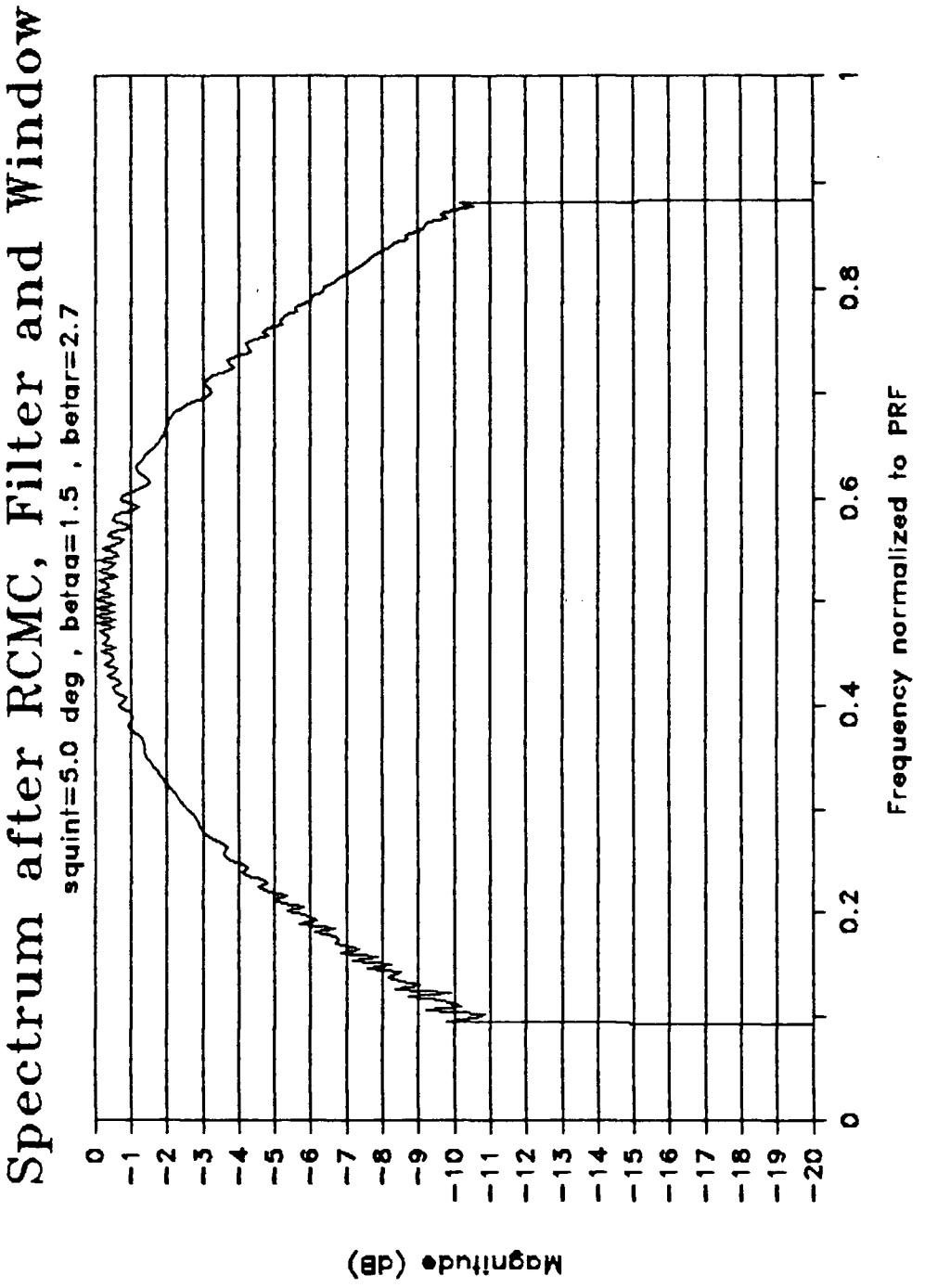

Figure 3.11. Azimuth spectrum after RCMC, matched filter, and windowing.

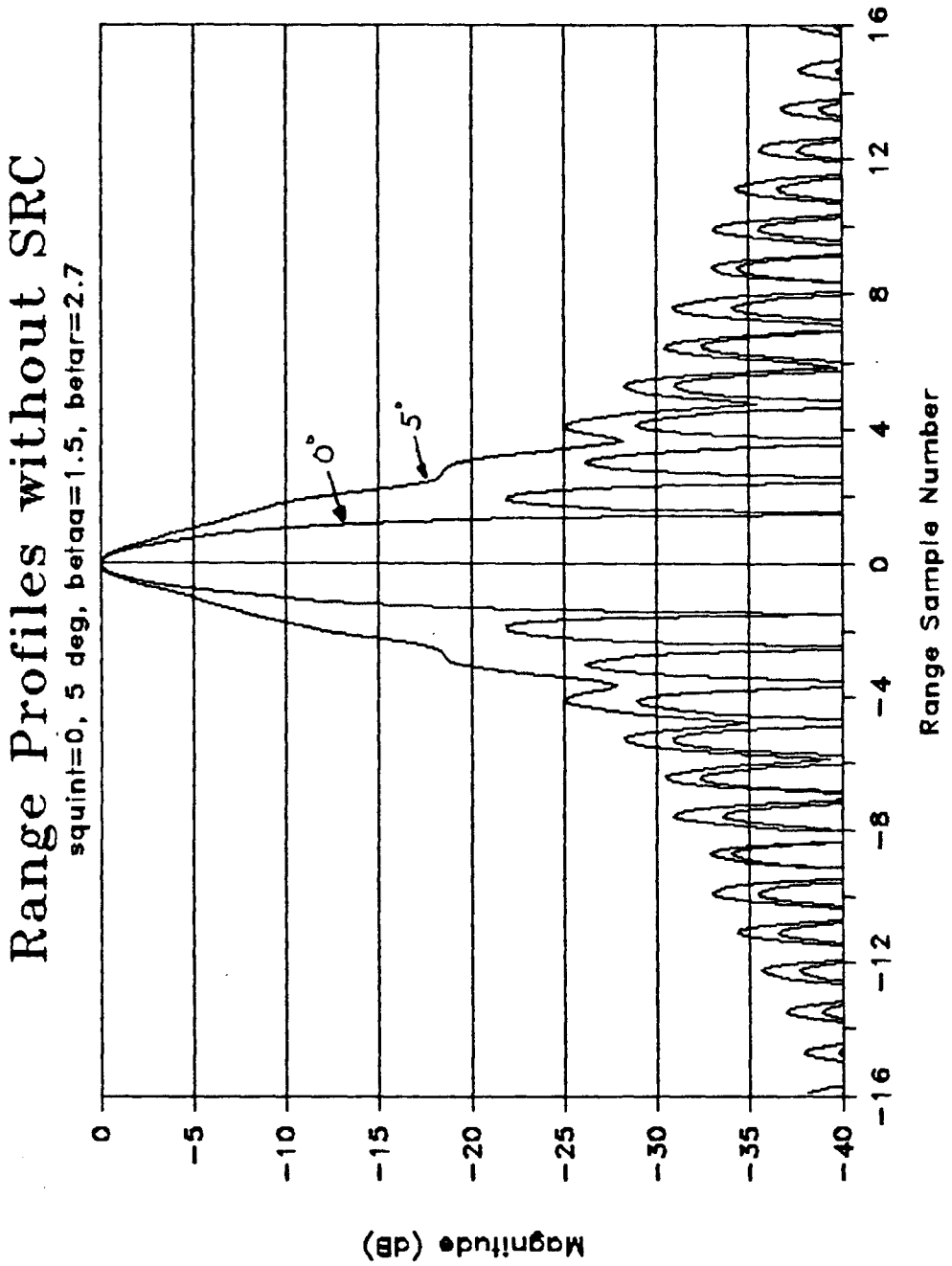

Figure 3.12. Fully compressed range profile without SRC for 0° and 5° squint using a length 16 RCMC interpolator.

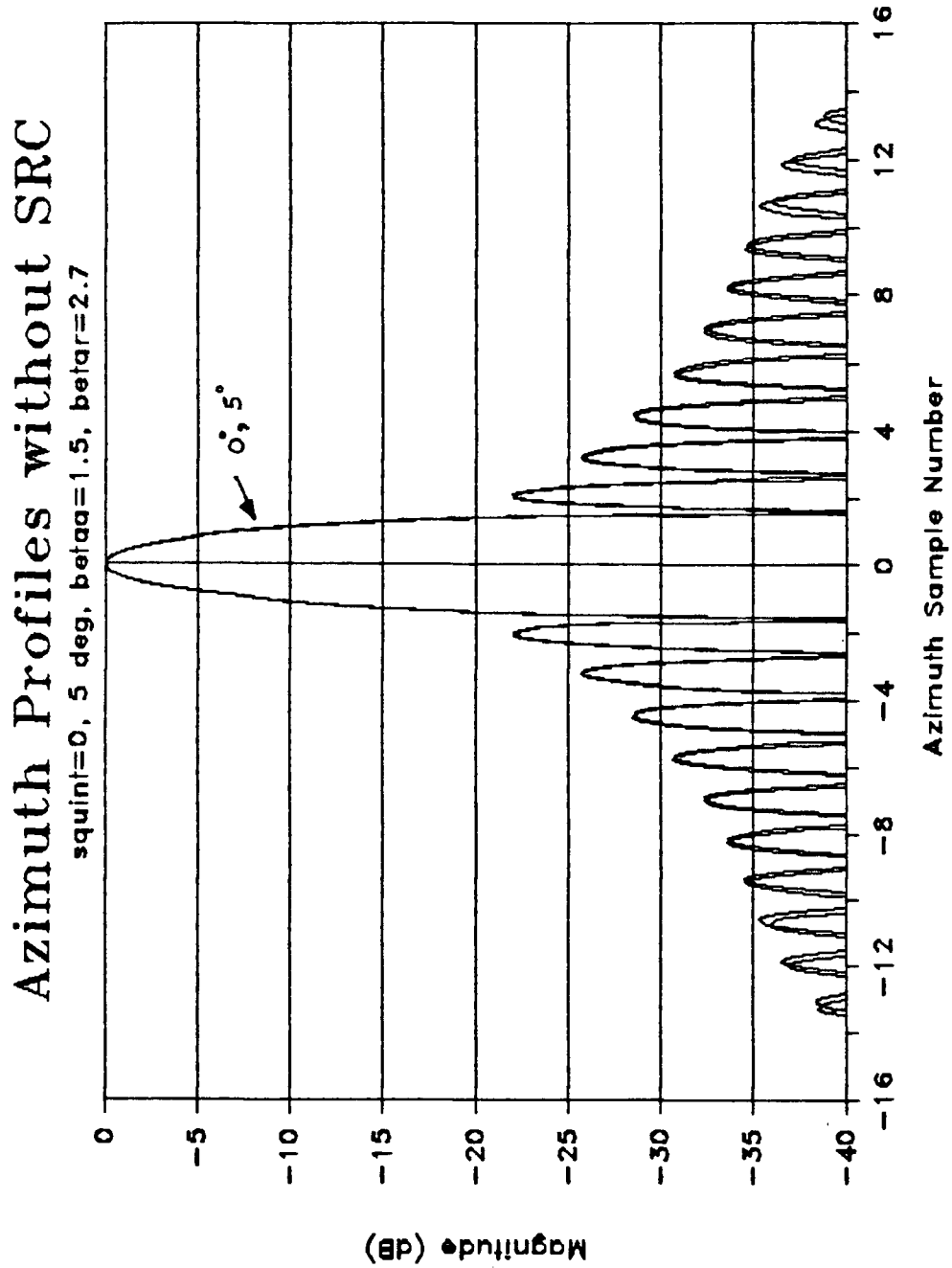

Figure 3.13. Fully compressed azimuth profile without SRC for 0° and 5° squint using a length 16 RCMC interpolator.

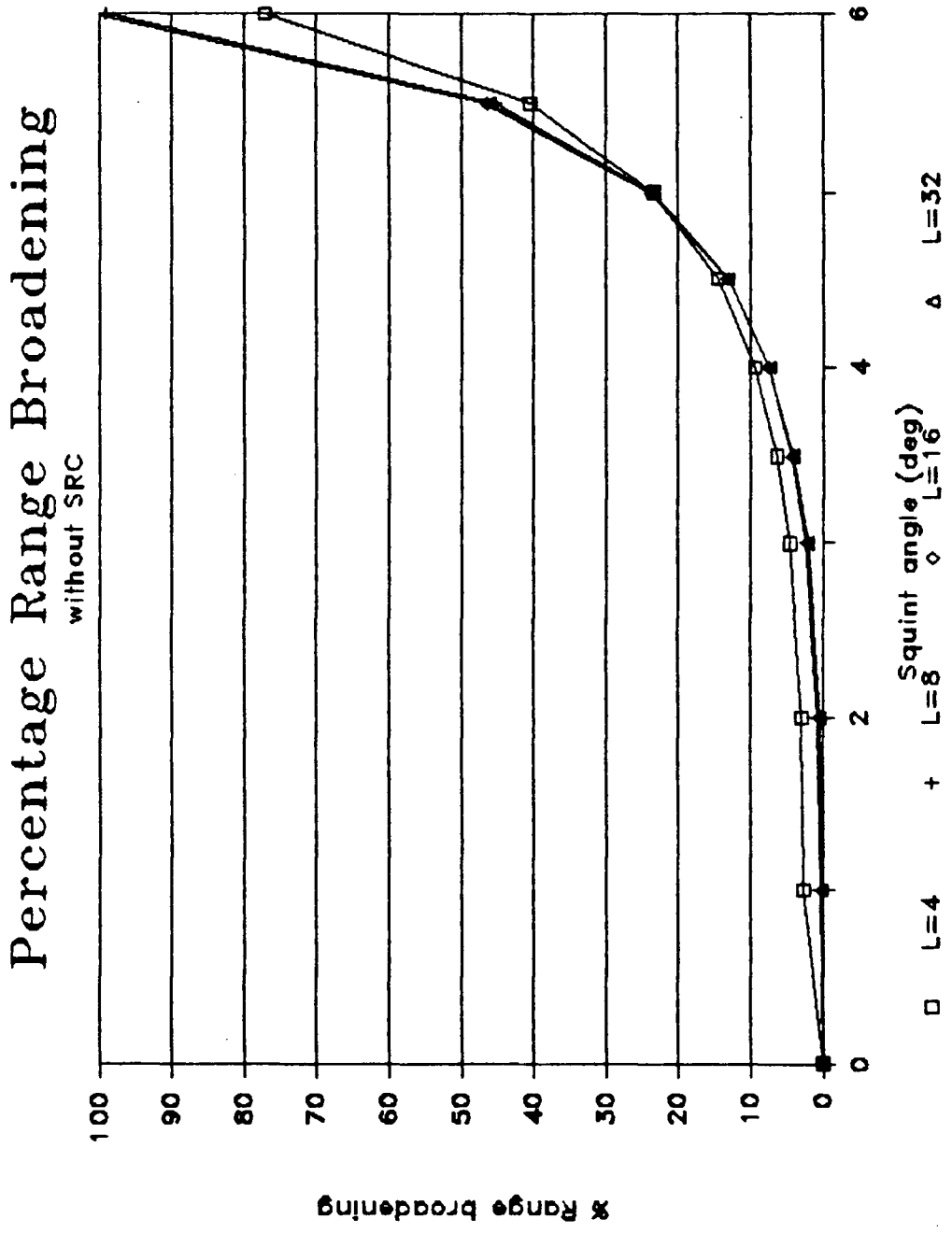

Figure 3.14. Range broadening of point target response without SRC for various RCMC interpolator lengths.

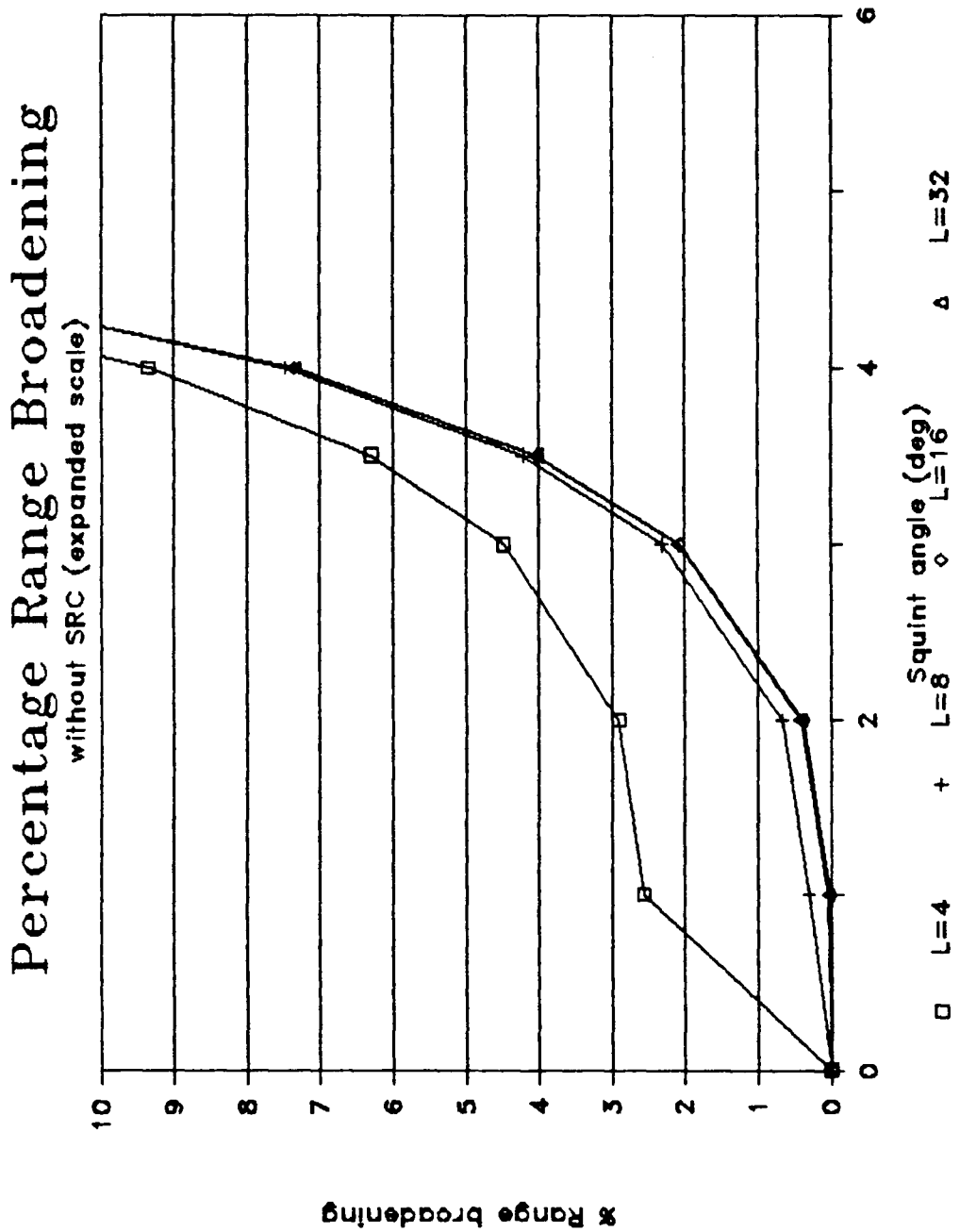

Figure 3.15. Range broadening of point target response (expanded) without SRC for various RCMC interpolator lengths.

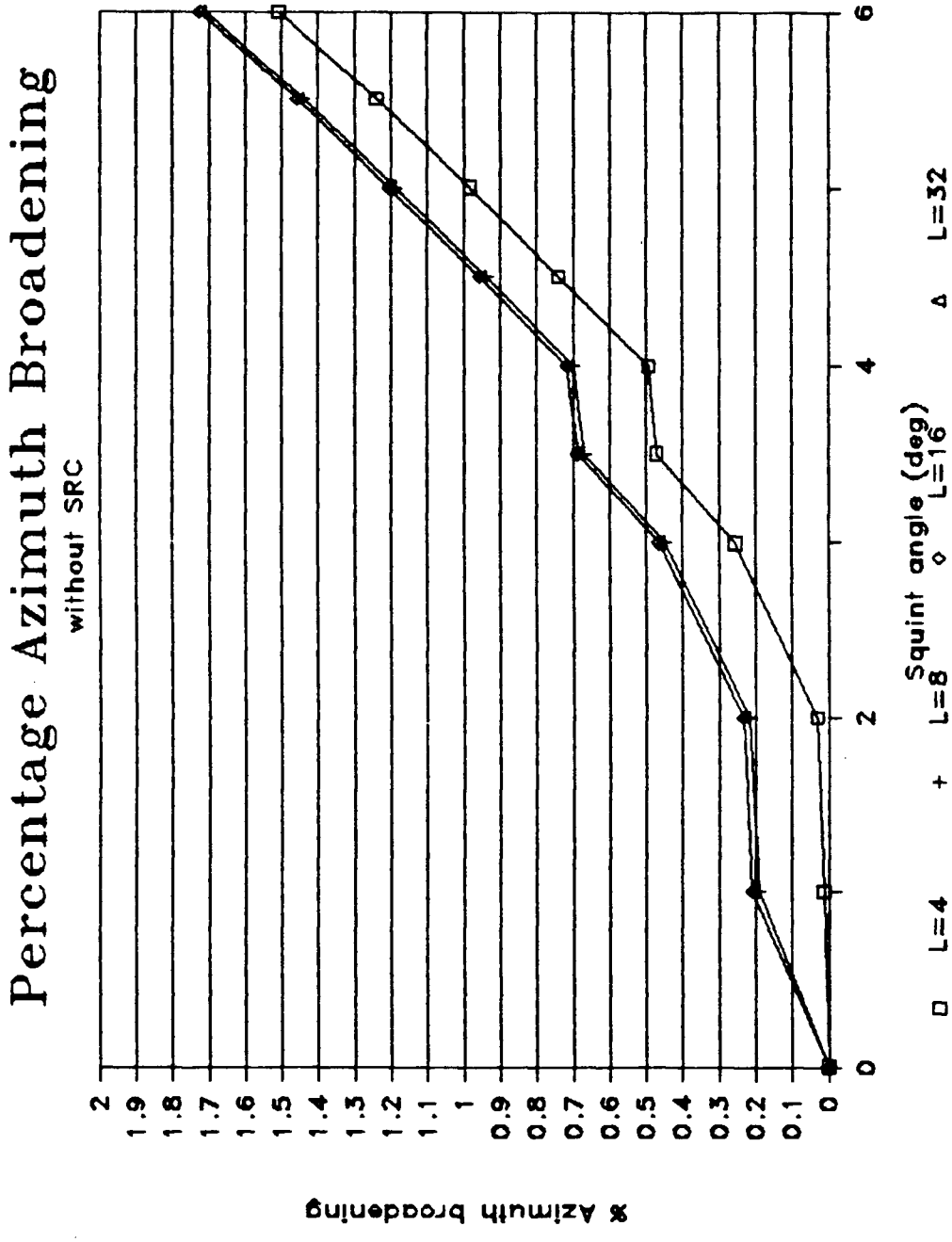

Figure 3.16. Azimuth broadening of point target response without SRC for various RCMC interpolator lengths.

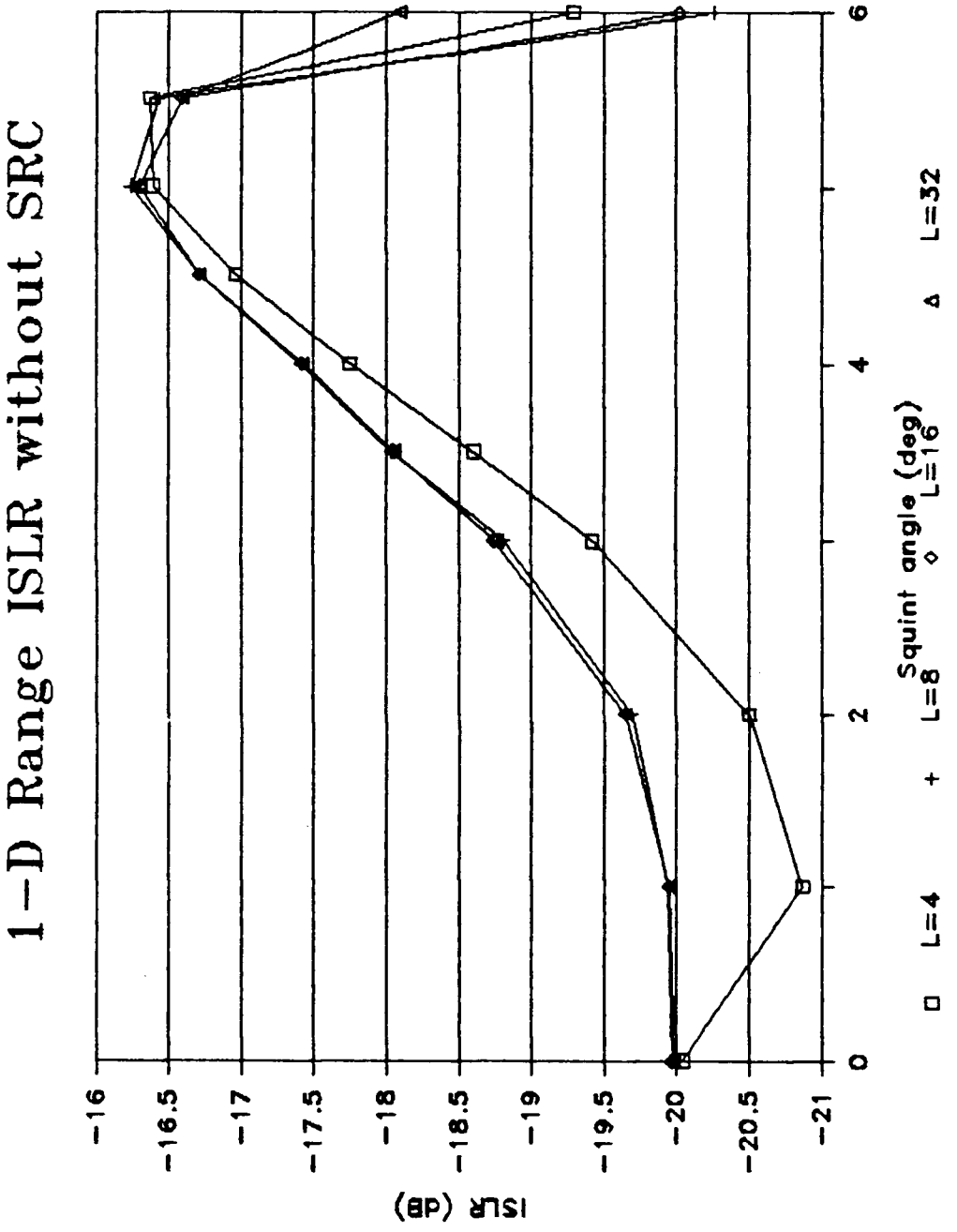

Figure 3.17. 1-D range integrated sidelobe ratios without SRC for various RCMC interpolator lengths.

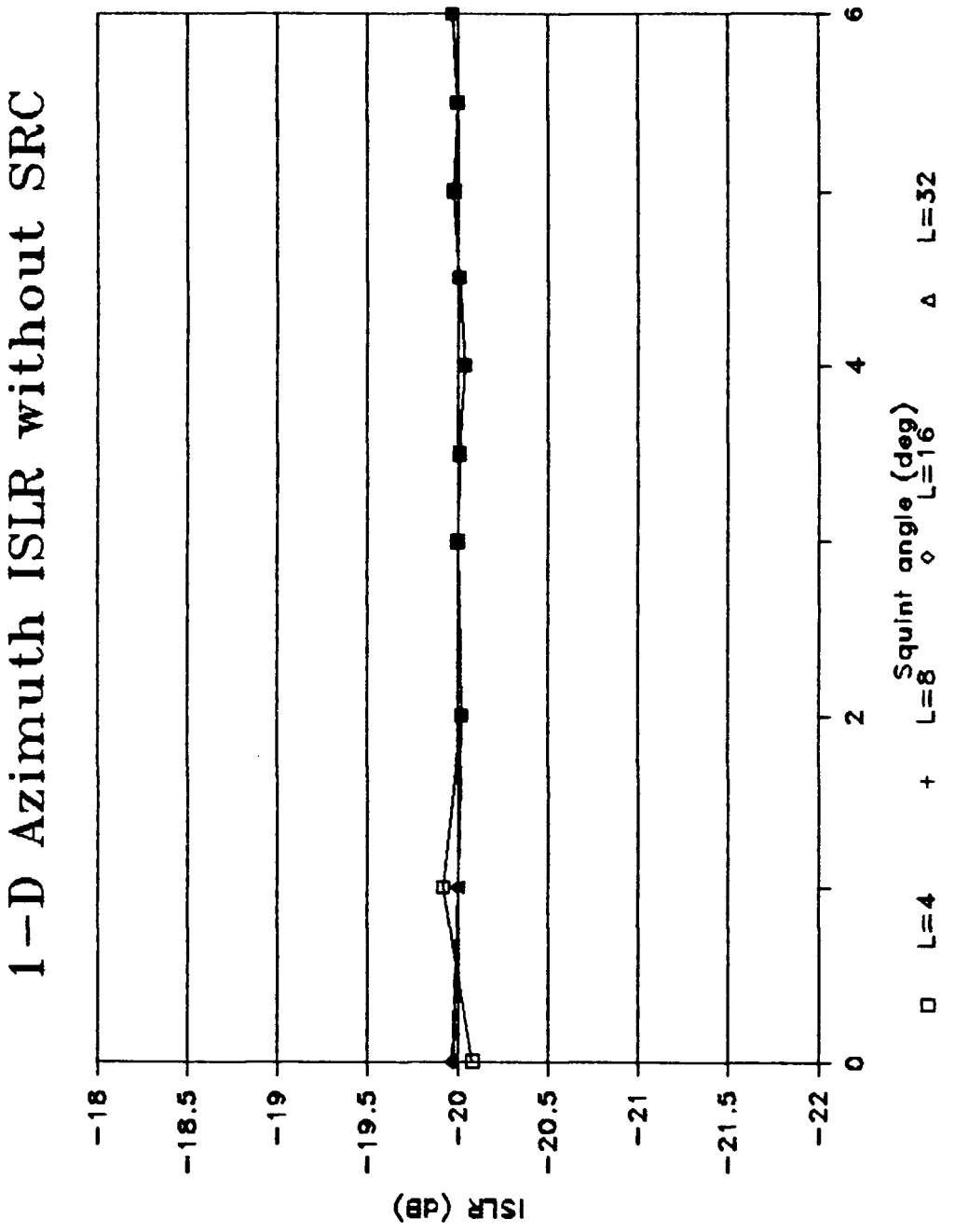

Figure 3.18. 1-D azimuth integrated sidelobe ratios without SRC for various RCMC interpolator lengths.

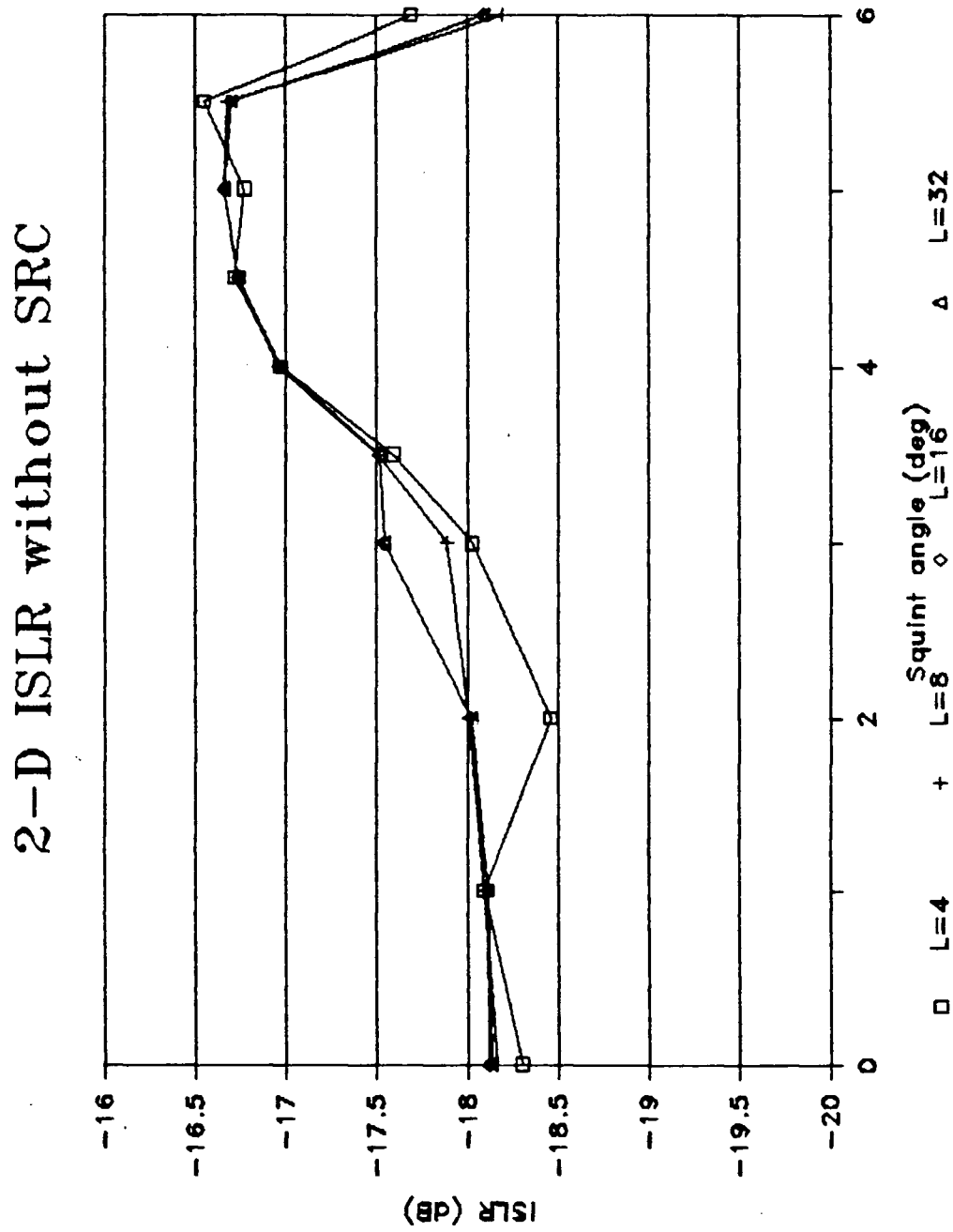

Figure 3.19. 2-D integrated sidelobe ratios without SRC for various RCMC interpolator lengths.

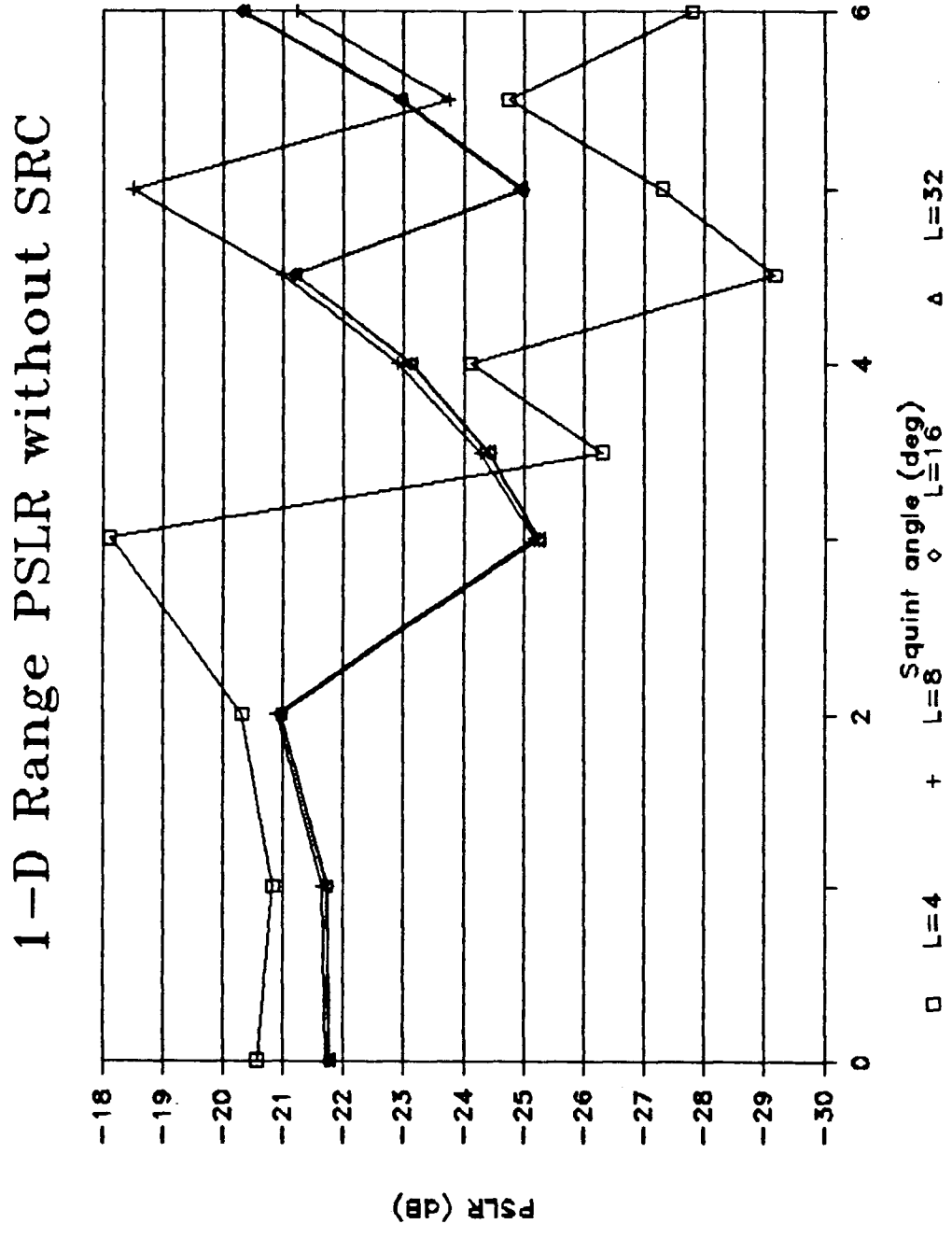

Figure 3.20. 1-D range peak sidelobe ratios without SRC for various RCMC interpolator lengths.

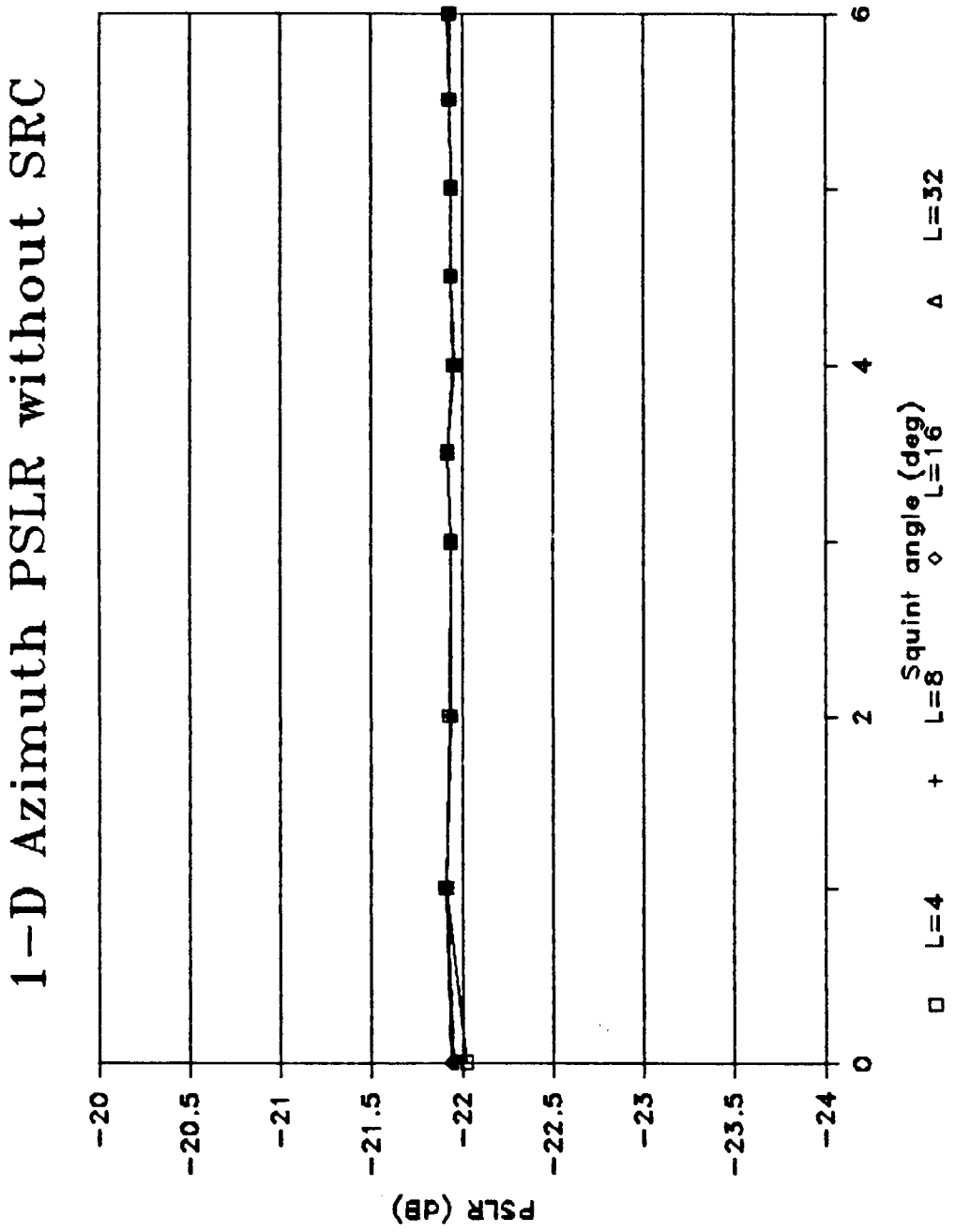

Figure 3.21. 1-D azimuth peak sidelobe ratios without SRC for various RCMC interpolator lengths.

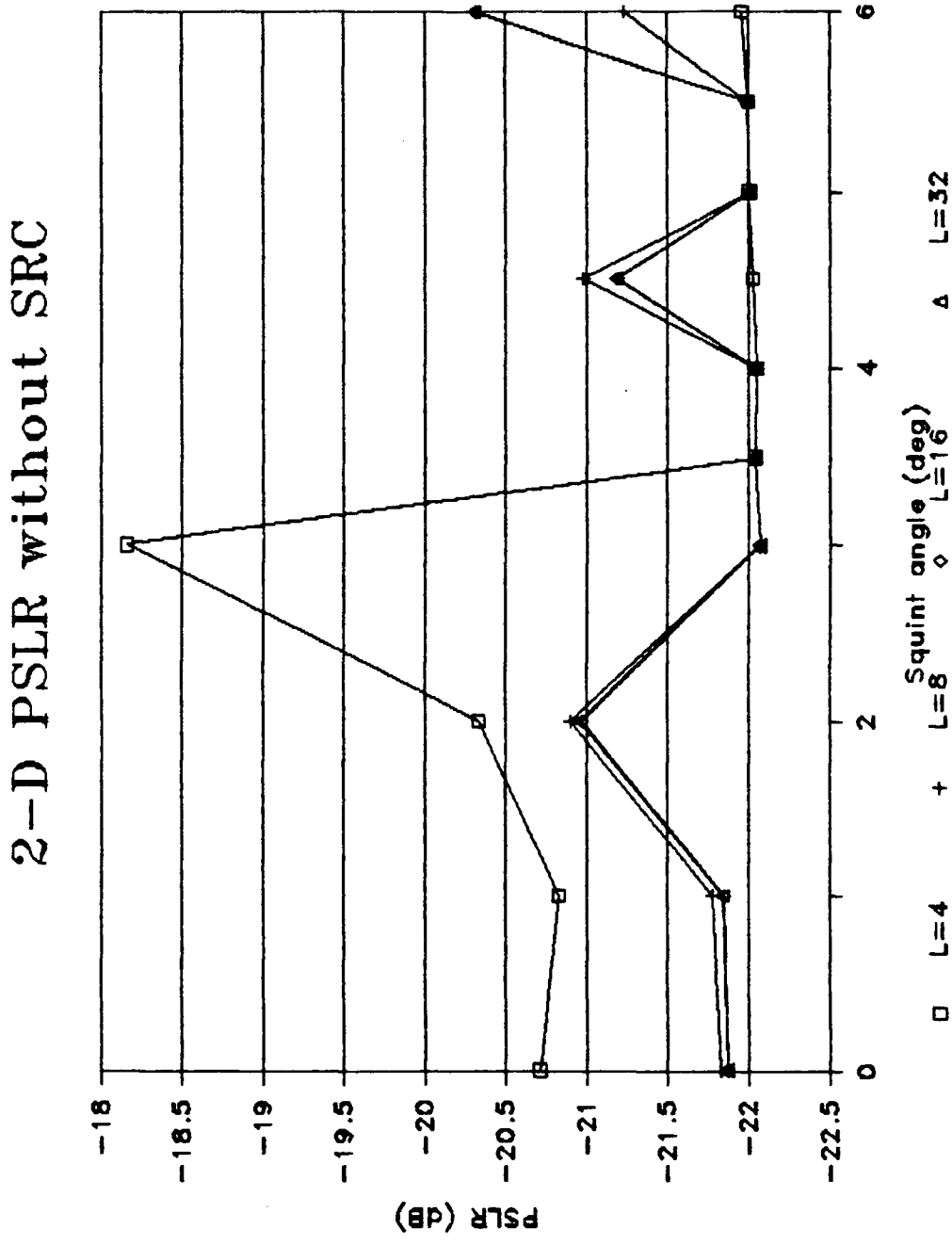

Figure 3.22. 2-D peak sidelobe ratios without SRC for various RCMC interpolator lengths.

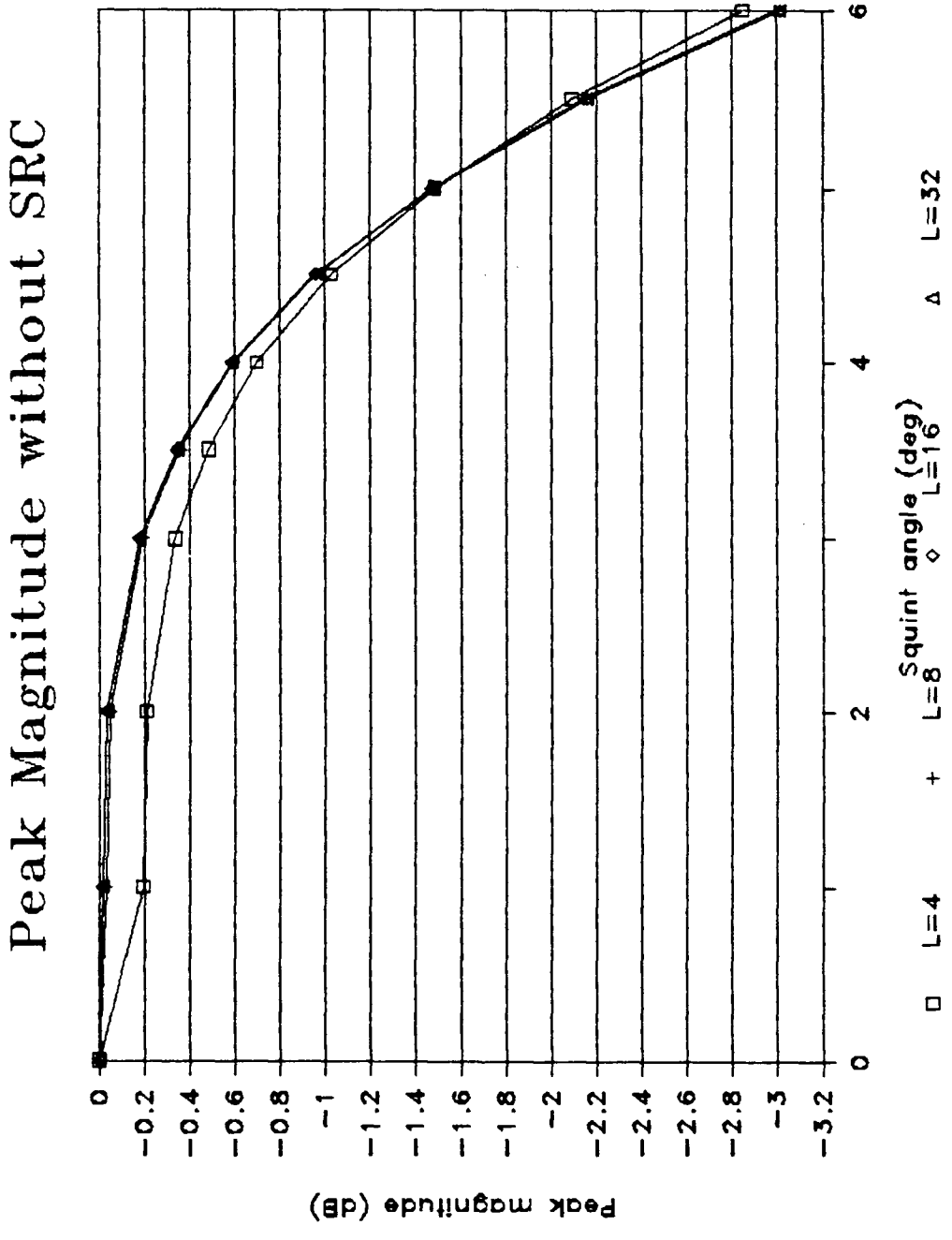

Figure 3.23. Degradation of peak magnitude without SRC for various RCMC interpolator lengths.

4. ANALYSIS OF BROADENING IN RANGE/DOPPLER COMPRESSION

This section presents a theory which characterizes the broadening, primarily in range, which occurs at high squint angles in basic range/Doppler processing without SRC. The theory extends the range broadening model of Jin and Wu [13] to include the effects of the range sidelobe control window. The principle of stationary phase, which was used in the previous chapter to relate the azimuth spectrum to the azimuth time domain signal, is replaced by an approximate Fourier transform which accounts for the spectrum broadening which occurs in low TBP linear FM signals. Measurements of the simulated azimuth TBP and spectral broadening in both the azimuth frequency and range time directions are presented.

Azimuth broadening is shown to be accurately predicted by the decrease in processed bandwidth with increasing squint angle, a quality which is inherent to the simulation models. Little, if any, azimuth broadening is caused by the azimuth spectral broadening.

4.1 BROADENING MODEL FOR RANGE/DOPPLER COMPRESSION WITHOUT SRC

The previous chapter presented a theory of range and azimuth compression for the basic range/Doppler algorithm. It was shown that the 2-D range compressed signal can be expressed as :

$$h_{RC}(t,\eta) = h_A(t,\eta) *_t h_{RCP}(t) \tag{58}$$

where

$$h_A(t,\eta) = w_a(\eta) \exp[-j4\pi r(\eta)/\lambda] \; \delta[t-2r(\eta)/c] \tag{59}$$

and $h_{RCP}(t)$ is the 1-D range compressed profile which is usually similar in shape to a sinc function.

The first step after range compression in basic range/Doppler azimuth compression is the computation of the azimuth fast Fourier transform (FFT) of the range compressed signal. In continuous-time theory this is replaced by a continuous azimuth Fourier transform. In general, the azimuth Fourier transform of the range compressed signal cannot be represented exactly in closed form, or even in a separable form.

A major approximation is now made which allows the azimuth spectrum to be expressed in a form which restricts the range-azimuth coupling to a delta line function as in the azimuth time domain signal in equation (58). A similar approximation was originally presented in [13] but its validity was not fully discussed. The convolution in range is approximated by a convolution in azimuth as :

$$h_{RC}(t,\eta) \simeq h_A(t,\eta) *_\eta h_{RCP}(c_1\eta) \tag{60}$$

$$= \{ w_a(\eta) \exp[-j(4\pi/\lambda)r(\eta)] \delta[\eta - r^{-1}(ct/2)] \}$$

$$*_\eta h_{RCP}(c_1\eta) \tag{61}$$

where $r^{-1}(r)$ is the inverse function of the RCM equation, $r(\eta)$, and c_1 is the slope of the RCM curve at the beam center time given by :

$$c_1 = - \lambda f_C / c \tag{62}$$

The approximation can be viewed as a linear projection of the range profile about the RCM curve into azimuth time with the position of the peak of the profile corrected to lie along the RCM curve. Two major assumptions have been made :

1. The shape of the amplitude profile in the azimuth direction is assumed to be the same as the range compressed profile with the exception of a scaling constant. In reality the azimuth profile is slightly asymmetric due to range curvature.

2. The scaling constant, which is the slope of the RCM curve, is assumed to be constant over the azimuth processing interval. Actually the slope varies slowly

over the processing interval again due to range curvature.

The first assumption seems reasonable when the azimuth timewidth is small, i.e., when the amount of range curvature over the -3dB azimuth timewidth is much less than the range resolution. Fortunately, this condition occurs at larger squint angles where spectrum broadening is of most interest. The assumption may break down at small squint angles where little broadening occurs.

The second assumption may be more sensitive to range curvature since linearity is assumed over the entire azimuth processing interval. For RADARSAT parameters range curvature is very small and the slope of the RCM curve does not vary appreciably over the processed azimuth aperture. However for longer wavelength SARs, the slope may vary somewhat. The chapter on multilook processing addresses this assumption in more detail.

Applying the azimuth Fourier transform and using the convolution theorem leads to the following equation for the range compressed spectrum :

$$H_{RC}(t,f) = W_a(f) *_f F\{ \exp[-j(4\pi/\lambda)r(\eta)] \} *_f$$

$$[F\{\delta[\eta - r^{-1}(ct/2)]\} \bullet F\{h_{RCP}(c,\eta)\}] \qquad (63)$$

where $W_a(f)$ is the Fourier transform of the azimuth antenna

weighting function, $w_a(\eta)$. In this form the azimuth spectrum consists of the convolution of three functions in azimuth frequency.

The second two functions will be evaluated explicitly. The middle function is the Fourier transform of the phase along the RCM curve. Using the quadratic approximation of equation (12), it can be evaluated in closed form [17] as :

$$F\{ \exp[-j(4\pi/\lambda)r(\eta)] \} \simeq (1/\sqrt{|K_A|}) \exp[j\psi(f)] \qquad (64)$$

where

$$\psi(f) = -\pi(f-f_1)^2/K_A + (\pi/4)\mathrm{SIGN}(K_A) + \psi_0 \qquad (65)$$

$$\psi_0 = -4\pi r_1/\lambda \qquad (66)$$

and SIGN(x) denotes the sign of x. Although the quadratic approximation to the azimuth phase is used here, the exact transform will be substituted back after extracting a broadening function.

The delta function in the third term contains the range-azimuth coupling. Its transform is a linear phase complex exponential in which the rate of change of phase is a function of range :

$$F\{ \delta[\eta-r^{-1}(ct/2)] \} = \exp[-j2\pi f r^{-1}(ct/2)] \qquad (67)$$

Finally the transform of the scaled range compressed profile including the range window is given by :

$$F\{ h_{RCP}(c_1\eta) \} = (1/|c_1|)\ H_{RCP}(f/c_1) \tag{68}$$

The following substitutions and approximations were not shown in the paper by Jin and Wu but are essential to understanding the broadening model. Using the above transforms the second convolution in equation (63) can be rewritten as :

$$\frac{1}{|c_1|\ \sqrt{|K_A|}} \int_{-\infty}^{\infty} H_{RCP}(f'/c_1)\ e^{j\psi(f-f')}\ e^{-j2\pi f' r^{-1}(ct/2)} df' \tag{69}$$

$$= \frac{e^{j\psi(f)}}{|c_1|\ \sqrt{|K_A|}} \int_{-\infty}^{\infty} H_{RCP}(f'/c_1)\ e^{-j(\pi/K_A)f'^2}$$

$$e^{j2\pi f'[(f-f_1)/K_A\ -\ r^{-1}(ct/2)]}\ df' \tag{70}$$

The leading exponential can be recognized as the transform of the azimuth phase along the RCM curve in equation (64). Thus the exact time domain phase function will be substituted back.

The remaining integral defines the amplitude broadening and phase deviation along each azimuth line. Using the change of variable,

$$\eta_1 = f' \ / \ K_A \tag{71}$$

the integral can be expressed as :

$$A_1(f) *_f \delta[f-f_1-K_A r^{-1}(ct/2)] \tag{72}$$

where

$$A_1(f) = (1/|c_2|) \int_{-\infty}^{\infty} H_{RCP}(\eta_1/c_2)\ e^{-j\pi K_A \eta_1^2}\ e^{j2\pi f \eta_1}\ d\eta_1 \tag{73}$$

$$= F^{-1}\{\ (1/|c_2|)\ H_{RCP}(\eta_1/c_2)\ e^{-j\pi K_A \eta_1^2}\ \} \tag{74}$$

and

$$c_2 = c_1/K_A = -\lambda f_C/(cK_A) \tag{75}$$

As it stands, the broadening is expressed as a convolution in azimuth frequency which is dependent on range. To express the broadening in terms of range time, $A_1(f)$ must be projected back into range using the approximately constant slope, c_2, of the RCM curve in the azimuth frequency domain. This second projection of the signal model about the RCM curve was not discussed by Jin and Wu. The same conditions apply for this projection as before except that the signal is now in the azimuth frequency domain. The result is :

$$A_1(f) *_f \delta[f-f_1-K_A r^{-1}(ct/2)]$$

$$\simeq A_1(t/c_2) *_t \delta[t-(2/c)r([f-f_1]/K_A)] \qquad (76)$$

Since the azimuth antenna function is a slowly varying function of azimuth time and the remainder of equation (63) is an approximately linear FM signal, its convolution with the above terms can be approximated by a multiplication [17] with a scaled version of the antenna function. The scaling is defined by the azimuth frequency to azimuth time mapping, $\eta_i(f)$. This gives the final form of the azimuth transformed range compressed signal as :

$$H_{RC}(t,f) = w_a(\eta_i(f)) \bullet \mathcal{F}\{ \exp[-j(4\pi/\lambda)r(\eta)] \}$$

$$\bullet \{ A_1(t/c_2) *_t \delta[t-(2/c)r([f-f_1]/K_A)] \} \qquad (77)$$

Azimuth compression without SRC does not significantly alter the range dispersion defined by equation (77) since azimuth compression occurs primarily parallel to the RCM curve. Therefore the approximate range profile after azimuth compression is determined by $A_1(t/c_2)$ which is the inverse Fourier transform of a weighted linear FM signal.

When the width of the linear FM signal is small (i.e., when the phase at the -3dB points is much less than $\pi/2$ radians), the quadratic phase exponential in equation (74) produces little broadening of the inverse transform. This

occurs when c_2 and therefore also f_C and the squint angle are small. Thus for small squint angles, the range profile before and after the azimuth Fourier transform is approximately the same and little range broadening appears after compression without SRC.

4.2 BROADENING SIMULATIONS AND MEASUREMENTS

This section presents the results of simulating the range broadening function developed in the previous section. These are compared to measurements of the broadening of the range compressed point target response used in the previous simulations. These simulations are similar to those presented by Jin and Wu. However the range window has been added and detailed quantitative image quality measurements are performed.

Measurements of the azimuth TBP are presented to relate measurements of azimuth spectral broadening to the decrease in azimuth TBP.

A predicted azimuth broadening curve is shown which is based on the decrease in processed bandwidth with increasing squint angle.

The range broadening function, $A_1(t/c_2)$, provides a model for the range broadening of the azimuth spectrum which occurs in the azimuth Fourier transform. This function has been simulated with nominal RADARSAT parameters with the same range window parameter (β_R=2.7) that was used in previous simulations. The -3dB range widths have been

measured for various squint angles and are summarized in figure 4.1.

The simulated broadening function was generated according to equation (74) with f replaced by t/c_2 and the inverse Fourier transform integral approximated by an inverse FFT. The range compressed range spectrum, $H_{RCP}(\eta_1/c_2)$, was simulated as having zero phase with a magnitude defined by the range window function. This was multiplied by the quadratic phase broadening term. The functions were generated in a length N (N=2048) discrete frequency domain array with maximum frequency equal to the range sampling rate. An inverse FFT was applied to form a discrete, range time domain, broadening function. The resulting response width was measured with the image quality measurement programs discussed earlier.

The range broadening predicted by the broadening function agrees well with the actual range broadening results shown in figure 3.14 of the previous chapter. Additional broadening occurs with smaller RCMC interpolators, especially at large squint angles, due to the interpolator windowing.

Since the range broadening model is based upon predictions of azimuth spectrum broadening, the shapes of the azimuth time and frequency domain signals were examined. Figures 4.2 to 4.6 show the relationship between the azimuth timewidth of the simulated range compressed signal and its bandwidth after the azimuth FFT. The upper graphs show the

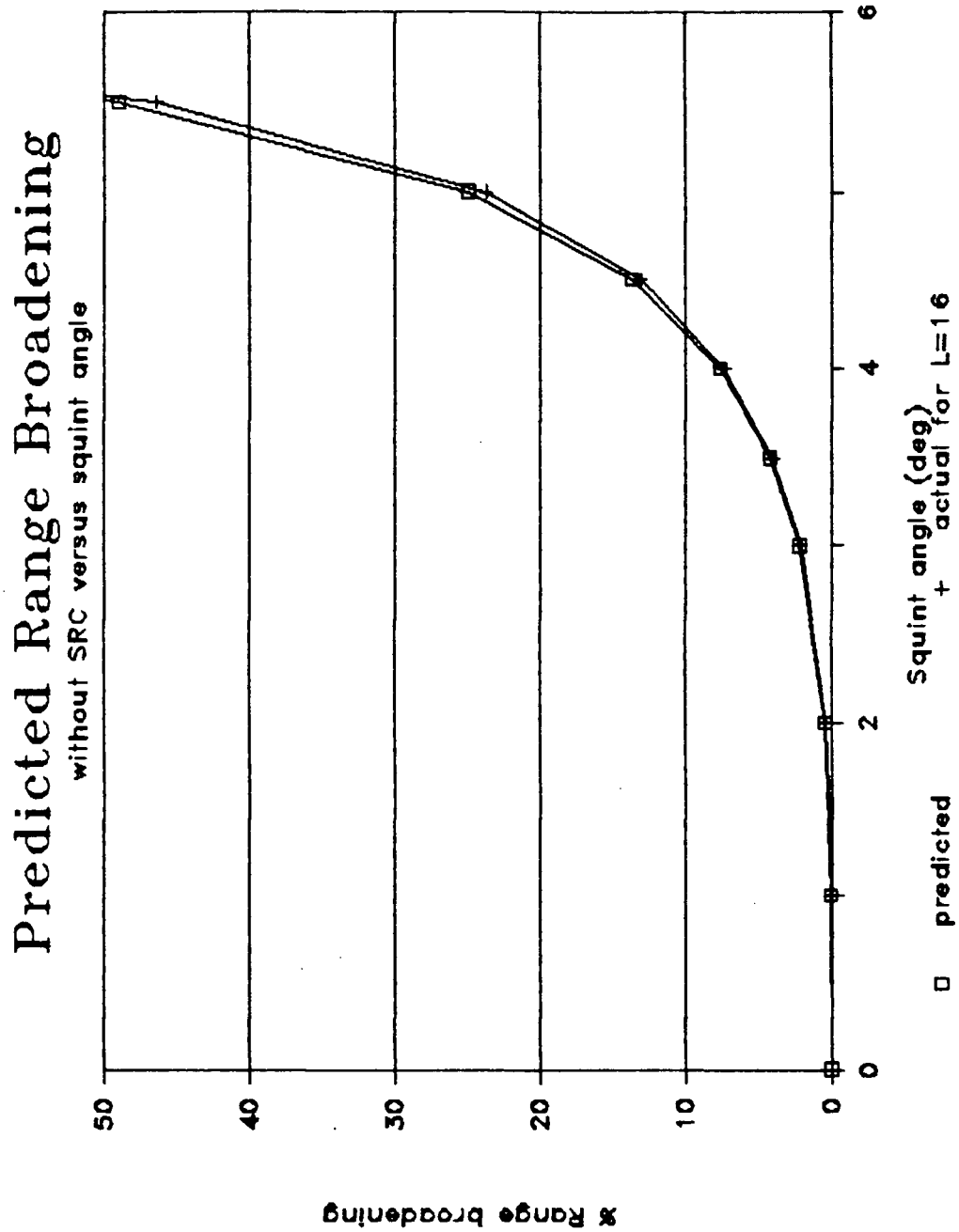

Figure 4.1. Range broadening of the simulated, theoretical, range broadening function without SRC.

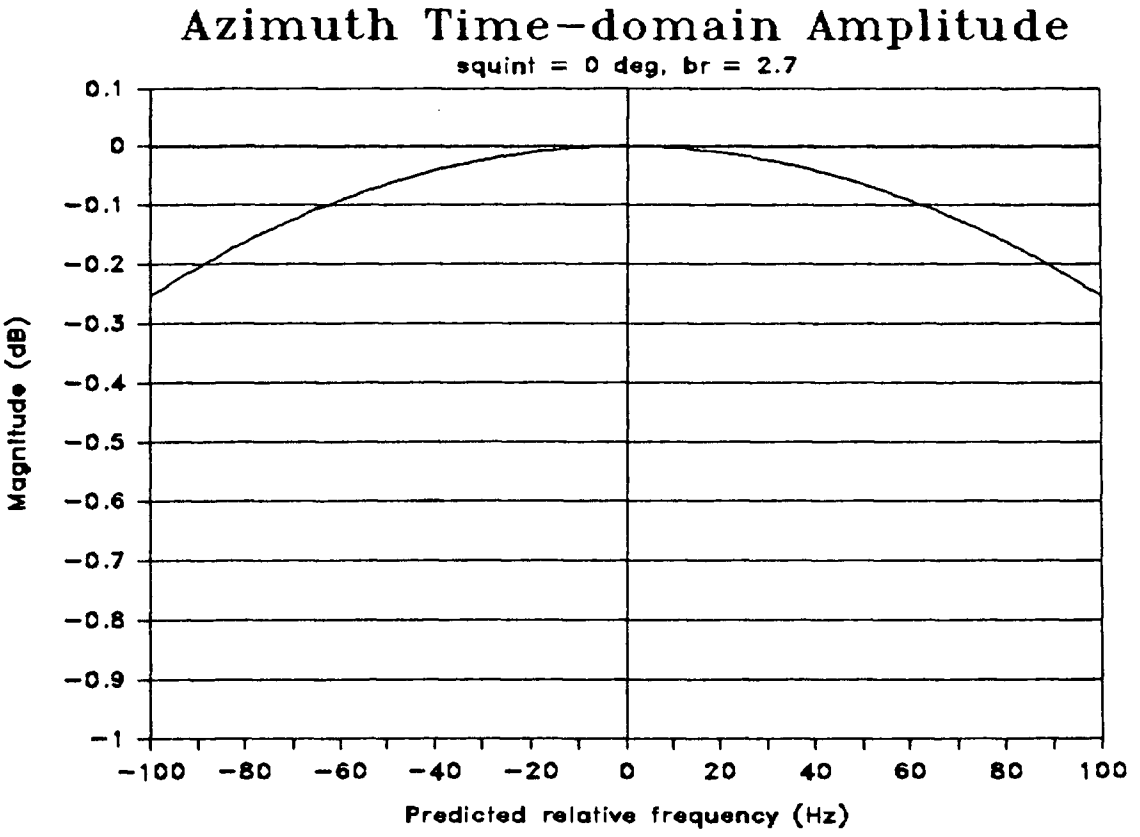

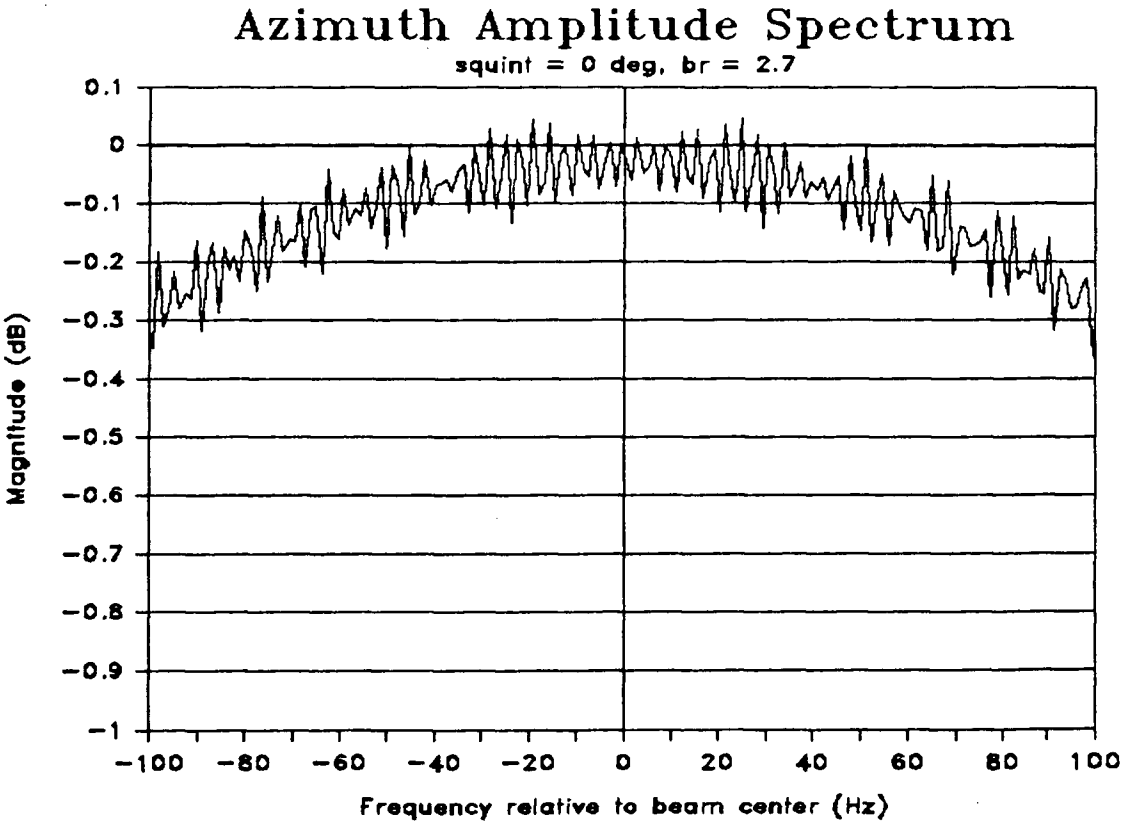

Figure 4.2. Predicted and actual azimuth spectra for 0° squint.

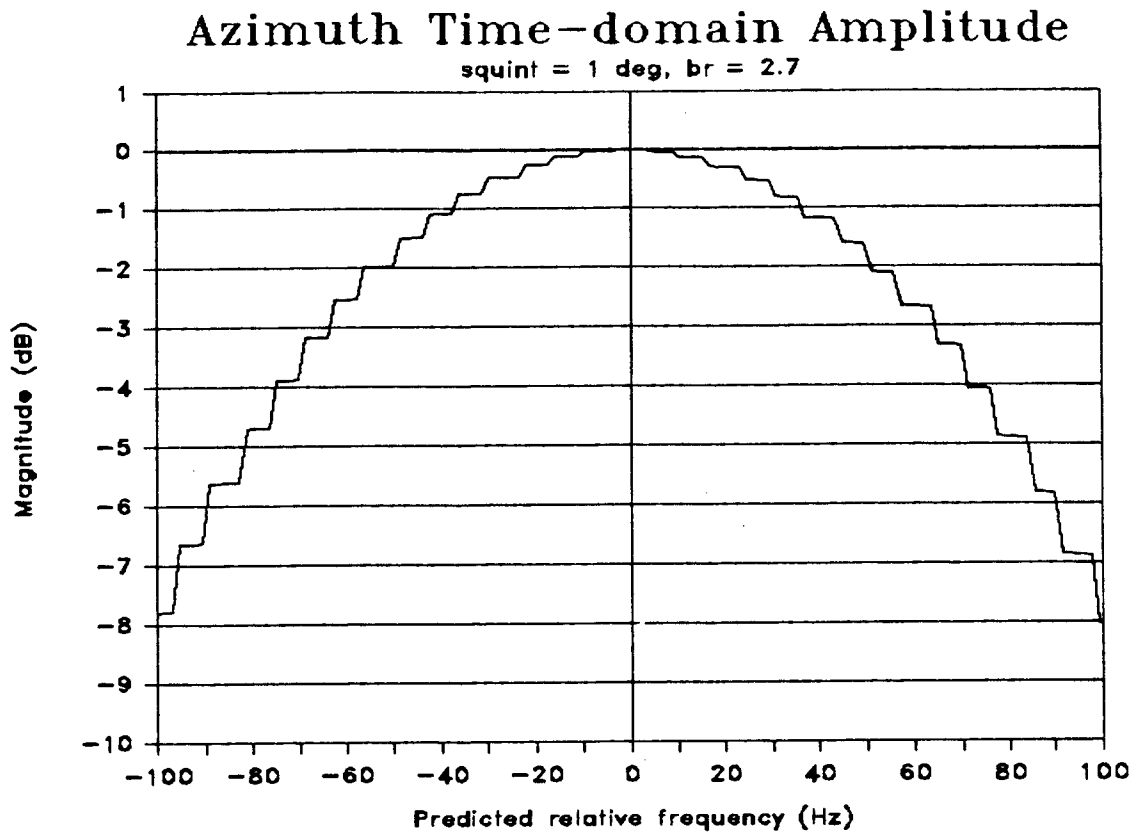

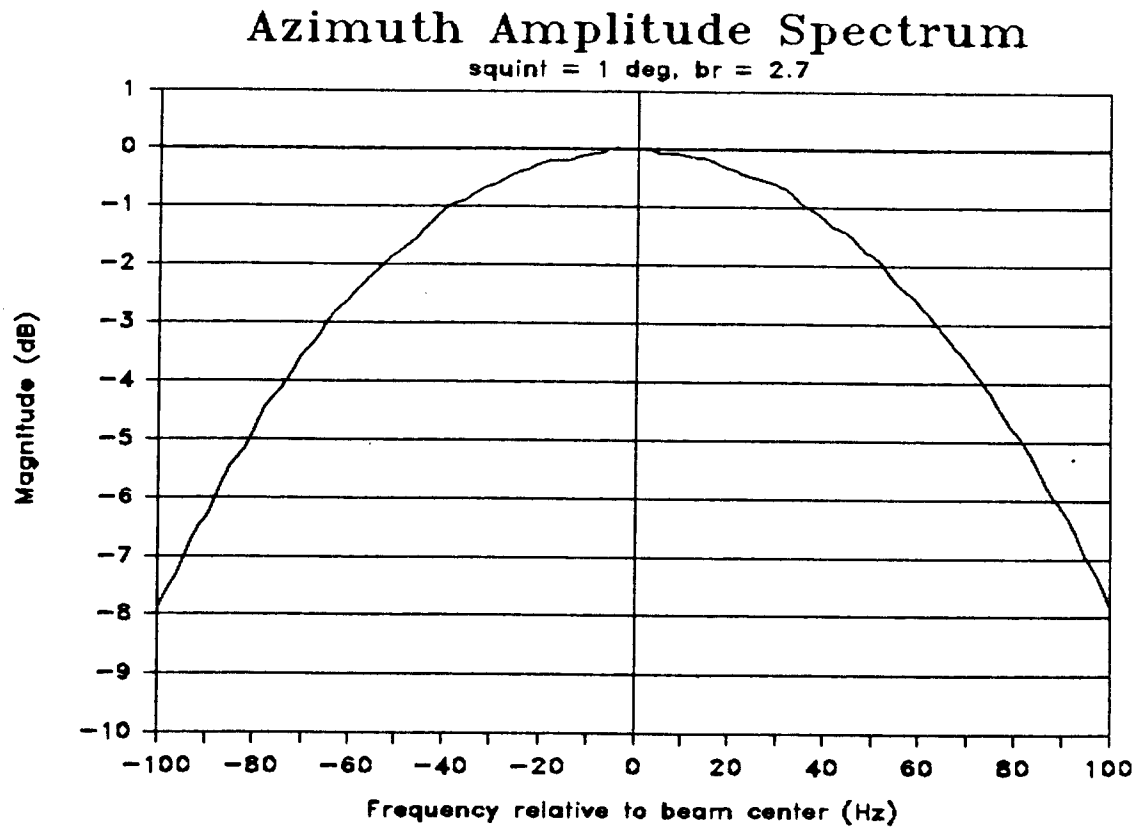

Figure 4.3. Predicted and actual azimuth spectra for 1° squint.

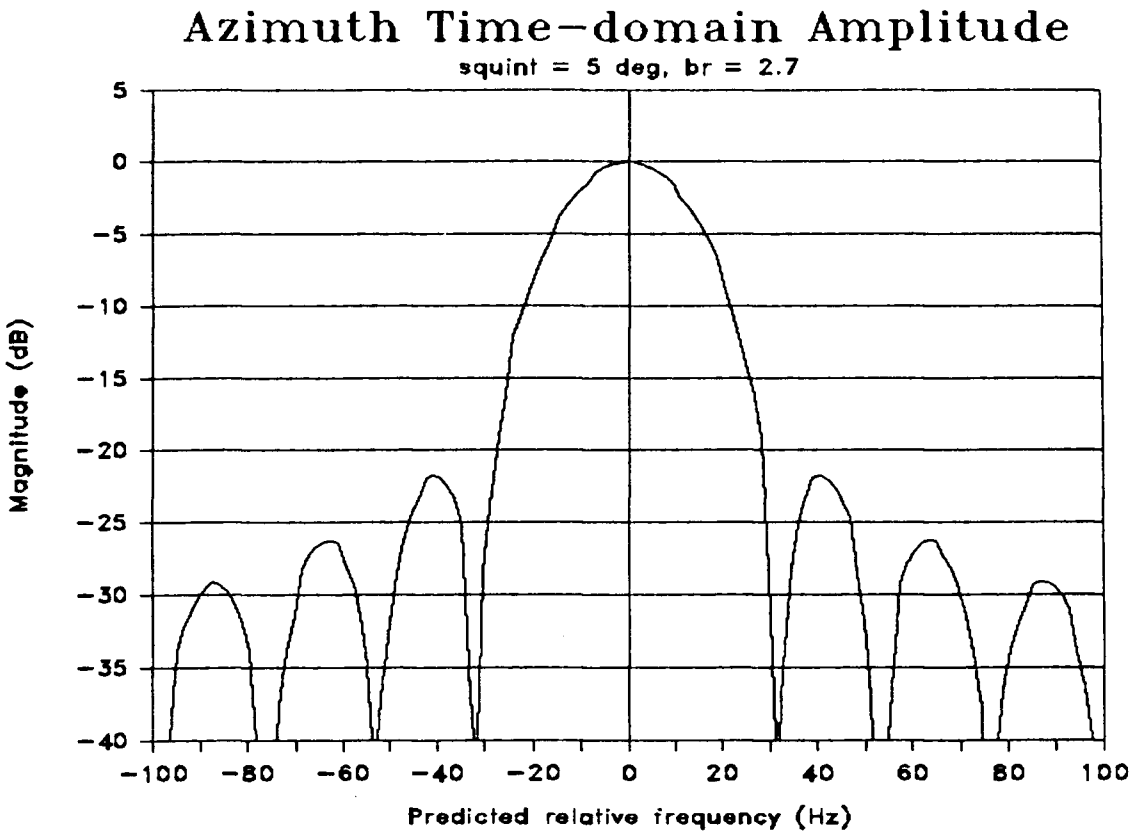

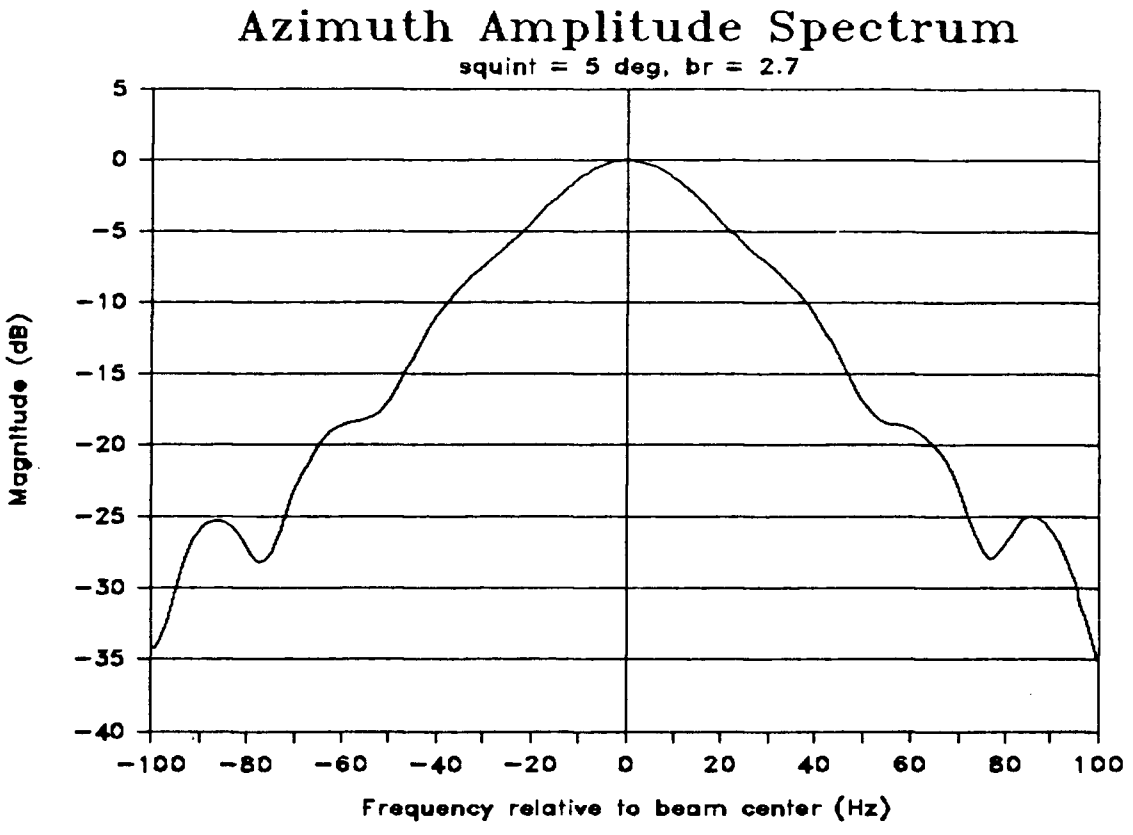

Figure 4.4. Predicted and actual azimuth spectra for 5° squint.

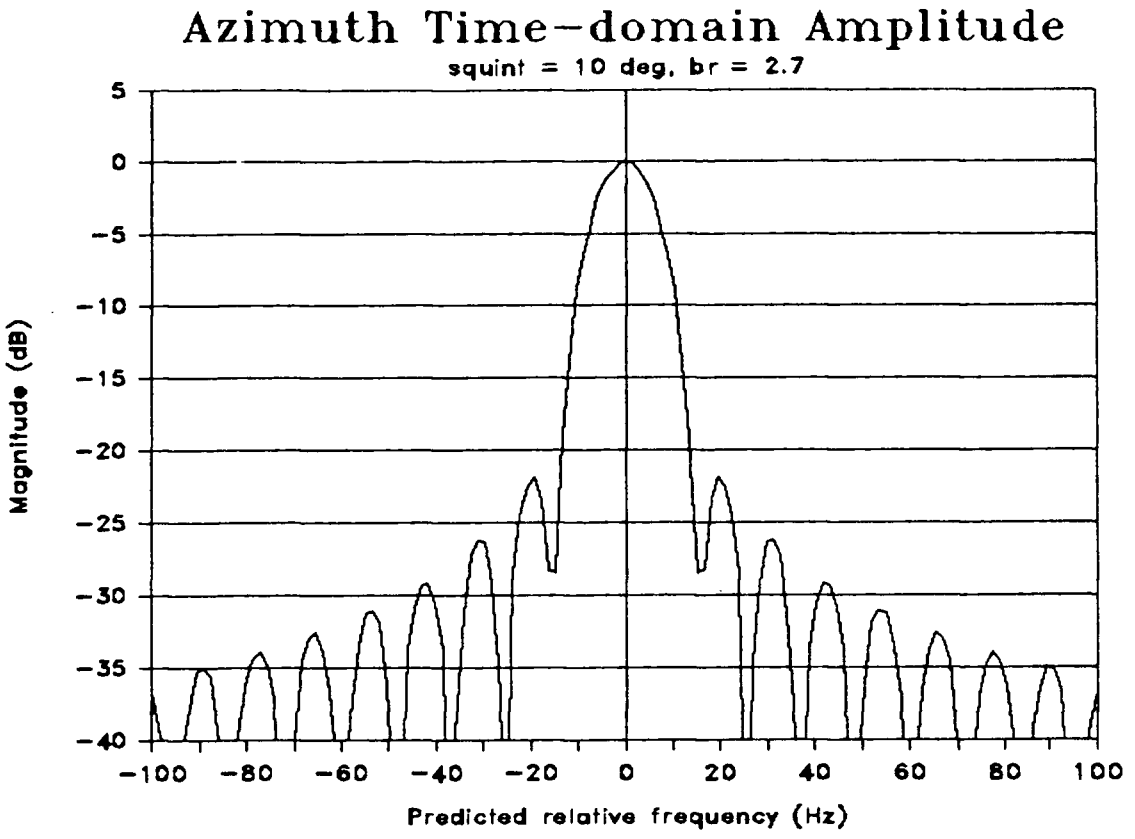

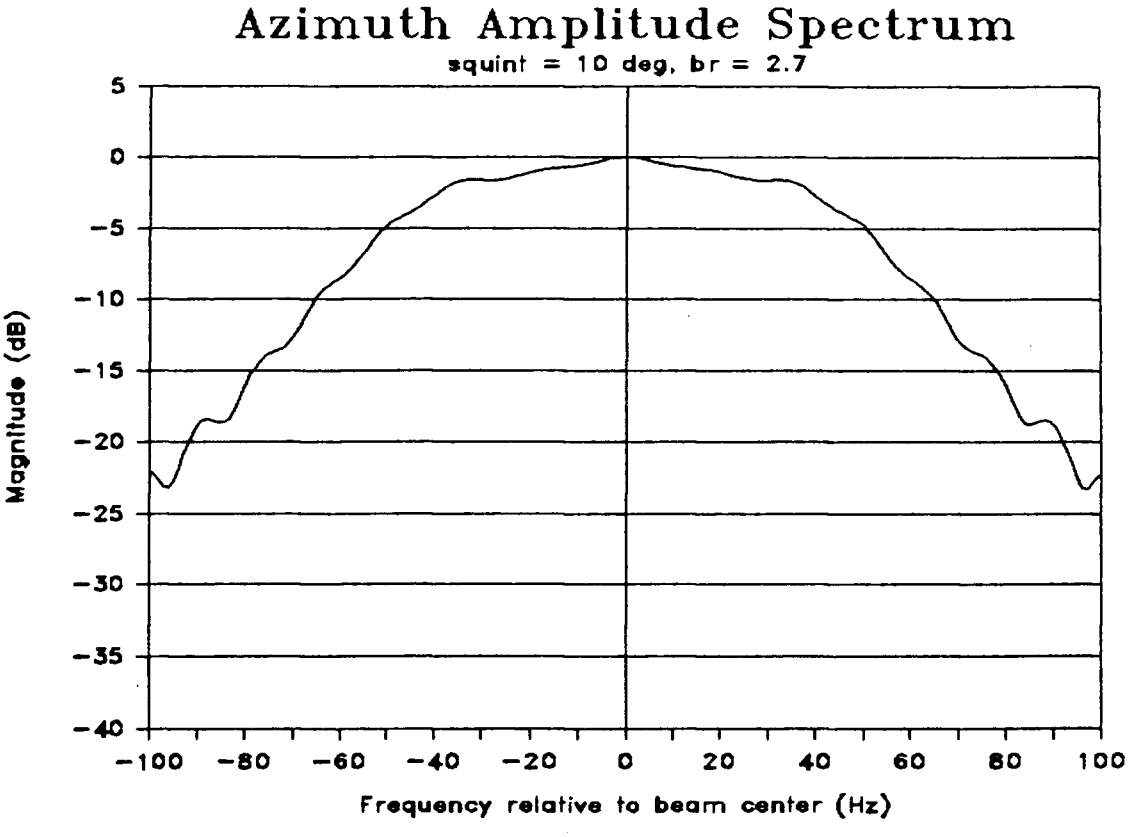

Figure 4.5. Predicted and actual azimuth spectra for 10° squint.

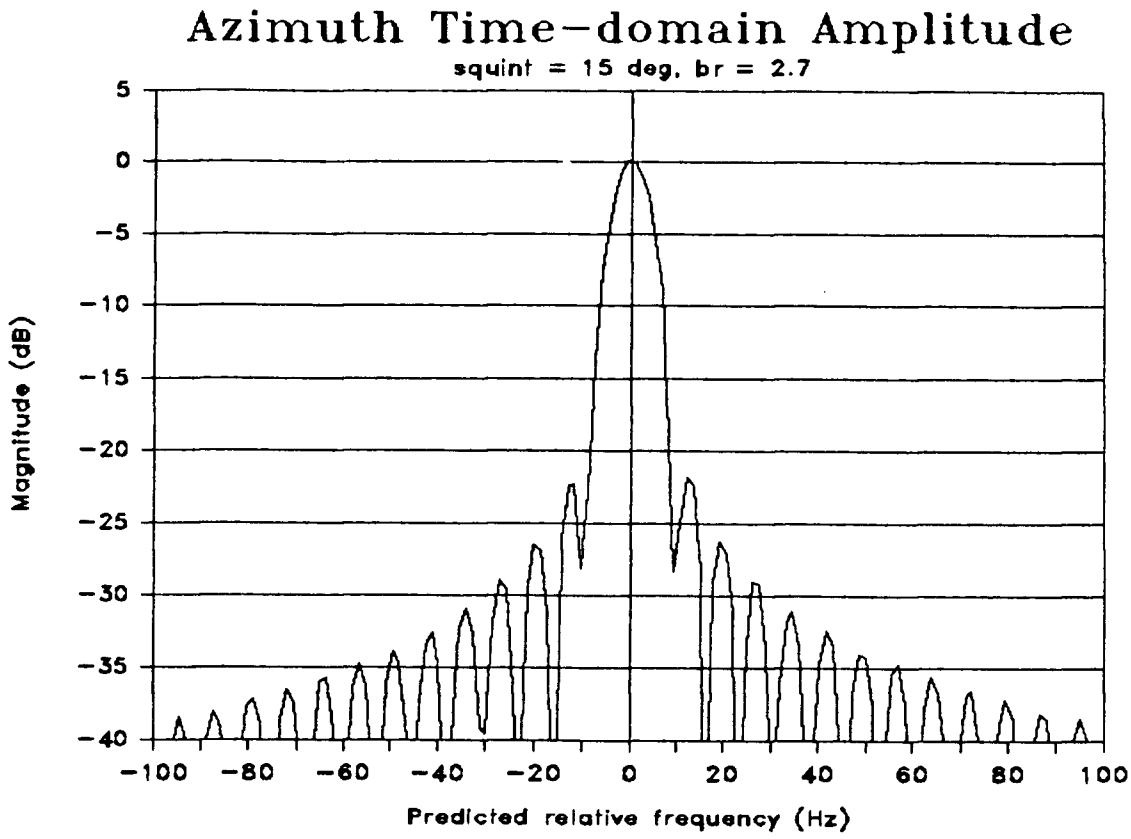

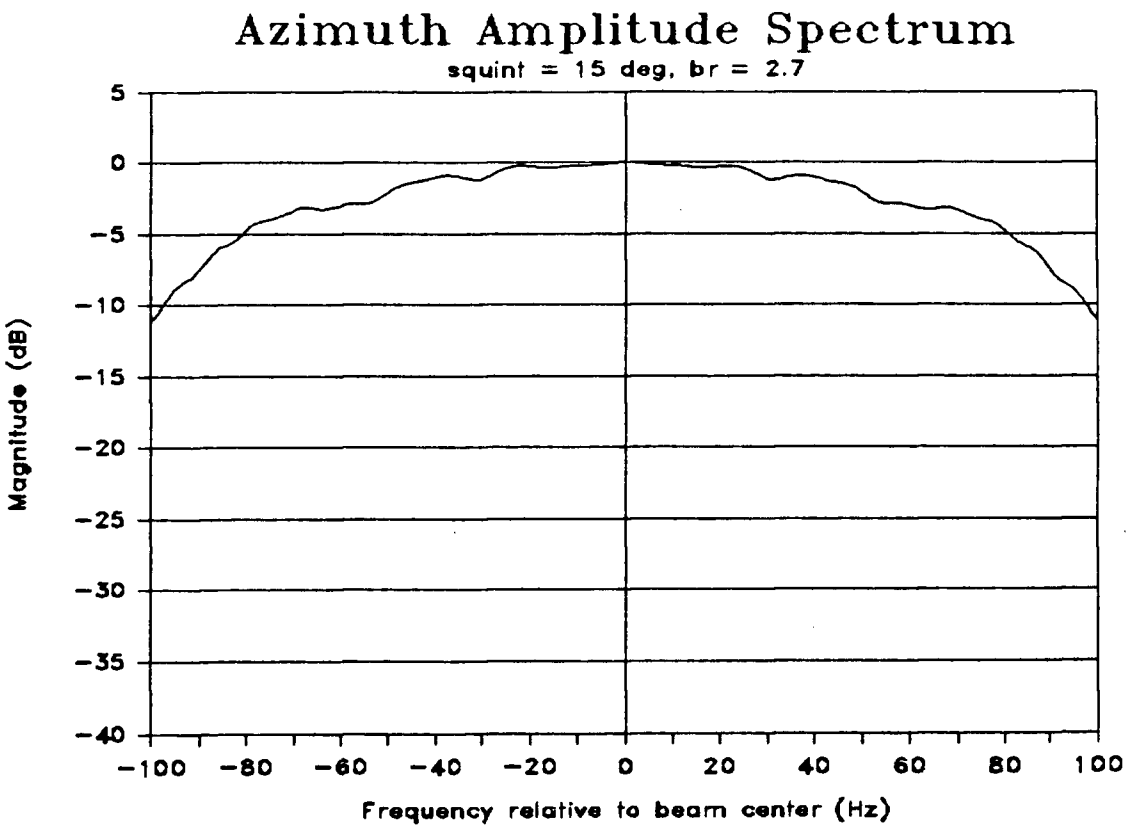

Figure 4.6. Predicted and actual azimuth spectra for 15° squint.

timewidths with the time scale converted to predicted frequency using the azimuth FM rate at the beam center as follows :

$$f_{predicted} - f_C \simeq K_A(\eta - \eta_C) \tag{78}$$

The lower graphs show the actual bandwidths. The graphs are plotted for squint angles of 0, 1, 5, 10, and 15 degrees. At small squint angles (0° and 1°) the time and frequency domain signals are very similar. At 5° significant spectrum broadening is evident. At 10° and 15° the broadening is so severe that the actual spectra no longer resemble the predicted spectra.

The amount of range and azimuth broadening of the simulated range compressed azimuth spectrum was measured to determine the accuracy of the range broadening model. The broadening measurements are summarized in figures 4.7 to 4.10. These measurements were performed after the azimuth FFT but before RCMC. Broadening in both the azimuth frequency and range time directions was measured at three points on the RCM curve as shown in figure 4.11 : at the lower azimuth processed bandwidth frequency (the far range cell); at the beam center frequency (the range cell nearest the beam center range); and at the upper azimuth processed bandwidth frequency (the near range cell).

The spectrum broadening measurements in the azimuth frequency direction at low squint angles are inaccurate due

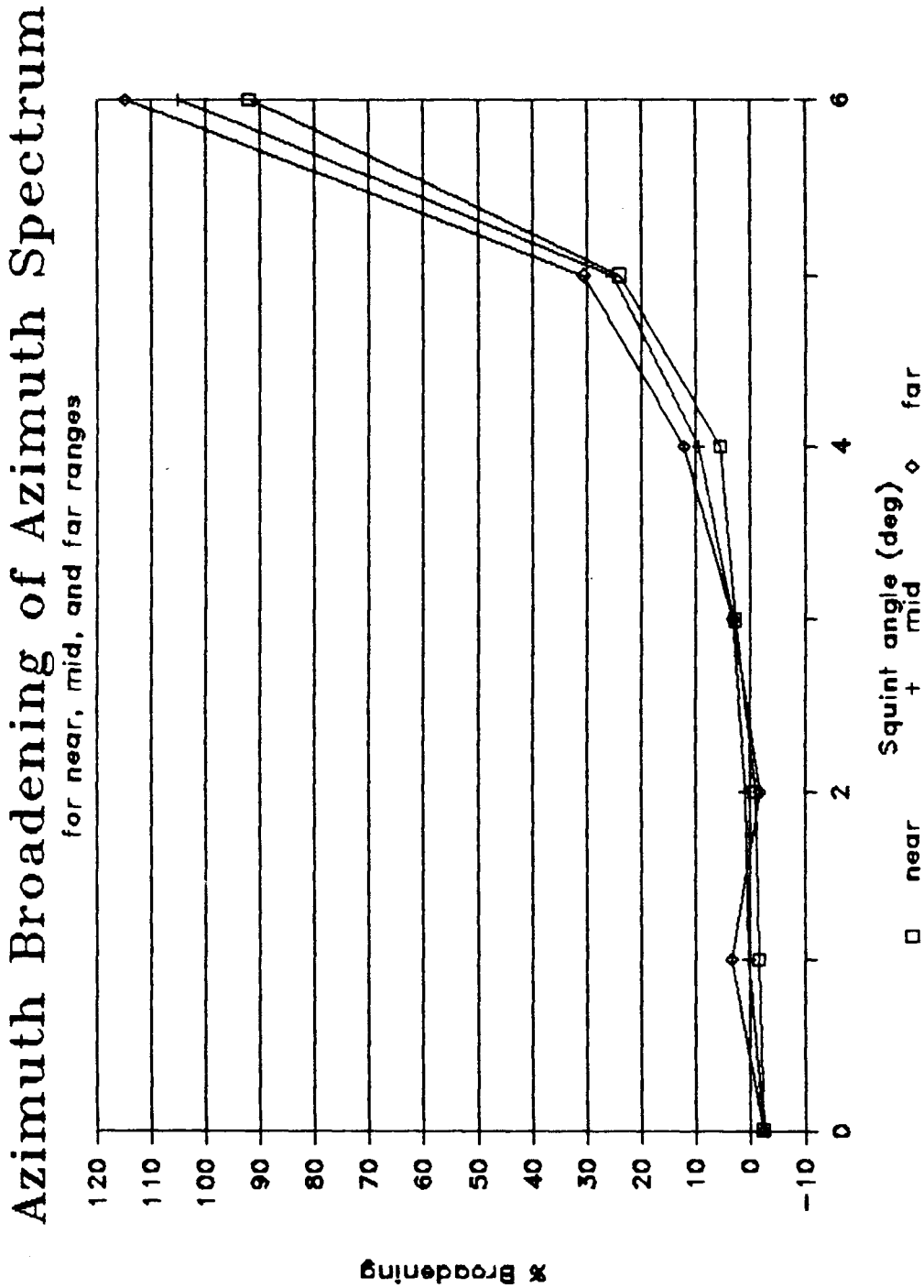

Figure 4.7. Measured azimuth spectrum broadening in the azimuth frequency direction in the near, beam center (mid), and far range cells.

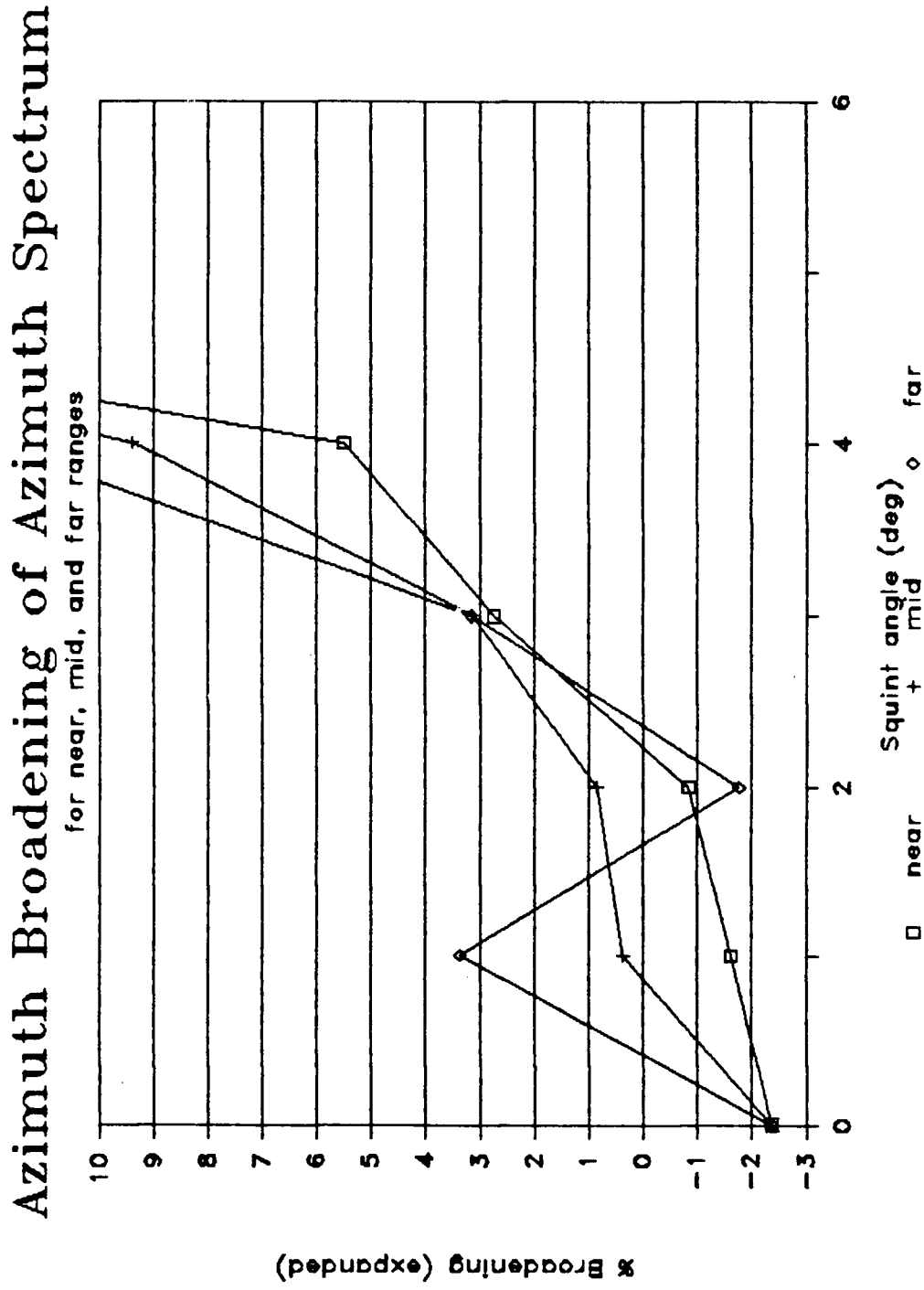

Figure 4.8. Measured azimuth spectrum broadening in the azimuth frequency direction in the near, beam center (mid), and far range cells (expanded).

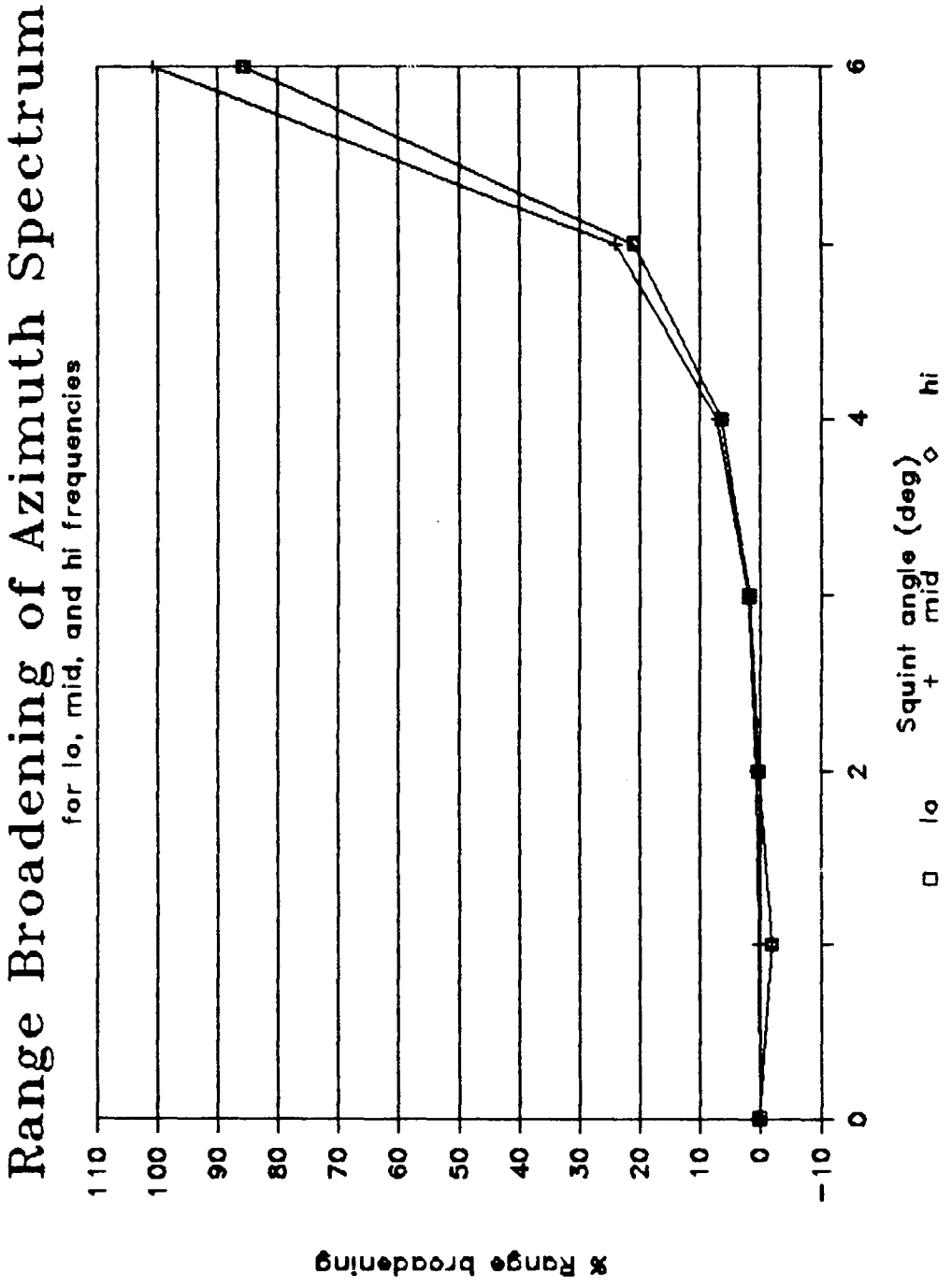

Figure 4.9. Measured azimuth spectrum broadening in the range time direction at the lower, the beam center, and the upper processed bandwidth frequencies.

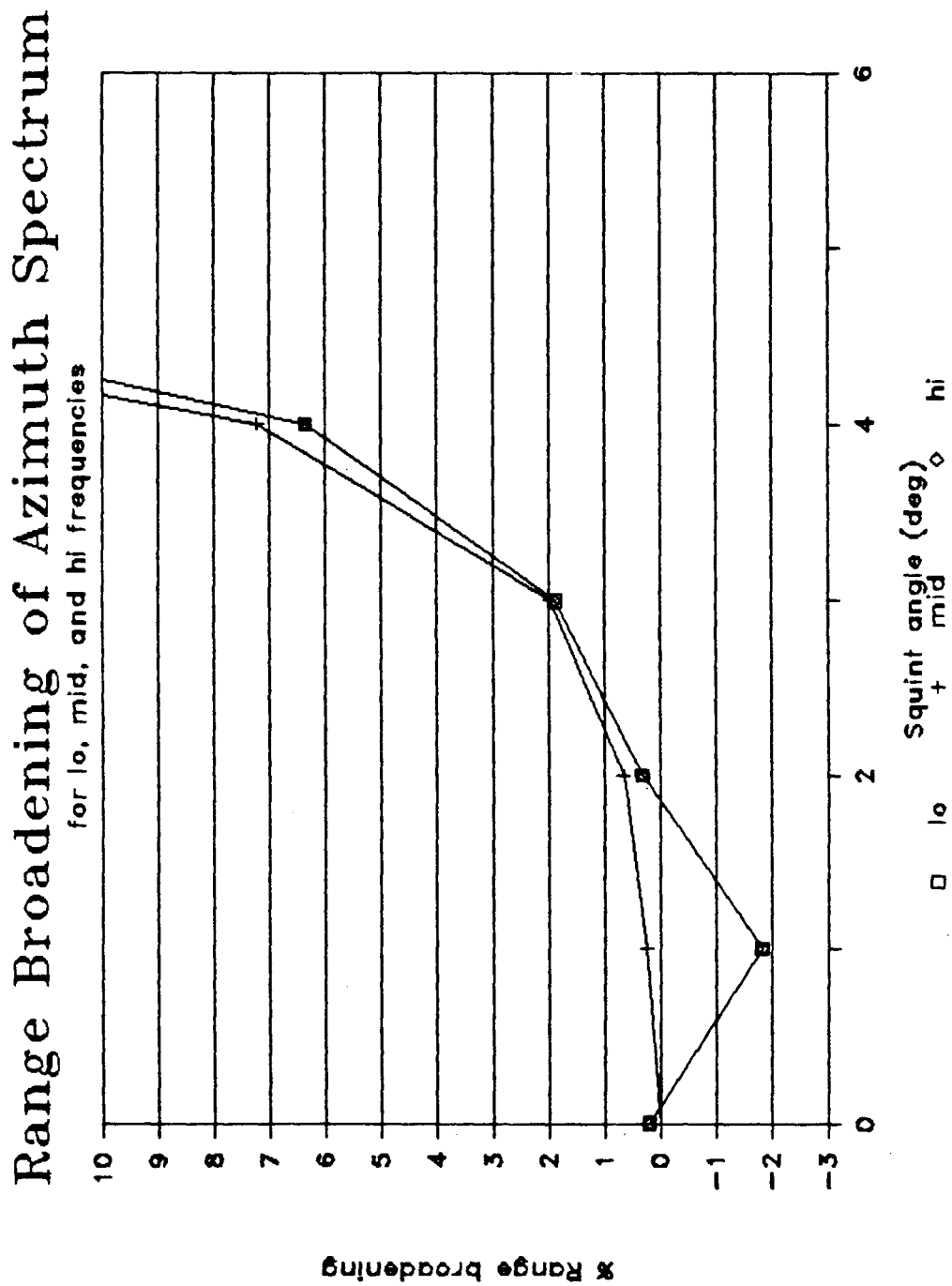

Figure 4.10. Measured azimuth spectrum broadening in the range time direction at the lower, the beam center, and the upper processed bandwidth frequencies (expanded).

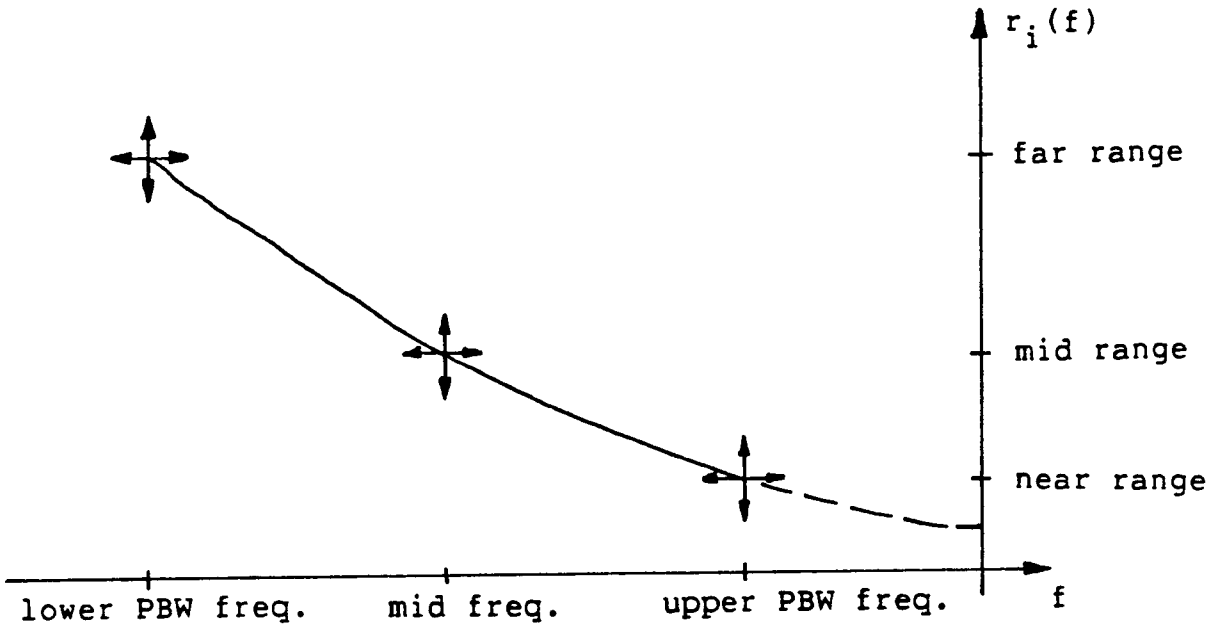

Figure 4.11. Points on the azimuth frequency domain RCM curve used for spectrum broadening measurements.

to the large spectrum ripples. At larger squint angles the azimuth spectrum is smoother allowing more accurate measurements. The broadening measurements agree well with the actual broadening results with large RCMC interpolators and the range broadening predicted by the broadening model. The broadening is somewhat greater at the low frequency (far range) end of the RCM curve and slightly smaller at the high frequency (near range) end. This is due to the small change in RCM slope over the processed bandwidth caused by range curvature.

As the squint angle increases, the slope of the RCM curve in the beam center range cell increases causing a decrease in the azimuth time width and TBP. For small TBP's, the shape of the azimuth spectrum after the azimuth FFT broadens and no longer closely resembles the azimuth time domain signal. Azimuth -3dB time width measurements of the range compressed signal were performed in order to calculate the azimuth time-bandwidth products (TBP) in the three range cells noted above as a function of squint angle. The resulting curves, figure 4.12, can be used to relate range broadening to the azimuth TBP. From a linear interpolation of the test points, the beam center azimuth TBP's corresponding to 5% and 10% range broadening are 0.76 and 0.57 respectively.

Azimuth broadening is much smaller than range broadening. The azimuth broadening which does occur can be attributed to the decrease in azimuth processed bandwidth

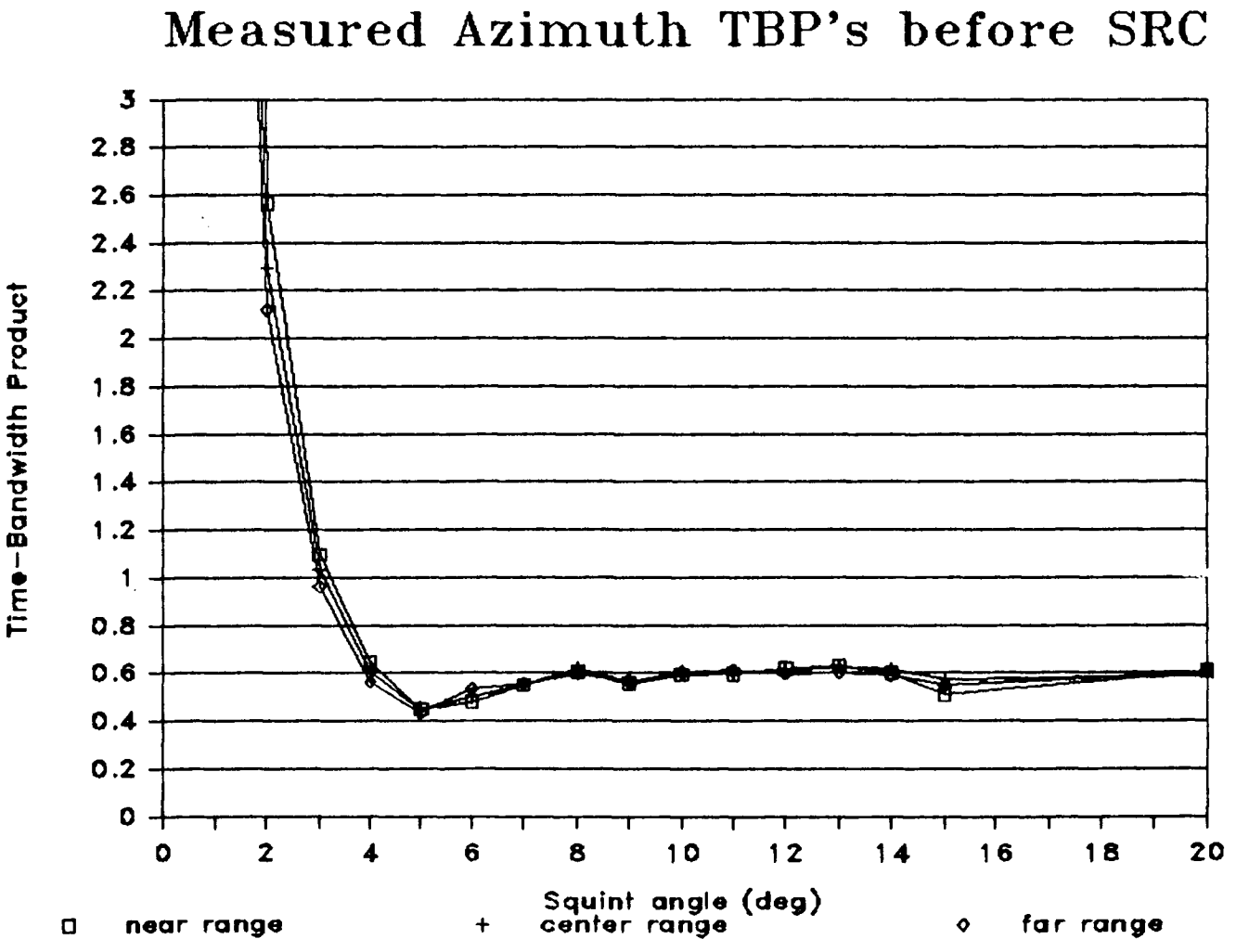

Figure 4.12. Measured azimuth time-bandwidth product (TBP) versus squint angle.

with increasing squint angle which is inherent to the simulation model of the azimuth antenna function. Since the azimuth -6dB (two-way) antenna time width was kept constant over changes in squint angle whereas the azimuth frequency rate varied, the processed bandwidth calculated by equation (54) decreased with increasing squint angle. Since the azimuth resolution is inversely proportional to the processed bandwidth, the percentage azimuth broadening can be predicted by calculating the percentage decrease in processed bandwidth as shown in figure 4.13. The predicted azimuth broadening agrees very closely with the measured results.

Very little azimuth broadening is caused by the spectrum broadening which causes range broadening since the distortion of the azimuth phase spectrum under low azimuth TBP conditions is very small over the -3dB azimuth bandwidth. Since azimuth compression is mainly a function of the phase spectrum, little azimuth broadening occurs.

Finally, figure 4.14 shows how the total amount of RCM over the processed aperture varies with squint angle for the given set of RADARSAT parameters. RCM increases almost linearly with squint angle as is expected for a predominantly quadratic curve.

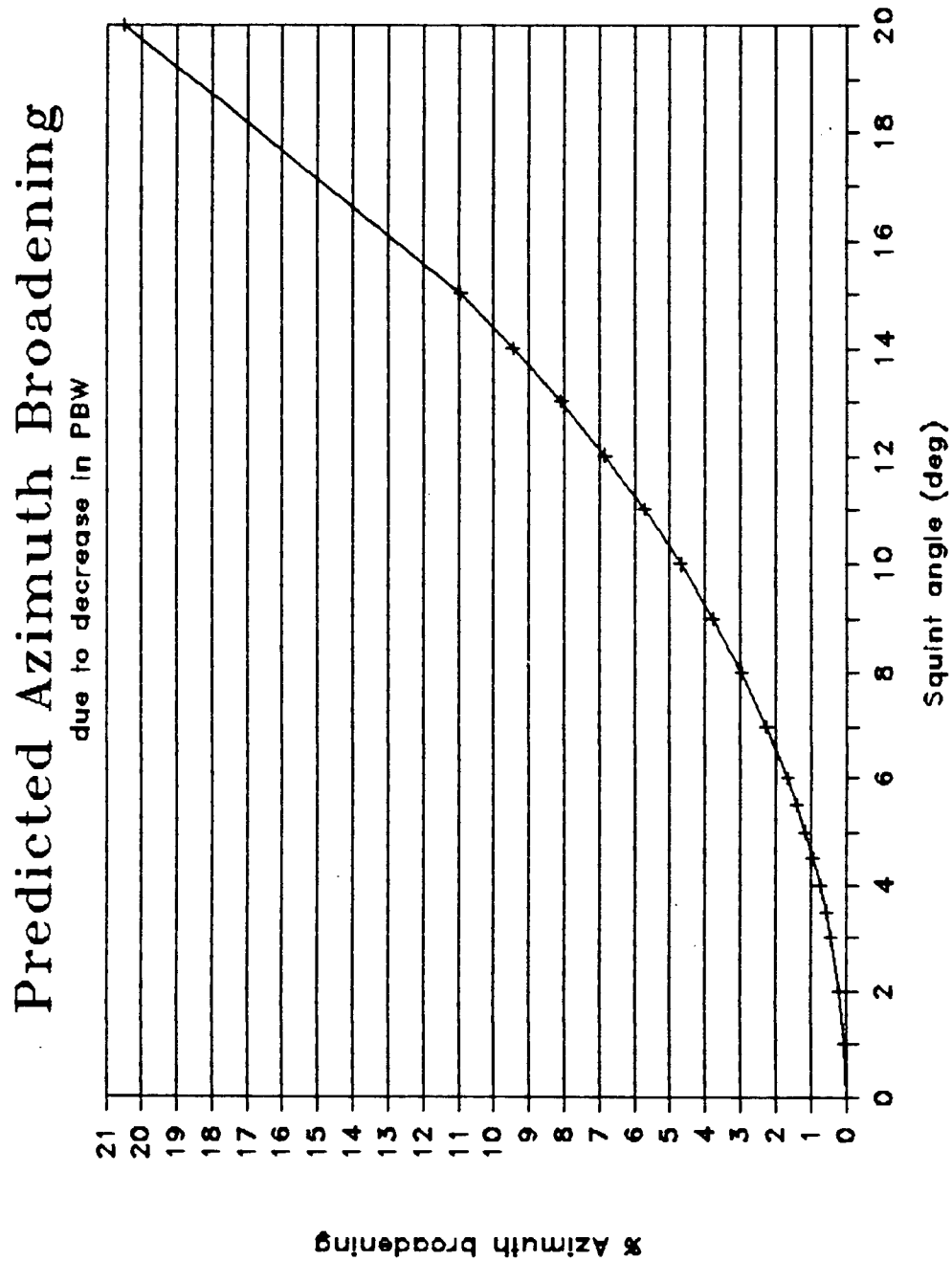

Figure 4.13. Azimuth broadening predicted by decrease in azimuth processed bandwidth.

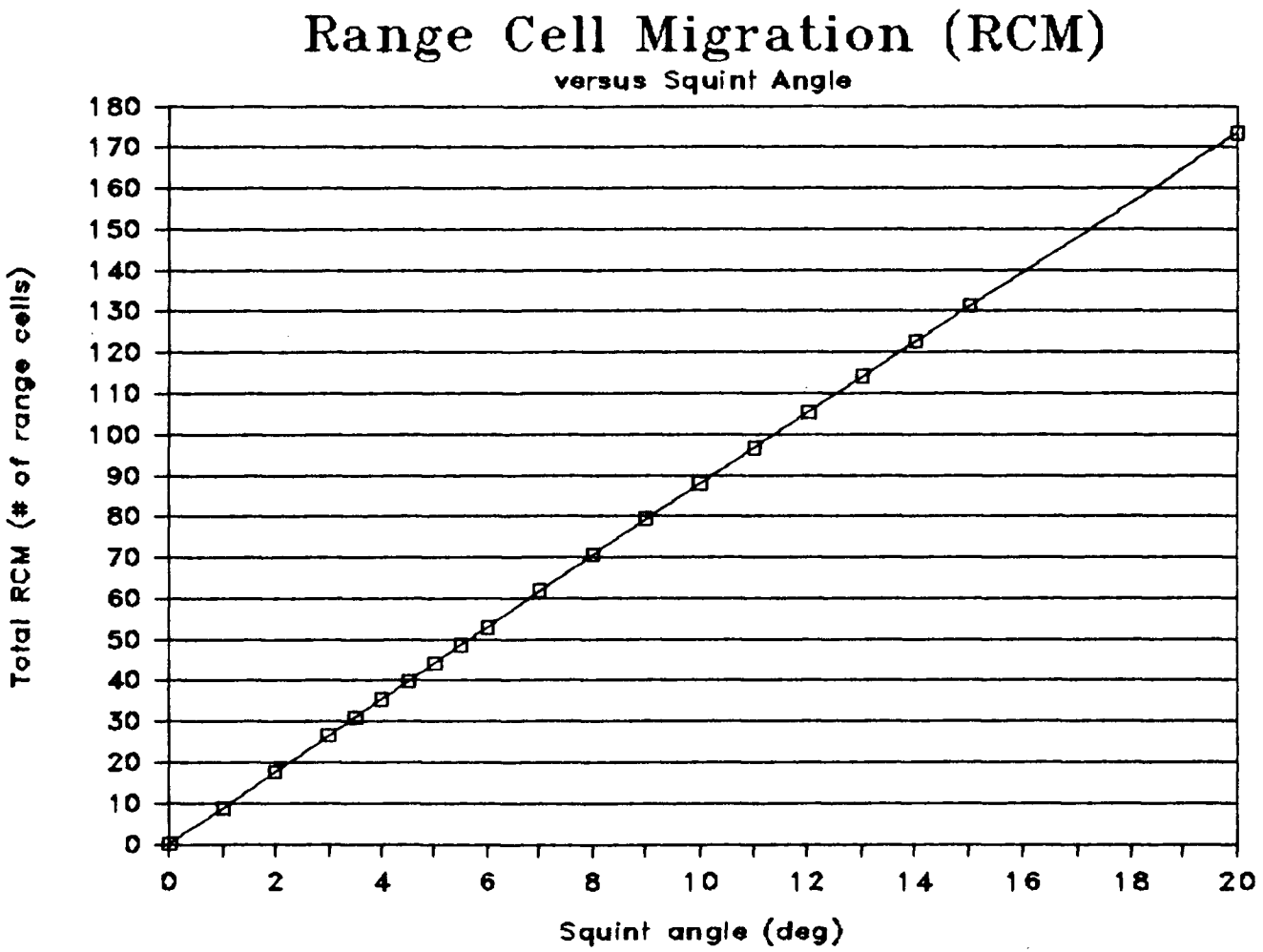

Figure 4.14. Range cell migration over processed aperture.

5. SECONDARY RANGE COMPRESSION (SRC)

This chapter introduces a new secondary range compression (SRC) algorithm which compensates for the range broadening which occurs in the azimuth FFT and which is not accounted for in the basic range/Doppler algorithm. A mathematical theory for the SRC algorithm is developed directly from the point target response model in chapter 3. Two new discrete implementations are developed : azimuth SRC and range SRC. It is shown with simulations that the SRC algorithms provide excellent recompression of the energy which is spread by the azimuth FFT at large squint angles (small azimuth TBP's) for nominal RADARSAT parameters.

5.1 THEORY OF AZIMUTH MATCHED FILTERING AND SRC

This section extends the theory of azimuth compression developed in chapter 3 to show how SRC can be used to recompress the energy which is dispersed by the azimuth Fourier transform.

The ideal matched filter for a point target signal is :

$$h^*(-t,-\eta) = h_A^*(-t,-\eta) * h_R^*(-t,-\eta) \tag{79}$$

Chapter 3 described the theory of range compression in which the range compressed signal $h_{RC}(t,\eta)$ is formed by convolving with the range matched filter $h_R^*(-t,-\eta)$ and a range window used to control sidelobes.

Azimuth compression consists of convolving the range compressed signal with an azimuth reference phase filter, $h_F^*(-t,-\eta)$, and an azimuth window to control sidelobes. The idealized azimuth reference phase function was given previously in equation (32) as :

$$h_F(t,\eta) = \exp[-j4\pi r(\eta)/\lambda]\ \delta[t-2r(\eta)/c] \tag{80}$$

Its azimuth Fourier transform can be evaluated using the Fourier transforms from chapter 4 :

$$H_F(t,f) = F\{\exp[-j4\pi r(\eta)/\lambda]\} *_f F\{\delta[t-2r(\eta)/c]\} \tag{81}$$

$$\simeq \frac{e^{j\psi(f)}}{\sqrt{|K_A|}} *_f e^{-j2\pi f r^{-1}(ct/2)} \tag{82}$$

$$= \frac{1}{\sqrt{|K_A|}} \int_{-\infty}^{\infty} e^{j\psi(f-f')}\ e^{-j2\pi f' r^{-1}(ct/2)}\ df' \tag{83}$$

$$= \frac{e^{j\psi(f)}}{\sqrt{|K_A|}} \int_{-\infty}^{\infty} e^{-j(\pi/K_A)f'^2}\ e^{j2\pi f'[(f-f')/K_A - r^{-1}(ct/2)]}\ df' \tag{84}$$

Using the same change of variables as before, $\eta_1 = f'/K_A$, and substituting back the exact Fourier transform of the azimuth phase, the filter becomes :

$$H_F(t,f) = \mathcal{F}\{ \exp[-j4\pi r(\eta)/\lambda] \}$$

$$\bullet \{ A_2(f) *_f \delta[f-f_1-K_A r^{-1}(ct/2)] \} \tag{85}$$

where

$$A_2(f) = |K_A| \int_{-\infty}^{\infty} e^{-j\pi K_A \eta_1^2} e^{j2\pi f \eta_1} d\eta_1 \tag{86}$$

$$= \mathcal{F}^{-1}\{ |K_A| e^{-j\pi K_A \eta_1^2} \} \tag{87}$$

$$= \sqrt{|K_A|} e^{j(\pi/K_A)f^2} e^{-j(\pi/4)SIGN(K_A)} \tag{88}$$

The azimuth spectrum broadening function $A_2(f)$ is similar in form to $A_1(f)$ of chapter 4 except that no range windowing is applied.

The reference phase filter defined by equation (85) could be applied to the range compressed response as a convolution in the azimuth frequency direction. However, since the width of the azimuth spectrum is usually larger in the azimuth direction than in the range time direction (in terms of the number of samples), it is more efficient to apply the filter in the range time direction. This is accomplished by projecting the filter into range time using the approximately linear slope, c_2, of the azimuth frequency domain RCM curve :

$$H_F(t,f) \simeq F\{ \exp[-j4\pi r(\eta)/\lambda] \} \bullet \{ A_2(t/c_2) *_t \delta[t-(2/c)r([f-f_1]/K_A)] \} \quad (89)$$

This projection uses the same assumption of a linear RCM curve which was used in chapter 4.

This filter can now be applied to the range compressed spectrum along with an azimuth window function $W_A(f-f_C)$ to perform azimuth compression with SRC. The peak of the window function is centered at the beam center frequency, f_C, for proper windowing. This produces the following form for the azimuth compressed frequency domain signal :

$$\sigma(t,\eta) = F^{-1}\{ [H_{RC}(t,f) *_t H_F^*(-t,f)] W_A(f-f_C) \} \quad (90)$$

$$= F^{-1}\{[H_{RC}(t,f) *_t g_C(t,f)]F^*\{\exp[-j4\pi r(\eta)/\lambda]\}W_A(f-f_C)\} \quad (91)$$

where

$$g_C(t,f) = g(t) *_t \delta[t+(2/c)r([f-f_1]/K_A)] \quad (92)$$

$$= g(t+(2/c)r([f-f_1]/K_A)) \quad (93)$$

$$g(t) = A_2^*(-t/c_2) \quad (94)$$

$$= \sqrt{|K_A|}\ e^{j(\pi/4)SIGN(K_A)}\ e^{-j\pi K_{SRC}t^2} \quad (95)$$

$$K_{SRC} = 1/(K_A c_2^2) = K_A[c/(\lambda f_C)]^2 \tag{96}$$

Equation (91) describes one form of SRC algorithm in which the SRC filter, g(t), is applied during azimuth compression as a range time convolution. Instead of applying the SRC filter, g(t), separately as suggested by Jin and Wu [13], it can be combined with the RCMC interpolator to form a combined SRC/RCMC filter, $g_C(t,f)$. This type of implementation will be called azimuth SRC.

Alternatively the SRC filter can be implemented during range compression in the range frequency domain. This type of algorithm will be called range SRC. If the transmitted range pulse is linear FM, the SRC filter can be combined with the range compression matched filter by simply modifying the linear FM rate of the filter. Both of these implementations will be examined in following sections.

5.2 AZIMUTH SRC

This section describes the azimuth SRC implementation. Equation (91) describes the basic form of the azimuth SRC azimuth compression algorithm. After transformation into the azimuth frequency domain, the 2-D range compressed signal, $H_{RC}(t,f)$, is convolved in range with a combined SRC/RCMC filter, $g_C(t,f)$, which is azimuth frequency dependent. The result is a 1-D azimuth signal. This is then multiplied by the azimuth reference phase filter and the azimuth window. Upon inverse transformation with an inverse azimuth FFT, a

single compressed azimuth line is obtained.

The SRC/RCMC filter, $g_C(t,f)$, is formed by the convolution of two components :

1. the SRC filter, $g(t)$, which compresses the dispersion caused by the azimuth Fourier transform in both range and azimuth.

2. a range-azimuth coupled delta function which extracts energy along the RCM curve, i.e., performs RCMC.

Since the range compressed signal exists only for discrete range and azimuth time, discrete SRC and RCMC filters are required. These can be formed by bandlimiting the ideal continuous filters to the range and azimuth sampling rates.

There are several ways of implementing the filters. For SRC processing in the azimuth frequency domain, it is most efficient to combine the SRC filter and RCMC interpolator. This combined filter, $g_C(t,f)$, is the same as the 1-D SRC filter, $g(t)$, but is shifted in range by an amount which varies with azimuth frequency. Although azimuth frequency is discrete, the range time shift required for the SRC/RCMC filter can take on any continous value due to the coupling between range and azimuth.

To avoid creating a new shifted filter version for each discrete azimuth frequency, the continuous shift may be

approximated by an integer shift and a fractional shift as was done with the RCMC interpolator in chapter 3. Integer range sample shifts are handled by shifting the entire filter the required number of samples. Fractional shifts are approximated by choosing the best of several precomputed versions of the filter each of which is shifted by a fraction of a range sample. The shifted versions are produced by interpolating the filter by an integer factor I and then extracting the different phases. This is the same approximation that was previously used to form the basic RCMC interpolator except that the combined filter now has a small quadratic phase and is broadened in amplitude.

Several steps are required to produce a suitable discrete SRC/RCMC filter :

1. Form an analytical SRC filter in the continuous range frequency domain.

$$G(f_r) = \mathcal{F}\{ g(t) \} \tag{97}$$

$$= (\lambda f_C/c)\ e^{j\pi f_r^2/K_{SRC}} \tag{98}$$

2. Bandlimit the function to the range sampling frequency, F_{sr}, to prevent aliasing.

$$\mathrm{rect}(\ f_r/F_{sr}\ )\ G(f_r) \tag{99}$$

3. Sample the continuous range frequency function with sample spacing $1/T = F_{sr}/K_r$ to get K_r samples. T is one period of the corresponding range time domain function. It must be chosen to be much larger than the -3dB range timewidth of $H_{RC}(t,f)$ to prevent serious time domain aliasing.

$$\tilde{G}(k_r) = \mathrm{rect}(k_r/K_r)\ G(k_r/T)\ ,\ -K_r/2 < k_r \le K_r/2 \qquad (100)$$

4. Zero pad the array on both ends to a length of IK_r where I is the interpolation factor which defines the number of fractionally shifted versions of the filter.

$$\tilde{G}_I(k_r) = \begin{cases} \tilde{G}(k_r)\ , & -K_r/2 < k_r \le K_r/2 \\ 0\ , & -IK_r/2 < k_r \le -K_r/2 \\ \ , & K_r/2 < k_r \le IK_r/2 \end{cases} \qquad (101)$$

5. Apply an inverse range FFT of length IK_r.

$$\tilde{g}_I(m_I) = FFT^{-1}\{\ G(k_r)\ \}\ ,\ -IK_r/2 < m_I \le IK_r/2 \qquad (102)$$

6. Multiply by a length IL window, $w_1(m_I)$, to get a filter of minimum length where L is the length of each filter version.

$$\tilde{g}_I(m_I)\ w_1(m_I)\ ,\ -IL/2 < m_I \le IL/2 \qquad (103)$$

7. Extract the fractionally shifted versions of the filter.

$$\tilde{g}_i(m) = \tilde{g}_I(mI+i)\ w_1(mI+i)\ ,\ 0 \le i \le I-1\ ,\ -L/2 < m \le L/2 \tag{104}$$

In the current simulations, 16 versions (I=16) and four different filter lengths (L = 4, 8, 16, or 32) are used. Figure 5.1 shows the magnitudes of several SRC/RCMC filters of length 16 after interpolation by a factor of 16 for several squint angles. It is seen that the filters resemble the sinc type of interpolator for small angles but broaden for larger angles. Consequently, larger squint angles also require longer filters to gather all the dispersed energy.

In basic range/Doppler processing without SRC, $\tilde{g}_i(m)$, is approximated by a zero phase finite length interpolator which corresponds to the zero squint SRC/RCMC filter. The approximation holds for small squint angles since the nonlinear phase variation of $\tilde{G}(k_r)$ approaches zero as $|f_C|$ and the squint angle approach zero. Consequently, $\tilde{G}(k_r)$ approaches a rectangular signal with constant phase and $\tilde{g}_I(m_I)$ approaches a time aliased sinc function (or sampling function). The RCMC interpolator is shortened by multiplication with a finite length window, such as a Kaiser-Bessel window, to minimize the amount of computations while also minimizing the spreading and aliasing of the interpolator spectrum.

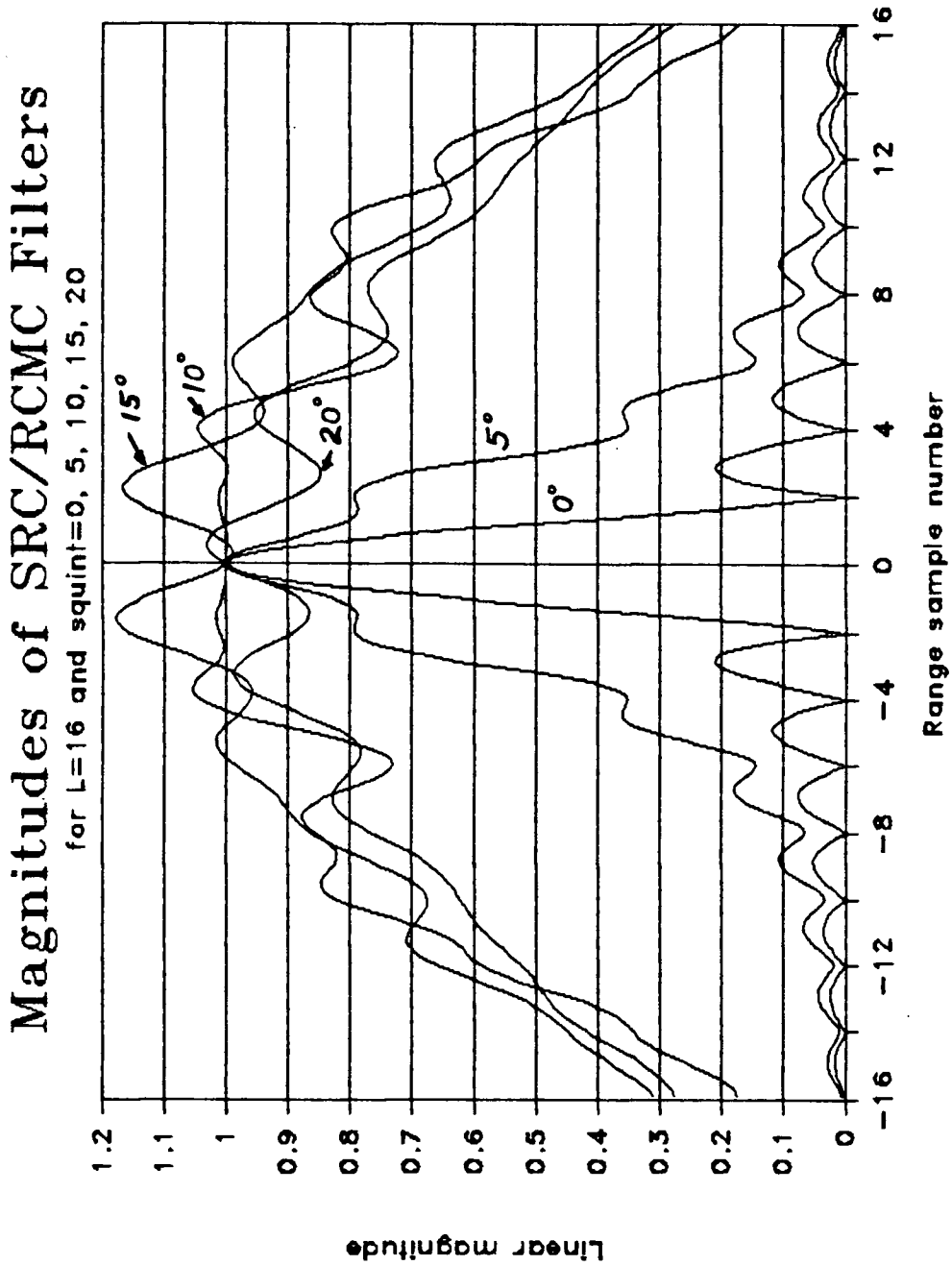

Figure 5.1. Magnitudes of the SRC/RCMC filters of length 16 for squint angles of 0°, 5°, 10°, 15°, and 20°.

5.3 SIMULATIONS OF AZIMUTH SRC

This section describes the results of computer simulations of the azimuth SRC algorithm. The algorithm is similar to the basic range/Doppler azimuth compression algorithm except that the RCMC interpolator is replaced by a combined SRC/RCMC filter.

Range compression is performed as in chapter 3 to produce a 1-D range compressed profile. This profile is used by the azimuth compression simulation routine to form a simulated 2-D range compressed signal. This signal is Fourier transformed in azimuth using an FFT of length 1024 for RADARSAT parameters. The combined SRC/RCMC filter is then applied as a discrete range time convolution to compensate for the dispersion caused by the azimuth FFT. The resulting 1-D azimuth signal is multiplied by the FFT of the exact azimuth reference phase filter and a Kaiser-Bessel window to control sidelobes. Finally the 1-D azimuth signal is passed through an inverse FFT to produce one azimuth line of the compressed image. The processing is repeated for each desired azimuth line. The processing parameters are as in Table 1.

The resulting compressed range and azimuth profiles are shown in figures 5.2 to 5.5. It is seen that very little broadening occurs in range when L is large. However severe broadening can still occur for smaller filters since an appreciable amount of energy is dispersed beyond the width of the shorter filters. The length of the SRC/RCMC filter

has little effect on the azimuth profile.

The -3dB percentage broadening measurements are summarized by figures 5.6 and 5.7 in range and figure 5.8 in azimuth. The results are shown for the four different lengths of SRC/RCMC filter.

The azimuth broadening results are the same as the results without SRC. The predicted azimuth broadening curve of chapter 4, figure 4.13, agrees closely with the actual results. The range broadening measurements show that for squint angles below about 7° with a length 16 filter the percentage range broadening and azimuth broadening are comparable and small (below 3%). Above 7° the range broadening quickly rises since significant energy is dispersed outside of the 16 sample width of the filter. It is seen that longer filters produce less range broadening.

Figures 5.9 and 5.10 summarize the 1-D ISLR measurements. From these it is seen that the azimuth ISLR remains almost constant whereas the range ISLR decreases (improves) as squint increases. The decrease is more rapid for the shorter filter lengths. This decrease in range ISLR for shorter filters corresponds to the larger range broadening. It appears that the windowing applied to shorter filters causes the range spectrum to be tapered. The result is more range broadening with lower range sidelobes. Figure 5.11 summarizes the 2-D ISLR measurements. Whereas the ISLR without SRC deteriorated with increasing squint angle, the ISLR with SRC improves slowly.

The peak sidelobe ratios (PSLR) in range, azimuth, and 2-D are summarized in figures 5.12 to 5.14. As with the ISLR's, the azimuth PSLR's are virtually constant with squint angle while the range PSLR's decrease with increasing squint angle and decreasing filter length. By comparing graphs, it can be seen that the decreases in ISLR and PSLR are less than about 3dB for squint angles smaller than the angle at which the range broadening is 5%.

In order to compare the peak magnitudes after compression, the peaks were normalized to the sum of the squares of the SRC/RCMC coefficients and the azimuth processed bandwidth. The results are summarized in figure 5.15. Whereas the peak strictly decreases without SRC, the normalized peak actually increases slightly for small squint angles before decreasing at larger squints. The reason for this increase is not clearly understood. However the smaller variations in peak magnitude with SRC indicate that an improved signal-to-noise ratio is achieved.

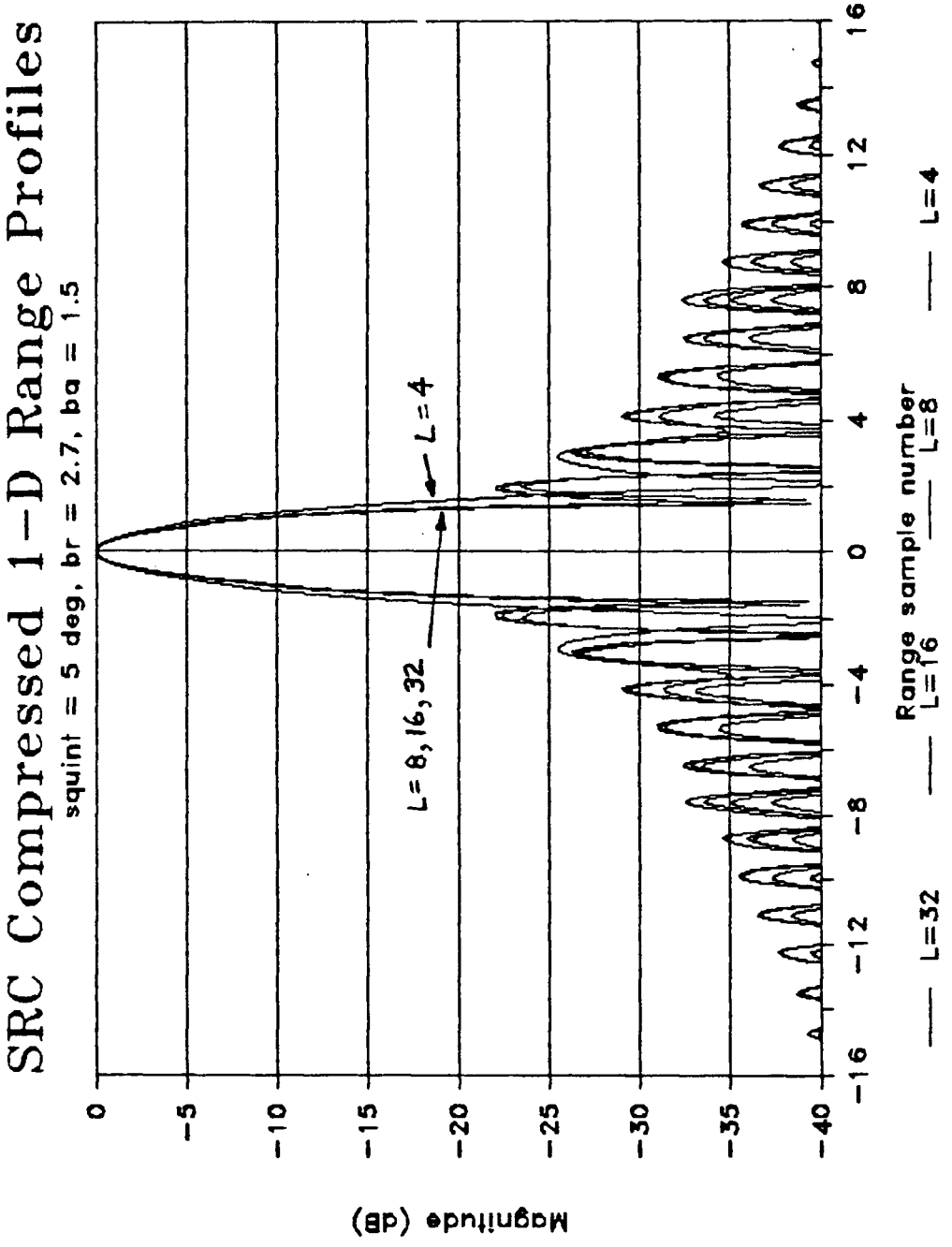

Figure 5.2. 1-D range profiles after SRC compression for 5° squint and various filter lengths.

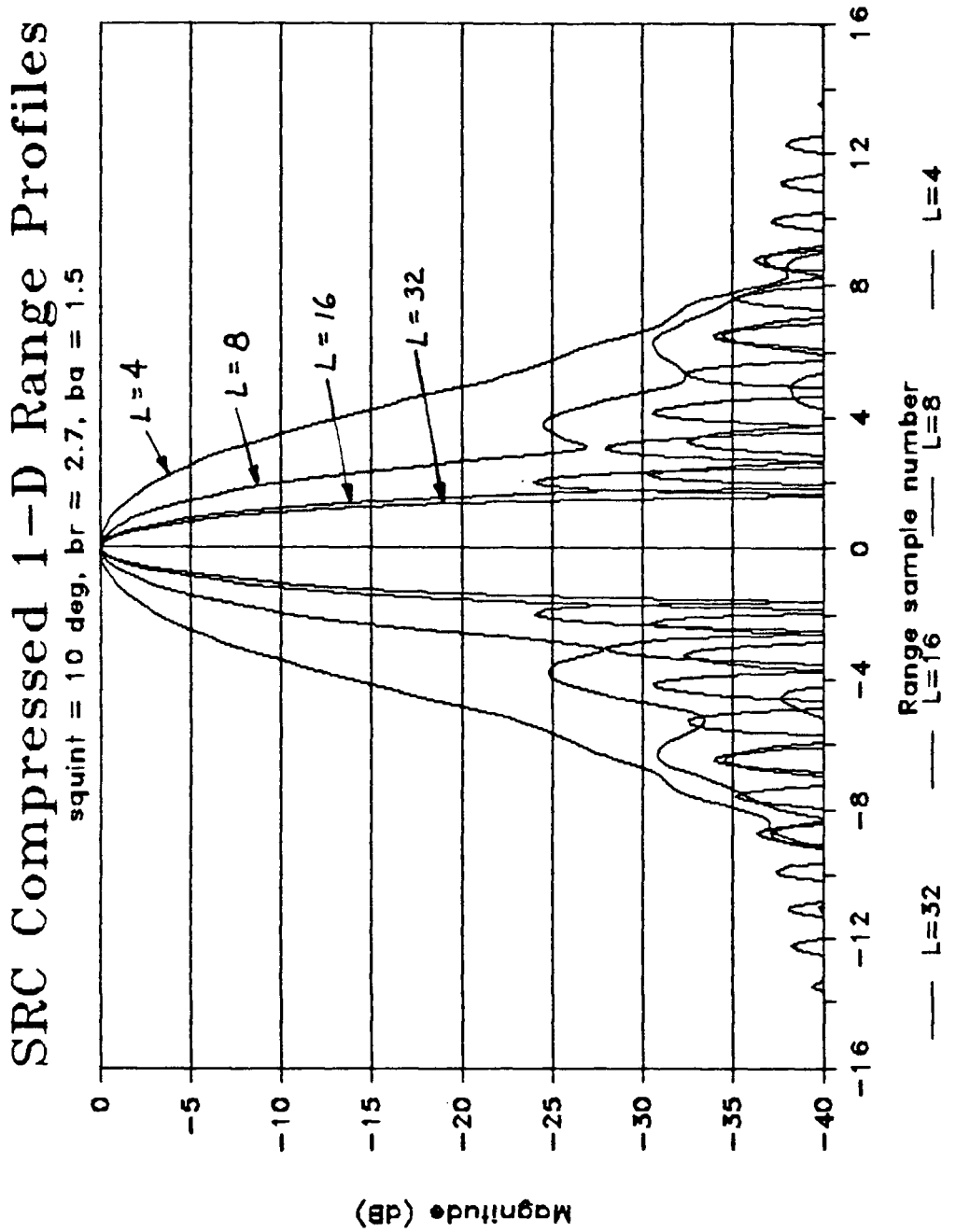

Figure 5.3. 1-D range profiles after SRC compression for 10° squint and various filter lengths.

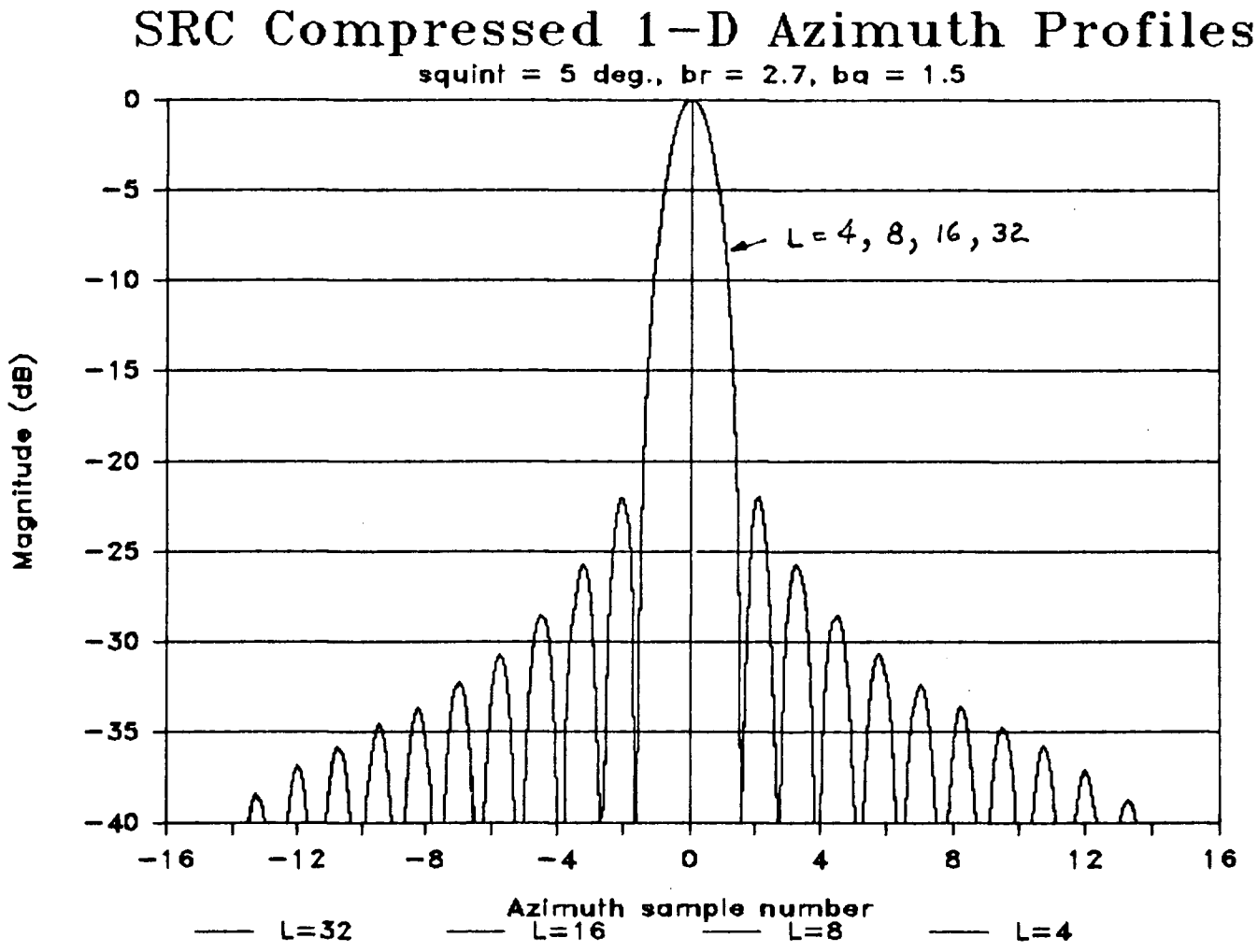

Figure 5.4. 1-D azimuth profiles after SRC compression for 5° squint and various filter lengths.

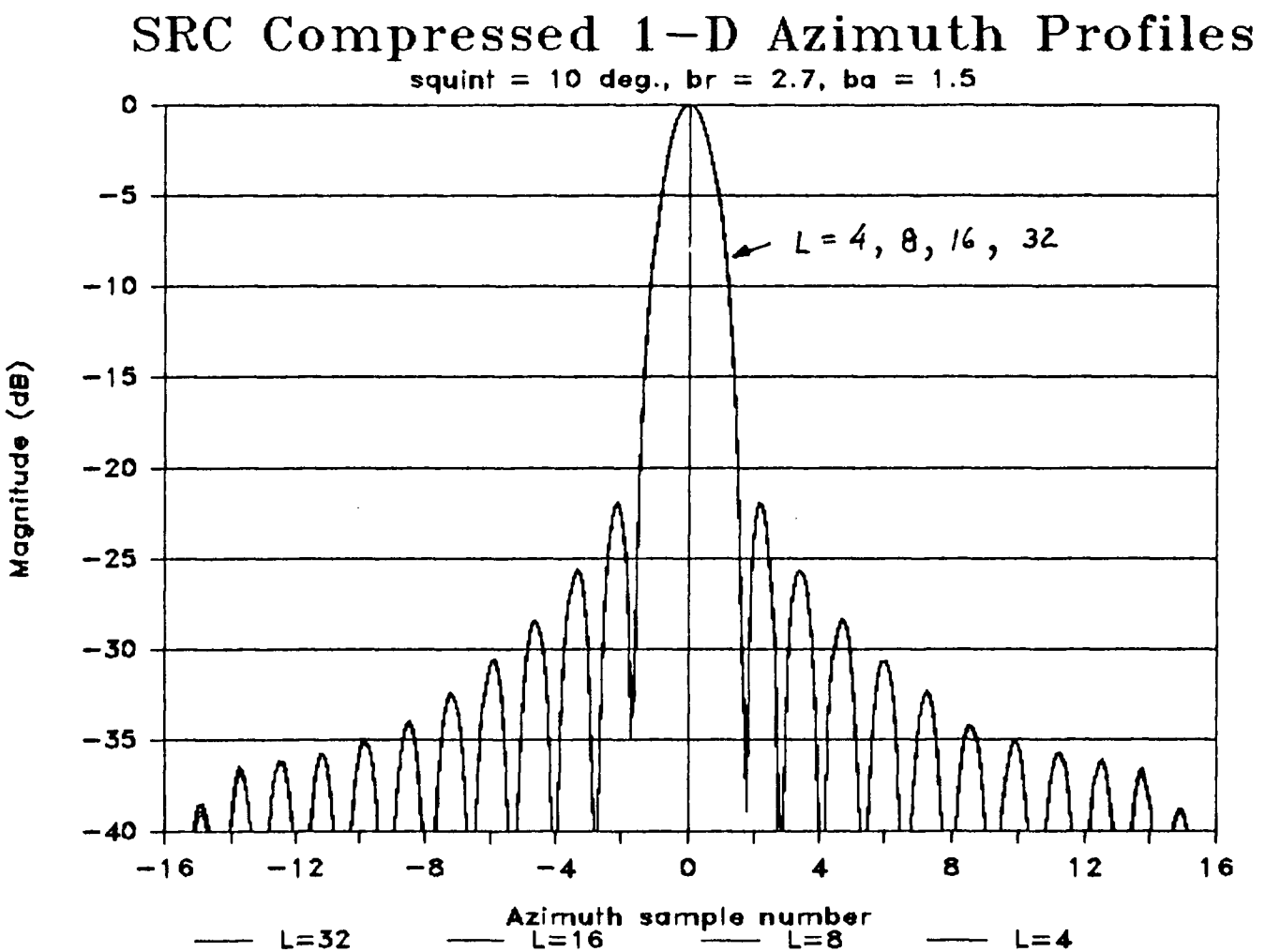

Figure 5.5. 1-D azimuth profiles after SRC compression for 10° squint and various filter lengths.

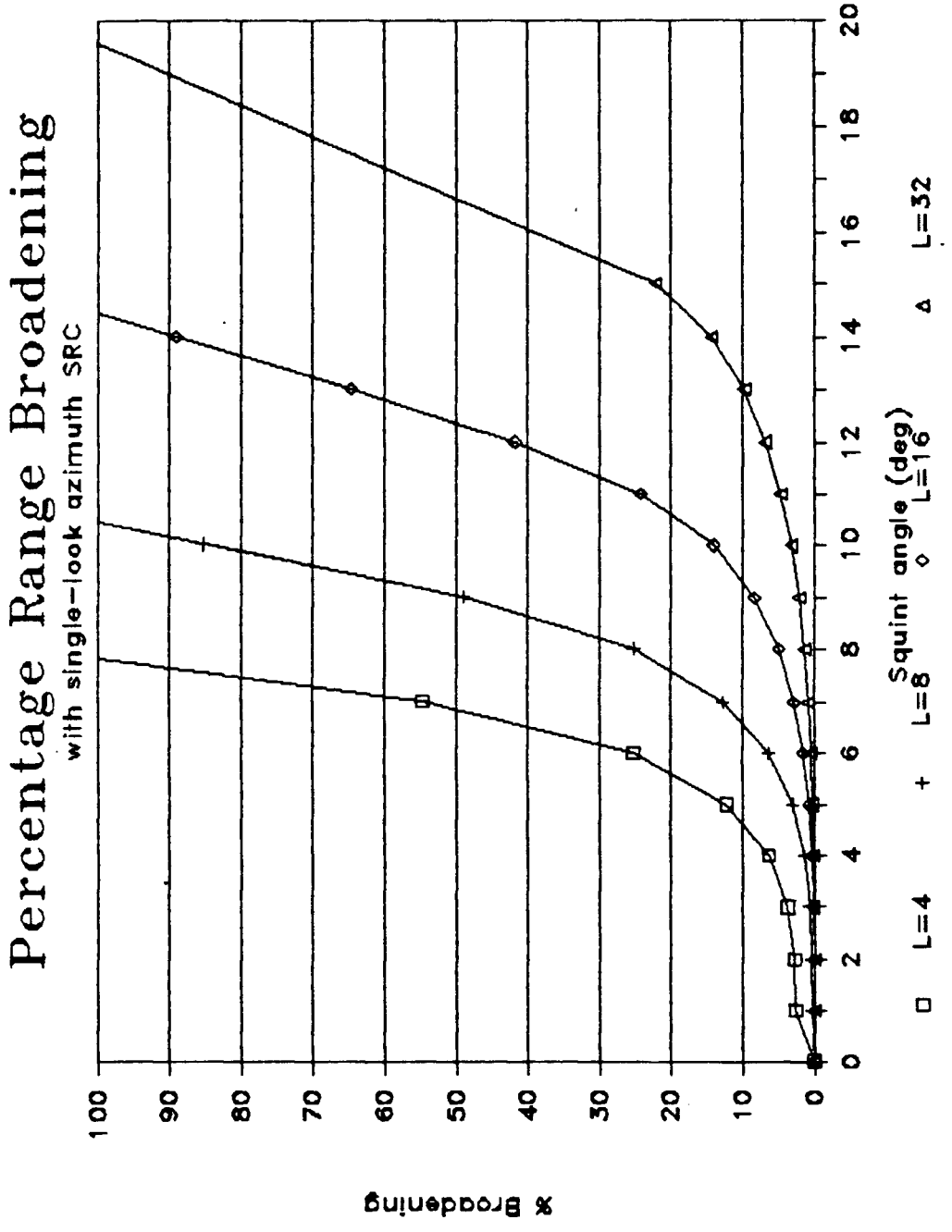

Figure 5.6. Percentage range broadening with single-look azimuth SRC as a function of squint angle and filter length.

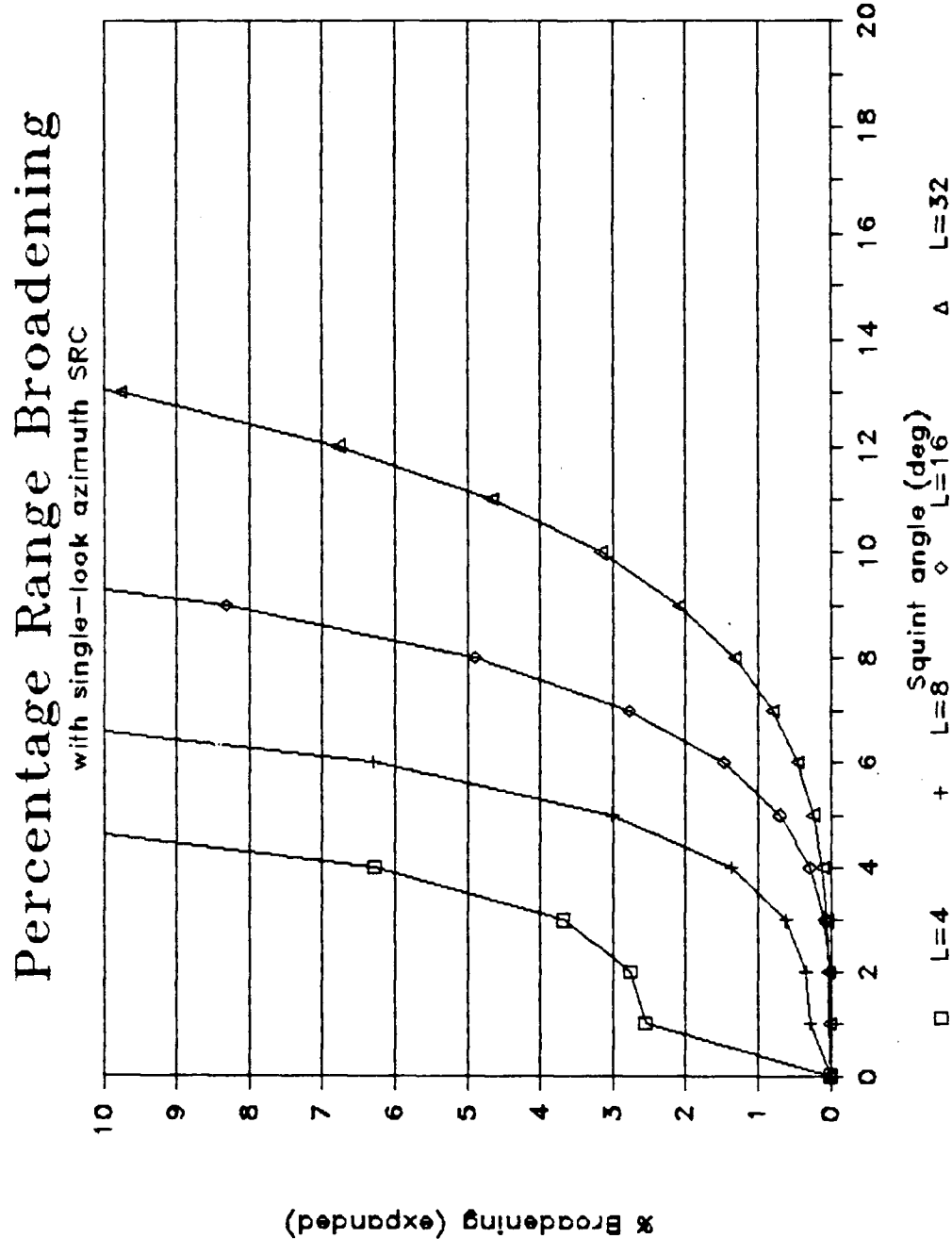

Figure 5.7. Percentage range broadening with single-look azimuth SRC as a function of squint angle and filter length (expanded scale).

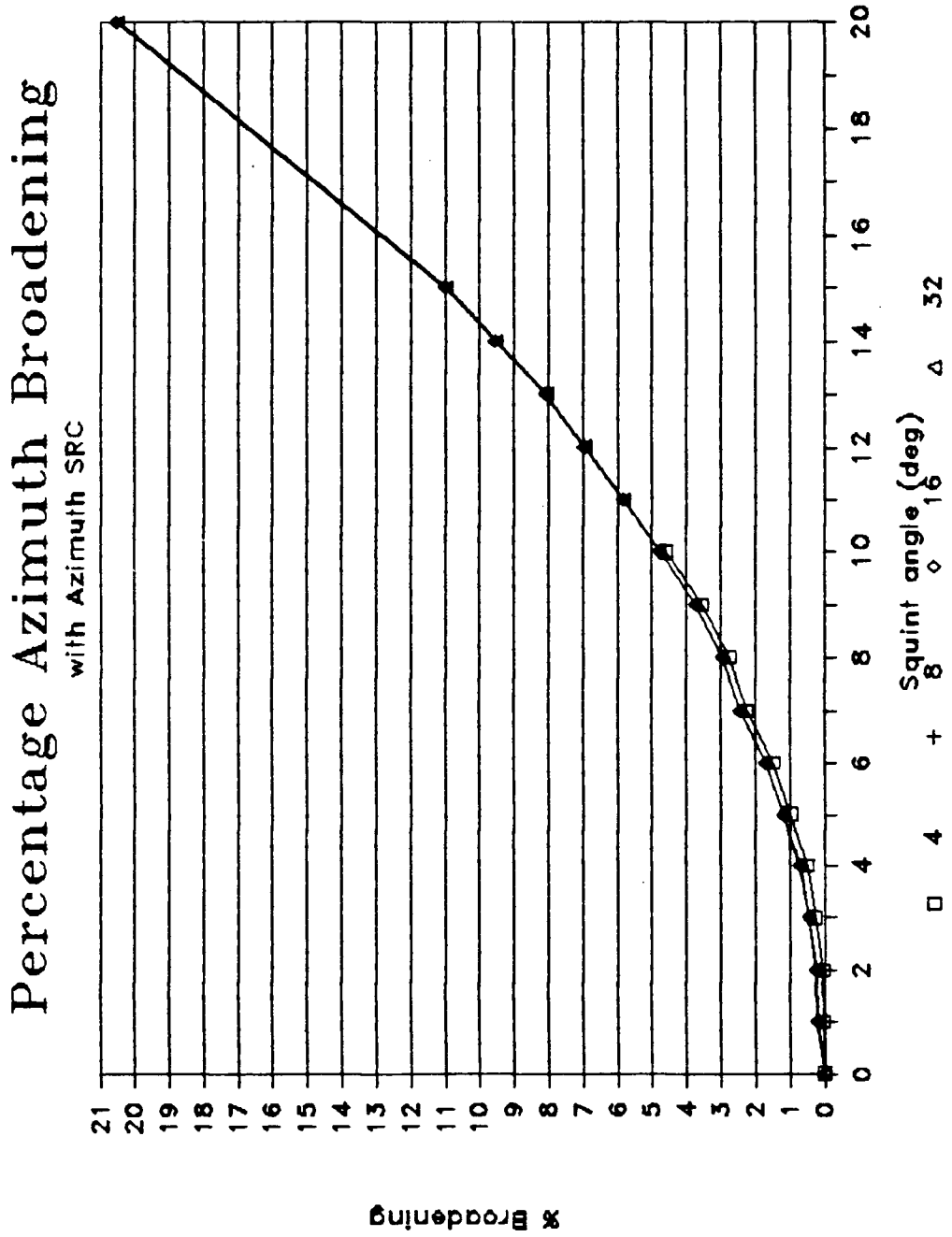

Figure 5.8. Percentage azimuth broadening with single-look azimuth SRC as a function of squint angle and filter length.

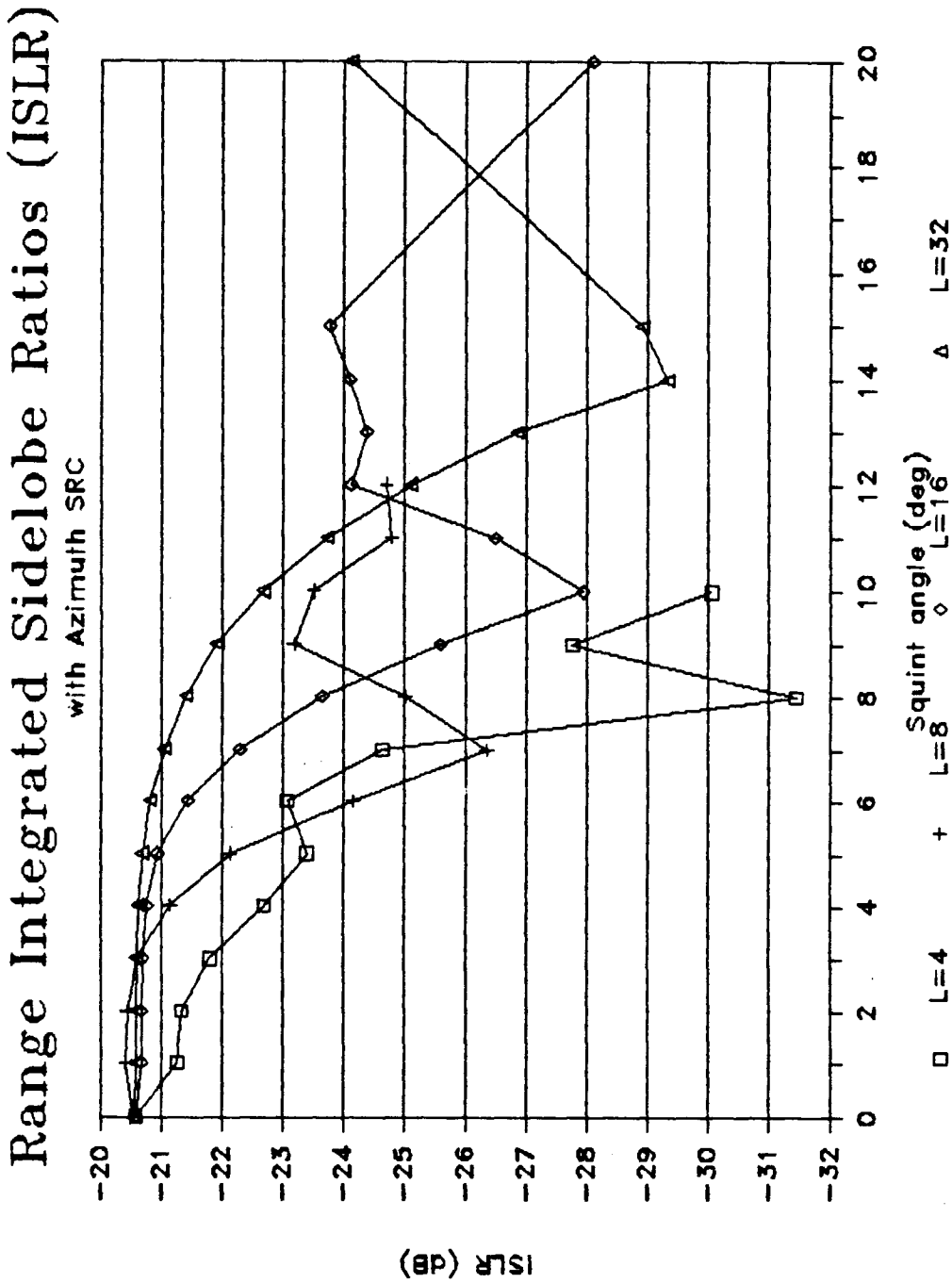

Figure 5.9. 1-D range ISLR with single-look azimuth SRC as a function of squint angle for various filter lengths.

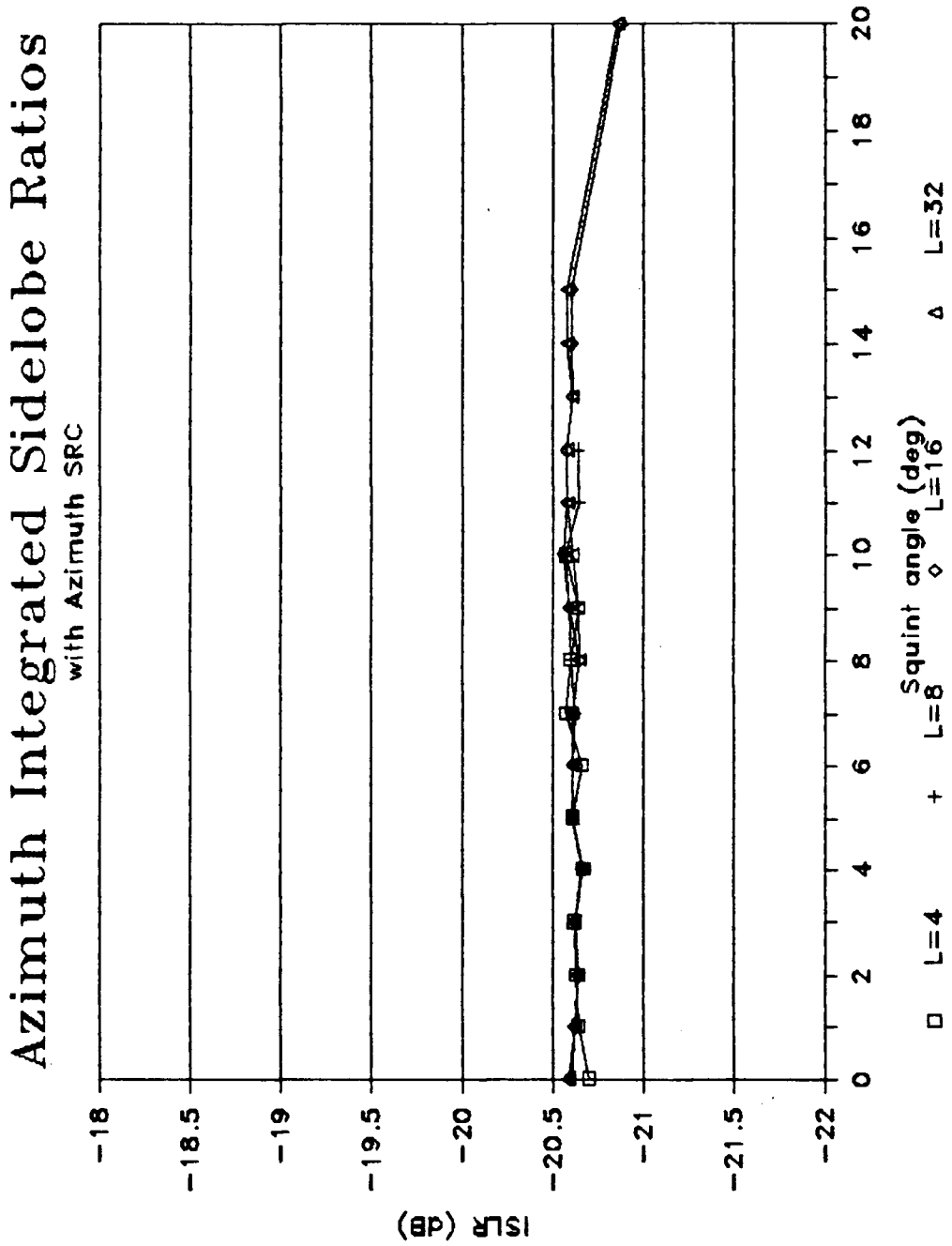

Figure 5.10. 1-D azimuth ISLR with single-look azimuth SRC as a function of squint angle for various filter lengths.

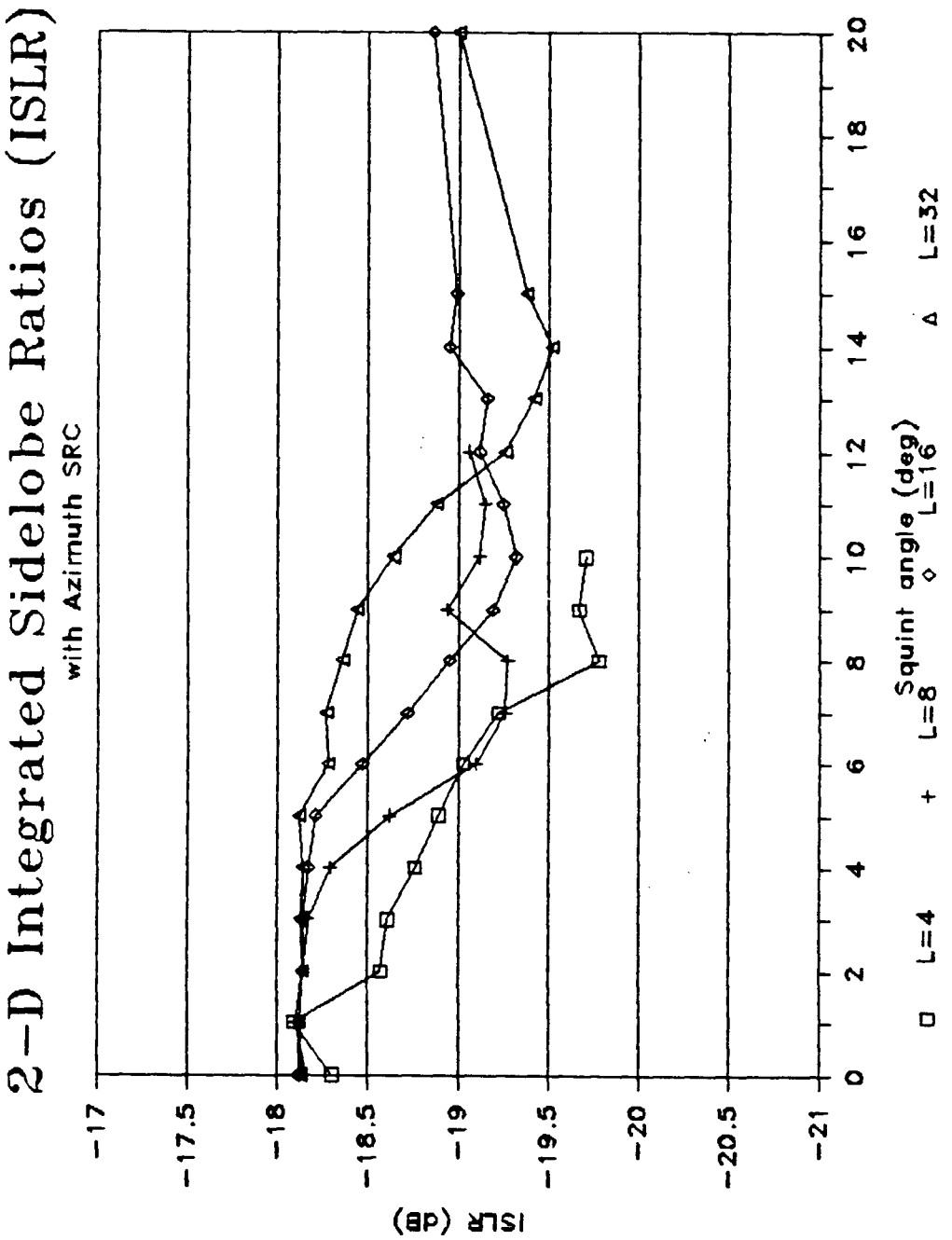

Figure 5.11. 2-D ISLR with single-look azimuth SRC as a function of squint angle for various filter lengths.

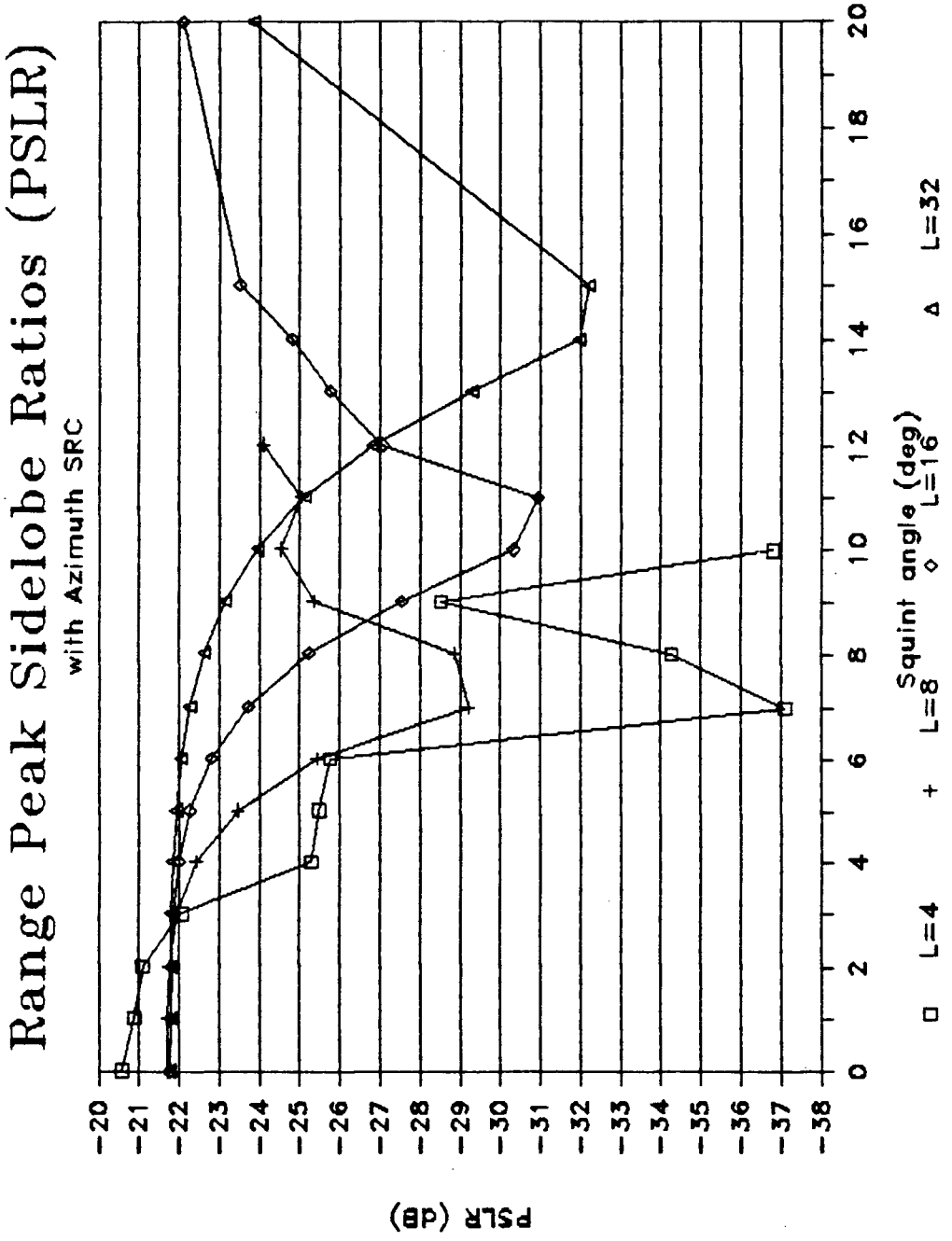

Figure 5.12. 1-D range PSLR with single-look azimuth SRC as a function of squint angle for various filter lengths.

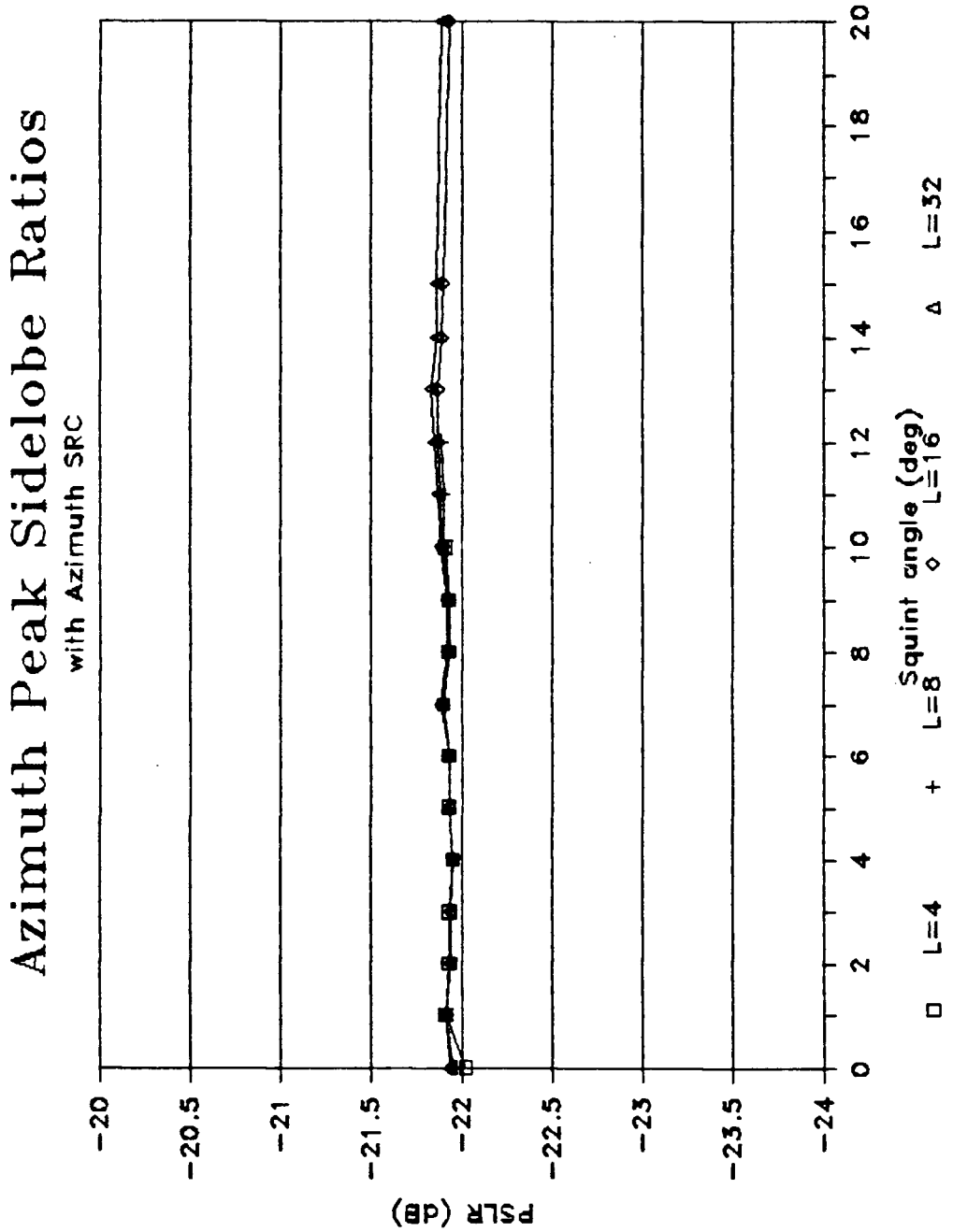

Figure 5.13. 1-D azimuth PSLR with single-look azimuth SRC as a function of squint angle for various filter lengths.

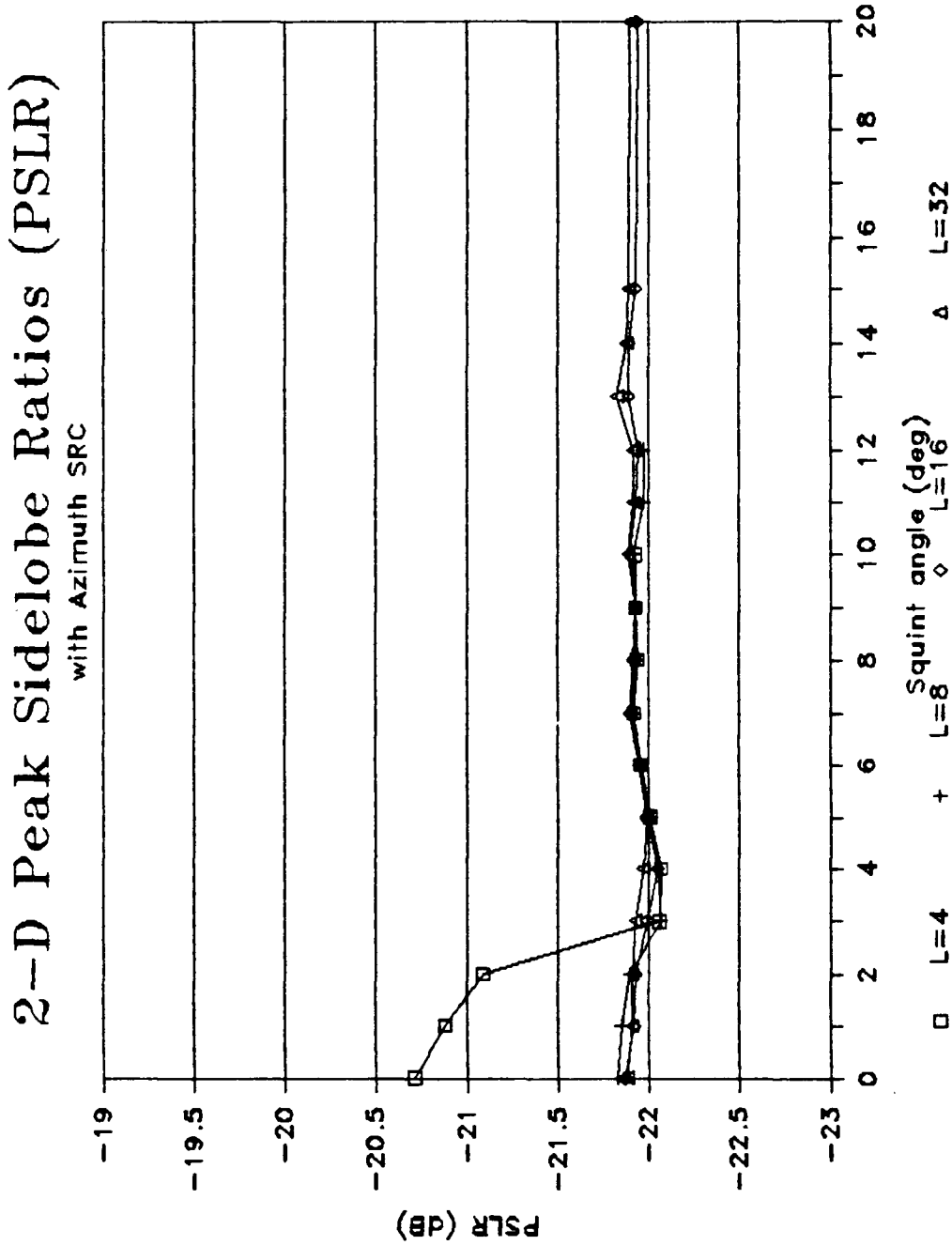

Figure 5.14. 2-D PSLR with single-look azimuth SRC as a function of squint angle for various filter lengths.

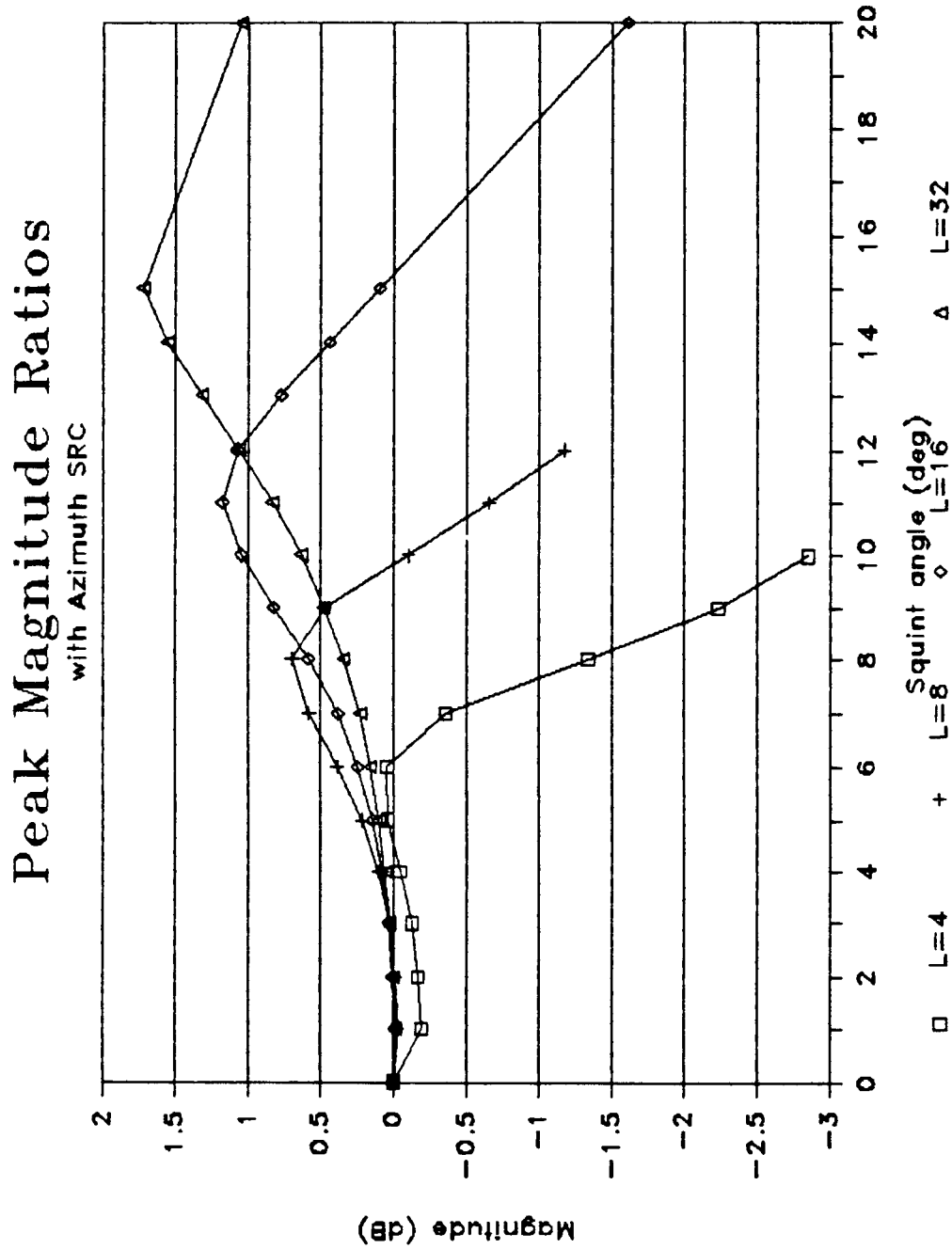

Figure 5.15. Peak compressed magnitude with single-look azimuth SRC as a function of squint angle for various filter lengths.

5.4 RANGE SRC

This section describes an alternate implementation of the SRC filter called range SRC. This method performs SRC in the range frequency domain during range compression. The SRC filter is combined with the range compression filter by simply altering the linear FM rate of the range compression filter. Since the resulting modified range compression filter has the same number of coefficients, no additional computations are required. In addition a shorter RCMC interpolator can be used for the subsequent azimuth compression even at large squint angles since the azimuth spectrum remains well compressed after the azimuth FFT.

One complication of this method is the range invariance of the SRC filter. Depending on the radar parameters and size of the range swath, the range swath may need to be subdivided into smaller range invariance regions for the purpose of range compression. The issue of invariance regions, which is also of concern in azimuth SRC, is examined in chapter 7.

The modified range compression filter can be expressed in the range time domain as :

$$h_{RM}(t) = s_T^*(-t) *_t g(t) \tag{105}$$

$$= [\ \mathrm{rect}(t/\tau)\ e^{j\pi K_R t^2}\ ] *_t g(t) \tag{106}$$

The range compression filter is implemented using fast

convolution in the range frequency domain. Applying the range Fourier transform to the filter gives the following form :

$$H_{RM}(f_r) = \mathcal{F}\{ \text{rect}(t/\tau)\ e^{j\pi K_R t^2} \}\ G(f_r) \tag{107}$$

Since the first term is the Fourier transform of a large TBP linear FM signal, it may be approximated using the principle of stationary phase as :

$$\mathcal{F}\{ \text{rect}(t/\tau)\ e^{j\pi K_R t^2} \}$$

$$\simeq \text{rect}(f_r/[K_R\tau])\ e^{-j\pi f_r^2/K_R} \tag{108}$$

The Fourier transform of the SRC filter, g(t), was given previously as :

$$G(f_r) = (\lambda f_C/c)\ e^{j\pi f_r^2/K_{SRC}} \tag{109}$$

Substituting back these transforms and dropping the constant magnitude terms gives the following form for the frequency domain combined filter :

$$H_{RM}(f_r) \simeq \text{rect}(f_r/[K_R\tau])\ e^{-j\pi f_r^2/K_{RM}} \tag{110}$$

$$\text{where } K_{RM} = K_R/[\ 1 - (K_R/K_{SRC})\ ] \tag{111}$$

Since $K_{SRC} >> K_R$, the modified reference function is also a large TBP signal. Therefore the principle of stationary phase can again be used to evaluate the inverse Fourier transform of the modified range compression filter :

$$h_{RM}(t) \simeq \mathrm{rect}(t/\tau)\ e^{j\pi K_{RM} t^2} \tag{112}$$

This equation shows that the combined SRC/range compression filter is a linear FM pulse with a modified FM rate, K_{RM}.

The modified FM rate is a function of both the range of closest approach of the point target, r_0, and the squint angle. The range of closest approach primarily affects the azimuth FM rate, K_A, and to a lesser extent the beam center frequency, f_C. The squint angle mainly affects the beam center frequency and to a smaller extent the azimuth FM rate. As the squint angle approaches zero, f_C also approaches zero and K_A approaches a constant. Therefore $K_{SRC} = K_A[c/(\lambda f_C)]^2$ approches infinity and the modified FM rate, K_{RM}, approaches the unmodified FM rate, K_R.

The range SRC algorithm is essentially the same as the basic range/Doppler algorithm presented in chapter 3 except that the linear FM rate of the range compression filter is modified according to the squint angle. Range SRC is superior to azimuth SRC since the equivalent range time domain SRC filter is much longer than practical SRC/RCMC filters used in azimuth SRC. Since the SRC filter in range SRC is applied over the entire range bandwidth, the

equivalent range time domain filter is very long, much longer than the practical SRC/RCMC filter lengths of between 8 and 16 samples used in azimuth SRC. The longer equivalent filter allows more of the dispersed energy to be recompressed (eventhough the recompression is implemented as a prefilter).

5.5 SIMULATIONS OF RANGE SRC

This section presents the results of simulating the range SRC algorithm with nominal RADARSAT parameters. The same simulation programs that were used for basic range/Doppler compression are used except that the modified linear FM rate, K_{RM}, developed in the previous section is used in the range compression filter. A single RCMC interpolator length, L = 16, was used for all the simulations.

Figure 5.16 shows the broadening of the range compressed profile after range SRC for squint angles of 5° and 10°. The broadening occurs because of the mismatch of the linear FM rates of the transmitted range pulse and the modified SRC/range compression filter. This predistorton becomes recompressed by the azimuth FFT.

Figures 5.17 and 5.18 show the range and azimuth profiles after azimuth compression. It is seen that very little broadening occurs in range whereas some broadening does occur in azimuth as predicted by the decrease in processed bandwidth. The percentage range and azimuth broadening with range SRC is summarized in figures 5.19 and

5.20. For squint angles below 15°, the range broadening is very small, less than 0.55%.

The ISLR and PSLR measurements are summarized in figures 5.21 and 5.22. Since little broadening occurs, both the ISLR and PSLR are approximately constant with squint angle. In fact the range ISLR and PSLR improve slowly with increasing squint angle.

The peak magnitudes are compared in figure 5.23. The absence of large variations indicates that the signal-to-noise ratio remains relatively constant with changes in squint angle.

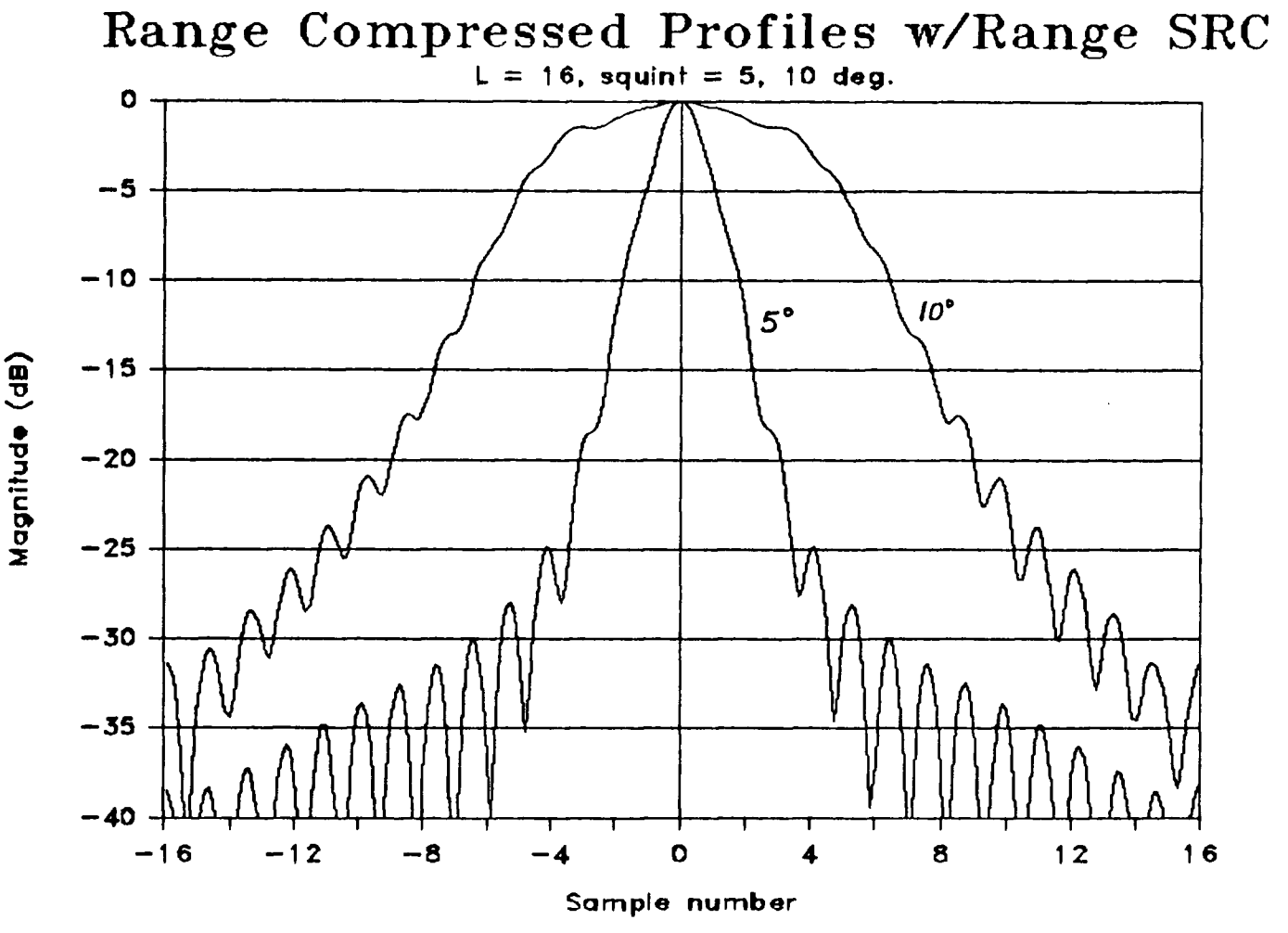

Figure 5.16. 1-D range compressed profiles after range compression with range SRC for 5° and 10° squint.

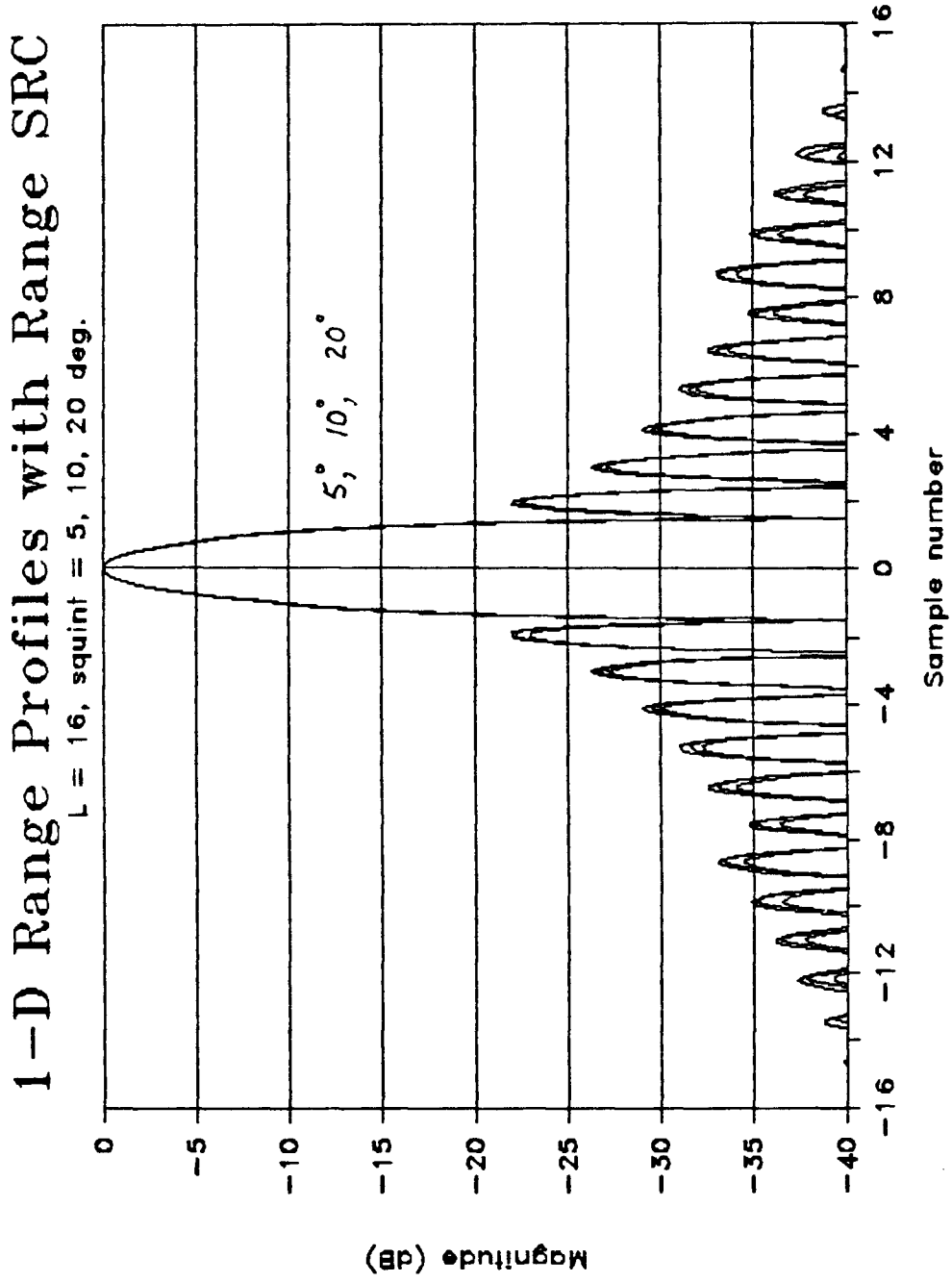

Figure 5.17. 1-D range profiles after azimuth compression with single-look range SRC for 0°, 5°, and 10° squint and a length 16 RCMC filter.

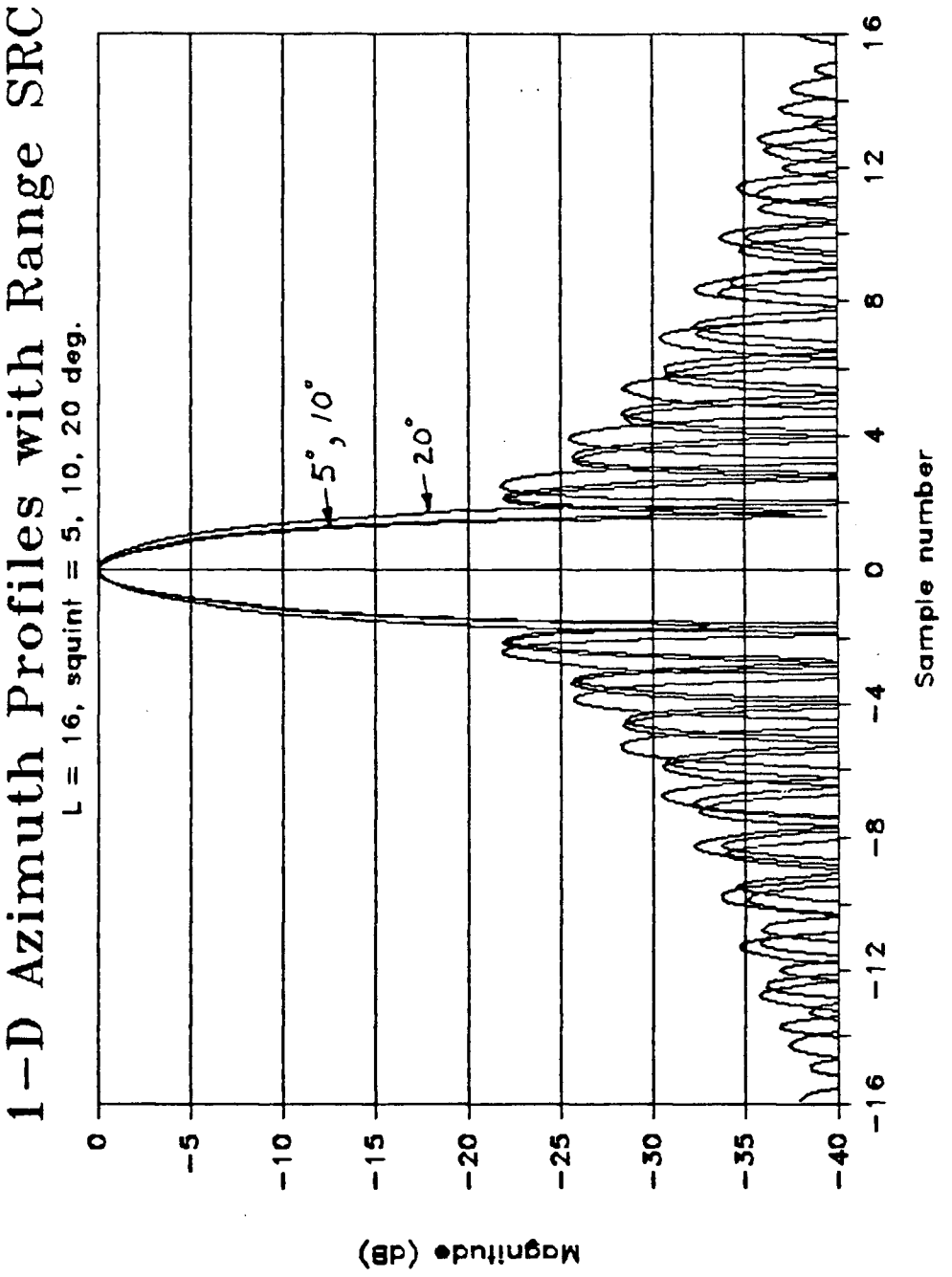

Figure 5.18. 1-D azimuth profiles after azimuth compression with single-look range SRC for 0°, 5°, and 10° squint and a length 16 RCMC filter.

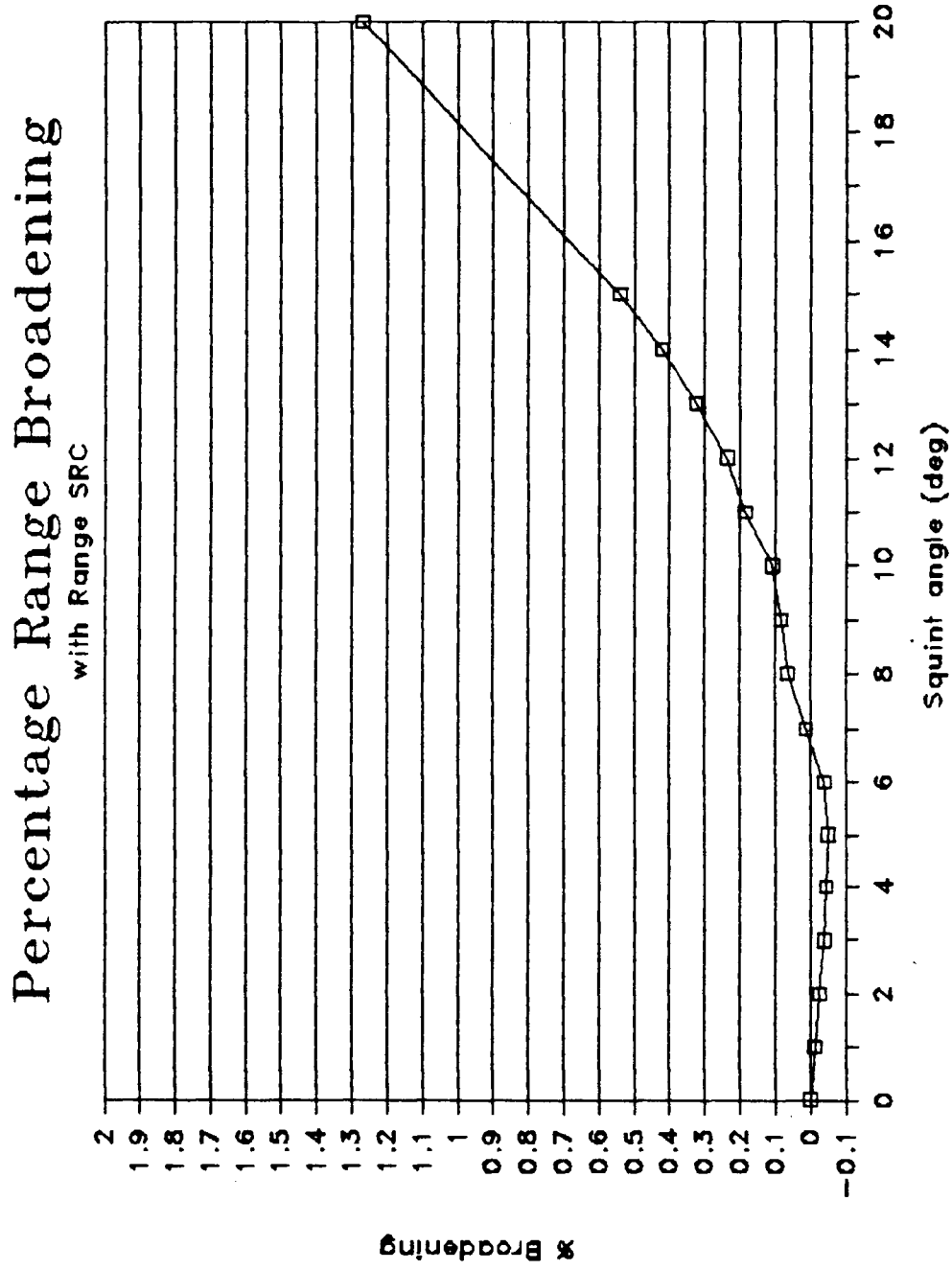

Figure 5.19. Percentage range broadening with single-look range SRC and a length 16 RCMC interpolator as a function of squint angle.

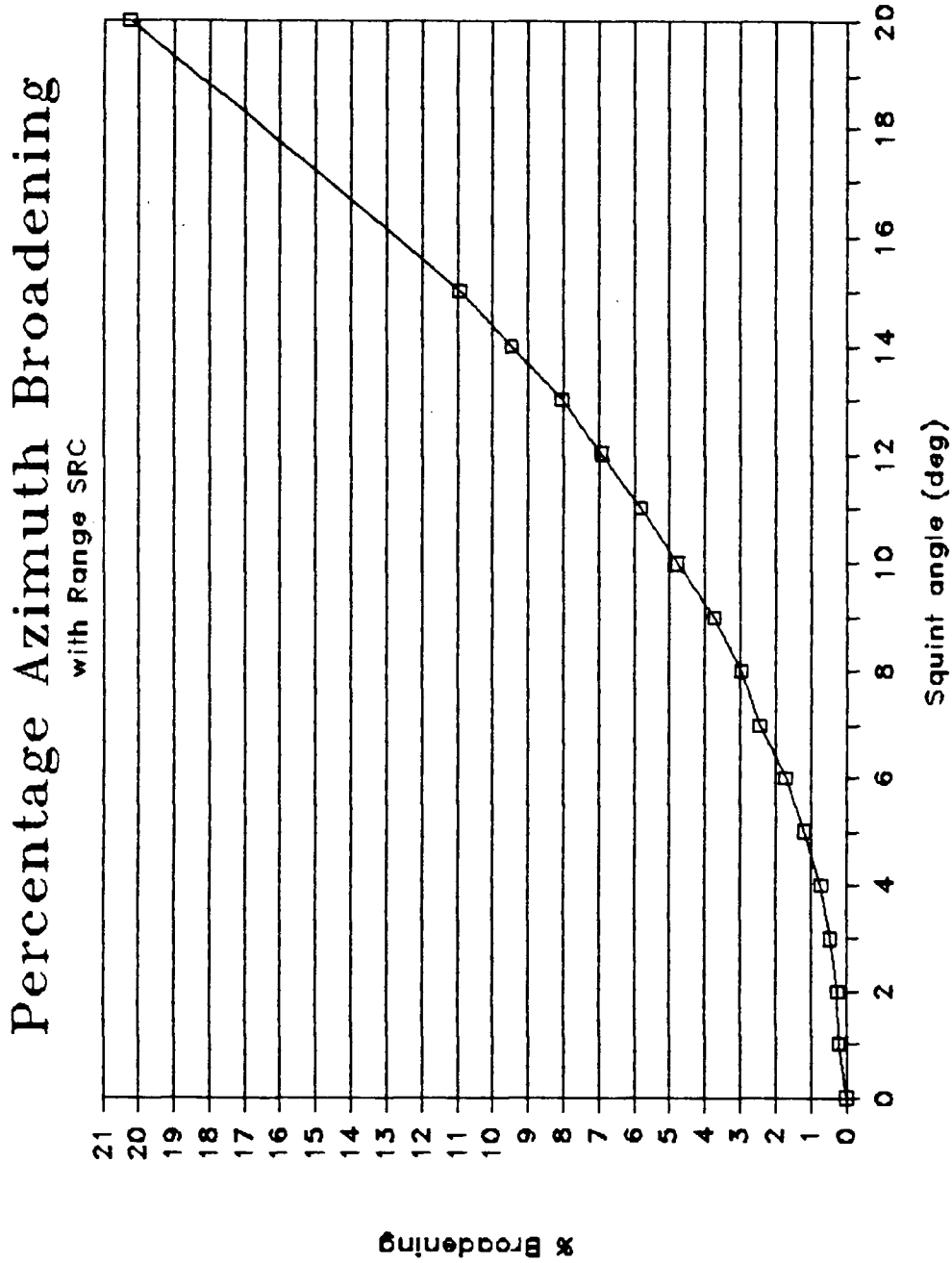

Figure 5.20. Percentage azimuth broadening with single-look range SRC and a length 16 RCMC interpolator as a function of squint angle.

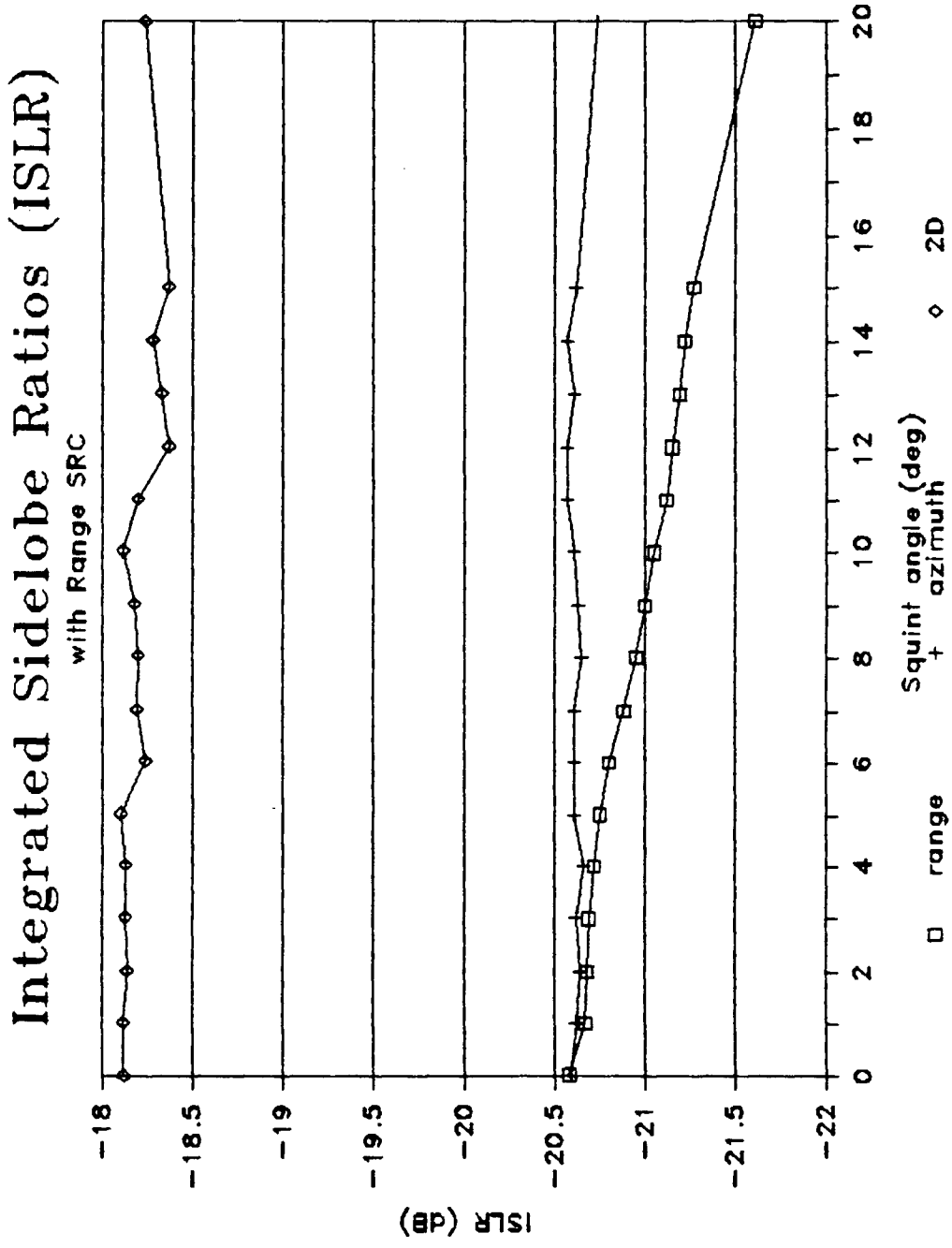

Figure 5.21. Range, azimuth, and 2-D integrated sidelobe ratios with single-look range SRC and a length 16 RCMC interpolator as a function of squint angle.

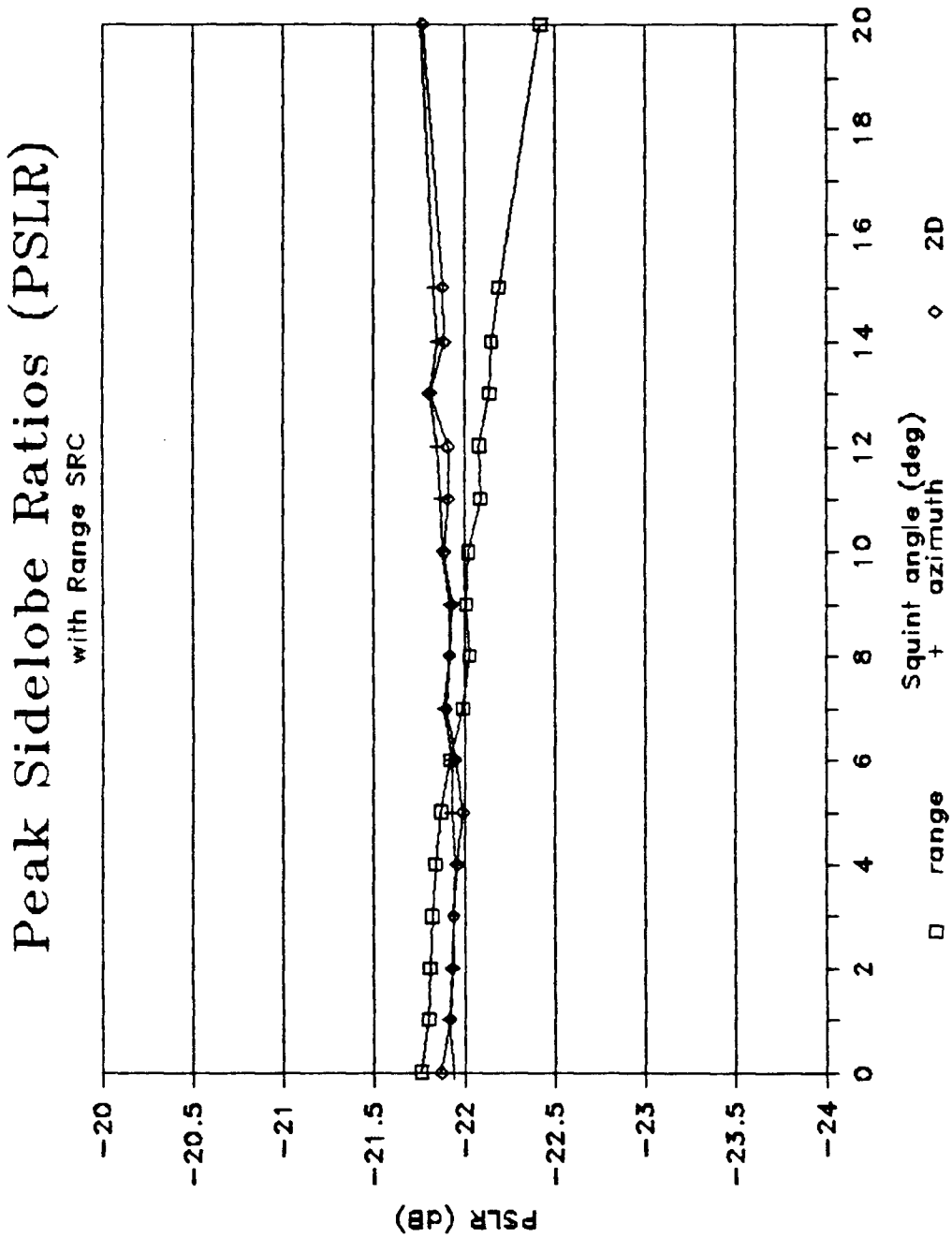

Figure 5.22. Range, azimuth, and 2-D peak sidelobe ratios with single-look range SRC and a length 16 RCMC interpolator as a function of squint angle.

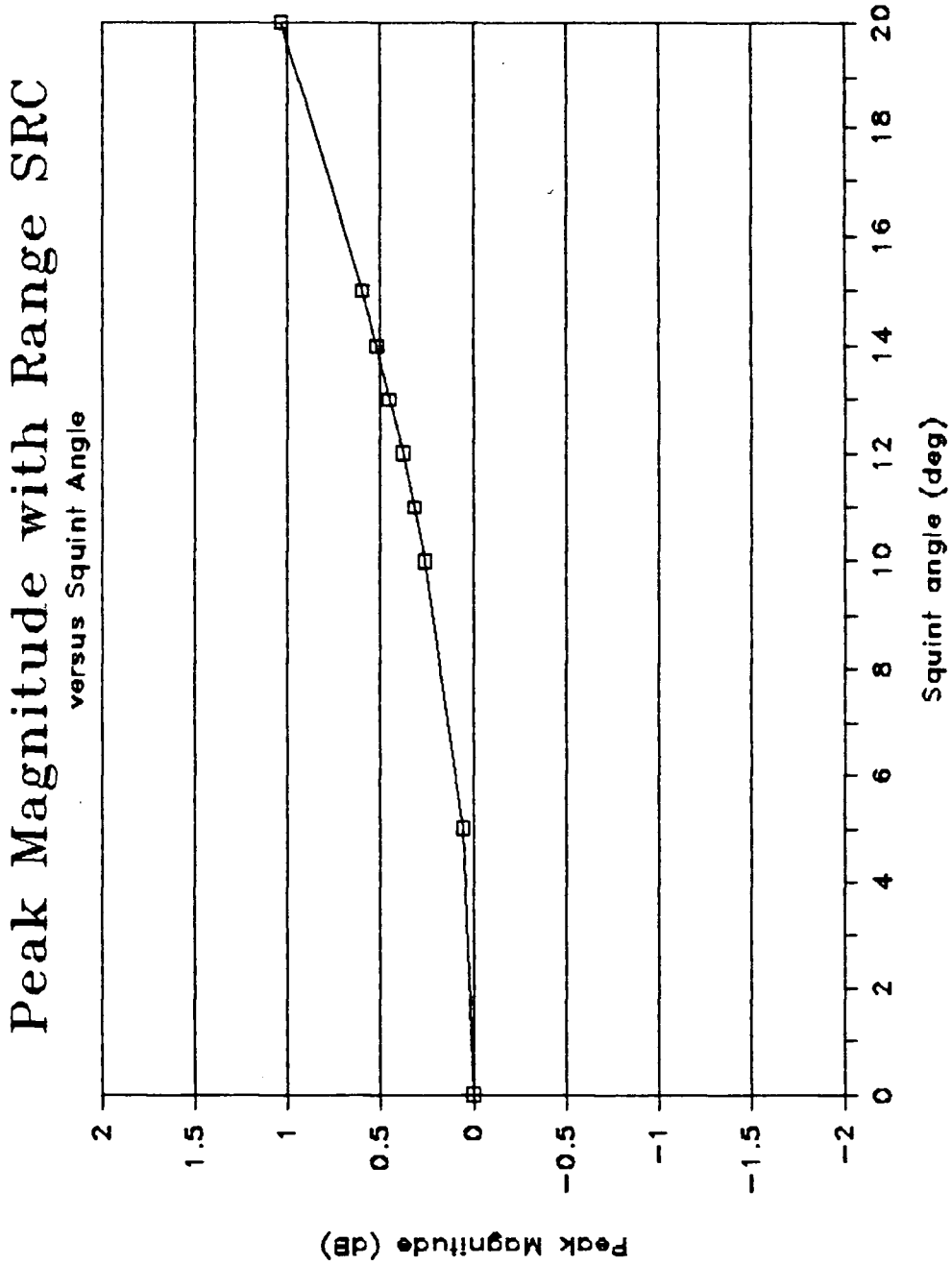

Figure 5.23. Peak magnitude degradation with single-look range SRC and a length 16 RCMC interpolator as a function of squint angle.

5.6 SUMMARY OF SINGLE-LOOK SRC

This chapter has presented the results of investigations into the use of an SRC algorithm for improving the range/Doppler compression algorithm at large squint angles. An SRC filter was developed by projecting the ideal matched filter into the range dimension after applying the azimuth FFT. This projection assumes linearity of the RCM curve over the processing interval. The approximate quadratic phase form of the azimuth phase is used to derive the SRC filter.

Two implementations were developed and simulated. The simulations show that both implementations work well at recompressing the energy dispersed by the azimuth FFT. Since the dispersion increases with squint angle, longer SRC/RCMC filters are required to recompress the dispersion at higher squint angles. The range SRC implementation provides an SRC filter which is effectively much longer than the SRC/RCMC filters used in azimuth SRC. Consequently at large squint angles range SRC performs much better than azimuth SRC.

For a length 16 filter the azimuth SRC algorithm extends the squint angle which causes 5% range broadening from 3.65° to 8.03°. For 10% range broadening, the squint angle is increased from 4.23° to 9.29°. In addition the range sidelobes are actually improved by the SRC algorithm indicating excellent compression.

For the range SRC algorithm with a length 16 RCMC interpolator, the range broadening remains very small over all the squint angles which were simulated being less than

1.3% for squint angles up to 20°. Thus the range SRC implementation provides better compression than the azimuth SRC algorithm. In practice this improved performance must be weighed against the possible complications caused by range invariance of the SRC filter. This issue is discussed further in chapter 7.

6. MULTILOOK RANGE/DOPPLER PROCESSING WITH SRC

In this chapter, methods of implementing SRC for multilook (specifically 4-look) processing are examined. In multilook processing the aperture is divided into several looks which are compressed separately and then summed incoherently in order to reduce speckle noise. Two new methods of implementing SRC are proposed and investigated :

1. Fixed Multilook SRC. This method uses the same SRC filter for each look. The filter is matched to the center frequency of the full aperture, i.e., the Doppler centroid. This is the same filter that was used previously for single-look processing.

2. Look-Dependent Multilook SRC. In this method, a different SRC filter is used for each look. This compensates for any changes in the slope of the range cell migration (RCM) curve between looks since each filter is matched to each look center frequency.

Simulations of multilook processing of a point target response are performed with and without the above SRC algorithms to quantify the improvements in image quality possible with multilook SRC.

6.1 MULTILOOK PROCESSING WITH SRC

This section further extends the theory of azimuth compression presented in chapter 5 to describe multilook range/Doppler processing both with and without the use of two new multilook SRC algorithms.

Multilook azimuth compression with the range/Doppler algorithm is essentially the same as full aperture range/Doppler processing except that the processed bandwidth is divided into separate, often overlapping, processing bands or looks, which are compressed individually and then incoherently summed. Due to the approximate correspondence between the time and frequency domains of the azimuth signal each frequency domain look corresponds to different intervals of the azimuth time domain aperture. For a point target signal, each look contains data collected from different time intervals which cover different ranges of incidence angles, or look angles. This change in look angle causes the speckle noise to have little correlation between looks. Thus incoherent summation of the compressed looks reduces the speckle noise level. Figure 6.1 shows how the processed bandwidth is divided into separate looks (in this case, 4 looks). Figure 6.2 shows the corresponding time domain look angles.

In multilook processing, range compression is performed as in single-look processing to produce a 2-D range compressed signal. In chapter 5, single-look azimuth compression was developed as an approximation to an exact

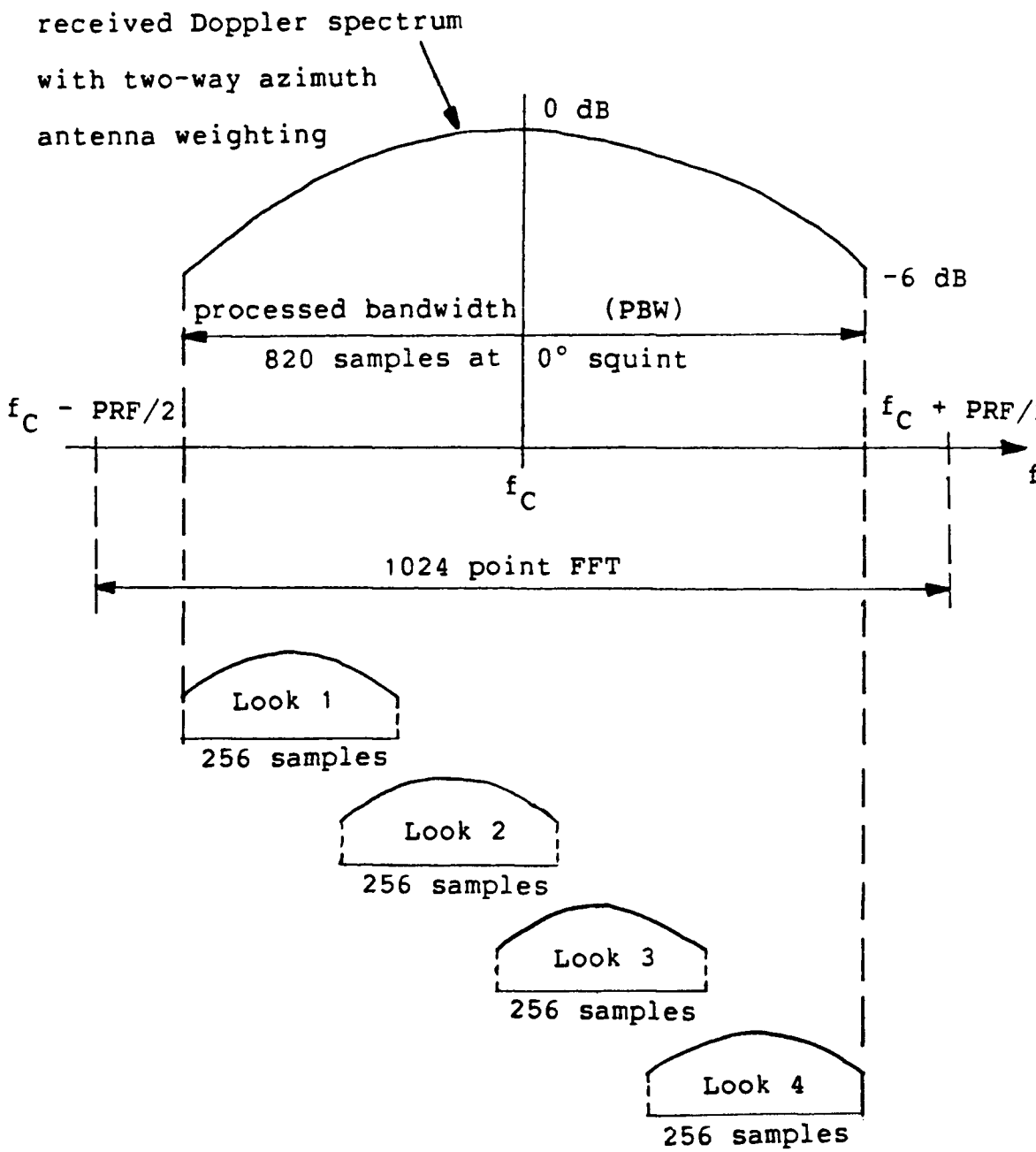

Figure 6.1. Division of the azimuth frequency domain aperture into 4 looks.

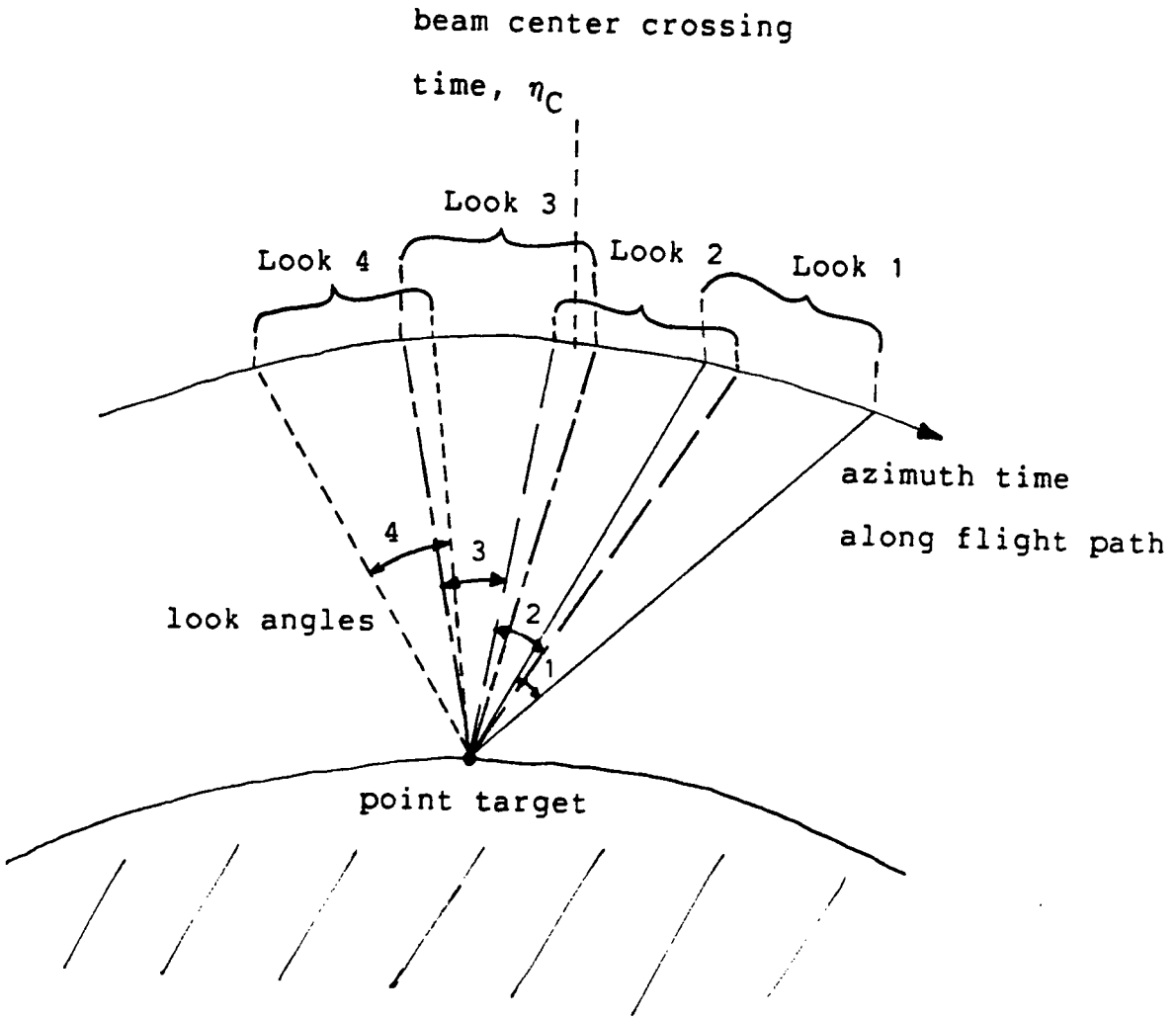

Figure 6.2. Corresponding time domain looks.

matched filter implemented in the azimuth frequency domain. For multilook processing, a similar compression algorithm is applied to each frequency band or look.

The formulation of the azimuth compression filter for each look proceeds as in chapter 5 up to equation (85) which expresses the 2-D compression filter in the azimuth frequency domain.

For single-look (full aperture) processing, the filter is usually truncated near the -3dB azimuth frequencies with some form of window function. The exact selection of processing bandwidth is a trade-off between factors such as ambiguity errors, aliasing noise, the desired azimuth resolution, and the type of window used. For the current research, the full aperture processed bandwidth has been arbitrarily chosen to be the -3dB one-way (-6dB two-way) azimuth antenna bandwidth.

As stated earlier, multilook processing divides the processed bandwidth into several looks which are often overlapping. For ease of implementation and computational efficiency of the inverse azimuth FFT's, each look has been chosen to be 256 samples long. For 4-look processing, which has been simulated here, these looks are overlapped to fit into the processed bandwidth. Since the processed bandwidth varies slowly with squint angle, the number of frequency domain samples in the processed bandwidth varies from 820 samples at zero squint down to 680 samples at 20 degrees of squint. The corresponding percentage overlaps range from

26.6% to 44.8% respectively.

A Kaiser-Bessel azimuth window function is applied separately to each look to control the azimuth sidelobe levels. Therefore the effective combined window for the full aperture, which is the summation of the individual look windows, extracts more energy from the outer looks than an equivalent single-look Kaiser-Bessel window applied to the full aperture. Since the bandwidth of each look is fixed, the compressed resolution of each look is approximately constant regardless of squint angle. The antenna weighting has little effect over the smaller look bandwidths since for the inner looks the amount of weighting is less and for the outer looks the weighting does not have a central maximum and is approximately linear.

In order to convert the above azimuth look compression filter from an azimuth frequency convolution to a more computationally efficient range convolution, the filter is projected into range as in chapter 5 using the approximately linear slope of the RCM curve. However there is now a choice of slopes to use for the individual look filters.

For a fixed azimuth SRC implementation, the same SRC/RCMC filter is used for all looks. Thus the slope at the center of the full aperture is used for the projection as in single-look SRC. This may introduce very small errors in the outer looks since the slope of the RCM curve in the outer looks differs slightly due to range curvature. For systems such as RADARSAT in which the range curvature is small over

the full aperture (about 0.23 range cells), the error is extremely small as will be demonstrated in the simulations.

For systems with larger range curvature such as longer wavelength SAR's including SEASAT, the error may be more significant. In such cases a look-dependent SRC implementation is possible in which the differences in RCM slope between looks are compensated by designing a separate SRC/RCMC filter for each look. For this method, the slope used for projecting the filter into range is taken as the slope at the look center frequency rather than the full aperture center frequency. This complicates the control and memory requirements for the azimuth processor since several SRC/RCMC filters (in this case 4 of them) need to be precomputed and stored.

For single-look SRC, the slope of the azimuth frequency domain RCM curve at the center frequency of the full aperture, or the beam center frequency, f_C, was expressed as :

$$c_2 = c_1/K_A = -\lambda f_C/(cK_A) \tag{113}$$

where K_A is the azimuth frequency rate at the beam center frequency.

This equation can be used to calculate the slope at any arbitrary look center frequency, f_L. To do this accurately, it is necessary to know the azimuth frequency rate at that frequency. This is accomplished by using equations (37),

(38), and (56) :

$$\eta_i(f) = r_o \;/\; \{ \; v_{eq} \; [(2v_{eq}/(\lambda f))^2 - 1]^{1/2} \; \} \tag{114}$$

$$r_i(f) = r_o \;/\; [\; 1 - (\lambda f/(2v_{eq}))^2 \;]^{1/2} \tag{115}$$

$$K_A(f) = -(2v_{eq}^2/[\lambda r_i(f)]) \; [1 - (v_{eq}\eta_i(f)/r_i(f))^2] \tag{116}$$

The first two equations determine the azimuth look center time, $\eta_i(f_L)$, and look center range, $r_i(f_L)$. These are substituted into the third equation to determine the look center frequency rate, $K_A(f_L)$. Finally the slope, c_L, of the azimuth frequency domain RCM curve at the look center frequency is calculated by substituting into the equation for c_2 :

$$c_L \;=\; -\lambda f_L/[cK_A(f_L)] \tag{117}$$

The filter is projected into range as in equation (89) of chapter 5 with c_2 replaced by c_L :

$$H_F(t,f) \simeq \mathcal{F}\{ \; \exp[-j4\pi r(\eta)/\lambda] \; \}$$

$$\bullet \; \{A_2(t/c_L) \; *_t \; \delta[t-(2/c)r([f-f_1]/K_A)]\} \tag{118}$$

where K_A denotes the azimuth frequency rate at the beam center frequency, i.e. $K_A(f_C)$. For fixed SRC, c_L is computed

using the beam center frequency, f_C, while for look-dependent SRC, the look center frequency of each look is used.

The resulting algorithm for compressing each look is given by equations (90) to (96) with c_2 again replaced by the appropriate c_L.

As in single-look processing, there are several alternative methods for implementing the SRC filter. Fixed range SRC can provide better compression due to the longer effective length of the SRC filter. However the range SRC method becomes less efficient if look-dependent SRC is required because a separate range compression would be required for each look. Look-dependent azimuth SRC is more efficient since only the additional look-dependent filters need to be generated.

For the azimuth SRC implementation, the combined SRC/RCMC filter, $g_C(t,f)$, is implemented as a range convolution with the azimuth spectrum. As in single-look azimuth SRC, the filter is approximated by precomputing 16 interpolated versions of the SRC filter g(t). The convolution is implemented by computing the integer and fractional range cell shifts for RCM correction (RCMC) and using the appropriately shifted version of the precomputed filter. The window, $W_A(f-f_L)$, is shifted to the appropriate look center frequency for each look. The time domain image for each look is computed by applying an inverse azimuth FFT of length 256.

Before look detection and look summation, each look image, which is still in complex form, must first be interpolated in order to reduce aliasing of the increased bandwidth of the detected signal. Although an interpolation factor of 2 is sufficient, the simulations interpolate each look by a factor of 8 in both range and azimuth before detection and look summation as part of the image quality measurement process. The interpolated look images are detected and summed together to form the final multilook image.

For simulations of multilook processing without SRC, the combined SRC/RCMC filter $g_C(t,f)$ was replaced by the zero phase RCMC interpolator of chapter 3 which is the same for each look.

For multilook range SRC, only fixed SRC was simulated since look-dependent multilook range SRC was inefficient. The same modified linear FM rate was used for the combined SRC/range compression filter as in single-look range SRC.

The following sections describe the results of simulations of the both fixed and look-dependent multilook SRC algorithms as well as simulations of multilook processing without SRC which are used as a baseline for comparison.

The simulations were performed using the nominal set of RADARSAT parameters listed in Table 1. The azimuth Kaiser-Bessel window parameter was changed from 1.5 to 2.7. More weighting is required in multilook processing since the

antenna weighting has much less effect over the reduced look bandwidths. The value of 2.7 was chosen to produce azimuth sidelobe levels which are comparable in size to the range sidelobes as in earlier simulations.

6.2 SIMULATIONS OF 4-LOOK PROCESSING WITHOUT SRC

This section discusses simulations of 4-look, range/Doppler processing without SRC. Simulations were performed with a length 16 RCMC filter. The simulation results are summarized by figures 6.3 to 6.14.

Figures 6.3 and 6.4 show the 1-D range and azimuth profiles after 4-look azimuth compression for squint angles of 0°, 5°, and 10°. The simulations were performed as outlined in the previous section including look detection, and look summation. The profiles were interpolated by a factor of 8 before detection by zero padding in the frequency domain to preserve the signal bandwidth after detection and to increase the accuracy of the image quality measurements.

The range profiles are very similar to the single-look profiles shown earlier. This is expected since the range broadening is primarily due to the azimuth FFT which is applied in both single-look and multilook compression. Small differences are expected because of small variations in range width over the azimuth spectrum before azimuth compression which are caused by range curvature.

The azimuth profiles are also similar to the single-look results. However the mainlobe widths are approximately 3.3 times wider than the single-look results. This is primarily due to the smaller bandwidth of each look compared to the full aperture processed bandwidth. The azimuth sidelobe levels differ slightly because of the larger azimuth window parameter.

The range and azimuth broadening results for both single-look processing and 4-look processing are shown in figures 6.5 to 6.7 for squint angles of 0 to 6 degrees. The 4-look range broadening results are the same as the single-look results. As explained above, this is expected since range broadening occurs primarily in the azimuth FFT.

Azimuth broadening for single-look processing increases with squint angle due to the reduced processed bandwidths. In contrast, there is very little azimuth broadening for 4-look processing since each look contains essentially the same bandwidth. The azimuth antenna weighting has less broadening effect on the reduced bandwidths of the individual looks.

Figures 6.8 to 6.10 show that the range, azimuth, and 2-D integrated sidelobe ratios (ISLR) for 4-look and single-look processing behave similarly with increasing squint angle. The range ISLR curves increase with increasing squint angle due to the spreading of energy from the mainlobe to the sidelobes. The apparent drop in ISLR past 5 degrees is due to the finite integration area of the image

quality measurements. For squint angles over 5 degrees, the range broadening is over 25%. This causes a significant amount of energy to lie in the sidelobes outside of the integration area. Consequently the ISLR measurements are inaccurate for large amounts of broadening. The azimuth ISLR curves show very little variation with squint angle whereas the 2-D ISLR curve is a composite of the range and azimuth curves.

The peak sidelobe ratio (PSLR) measurements are shown in figures 6.11 to 6.13. Again the single-look and 4-look results are similar with the range results varying with squint angle and the azimuth results essentially constant. The 2-D measurements are somewhat lower than the 1-D measurements since they are measured with a much coarser sample spacing (interpolated by 8) than the 1-D measurements (interpolated by 128).

Finally the peak magnitude ratios, which compare the peak compressed magnitude to that obtained for zero squint, are shown in figure 6.14. The peak magnitudes are normalized by the sum of squares of the RCMC filter coefficients as would be appropriate for white noise identically distributed over the range cells. In reality the noise is only approximately evenly distributed over range cells so that care must be used in relating the peak magnitude results to signal-to-noise ratios.

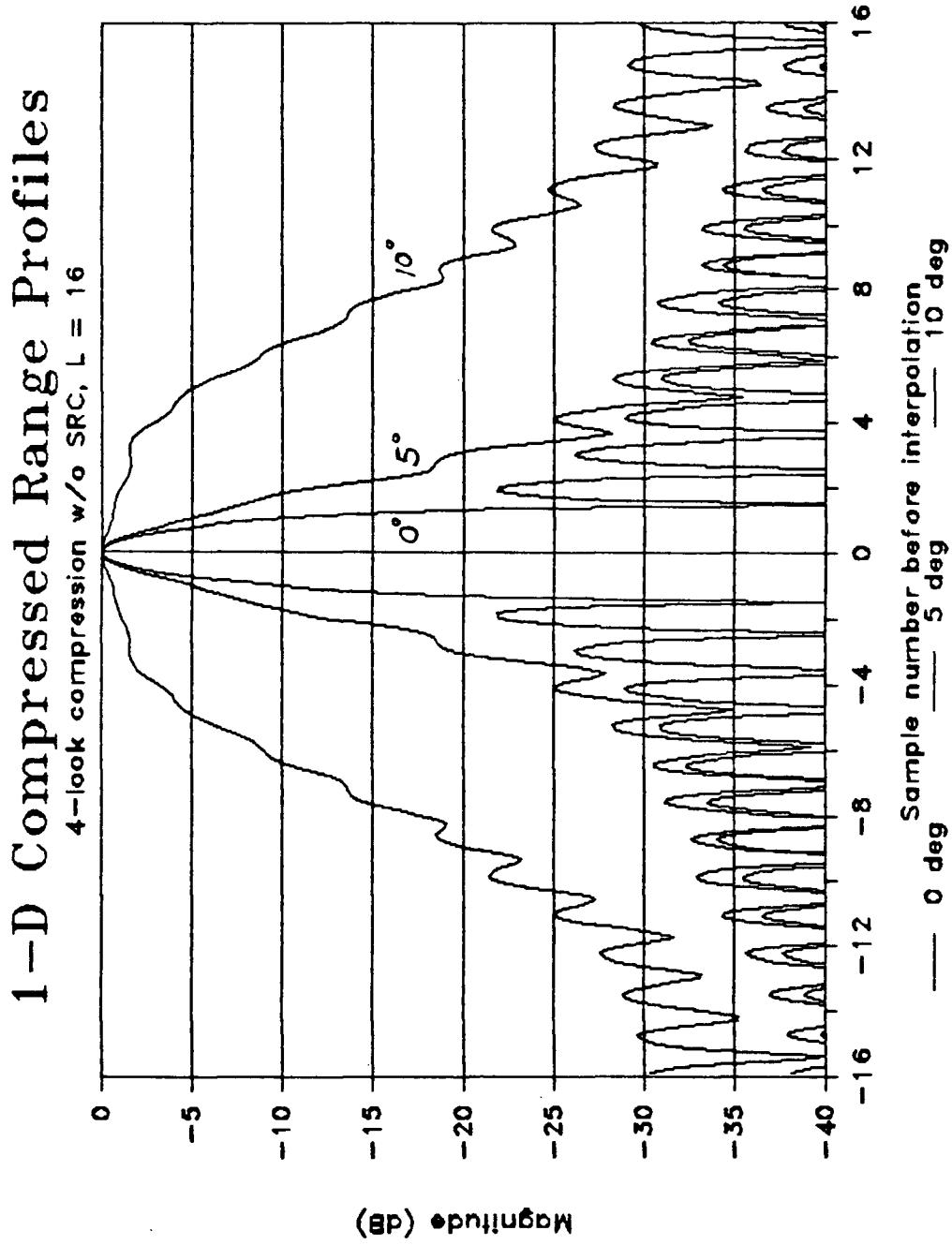

Figure 6.3. Interpolated 1-D range profiles after 4-look compression without SRC for squint angles of 0°, 5°, and 10° and a length 16 RCMC interpolator.

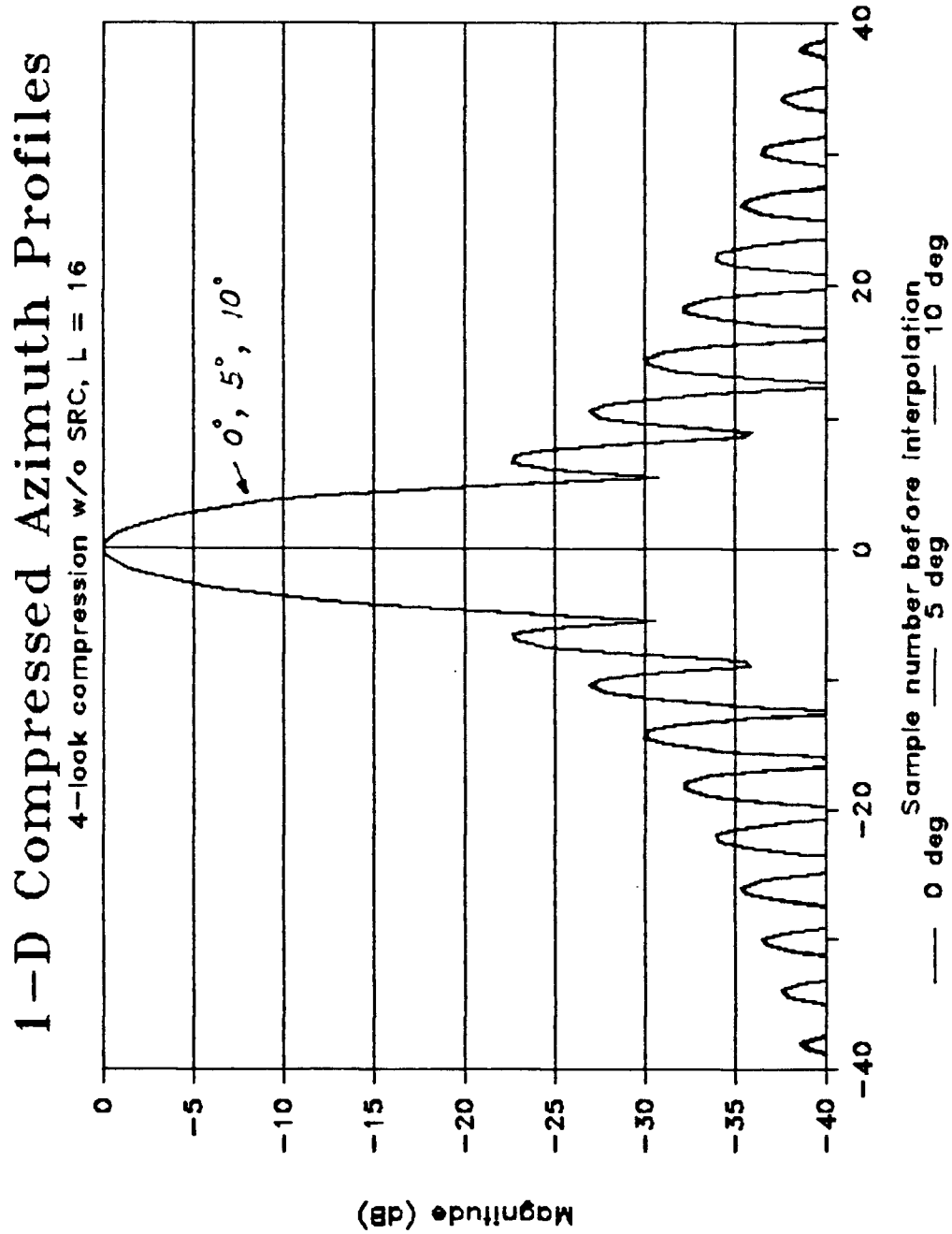

Figure 6.4. Interpolated 1-D azimuth profiles after 4-look compression without SRC for squint angles of 0°, 5°, and 10° and a length 16 RCMC interpolator.

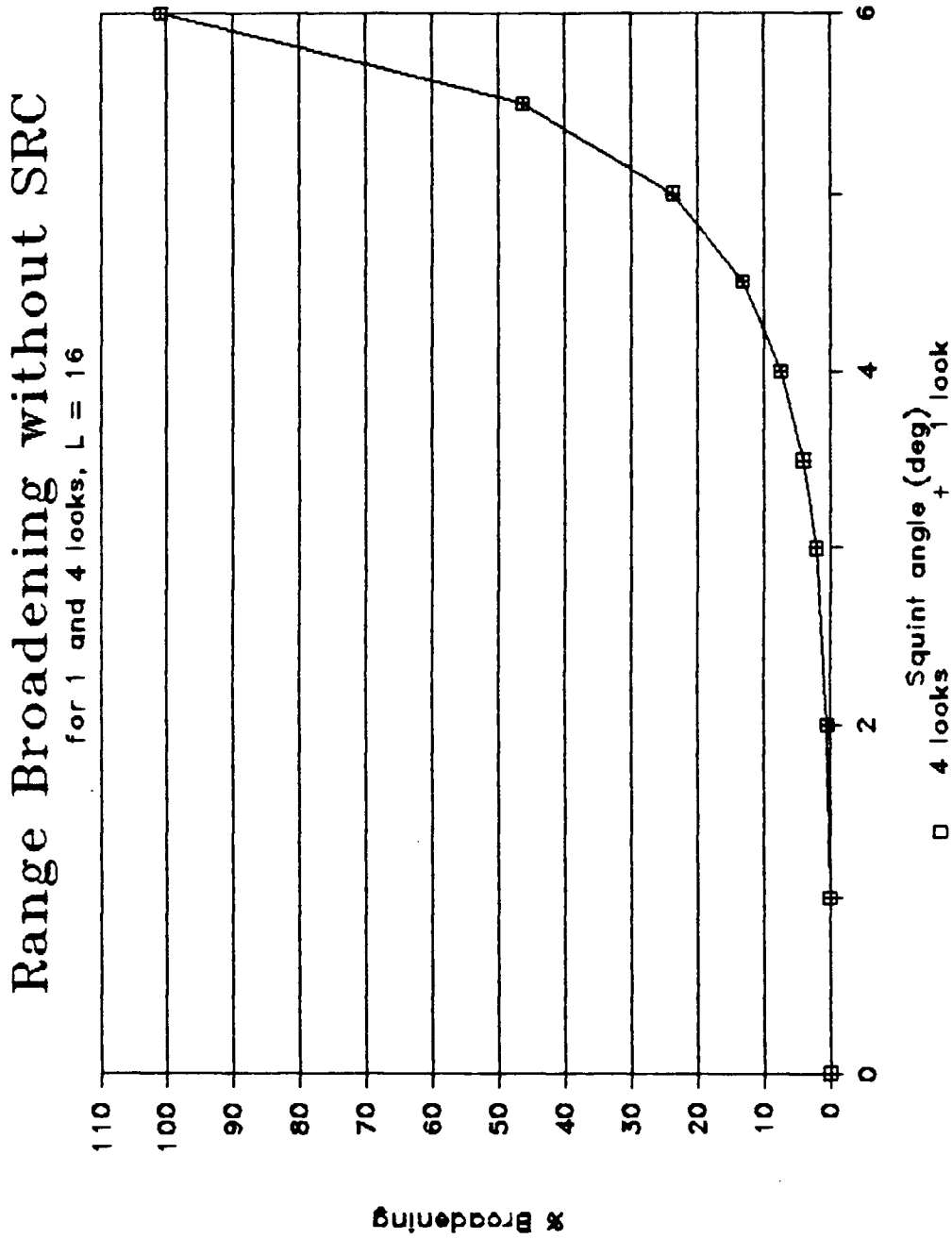

Figure 6.5. Range broadening for single-look and 4-look compression without SRC using a length 16 RCMC interpolator.

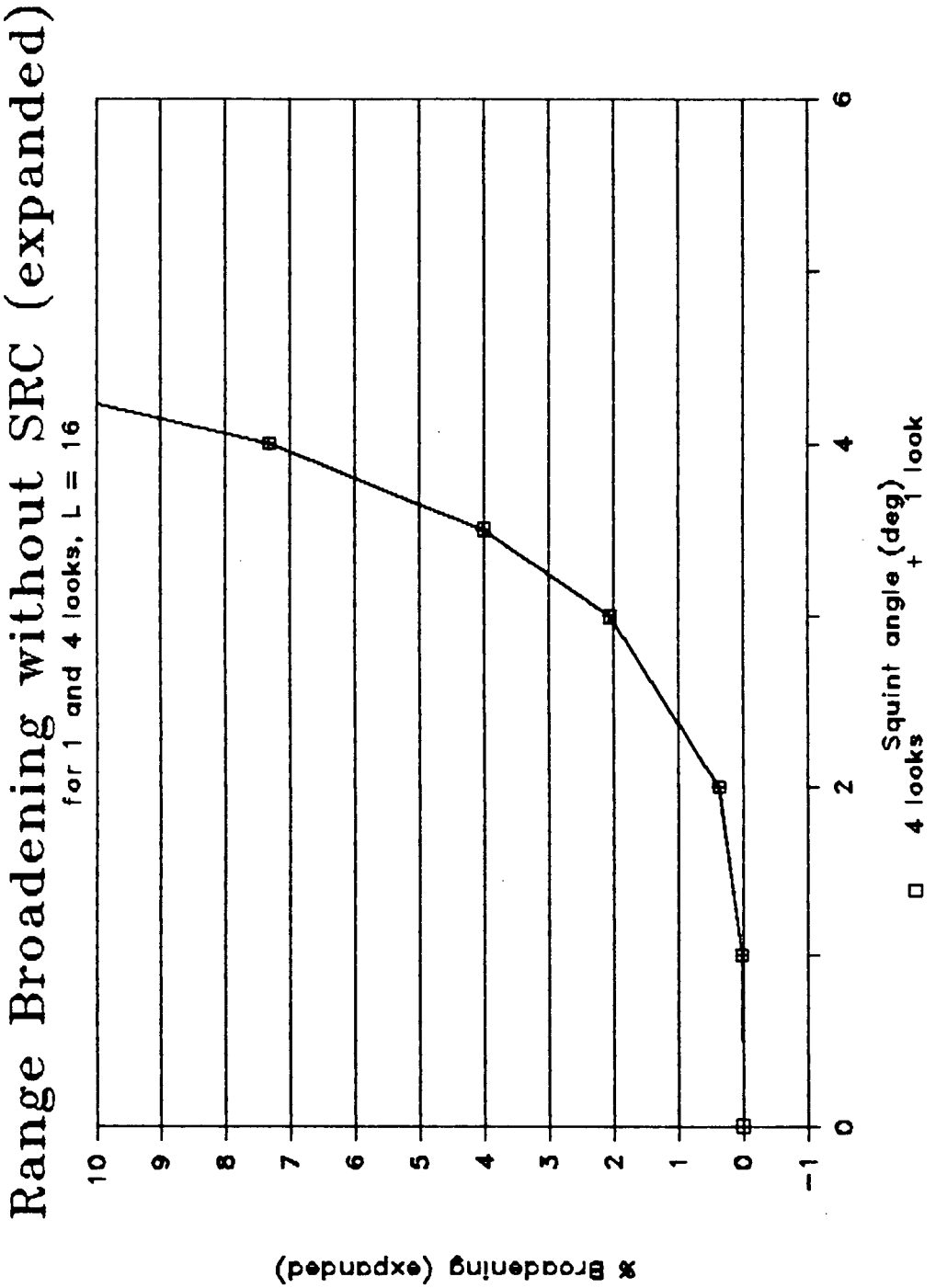

Figure 6.6. Range broadening for single-look and 4-look compression without SRC using a length 16 RCMC interpolator (expanded scale).

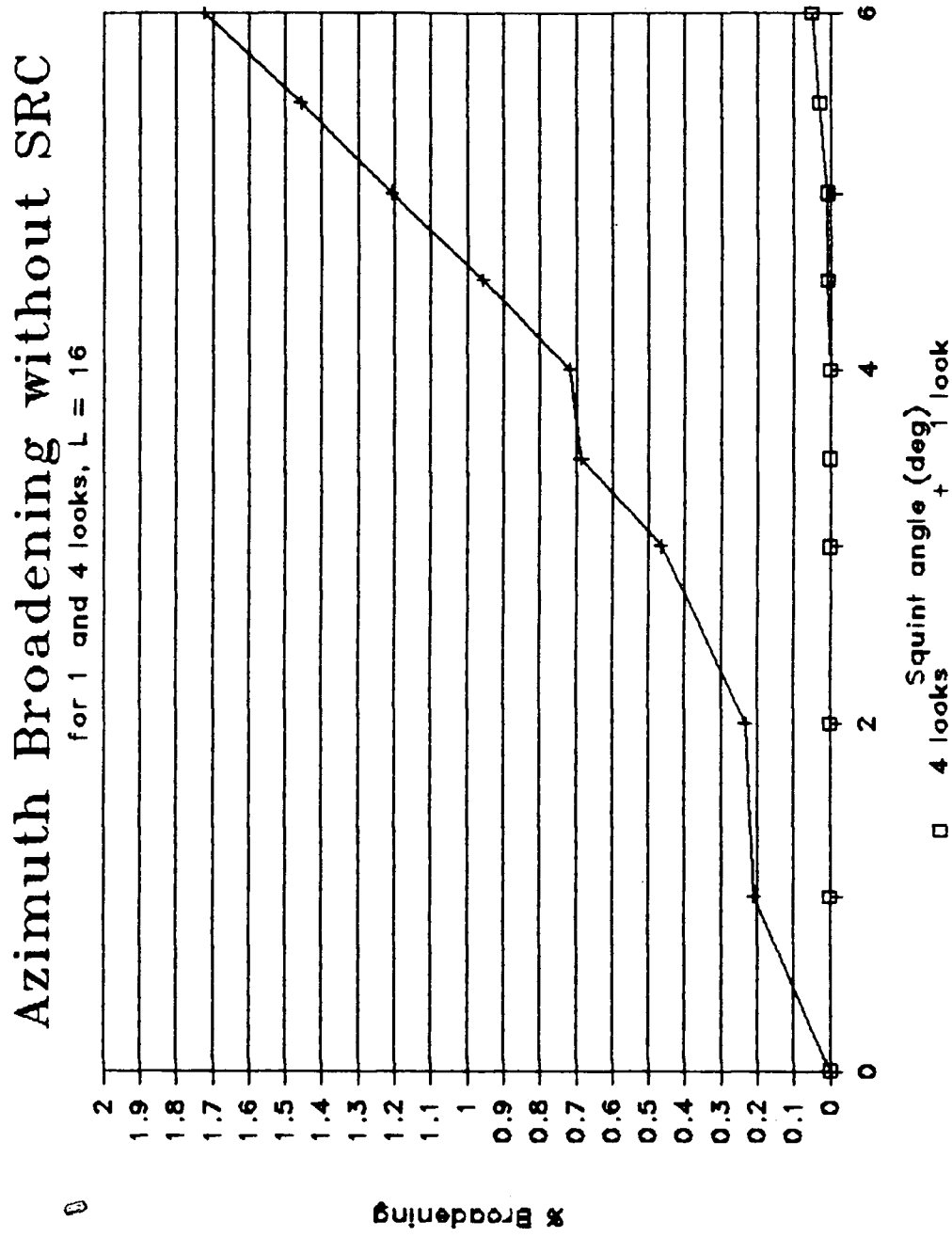

Figure 6.7. Azimuth broadening for single-look and 4-look compression without SRC using a length 16 RCMC interpolator.

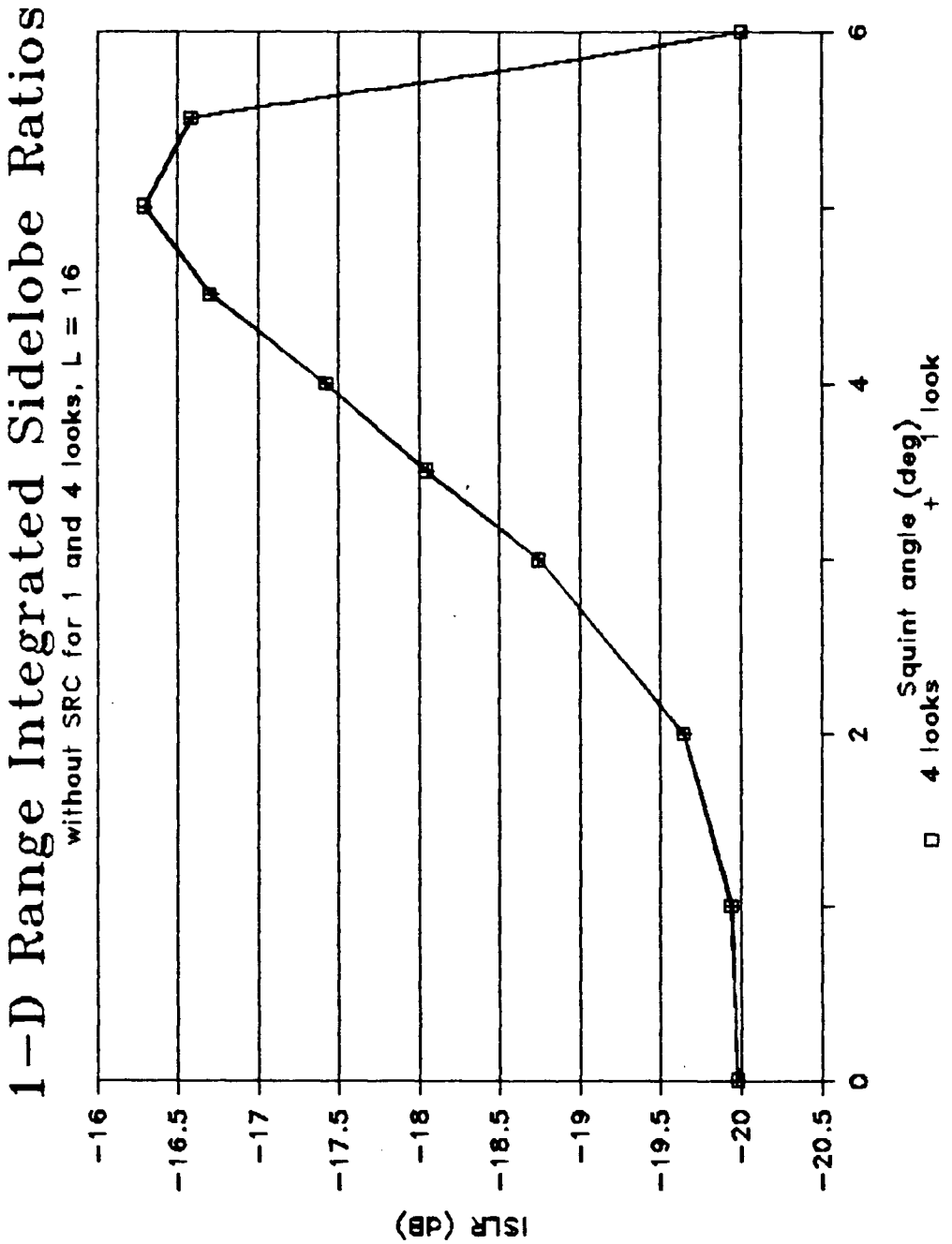

Figure 6.8. 1-D range integrated sidelobe ratios for single-look and 4-look compression without SRC using a length 16 RCMC interpolator.

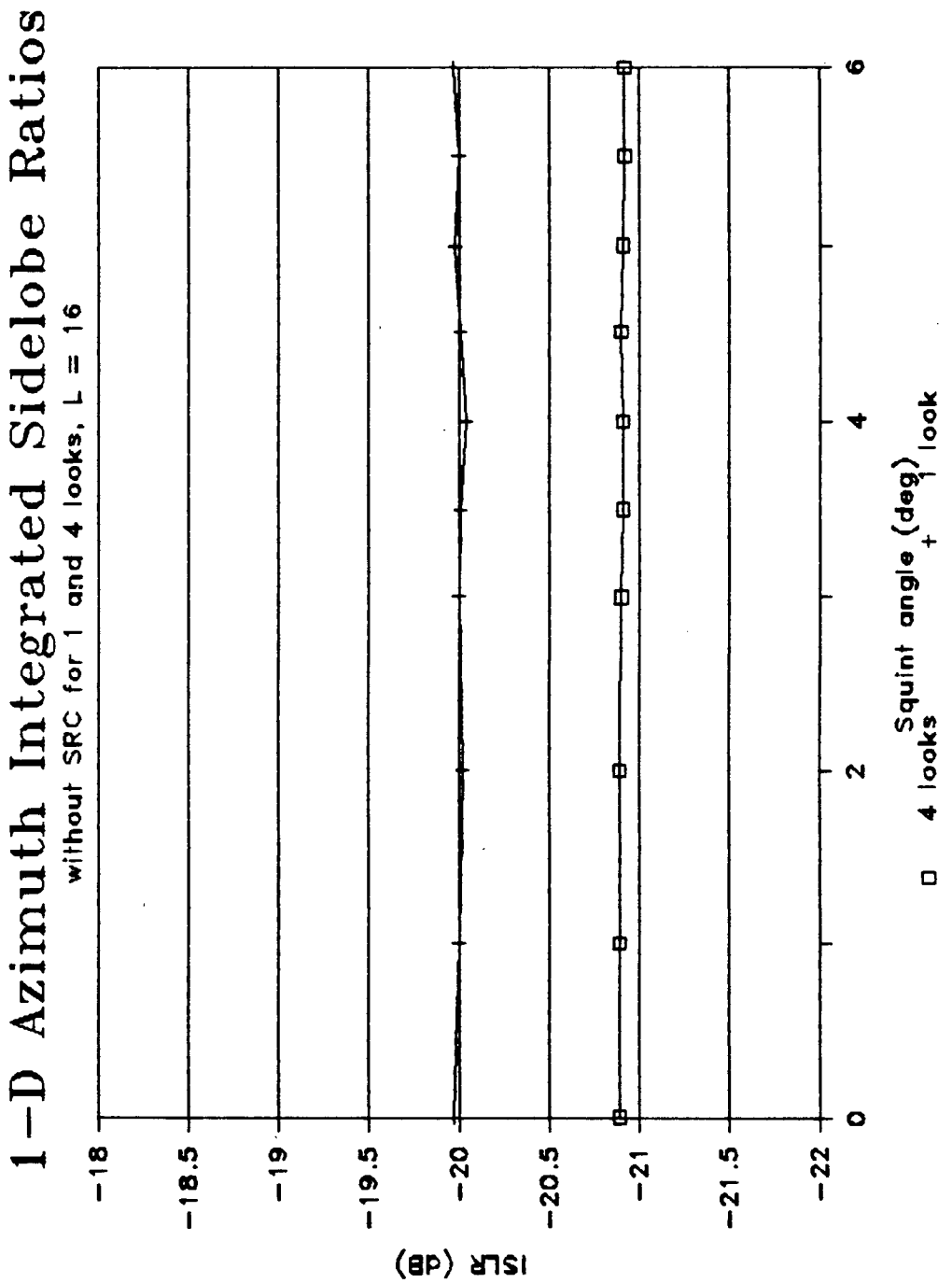

Figure 6.9. 1-D azimuth integrated sidelobe ratios for single-look and 4-look compression without SRC using a length 16 RCMC interpolator.

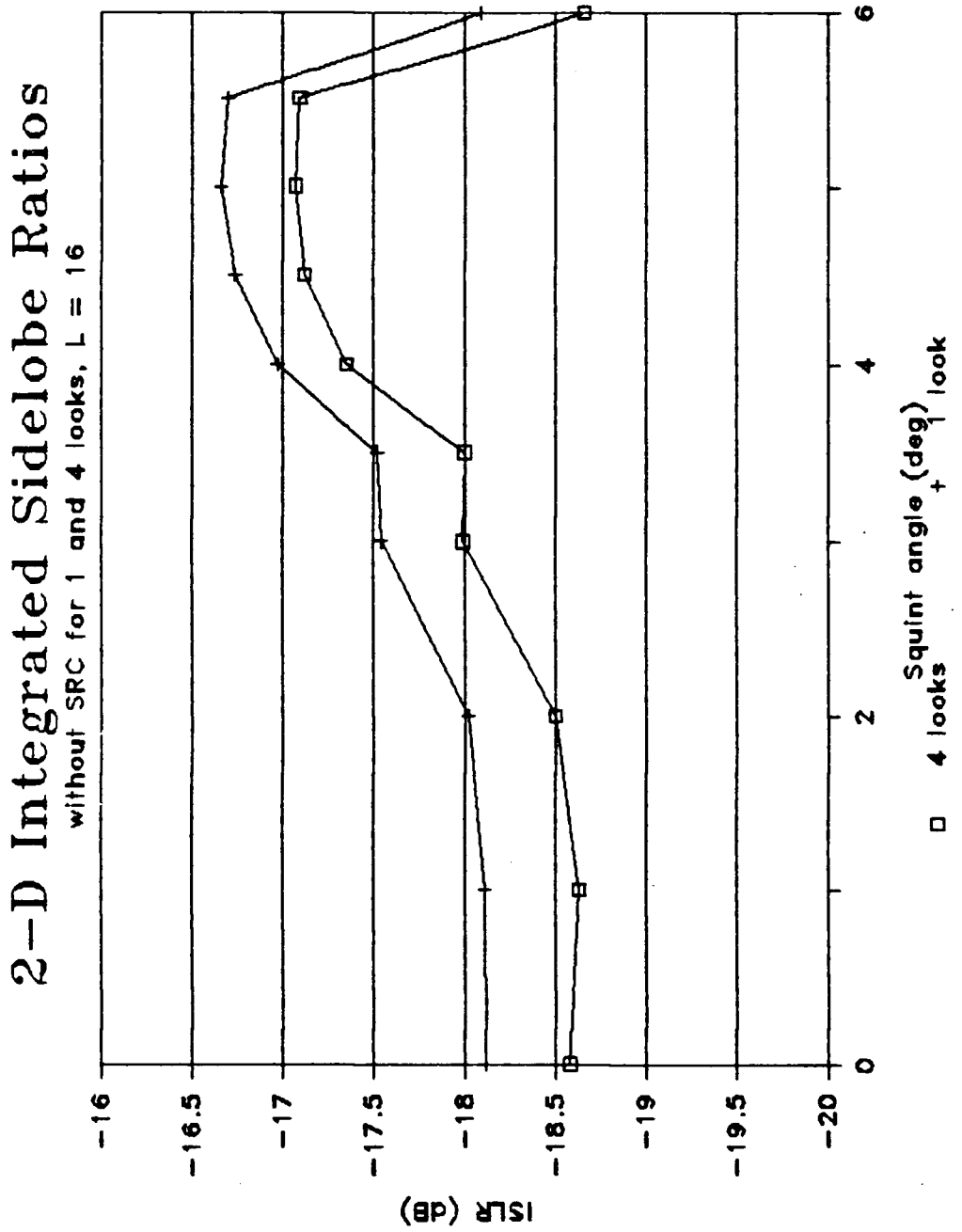

Figure 6.10. 2-D integrated sidelobe ratios for single-look and 4-look compression without SRC using a length 16 RCMC interpolator.

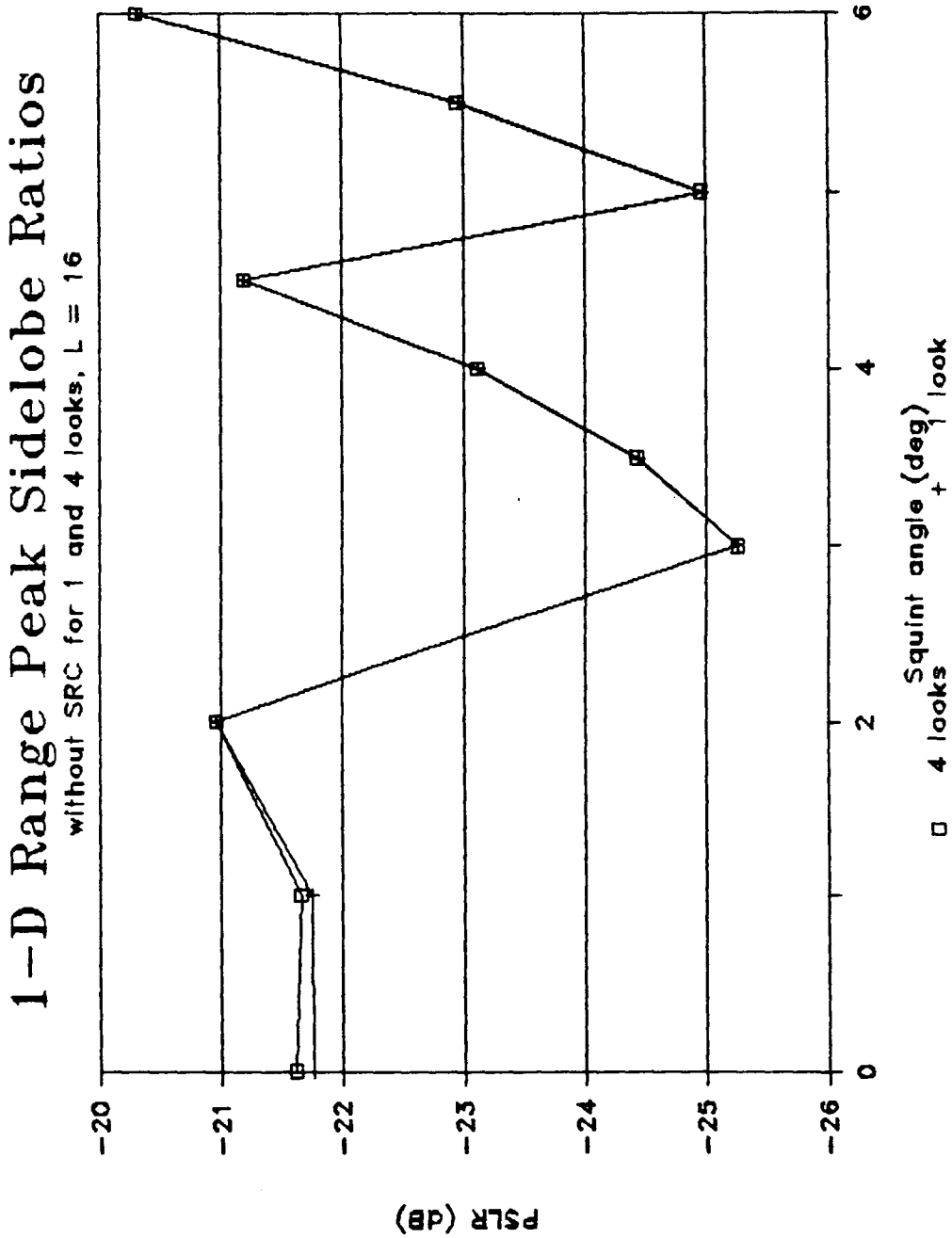

Figure 6.11. 1-D rarge peak sidelobe ratios for single-look and 4-look compression without SRC using a length 16 RCMC interpolator.

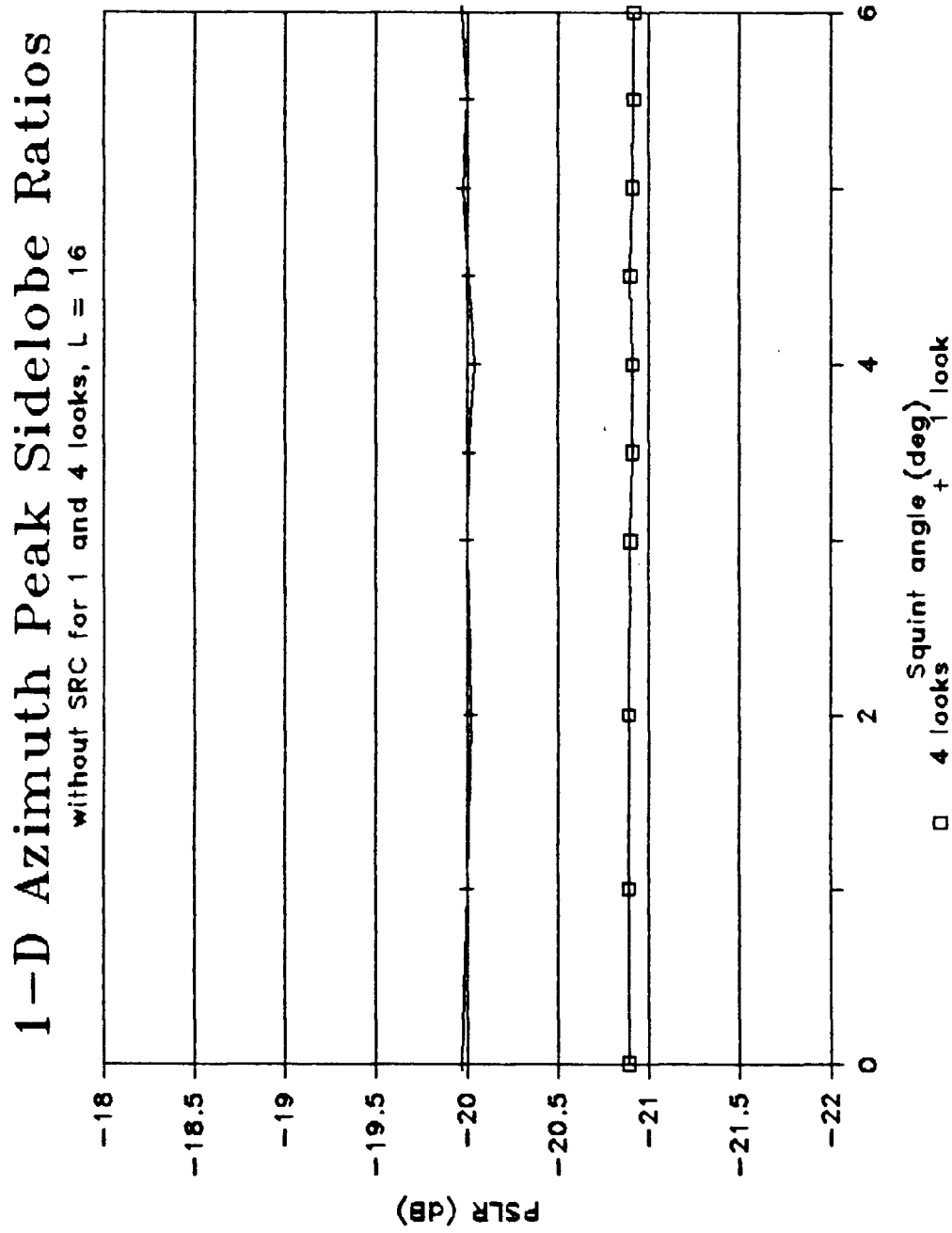

Figure 6.12. 1-D azimuth peak sidelobe ratios for single-look and 4-look compression without SRC using a length 16 RCMC interpolator.

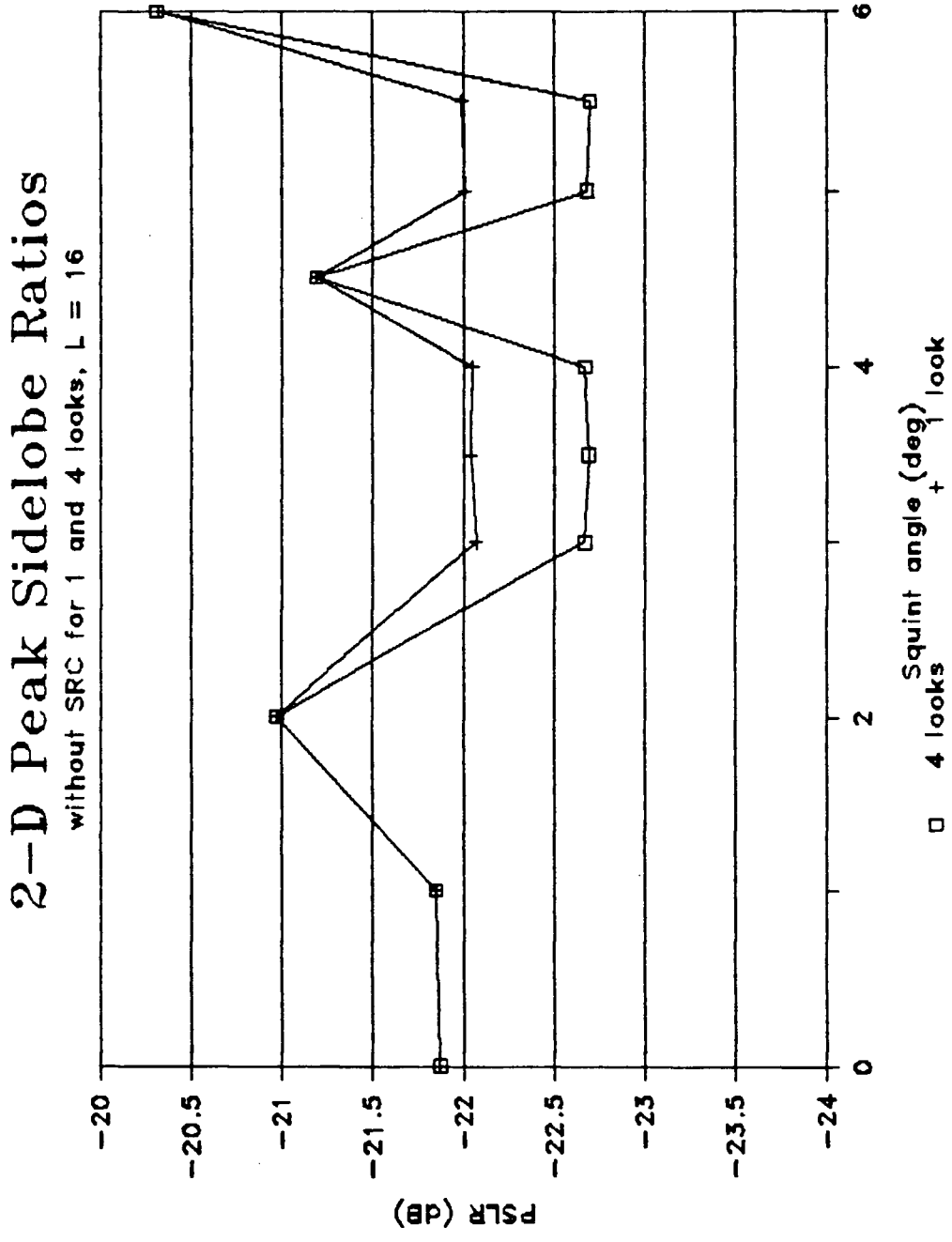

Figure 6.13. 2-D peak sidelobe ratios for single-look and 4-look compression without SRC using a length 16 RCMC interpolator.

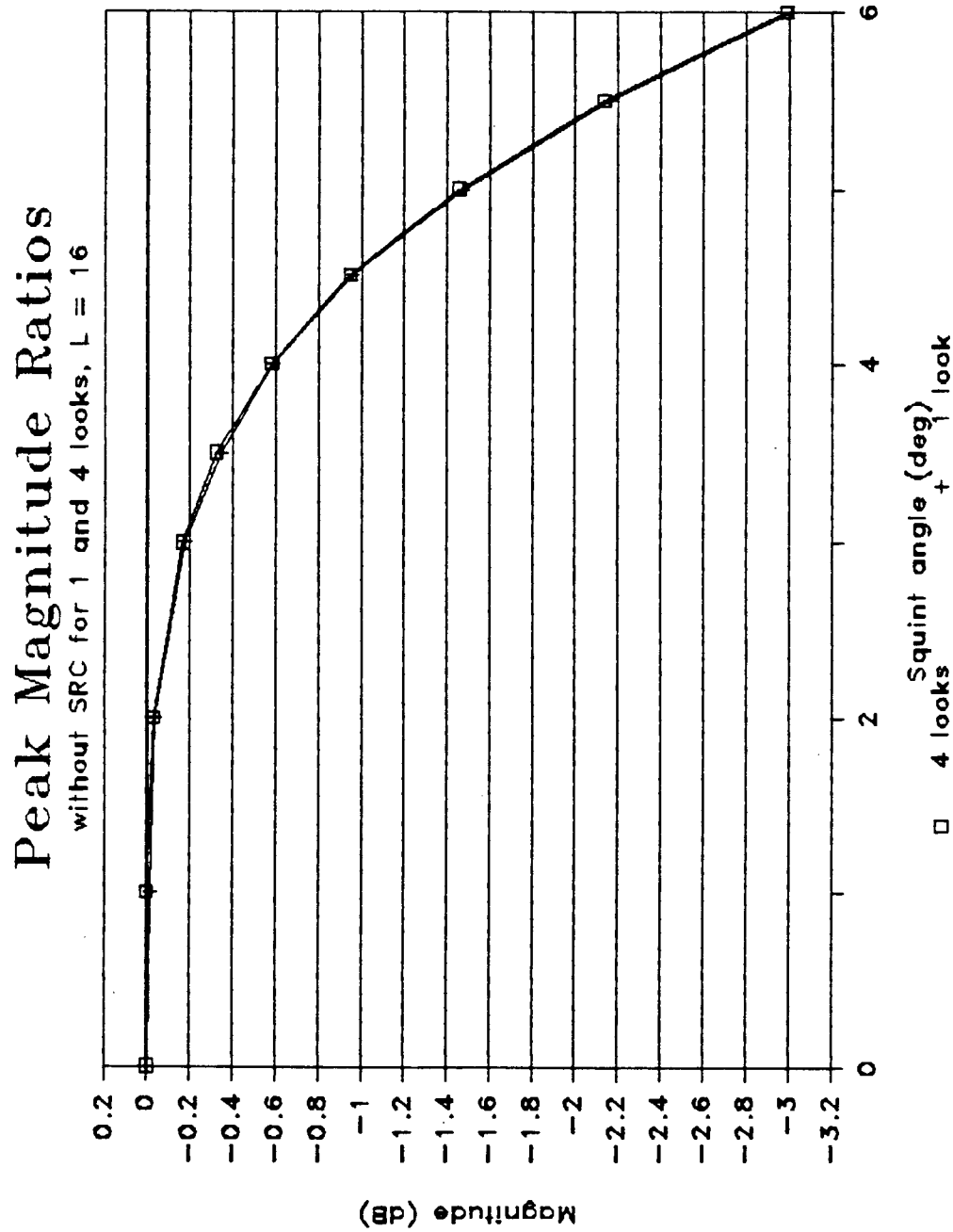

Figure 6.14. Peak magnitude ratios for single-look and 4-look compression without SRC using a length 16 RCMC interpolator.

6.3 SIMULATIONS OF 4-LOOK, FIXED AND LOOK-DEPENDENT, AZIMUTH SRC PROCESSING

The next section discusses simulations of 4-look processing performed with both fixed and look-dependent azimuth SRC. The results for the two algorithms were identical within the limits of the measurements. Consequently only one set of results are presented. This similarity shows that look-dependent processing is not necessary for RADARSAT.

The results are almost identical since the slope of the RCM curve varies very slowly over the aperture for RADARSAT parameters. Consequently the slopes at the individual look center frequencies are virtually the same. As stated earlier, systems such as SEASAT which exhibit larger range curvature may have larger variations in RCM curve slope over the aperture requiring look-dependent SRC processing.

The results of the simulations are contained in figures 6.15 to 6.26. A smaller selection of squint angles was used than in the single-look azimuth SRC simulations since the results are very similar. Simulations were performed for squint angles of 0, 1, 5, and 10 degrees and for SRC/RCMC filter lengths of 4, 8, 16, and 32.

Figures 6.15 and 6.16 show the range and azimuth profiles after azimuth 4-look compression for squint angles of 5 and 10 degrees. As in the previous section the processing included interpolation, look detection, and look summation. The range profiles show the broadening which occurs with smaller length SRC/RCMC filters at larger squint

angles. The azimuth profiles show negligible changes with filter length.

Figures 6.17 and 6.18 summarize the range and azimuth broadening results respectively. The broadening figures are computed from the -3dB response widths relative to the zero squint width for each filter length. Differences between the impulse response widths at zero squint for different filter lengths are very small (less than 0.2%) and are shown in figure 6.19.

The multilook broadening results can be compared to the single-look azimuth SRC results in figures 5.6 and 5.8. The 4-look range broadening results agree very closely with the single-look results. As in the simulations without SRC, almost no azimuth broadening occurs for 4-look processing.

The ISLR and PSLR measurements are shown in figures 6.20 to 6.22 and figures 6.23 to 6.25 respectively. The results agree closely with the single-look azimuth SRC curves. The azimuth sidelobes are lower by about 0.7dB due to the larger azimuth window parameter.

Figure 6.26 shows the peak magnitude variations with squint angle with the peaks normalized by the sum of the squared SRC/RCMC filter coefficients.

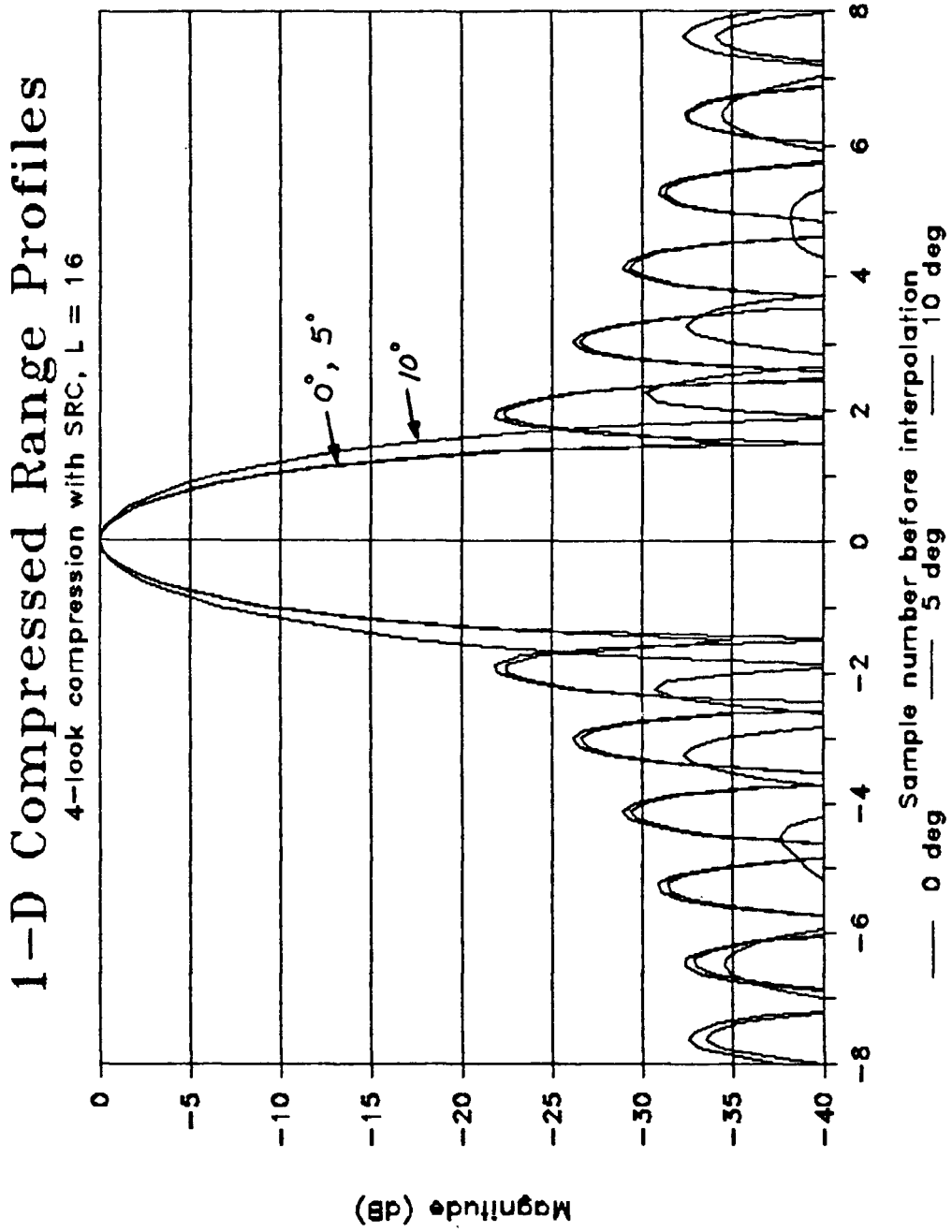

Figure 6.15. Interpolated 1-D range profiles after 4-look compression with both fixed and look-dependent SRC for squint angles of 0°, 5°, and 10° and a length 16 filter.

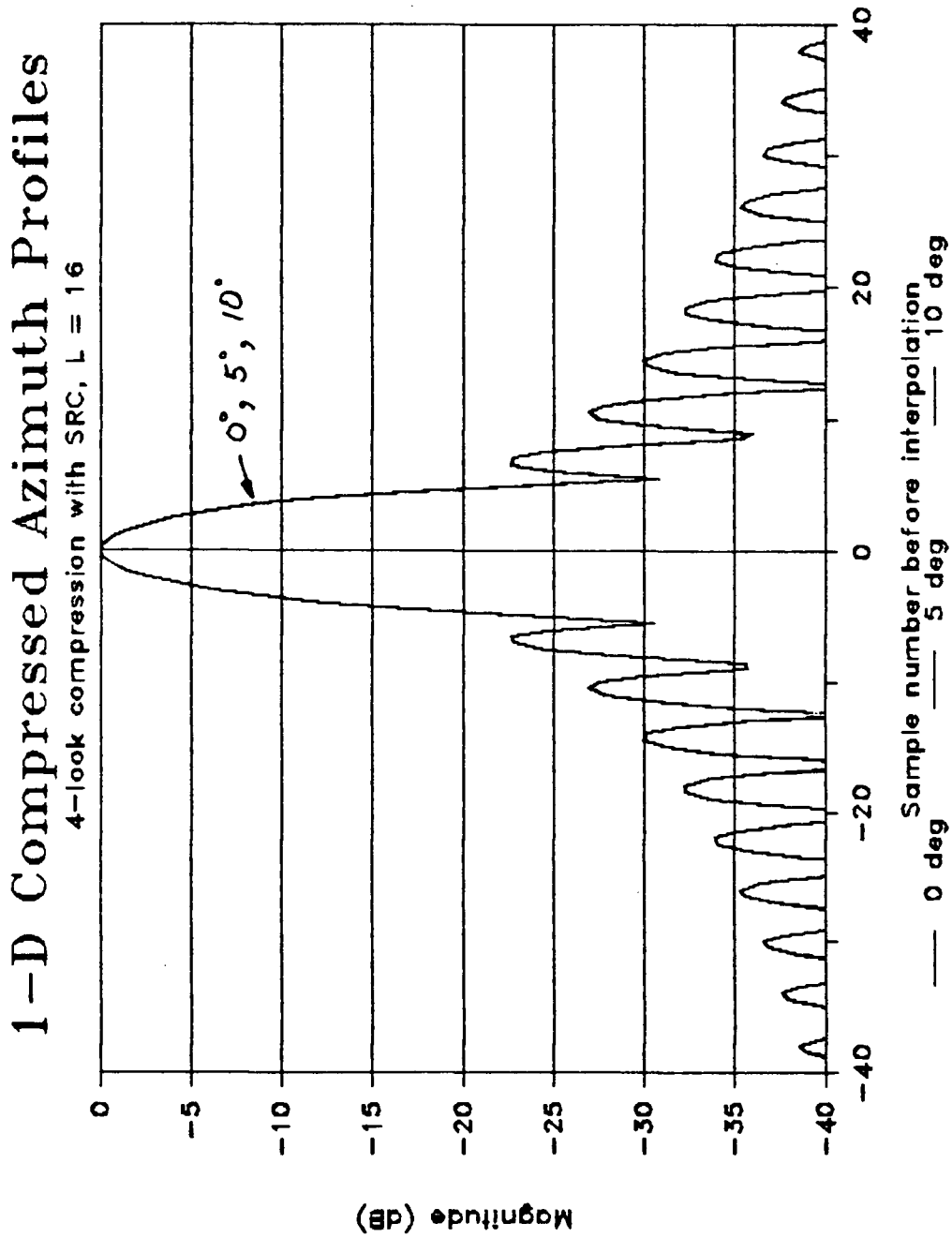

Figure 6.16. Interpolated 1-D azimuth profiles after 4-look compression with both fixed and look-dependent SRC for squint angles of 0°, 5°, and 10° and a length 16 filter.

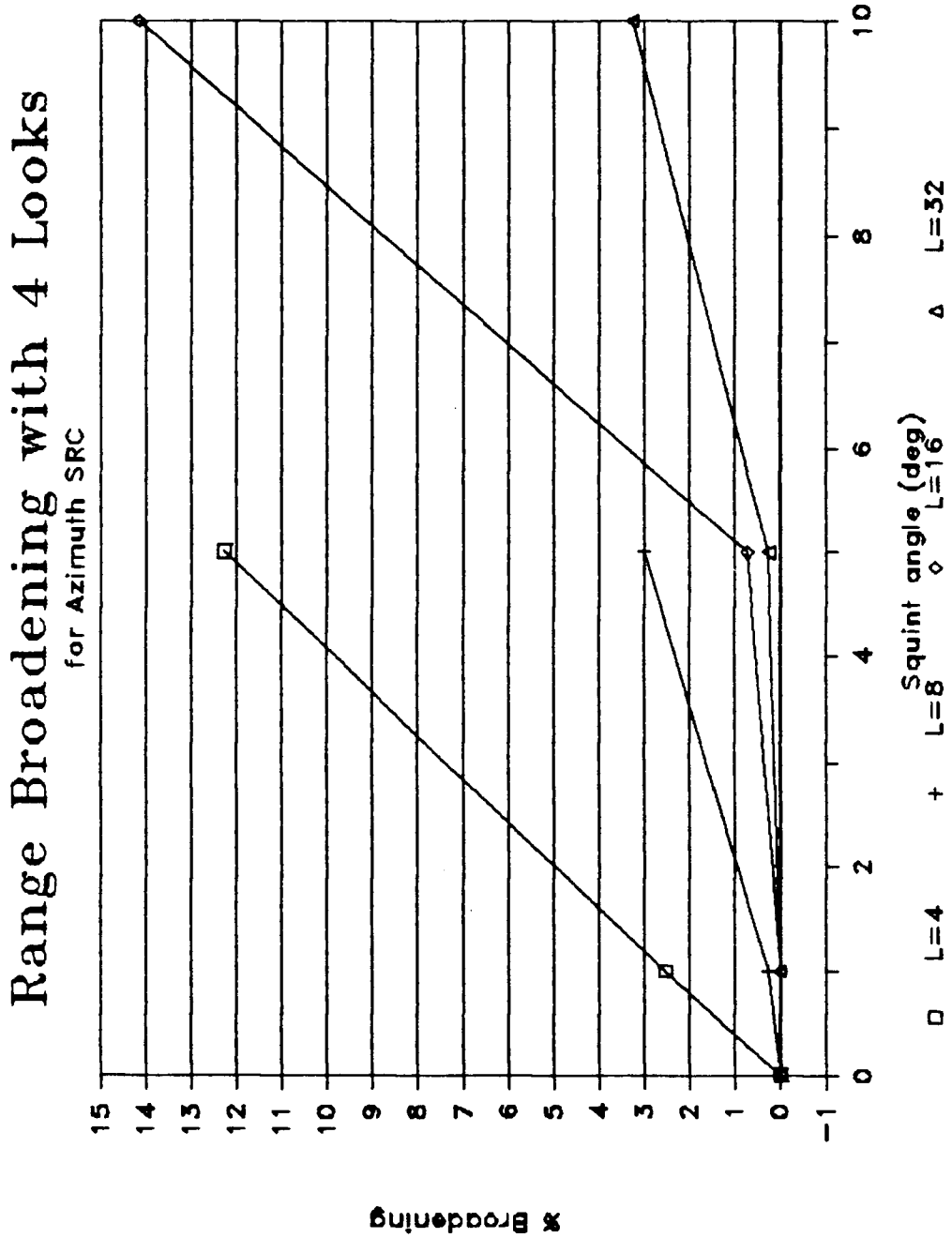

Figure 6.17. Range broadening for 4-look compression with both fixed and look-dependent SRC and various SRC/RCMC filter lengths as a function of squint angle.

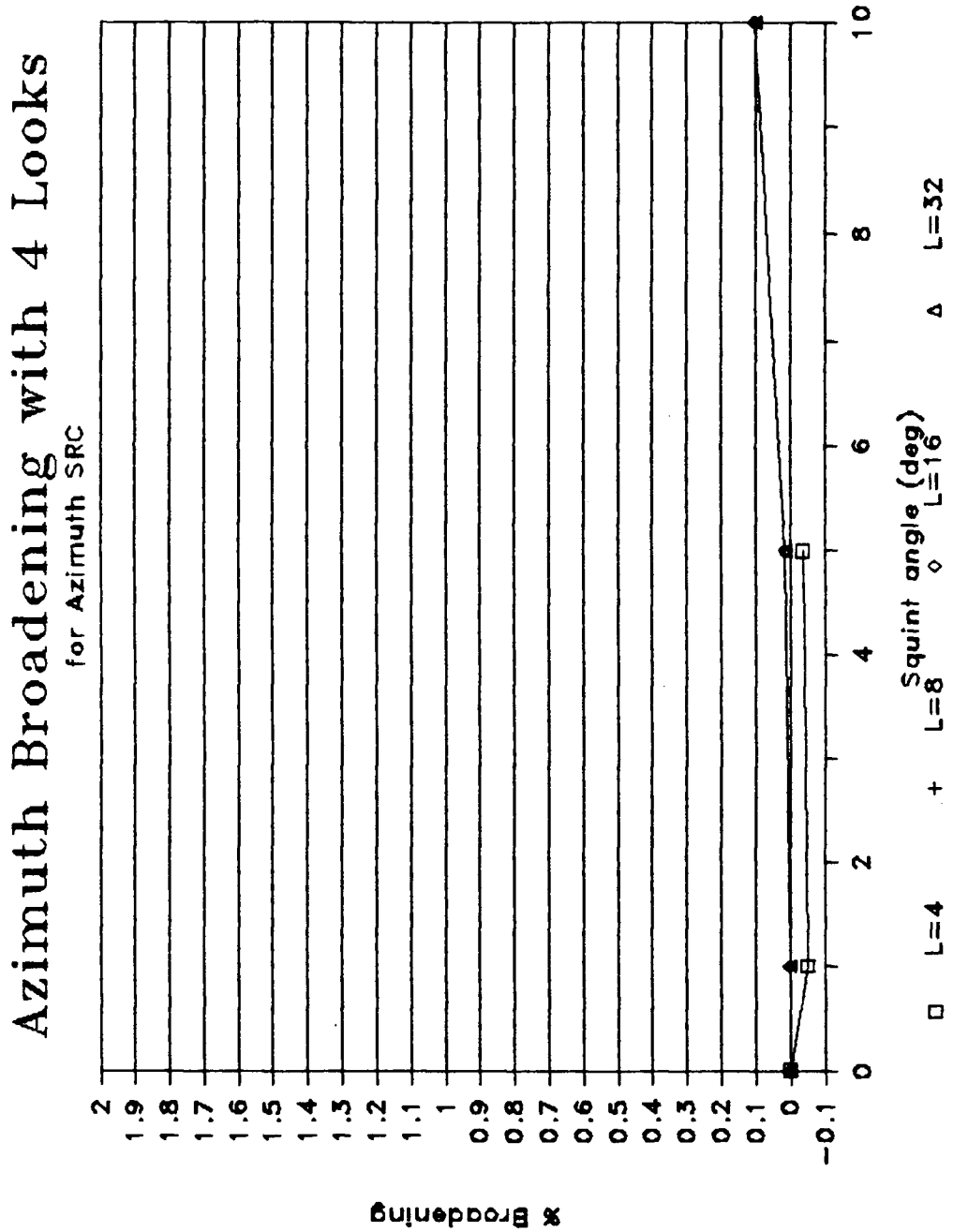

Figure 6.18. Azimuth broadening for 4-look compression with both fixed and look-dependent SRC and various SRC/RCMC filter lengths as a function of squint angle.

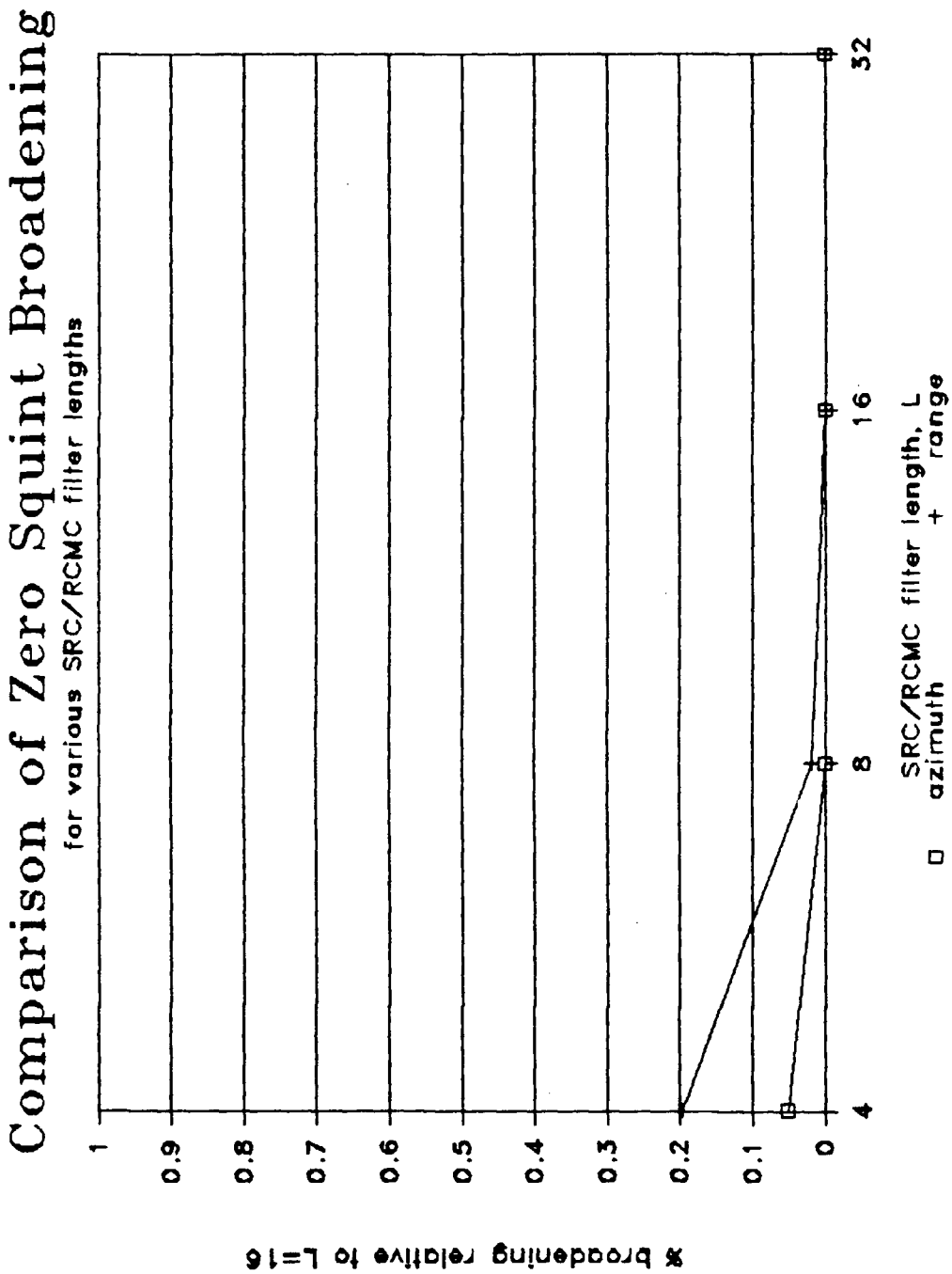

Figure 6.19. Comparison of range -3dB widths at 0° squint for 4-look compression with both fixed and look-dependent SRC and various SRC/RCMC filter lengths.

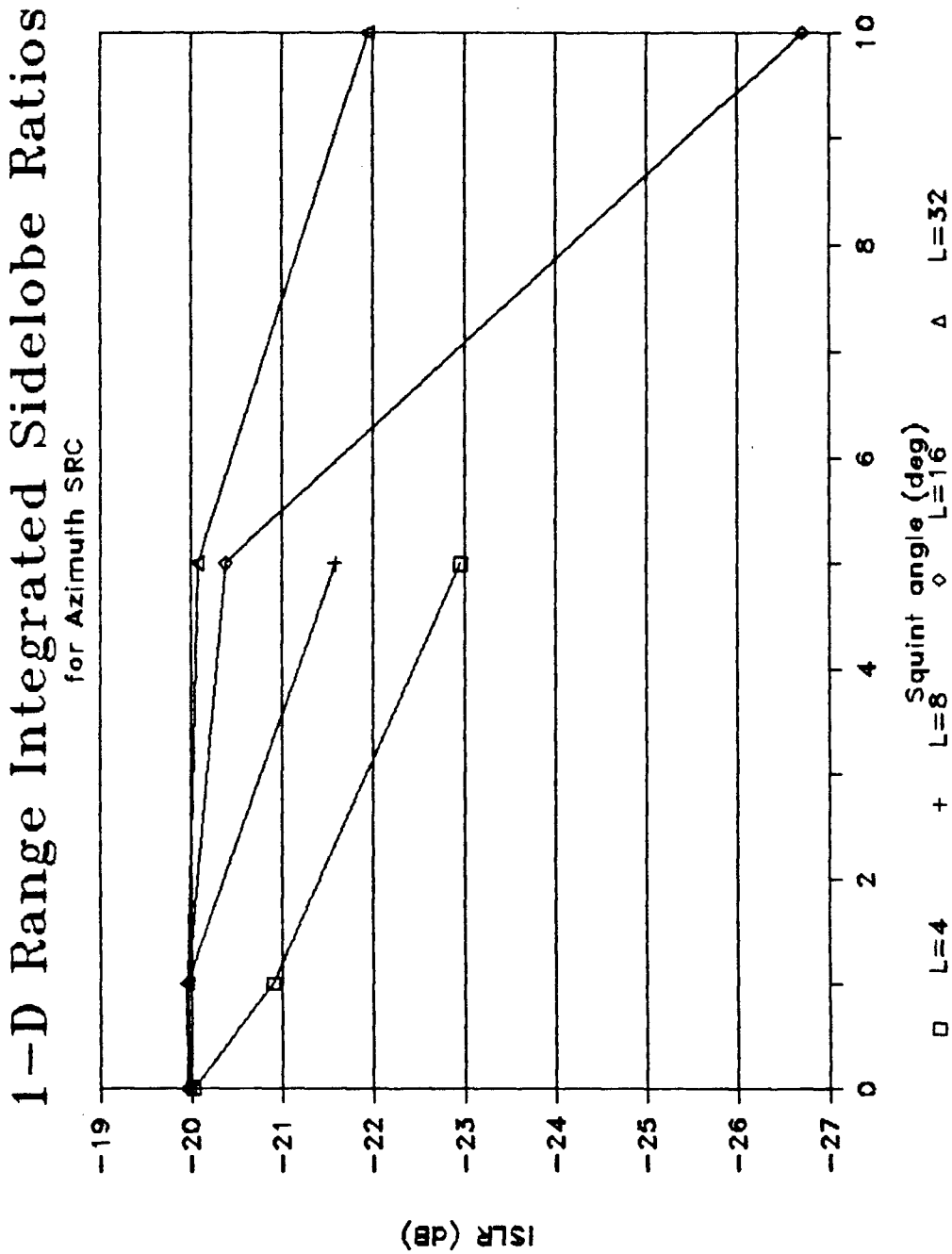

Figure 6.20. 1-D range integrated sidelobe ratios for 4-look compression with both fixed and look-dependent SRC and various SRC/RCMC filter lengths as a function of squint angle.

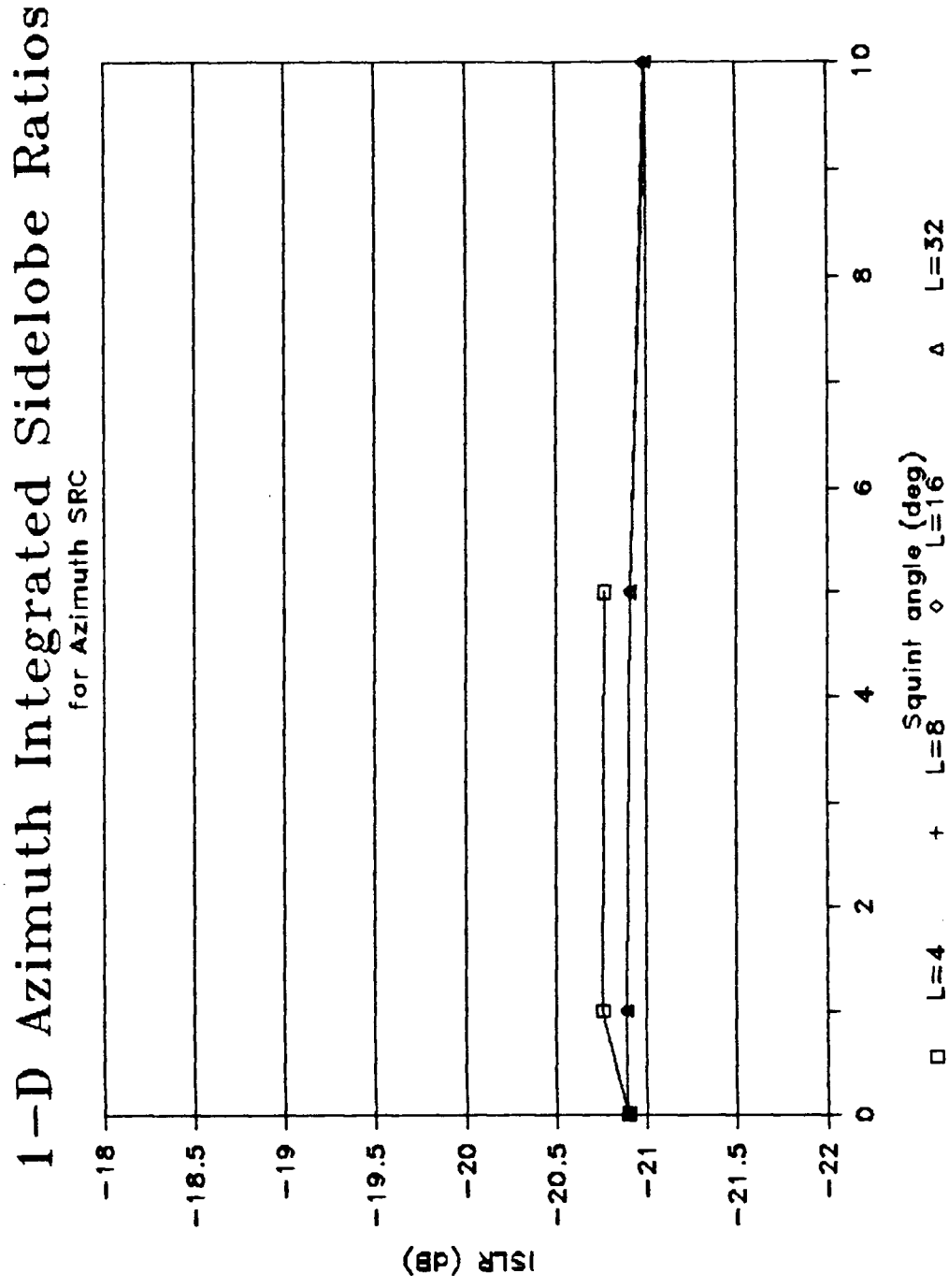

Figure 6.21. 1-D azimuth integrated sidelobe ratios for 4-look compression with both fixed and look-dependent SRC and various SRC/RCMC filter lengths as a function of squint angle.

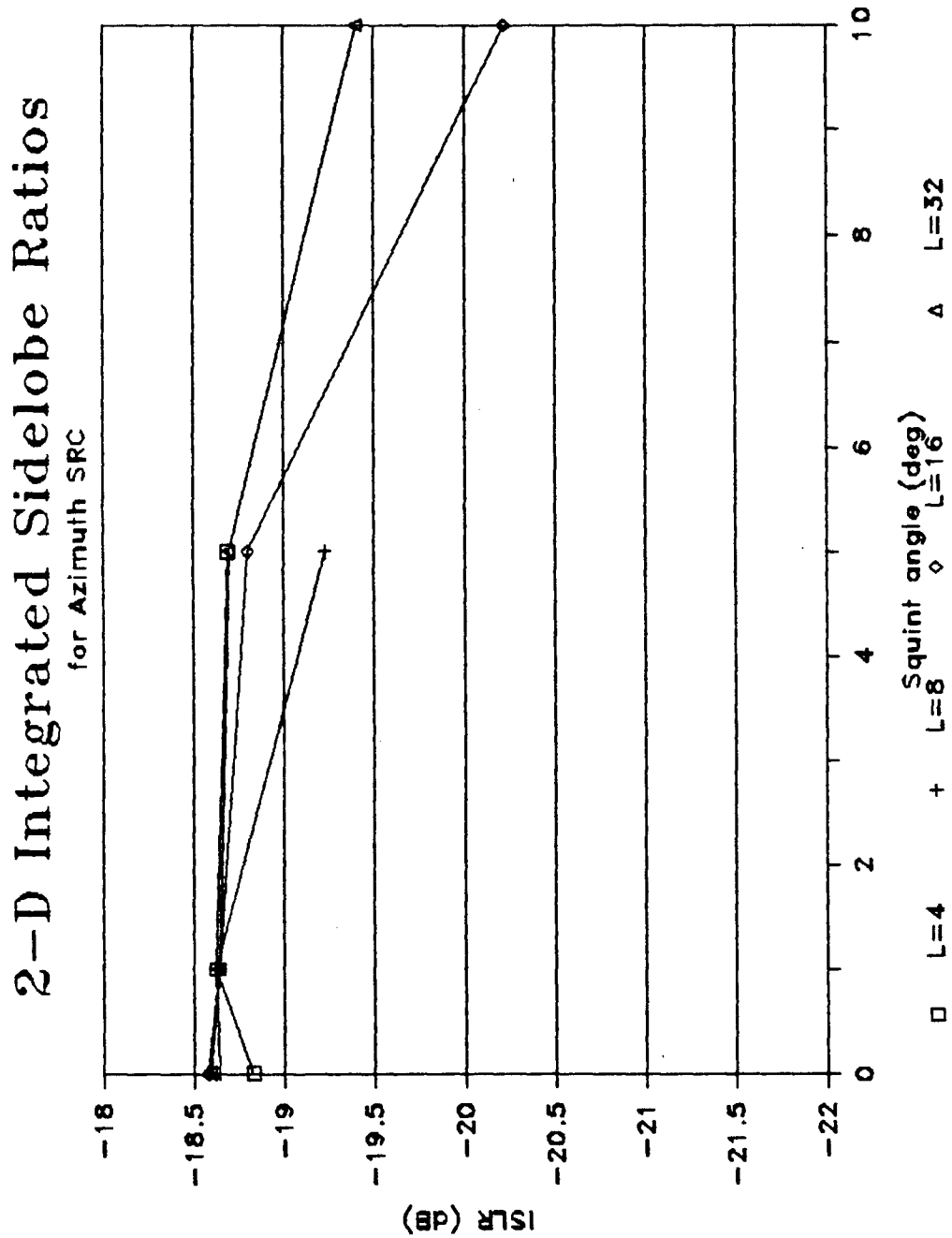

Figure 6.22. 2-D integrated sidelobe ratios for 4-look compression with both fixed and look-dependent SRC and various SRC/RCMC filter lengths as a function of squint angle.

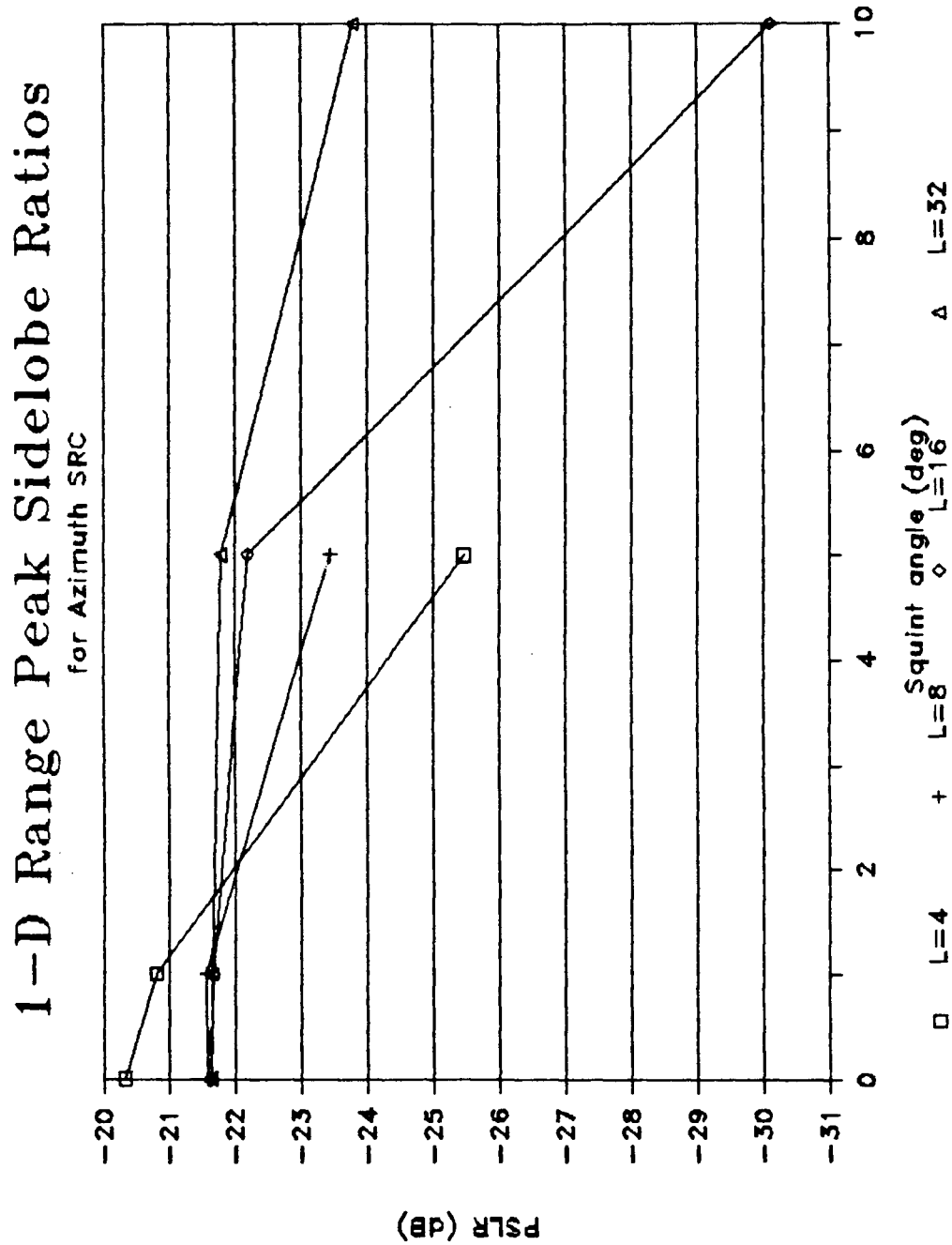

Figure 6.23. 1-D range peak sidelobe ratios for 4-look compression with both fixed and look-dependent SRC and various SRC/RCMC filter lengths as a function of squint angle.

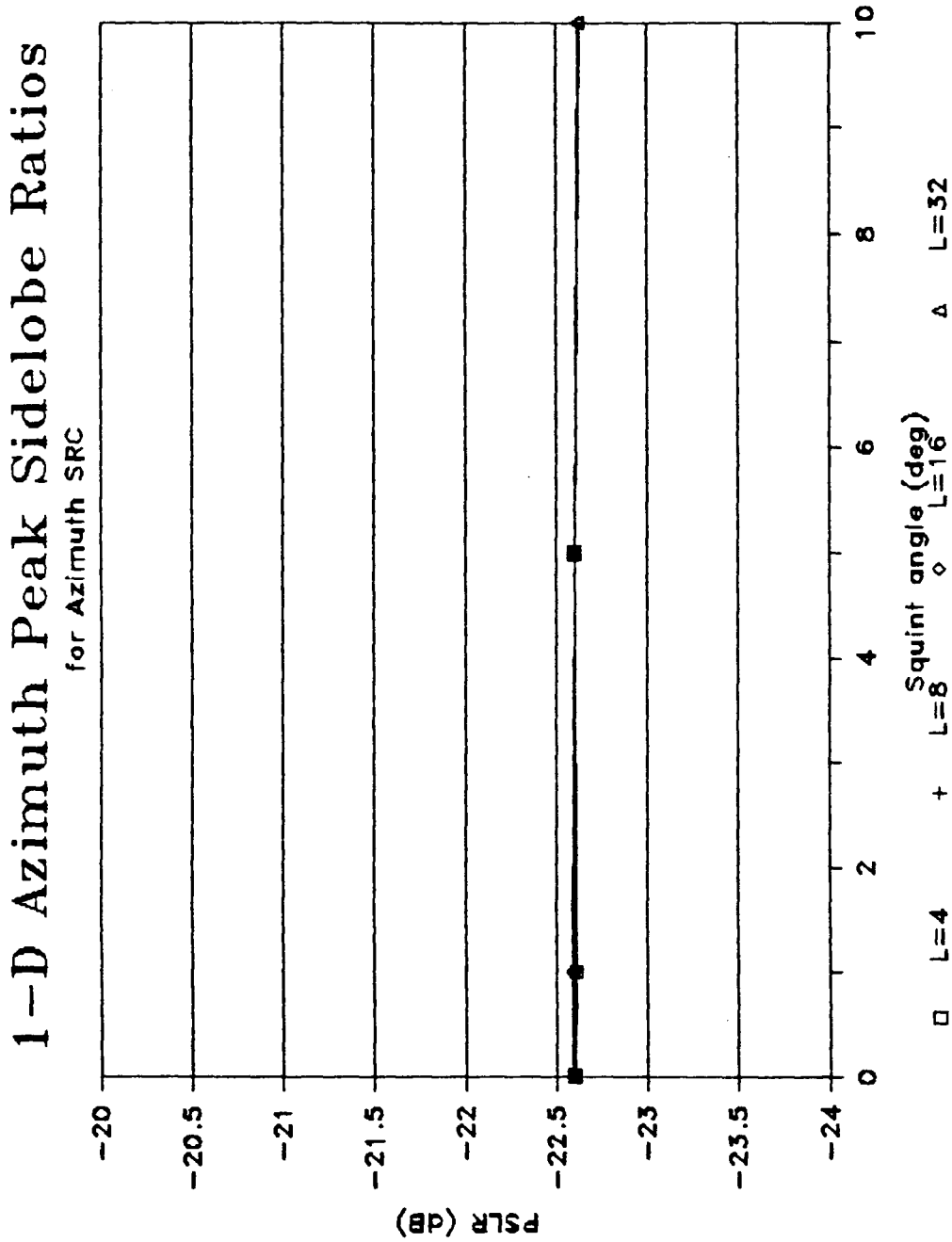

Figure 6.24. 1-D azimuth peak sidelobe ratios for 4-look compression with both fixed and look-dependent SRC and various SRC/RCMC filter lengths as a function of squint angle.

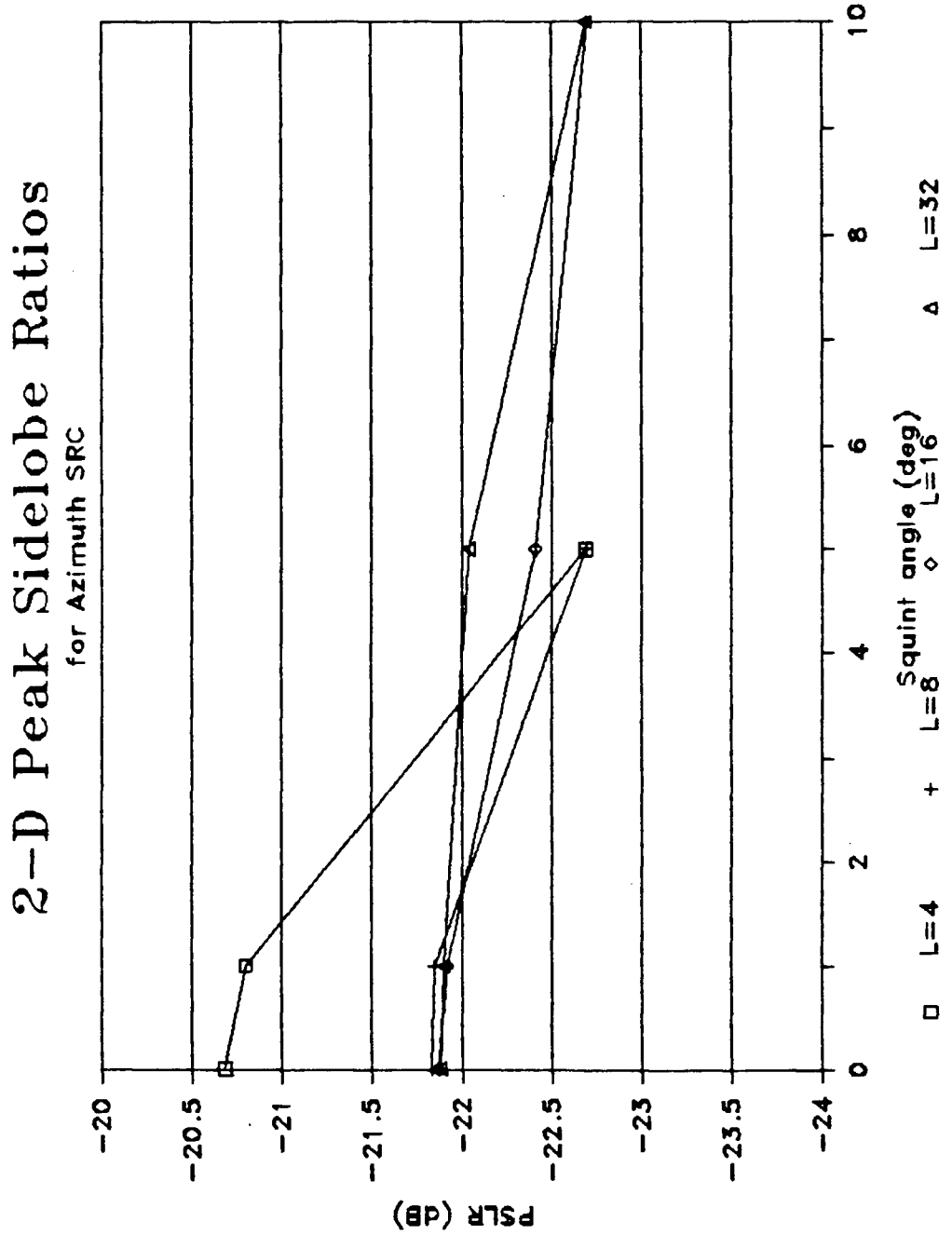

Figure 6.25. 2-D peak sidelobe ratios for 4-look compression with both fixed and look-dependent SRC and various SRC/RCMC filter lengths as a function of squint angle.

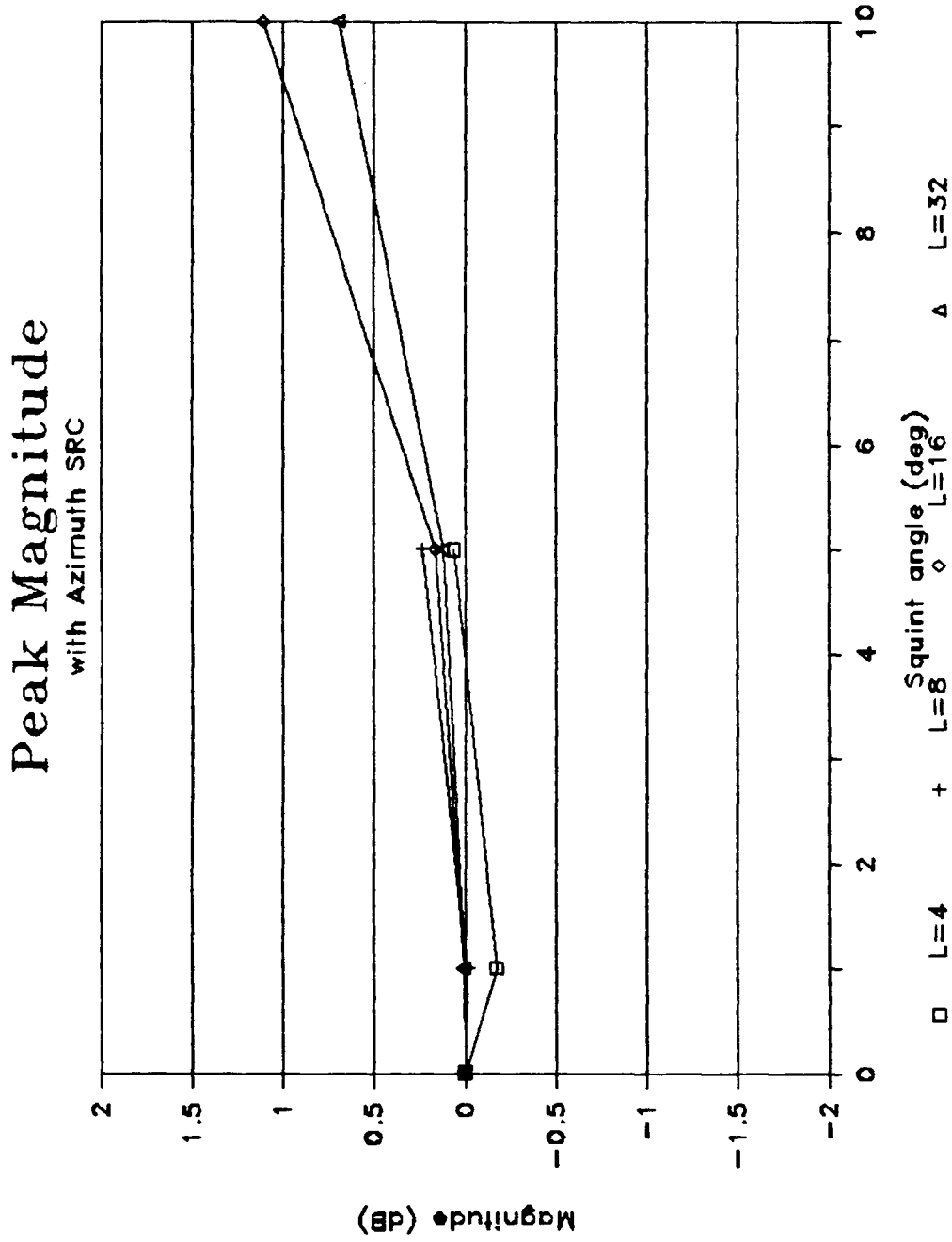

Figure 6.26. Peak magnitude ratios for 4-look compression with both fixed and look-dependent SRC and various SRC/RCMC filter lengths as a function of squint angle.

6.4 SIMULATIONS OF 4-LOOK, FIXED, RANGE SRC PROCESSING

This section presents the results of simulations of 4-look processing with a fixed range SRC algorithm.

Since the range SRC algorithm uses an SRC filter which is effectively much longer than the filter used in azimuth SRC, the range broadening caused by windowing of the SRC filter is expected to be much smaller. This was shown with the single-look range SRC simulations and is also true of the multilook implementation. Since very little broadening occurs, the range and azimuth compressed profiles are very similar to the zero squint, multilook profiles shown earlier and are therefore not shown here. Simulations are performed with a length 16 RCMC filter.

The measurements of range and azimuth broadening are summarized in figure 6.27. For squint angles up to 20° the range broadening is less than 1.8%. The integrated sidelobe ratios shown in figure 6.28 show that there is little variation in ISLR with squint angle (less than -1 dB for squint angles up to 20°). Similarly the peak sidelobe ratios summarized in figure 6.29 show an even smaller variation. Finally the peak magnitude measurements shown in figure 6.30 display only a small variation with squint angle. This indicates that there is little change in SNR for changes in squint angle.

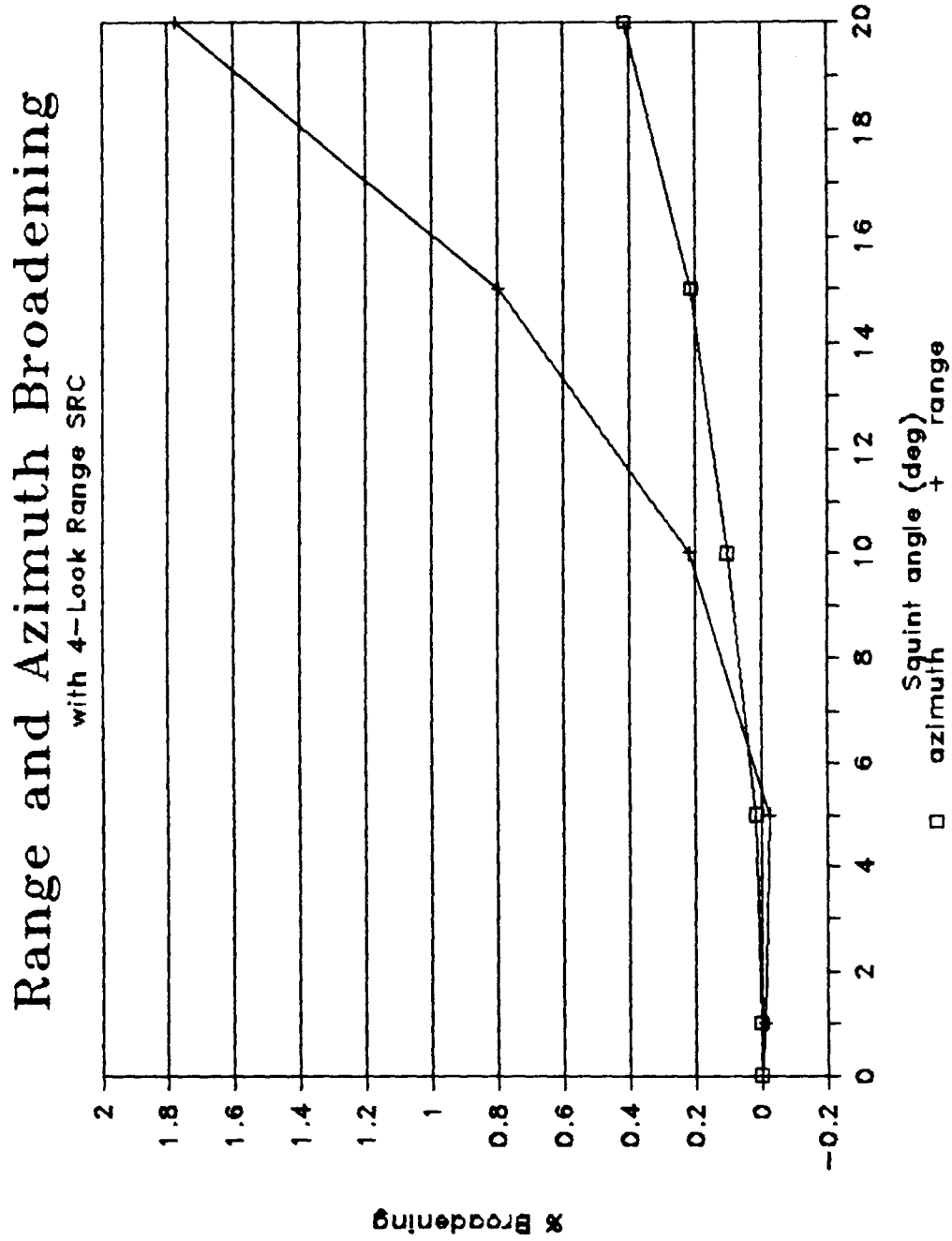

Figure 6.27. Range and azimuth broadening for 4-look compression with range SRC and a length 16 RCMC interpolator as a function of squint angle.

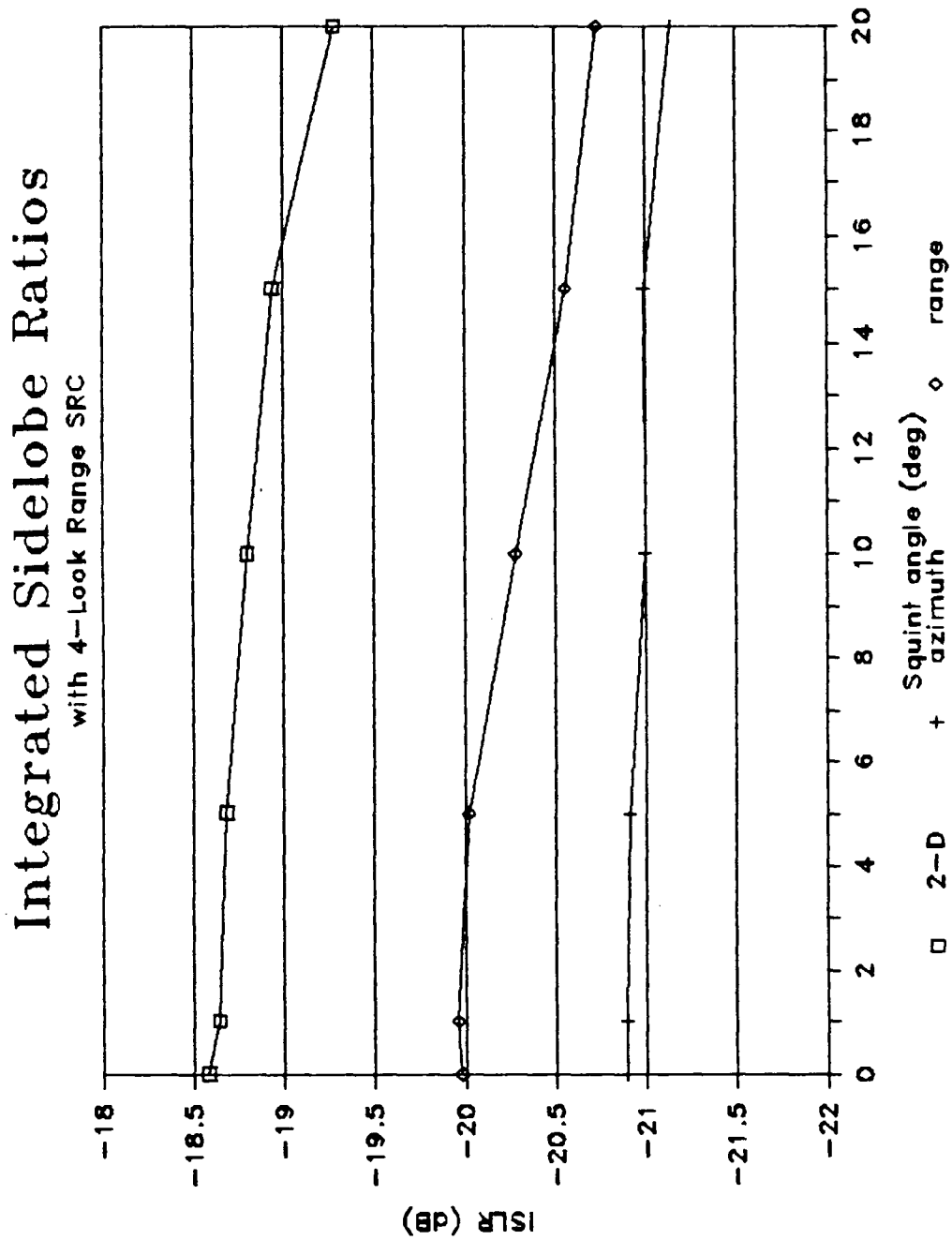

Figure 6.28. Range, azimuth, and 2-D integrated sidelobe ratios for 4-look compression with range SRC and a length 16 RCMC interpolator as a function of squint angle.

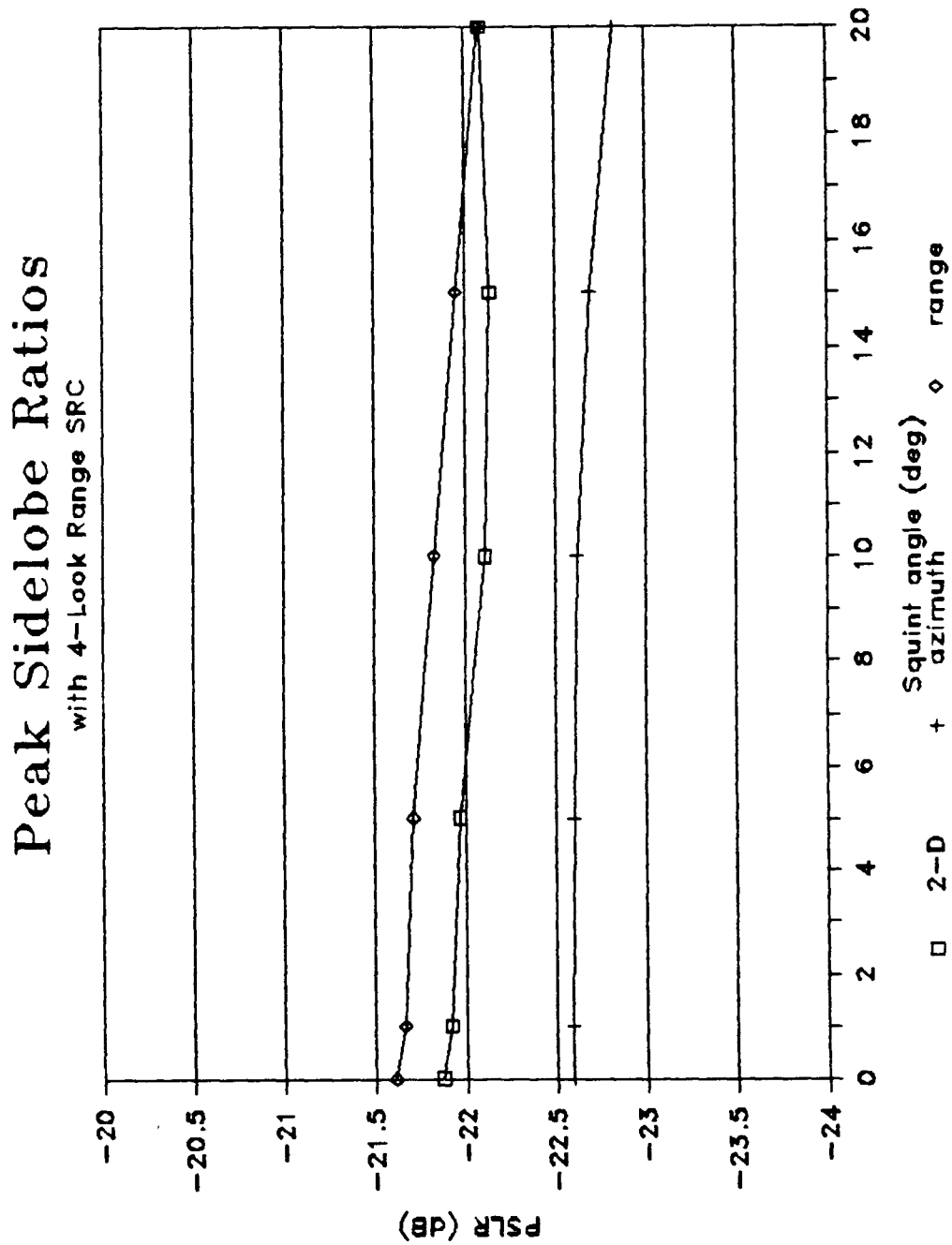

Figure 6.29. Range, azimuth, and 2-D peak sidelobe ratios for 4-look compression with range SRC and a length 16 RCMC interpolator as a function of squint angle.

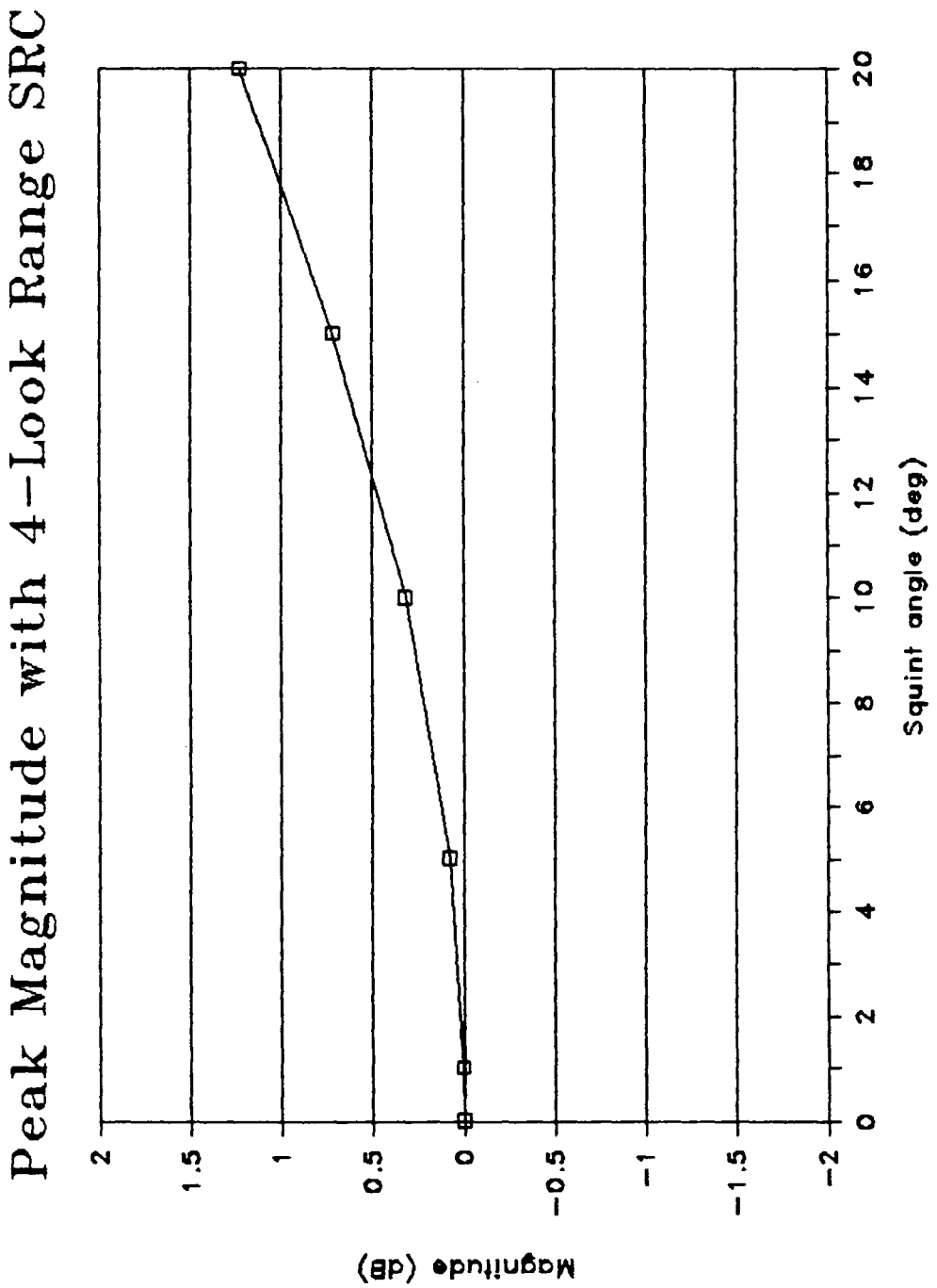

Figure 6.30. Peak magnitude degradation for 4-look compression with range SRC and a length 16 RCMC interpolator as a function of squint angle.

6.5 SUMMARY OF MULTILOOK SRC

This chapter has presented two forms of SRC algorithms to be used with multilook range/Doppler compression: fixed azimuth SRC, and look-dependent SRC. Both methods have been shown to be effective in reducing the range broadening which occurs at large squint angles. Comparisons of the simulation results of both multilook SRC algorithms for 4-look processing have shown that there are no measurable differences in image quality for RADARSAT parameters. As a result, fixed azimuth SRC should be used since it requires less memory and computation for its single SRC/RCMC filter. In fact the 4-look results are very similar in range to the single-look results indicating that the number of looks does not alter the effectiveness of the SRC algorithm.

The multilook SRC simulations show that use of the azimuth SRC algorithm can significantly reduce the point target response broadening which occurs at larger squint angles. The improvements increase with larger SRC/RCMC filter lengths since the larger filters can collect more of the energy which has been spread out by the azimuth FFT. For a nominal length 16 filter the 5% and 10% range broadening squint angles can be extended from 3.65° to 8.0° and from 4.23° to 9.3° respectively.

With the multilook range SRC algorithm the effective filter length is much longer. Thus the broadening is much less than with azimuth SRC. For squint angles up to 20° the range broadening is less than 1.8%.

7. EFFECTS OF SRC FM RATE ERRORS

This chapter examines the sensitivity of the SRC filter to SRC FM rate errors. SRC FM rate errors are caused by errors in both the beam center frequency, f_C, and the range of closest approach, r_o. Limits on the processing block size, or the invariance region, and parameter estimation errors are developed for specific broadening limits. Simulations are performed to quantify the broadening caused by SRC FM rate errors with various algorithms and filter lengths. Only errors in the SRC FM rate are simulated since the effects of parameter errors on other processing operations (e.g., RCMC, and the azimuth reference phase function) can be modelled and predicted independently.

The broadening results are parameterized in terms of the band-edge phase error in range frequency. The broadening without SRC is similarly parameterized by evaluating the equivalent band-edge phase error caused by not applying an SRC filter.

7.1 SENSITIVITY ANALYSIS OF THE SRC FM RATE

SRC FM rate errors arise from two sources : parameter estimation errors and filter invariance errors. Estimation errors occur since both the the beam center frequency, f_C, and the range of closest approach, r_o, are usually estimated from inexact measurements of the position and attitude of the radar platform. The beam center frequency estimate is often refined with a Doppler centroid estimation algorithm

[14].

SRC filter invariance errors are a result of block processing. The value of r_0 varies across the processed block but the SRC FM rate is only matched to one value of r_0, usually at the center of the block. The resulting mismatch in the SRC FM rate limits the range dimension of the processed block since point targets near the block edge become broadened. The range block size limit is called the SRC range invariance region. Both r_0 estimation errors and r_0 invariance errors must be added when determining the SRC range invariance region.

For the approximate geometric model used in this thesis, the beam center frequency is independent of r_0. However more sophisticated models predict a slow variation in beam center frequency across the processed range swath. Thus a beam center frequency invariance error can also occur. Although this error is not tabulated in this thesis, its effect can be predicted by adding the f_C invariance error to the f_C estimation error.

To examine the effects of parameter errors on the SRC filter, the SRC FM rate can be expressed in terms of f_C and r_0 as :

$$K_{SRC} = K_A c^2/(\lambda f_C)^2 \tag{119}$$

$$= - (2v_{eq}^2/[\lambda r_0]) (c/[\lambda f_C])^2 \{ 1 - (\lambda f_C/[2v_{eq}])^2 \}^{3/2} \tag{120}$$

In order to normalize the analysis to the range -3dB bandwidth, B_r, the phase of the SRC filter at the range band-edge frequency is used as a parameter. The band-edge phase is given in radians by :

$$\psi(B_r/2) = \pi(B_r/2)^2/K_{SRC} \tag{121}$$

Using partial derivatives, the band-edge phase error can be expressed approximately in terms of the beam center frequency error, Δf_C, and r_o error, Δr_o, as :

$$\Delta\psi(B_r/2) = \Delta r_o \frac{\partial}{\partial r_o}\psi(B_r/2) + \Delta f_C \frac{\partial}{\partial f_C}\psi(B_r/2) \tag{122}$$

$$= [\pi(B_r/2)^2/K_{SRC}] \bullet \{(\Delta r_o/r_o) + 2(\Delta f_C/f_C)[1 + (3/2)/[(2v_{eq}/[\lambda f_C])^2-1]]\} \tag{123}$$

Range broadening is small, typically less than 10%, when the magnitude of the band-edge phase error is less than $\pi/2$ radians. The corresponding error limits on Δf_C and Δr_o vary depending on the squint angle and the parameters used. Figures 7.1 and 7.2 show the SRC band-edge phase error in the range frequency domain for various squint angles (1° to 20°) as a function of Δf_C and Δr_o. The curves use exact calculations of the phase errors rather than the partial derivative expansion above. However the curves are almost

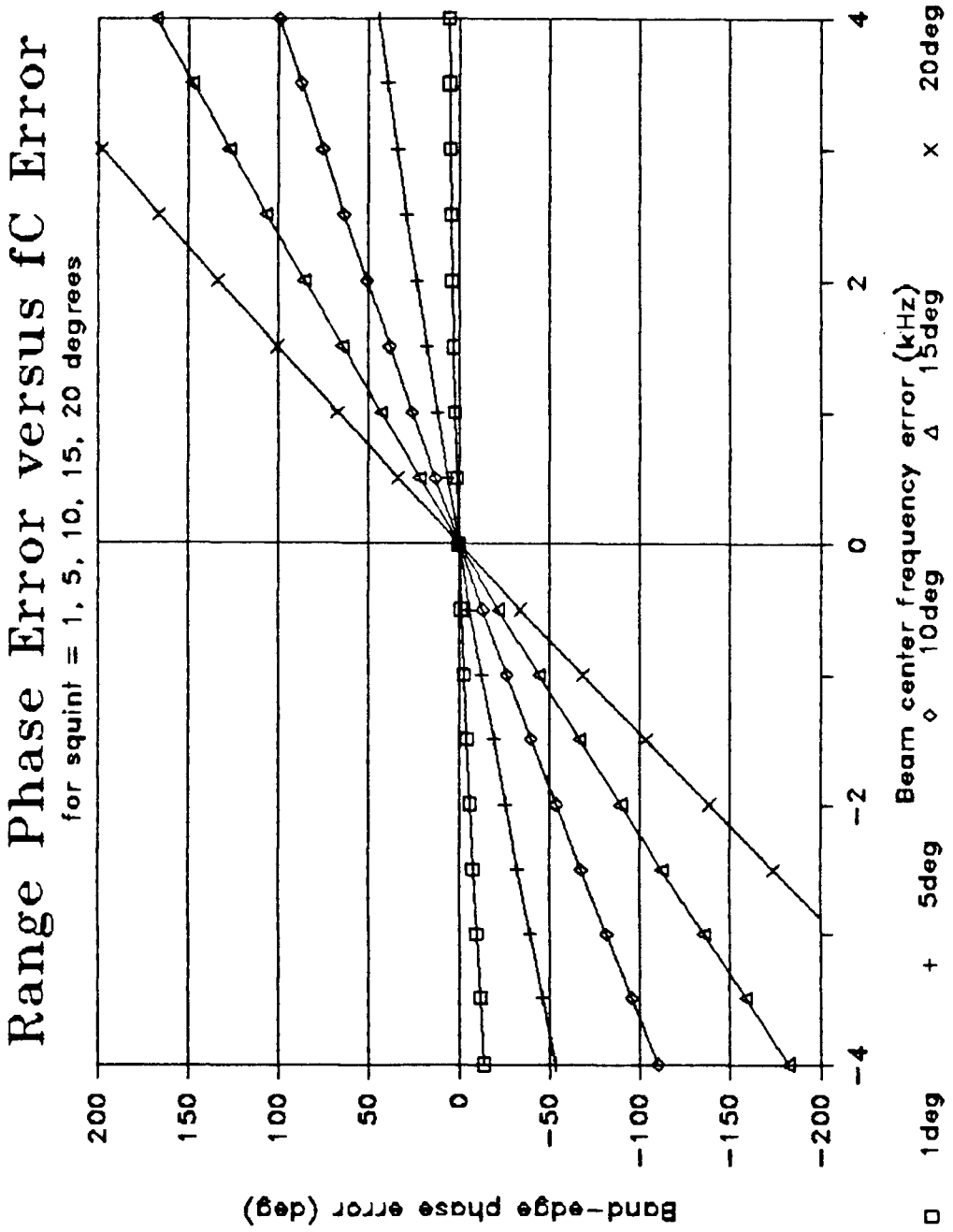

Figure 7.1. SRC band-edge phase error in the range frequency domain for squint angles of 1°, 5°, 10°, 15°, and 20° as a function of beam center frequency error.

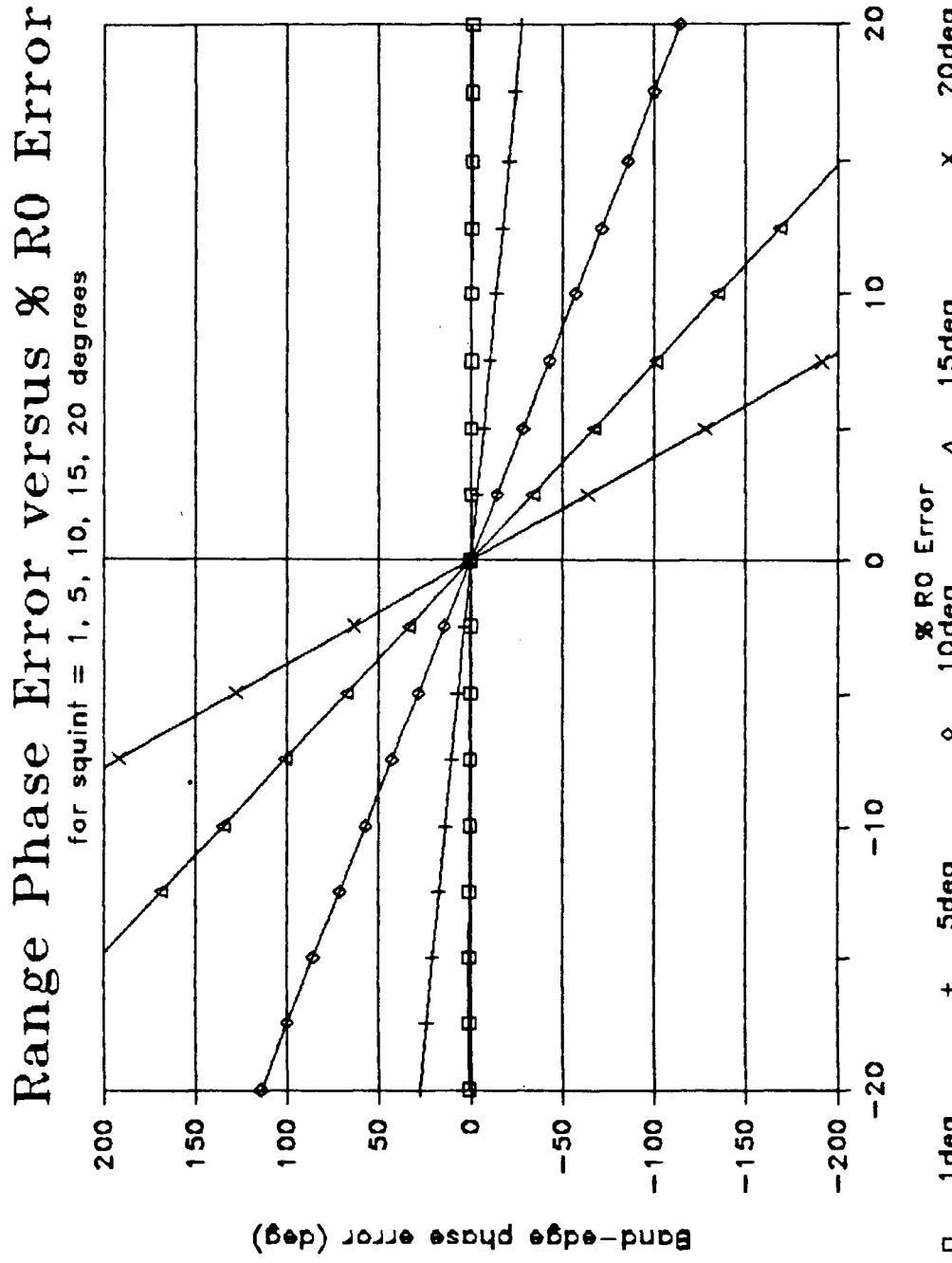

Figure 7.2. SRC band-edge phase error in the range frequency domain for squint angles of 1°, 5°, 10°, 15°, and 20° as a function of r_0 error.

linear which agrees with the partial derivative expansion. The magnitude of the phase error increases with increasing squint angle and increasing parameter error. For RADARSAT with squint angles less than 10°, the phase error is less than $\pi/2$ for beam center frequency errors less than +/- 3000 Hz and r_0 errors less than +/- 15%. The maximum expected beam center frequency error is much less (on the order of 100 Hz excluding range variances). The maximum expected r_0 is also less being on the order of +/- 5%.

More exact measurements of range broadening as a function of band-edge phase error for particular algorithms and filter lengths are performed by simulation in the next section.

The range broadening which occurs without SRC can be parameterized by an equivalent range frequency band-edge phase error. Since the broadening results in chapter 3 were shown as a function of squint angle, it is sufficient to relate the squint angle to the equivalent phase error. The error is given by the band-edge phase of the ideal SRC filter which can be computed from equation (121) by rewriting it in terms of the squint angle, θ_s, and r_0 to get :

$$\psi(B_r/2) = -2\pi(B_r/[2c])^2\lambda r_0 \tan^2\theta_s \, [1+\tan^2\theta_s]^{1/2} \qquad (124)$$

This relation is plotted in figure 7.3. The 5% and 10% range broadening squint angles given in chapter 3 correspond to

equivalent range phase errors of -74° and -100° respectively. Thus the 90° phase limit used earlier as a 10% range broadening limit is reasonably close. For comparison with the results in the next section, the broadening results without SRC are replotted in figure 7.4 as a function of equivalent range phase error instead of squint angle.

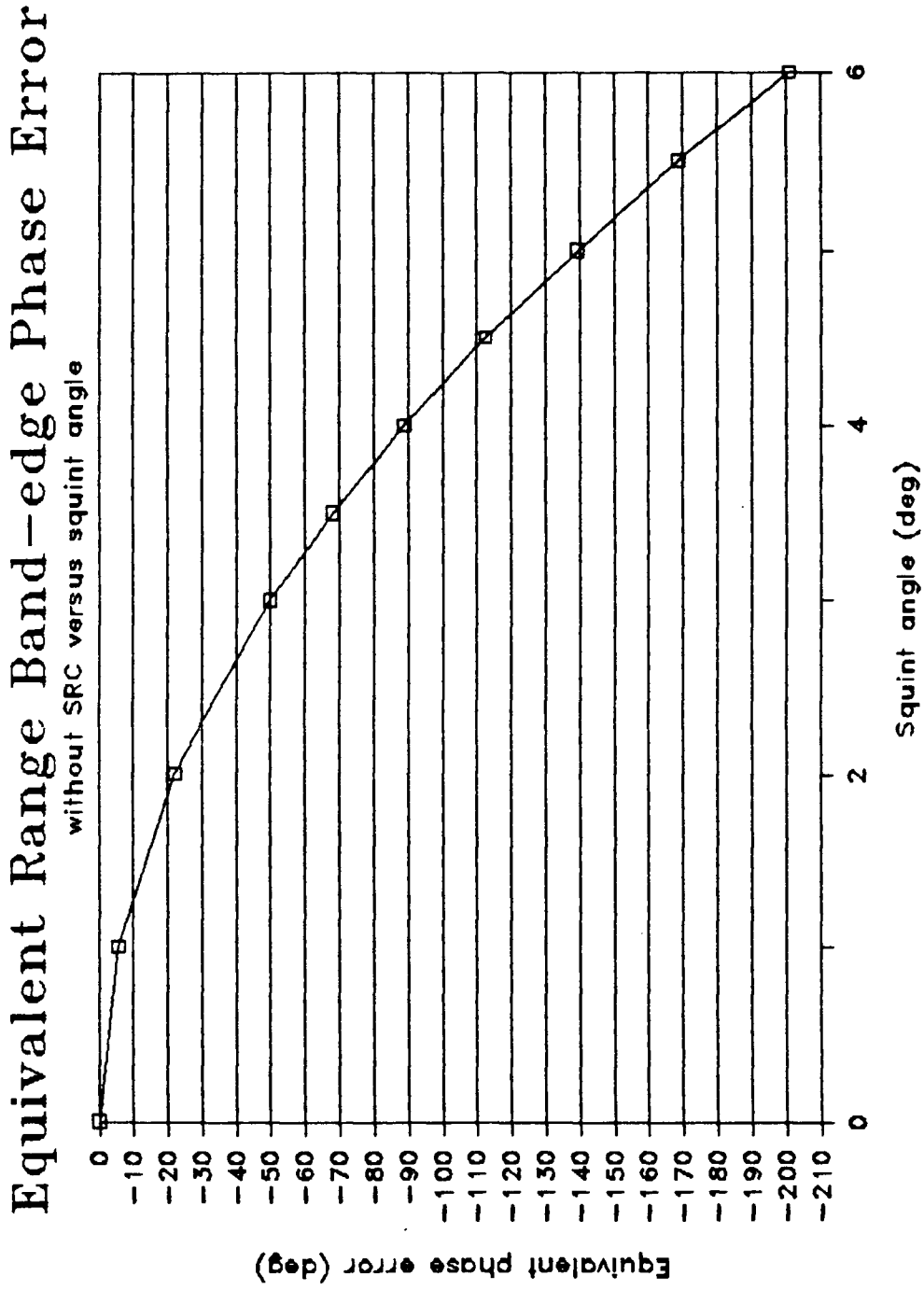

Figure 7.3. Equivalent SRC band-edge phase error in the range frequency domain without SRC as a function of squint angle.

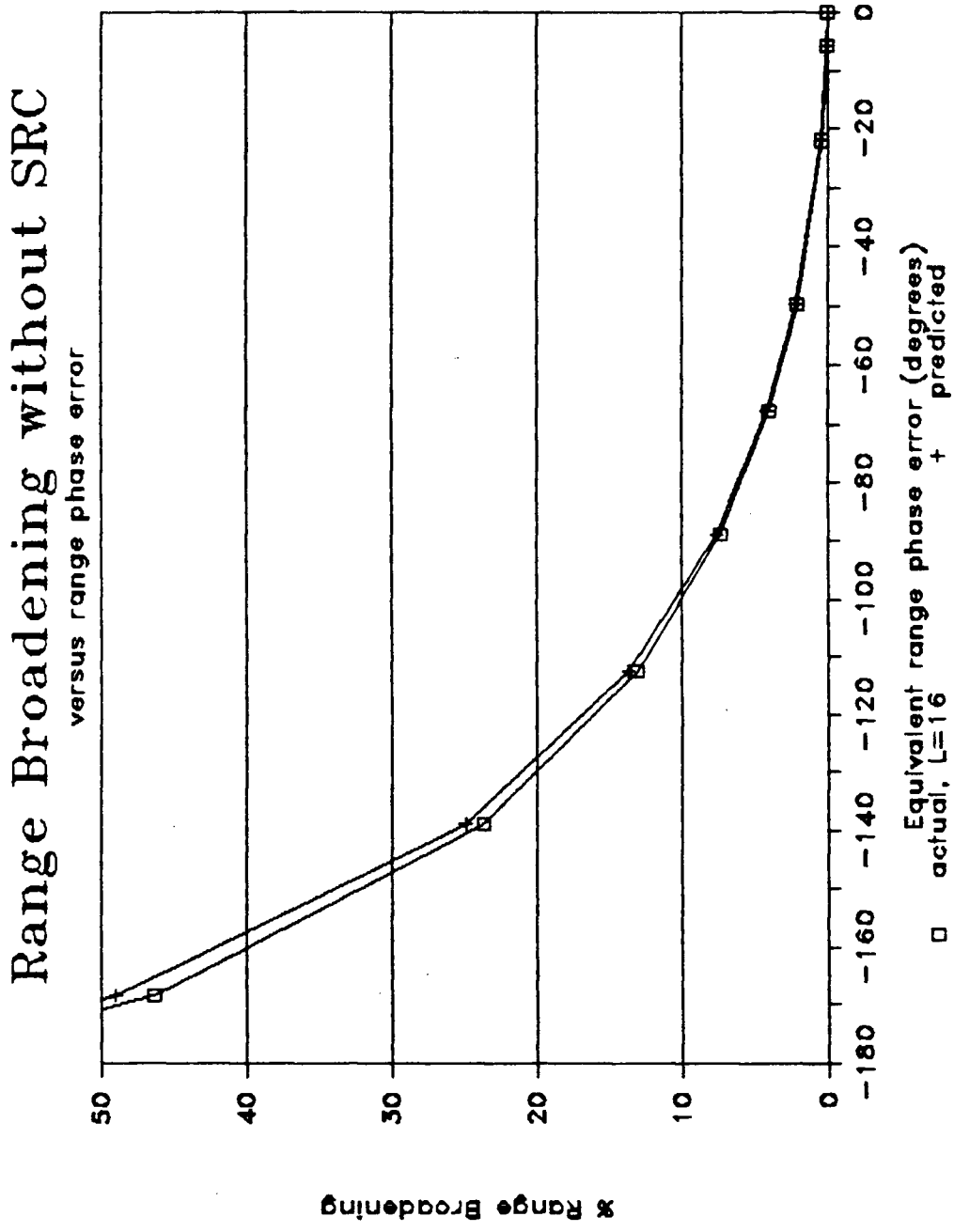

Figure 7.4. Actual range broadening without SRC with a length 16 RCMC interpolator and predicted range broadening as a function of equivalent range band-edge phase error.

7.2 SIMULATIONS OF SRC FM RATE ERROR BROADENING

This section presents simulations of range broadening caused by SRC FM rate errors with various SRC algorithms. The results indicate that the band-edge phase error in range frequency is a good general measure of the expected range broadening. The specific amount of broadening varies somewhat with the size of SRC filter and the type of SRC algorithm.

As noted earlier, parameter errors were only simulated in the SRC filter. The remainder of the processing (RCMC, azimuth reference phase multiplication, etc.) was simulated without parameter errors. Thus the measured range broadening is solely the result of SRC FM rate errors. The range broadening was measured relative to the range response width without SRC FM rate errors so that only the additional broadening caused by the FM rate error was measured. Only negative band-edge phase errors were simulated since the positive phase error results are very similar.

The first simulation involved the single-look azimuth SRC algorithm. The maximum phase error simulated for each squint angle was chosen to include largest expected error from figures 7.1 and 7.2 of the previous section. Two squint angles, 5° and 10°, were simulated. The maximum simulated phase errors were -17° for 5° of squint and -68° for 10°. The range broadening measurements are summarized by figures 7.5 and 7.6 for SRC filter lengths of 4, 8, 16, and 32 samples. At 5° of squint the range broadening is less than

2% for all filter lengths. At 10° of squint, only the longer filters (of length 16 and 32) were used since the shorter filters produced unacceptably large broadening even without SRC FM rate errors (greater than 85%). The largest range broadening (for a phase error of -68°) was less than 8%.

The azimuth SRC simulations were repeated for multilook processing with almost identical results as shown in figures 7.7 and 7.8. This identical behaviour shows the independence of the range broadening process from the look extraction process.

The next simulation was performed with the single-look range SRC algorithm. A 16 sample range interpolator was used for RCMC. Since the broadening results without errors indicated that range SRC could be used for larger squint angles, squint angles of 15° and 20° were used in addition to the 5° and 10° squints used before. The maximum simulated phase errors were again selected to include the maximum expected phase errors at each squint angle. The chosen values were -17° for 5° of squint, -68° for 10° of squint, and -136° for both 15° and 20° of squint. The range broadening is summarized in figure 7.9. The broadening levels vary only slightly with different squint angles. The maximum broadening at 10° of squint (again for a phase error of -68°) is smaller with range SRC than with azimuth SRC (less than 5% compared with 8% for azimuth SRC).

Since the multilook azimuth SRC measurements of broadening wih SRC FM rate errors were essentially the same

as the single-look results, the multilook range SRC results should also be very similar to the single-look range SRC results. Consequently the multilook range SRC algorithm was not simulated.

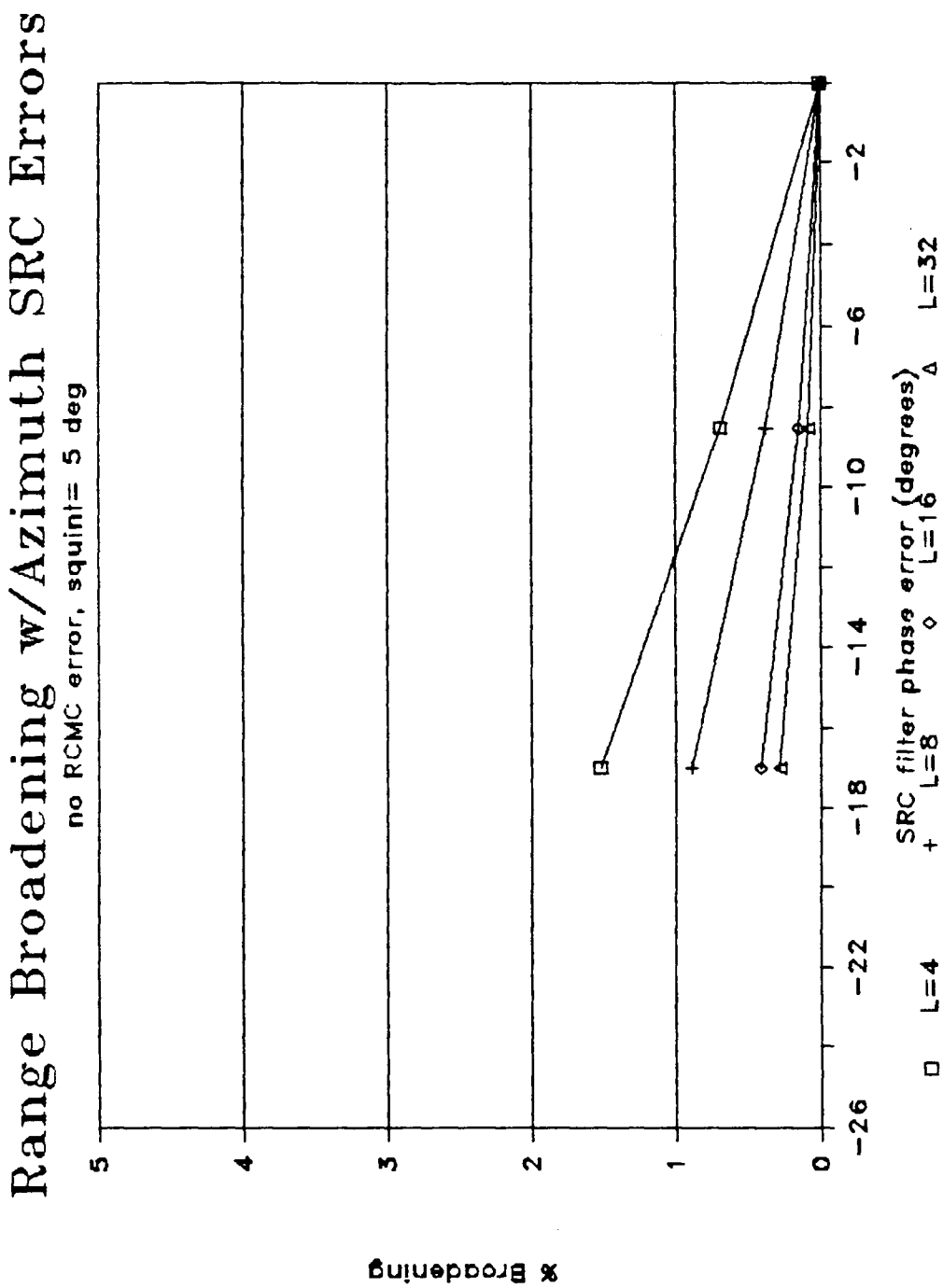

Figure 7.5. Range broadening with single-look azimuth SRC at 5° of squint with various SRC/RCMC filter lengths as a function of range band-edge phase error.

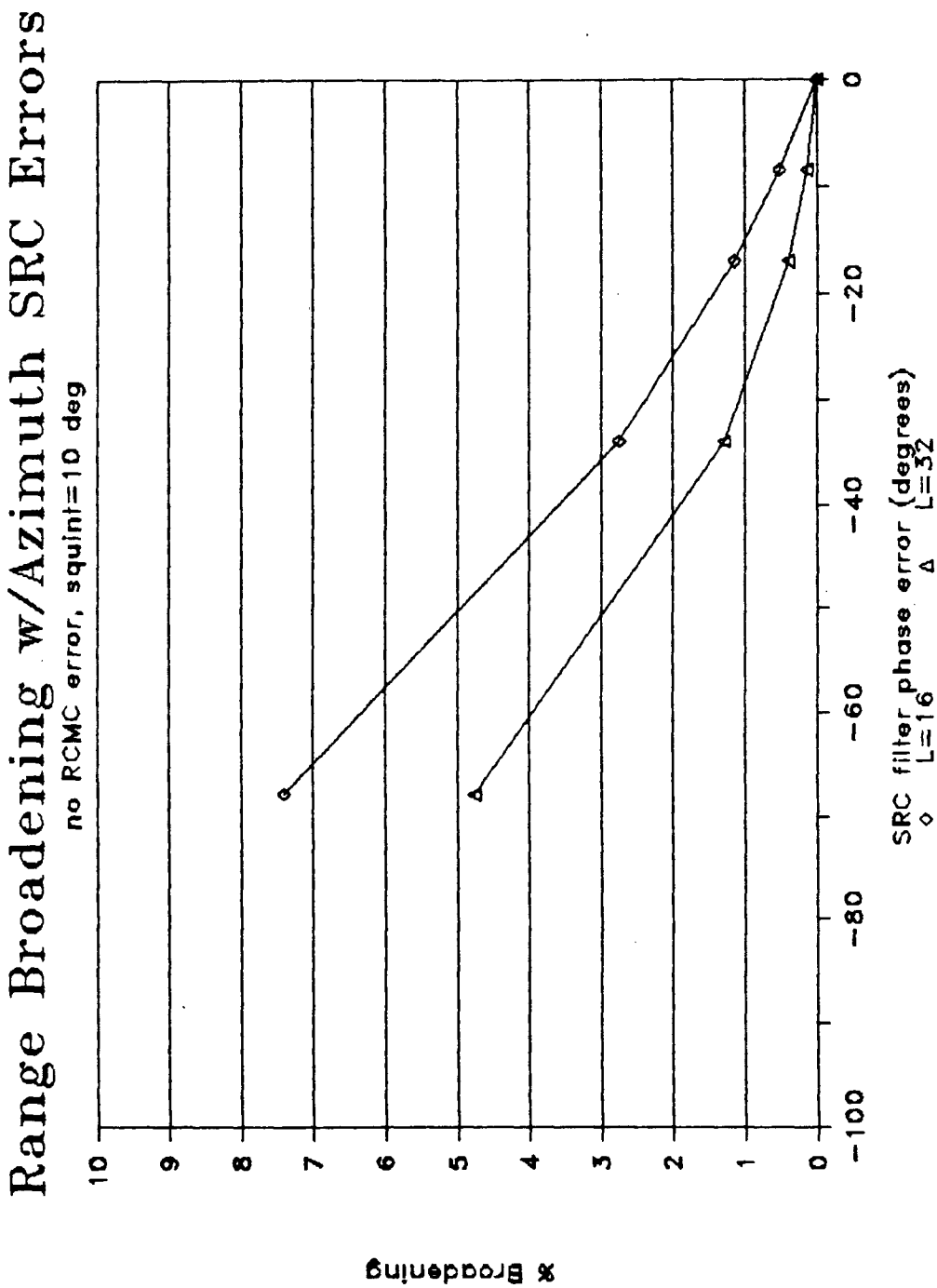

Figure 7.6. Range broadening with single-look azimuth SRC at 10° of squint with various SRC/RCMC filter lengths as a function of range band-edge phase error.

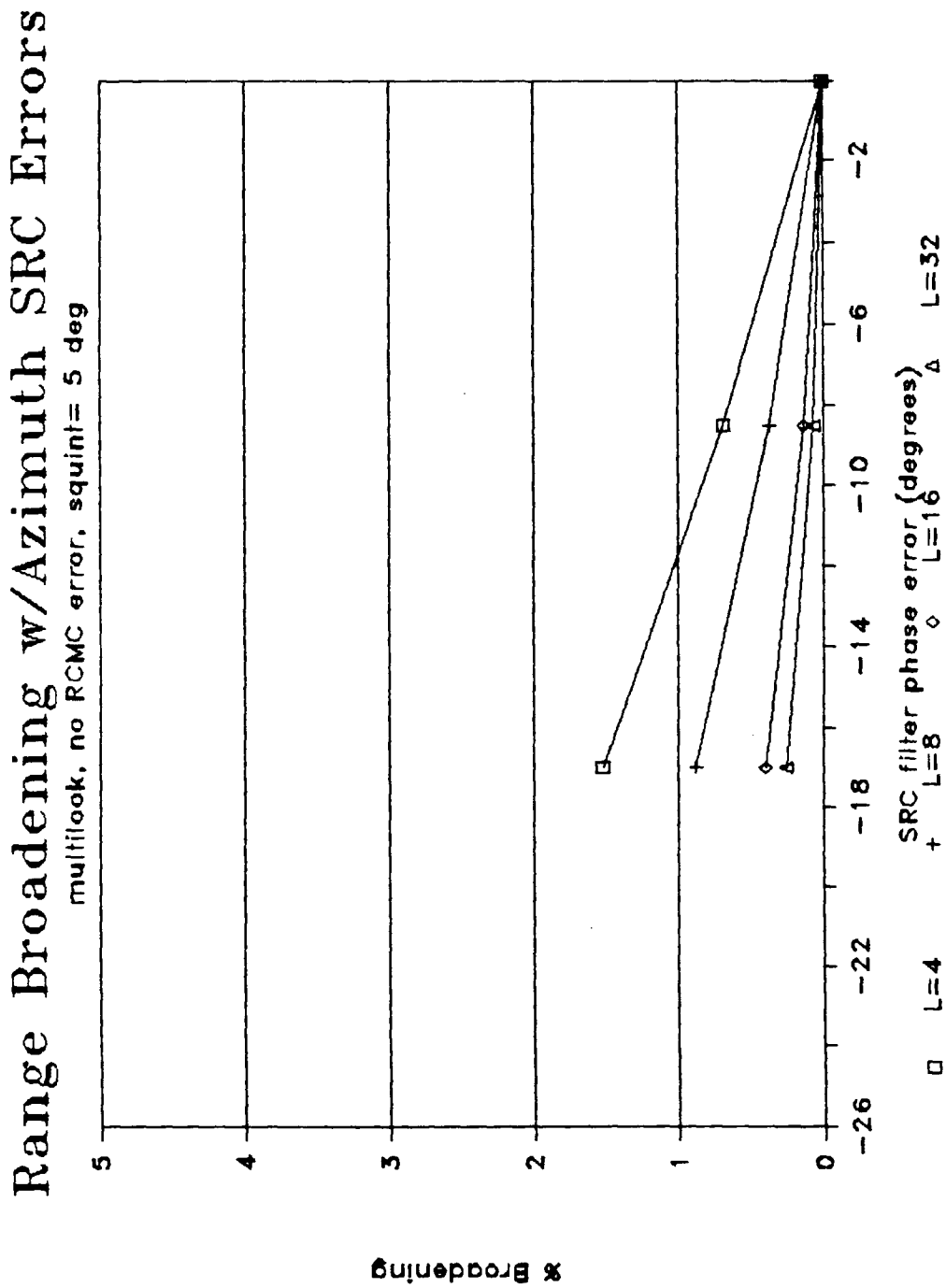

Figure 7.7. Range broadening with multilook azimuth SRC at 5° of squint with various SRC/RCMC filter lengths as a function of range band-edge phase error.

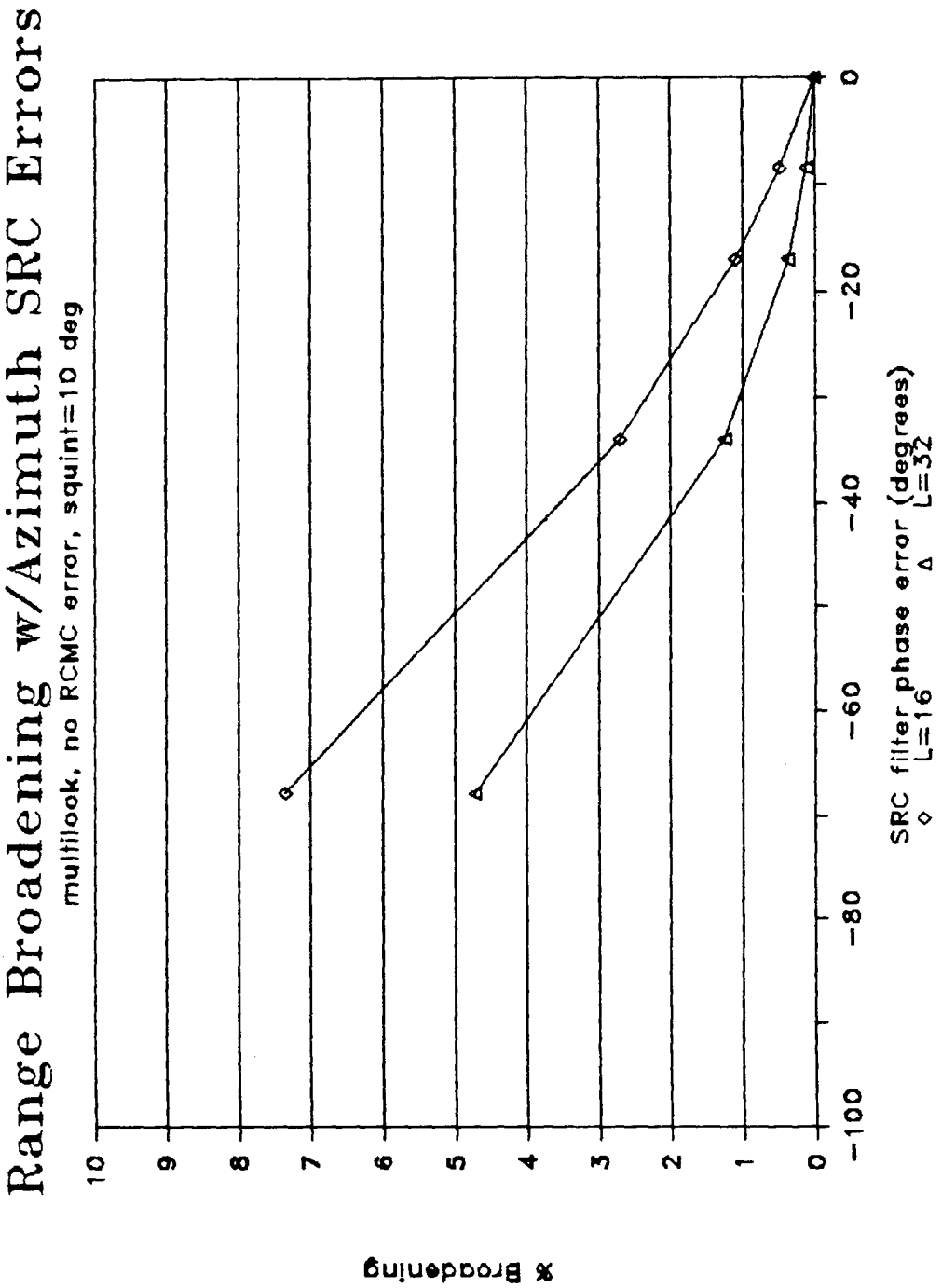

Figure 7.8. Range broadening with multilook azimuth SRC at 10° of squint with various SRC/RCMC filter lengths as a function of range band-edge phase error.

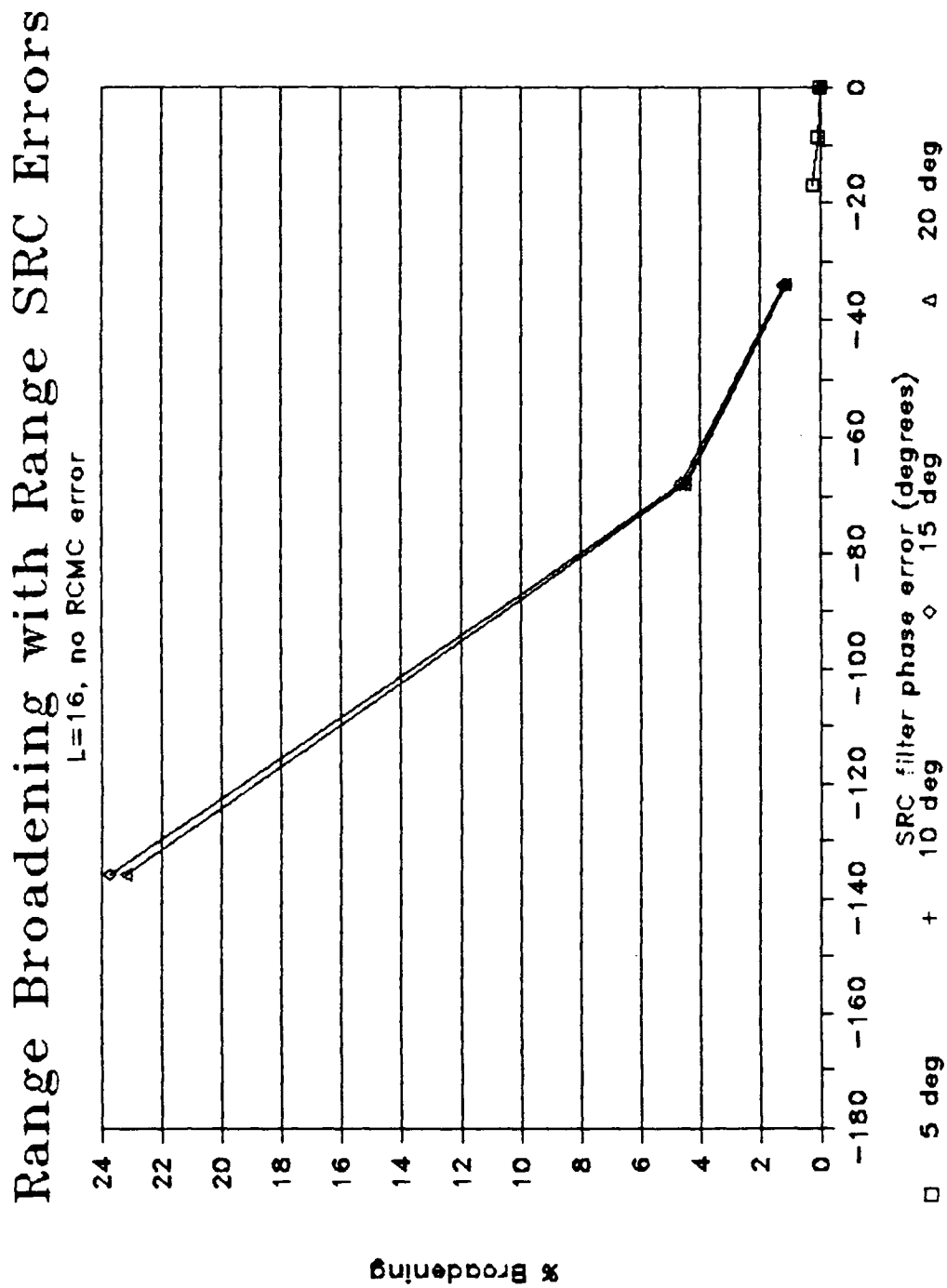

Figure 7.9. Range broadening with single-look range SRC at 5°, 10°, 15°, and 20° of squint with a length 16 RCMC interpolator as a function of range band-edge phase error.

8. SUMMARY AND CONCLUSIONS

This thesis has shown that a new algorithm, called secondary range compression (SRC), significantly reduces the amount of range broadening which occurs at large squint angles in the basic range/Doppler compression algorithm. The SRC algorithm was first suggested by Jin and Wu [13] in 1984 for use with the SEASAT SAR. This thesis has extended the theory of the SRC algorithm to examine the approximations involved and to explore alternate implementations. In addition to the azimuth SRC implementation presented by Jin and Wu, a new implementation of SRC, called range SRC, which is performed during range compression, has been presented and examined. Also, two new multilook SRC algorithms have been developed for use in multilook azimuth compression.

Many simulations with nominal RADARSAT parameters have been performed to quantify the image quality improvements possible with SRC. A sensitivity analysis of SRC with respect to parameter errors has been included. The analysis indicates that the SRC algorithm is very tolerant to parameter estimation and invariance errors. In particular, with a range broadening limit of 5%, no SRC filter updating is required over the nominal 150 km. RADARSAT ground range swath for squint angles up to 15° using the range SRC implementation (assuming an r_0 error of less than +/- 5% and a beam center frequency error of less than +/- 200 Hz).

SRC provides a closer approximation to exact matched filtering when the azimuth time-bandwidth product (TBP) of

the range compressed point target response, as measured in the range cell nearest the beam center range, falls below unity. The SRC filter is formulated by using a quadratic phase approximation of the azimuth phase coding and a linear approximation to the range migration curve over the processed azimuth bandwidth. These approximations allow the azimuth Fourier spectrum to be derived analytically. The derived spectrum accounts for the spectrum broadening which occurs with low azimuth TBP's. The basic range/Doppler algorithm without SRC does not account for azimuth spectrum broadening since it is derived with the principle of stationary phase which is valid only for large TBP signals.

It has been shown that the range bandlimited azimuth matched filter exhibits similar azimuth spectrum broadening under low azimuth TBP conditions. When range curvature is small enough that the RCM curve can be considered linear over the processed azimuth aperture, as is the case for RADARSAT, the azimuth matched filter can be projected into the range time direction. The resulting application of the SRC filter in range instead of azimuth allows shorter and more efficient filters to be used. Combination of this range filter with the frequency domain RCMC interpolator leads to the new azimuth SRC algorithm. The effectiveness of this algorithm is proportional to the length of the SRC/RCMC filter. An effectively longer SRC filter can be formed by combining the SRC filter with the range compression filter during range compression. This results in a new range SRC

algorithm. When the range pulse is a large TBP linear FM signal as for RADARSAT the combined SRC/range compression filter differs from the original range compression filter only by a small change in linear FM rate.

Computer simulations with nominal RADARSAT parameters have verified the accuracy of the new SRC algorithms for a variety of filter parameters and squint angles. For single-look azimuth SRC processing with a 16 point SRC/RCMC filter, it was found that the squint angles which produce 5% and 10% range broadening can be extended from 3.65° and 4.23° respectively without SRC to 8.03° and 9.29° respectively with azimuth SRC. For single-look range SRC processing with a 16 point RCMC interpolator, the range broadening was shown to less than 1.3% for squint angles up to 20°, which is the largest squint angle simulated. The simulations of multilook SRC processing showed very similar results indicating that the separation of looks does not greatly affect the range broadening process. Somewhat surprisingly, the simulations showed that negligible azimuth broadening is caused by the azimuth spectrum broadening of the azimuth FFT. This indicates that frequency domain RCMC, with or without SRC, adequately extracts the azimuth phase spectrum along the RCM curve for compression in azimuth.

8.1 RECOMMENDATIONS FOR FURTHER RESEARCH

Since the concept of SRC is relatively new, several areas remain to be examined further.

The approximate geometric model used in this thesis, which assumes a locally flat earth below the radar platform, could be replaced with a more refined model which accounts for parameter variations over the curved earth. One alternative would be to use a consistent approximation to the range migration equation based on an ellipsoidal earth model such as presented by Barber [2]. Rather than the flat earth hyperbolic equation used here, a Taylor series approximation to the ellipsoidal model with several terms could be used. Such a model could also be used to incorporate satellite motions outside of the nominal orbit. The refined model would be useful for deriving more accurate filter parameters, especially for spaceborne SARs, and for determining more precise bounds on signal parameter errors and variations over the range and azimuth swaths.

In azimuth SRC and in range/Doppler processing without SRC, the SRC/RCMC filter is windowed in the range time domain in order to reduce the number of coefficient multiplications. This causes additional range broadening of the point target response. The action of the window is only partially understood and its optimality has not been established. It may be possible to develop a method of compensating for the range broadening effects of the window by modifying the SRC/RCMC filter spectrum before windowing.

Since one of the effects of the window is to taper the filter amplitude spectrum, the filter spectrum could be predistorted by amplifying the higher frequencies before windowing in order to obtain a spectrum closer to the ideal flat spectrum after windowing.

Finally the SRC algorithm has been examined for nominal RADARSAT parameters which involve very little range curvature over the processed azimuth bandwidth. Since the SRC filter is derived using a linear RCM assumption and a quadratic azimuth phase assumption, range curvature and higher order effects may be more significant in systems which exhibit larger range curvature such as longer wavelength spaceborne SAR's. Simulations of systems with much larger wavelengths should be performed to determine the limits to the above assumptions.

Bibliography

[1] D.A. Ausherman, A. Kozma, J.L. Walker, H.M. Jones, E.C. Poggio, "Developments in radar imaging", IEEE Trans. Vol. AES-20, No. 4, July 1984.

[2] B.C. Barber, "Theory of digital imaging from orbital synthetic-aperture radar", Int. J. Remote Sensing, Vol. 6, No. 7, 1985.

[3] G.A. Bendor, T.W. Gedra, "Single-pass fine-resolution SAR autofocus", IEEE National Aerospace and Electronics Conference, 1983, pp. 482-8.

[4] J.R. Bennett, I.G. Cumming, "A digital processor for the production of SEASAT synthetic aperture radar imagery", Symposium on Machine Processing of Remotely Sensed Data.

[5] J.R. Bennett, I.G. Cumming, "Digital techniques for the multi-look processing of SAR data with application to SEASAT-A", 5th Canadian Symposium on Remote Sensing, Victoria, B.C., Aug. 1978, pp. 506-516.

[6] J.R. Bennett, I.G. Cumming, R.A. Deane, "The digital processing of SEASAT synthetic aperture radar data", IEEE International Radar Conference, 1980, pp. 168-175.

[7] D.J. Bonfield, J.R.E. Thomas, "Synthetic-aperture-radar real-time processing", IEE Proc., Vol. 127, Pt. F, No. 2, April 1980.

[8] K.R. Carver, C. Elachi, F.T. Ulaby, "Microwave remote sensing from space", Proc. IEEE, Vol. 73, No. 6, June 1985.

[9] C.E. Cook, M. Bernfeld, Radar signals: an introduction to theory and application, Academic Press, New York, 1967.

[10] I.G. Cumming, J.R. Bennett, "Digital processing of SEASAT SAR data", Proc. of IEEE ICASSP, Washington, D.C., 1979, pp. 710-718.

[11] C. Elachi, T. Bicknell, R.L. Jordan, C. Wu, "Spaceborne

synthetic-aperture imaging radars: applications, techniques, and technology", Proc. IEEE, Vol. 70, No. 10, Oct. 1982.

[12] F.J. Harris, "On the use of windows for harmonic analysis with the discrete Fourier transform", IEEE Proc. Vol. 66, No. 1, Jan. 1978.

[13] M. Jin, C. Wu, "A SAR correlation algorithm which accomodates large-range migration", IEEE Trans. Vol. GE-22, No. 6, Nov. 1984.

[14] P.F. Kavanagh, "Doppler centroid ambiguity estimation for synthetic aperture radar", Master's thesis, University of British Columbia, Canada, Aug. 1985.

[15] J.C. Kirk, "A discussion of digital processing in synthetic aperture radar", IEEE Trans. Vol. AES-11, No. 3, May 1975.

[16] C.J. Oliver, "Fundamental properties of high-resolution sideways-looking radar", IEE Proc., Vol. 129, Pt. F, No. 6, Dec. 1982.

[17] A. Papoulis, Signal Analysis, McGraw-Hill, 1977.

[18] R.K. Raney, "Processing synthetic aperture radar data", URSI Open Symposium on Remote Sensing, Washington D.C., Aug. 1981.

[19] M. Sack, M.R. Ito, I.G. Cumming, "Application of efficient linear FM matched filtering algorithms to synthetic-aperture radar processing", IEE Proc., Vol. 132, Pt. F, No. 1, Feb. 1985.

[20] K. Tomiyasu, "Tutorial review of synthetic-aperture radar (SAR) with applications to imaging of the ocean surface", Proc. IEEE, Vol. 66, No. 5, May 1978.

[21] W.J. van de Lindt, "Digital techniques for generating synthetic aperture radar images", IBM J. Res. Develop., Sept. 1977.

[22]M.R. Vant, P. George, "The RADARSAT prototype synthetic-aperture radar signal processor", IGARSS '84.

[23]M.R. Vant, G.E. Haslam, "A theory of 'squinted' synthetic-aperture radar", Communications Research Centre, Dept. of Communications, Canada, Report No. 1339, Nov. 1980.

[24]C. Wu, "A digital approach to produce imagery from SAR data", AIAA System Design Driven by Sensor Conference, Paper 76-968, Pasadena, CA, Oct. 1976.

[25]C. Wu, B.Barkan, W.J. Karplus, D. Caswell, "SEASAT synthetic-aperture radar data reduction using parallel programmable array processors", IEEE Trans. Vol. GE-20, No. 3, July 1982.

[26]C. Wu, K.Y. Liu, M. Jin, "Modeling and a correlation algorithm for spaceborne SAR signals", IEEE Trans. Vol. AES-18, No. 5, Sep. 1982.